



저작자표시-비영리-변경금지 2.0 대한민국

이용자는 아래의 조건을 따르는 경우에 한하여 자유롭게

- 이 저작물을 복제, 배포, 전송, 전시, 공연 및 방송할 수 있습니다.

다음과 같은 조건을 따라야 합니다:



저작자표시. 귀하는 원저작자를 표시하여야 합니다.



비영리. 귀하는 이 저작물을 영리 목적으로 이용할 수 없습니다.



변경금지. 귀하는 이 저작물을 개작, 변형 또는 가공할 수 없습니다.

- 귀하는, 이 저작물의 재이용이나 배포의 경우, 이 저작물에 적용된 이용허락조건을 명확하게 나타내어야 합니다.
- 저작권자로부터 별도의 허가를 받으면 이러한 조건들은 적용되지 않습니다.

저작권법에 따른 이용자의 권리는 위의 내용에 의하여 영향을 받지 않습니다.

이것은 [이용허락규약\(Legal Code\)](#)을 이해하기 쉽게 요약한 것입니다.

[Disclaimer](#)

이학박사학위논문

**Development of Novel Fluorene-
Containing HCV NS5A Inhibitors and
Synthesis of New AIE-Based Organic
Fluorophores for Bioimaging**

플루오렌 구조를 포함하는 새로운 C형간염 NS5A
저해제 개발 및 생체영상화를 위한
응집유도발광 기반의 새로운 유기 형광체의 합성

2023년 2월

서울대학교 대학원
화학과 유기화학전공
김 병 욱

Development of Novel Fluorene-
Containing HCV NS5A Inhibitors and
Synthesis of New AIE-Based Organic
Fluorophores for Bioimaging

플루오렌 구조를 포함하는 새로운 C형 간염
NS5A 저해제 개발 및 생체영상화를 위한
응집유도발광 기반의 새로운 유기형광체의 합성

지도교수 김 병 문

이 논문을 이학박사 학위논문으로 제출함
2022 년 12 월

서울대학교 대학원
화학과 유기화학 전공
김 병 옥

김병옥의 박사학위논문을 인준함
2023 년 2 월

위 원 장	_____	(인)
부 위 원 장	_____	(인)
위 원	_____	(인)
위 원	_____	(인)
위 원	_____	(인)

Abstract

Development of Novel Fluorene-Containing HCV NS5A Inhibitors and Synthesis of New AIE-Based Organic Fluorophores for Bioimaging

Kim, Byeong Wook

Organic Chemistry Major

Department of Chemistry, College of Natural Sciences

Seoul National University

This dissertation describes our research results in two parts: I) approaches to the development of HCV NS5A inhibitors, and II) efforts to discover new organic fluorophores.

The first part delineates our efforts to develop a series of potent compounds inhibiting HCV NS5A. In **Chapter II**, we examined the mutagenicity of 9-substituted 2,7-diaminofluorene and diaminocarbazole derivatives to circumvent genotoxicity problem during our recent drug development program. Among 28 derivatives examined, 9,9-dibutyl-9*H*-fluorene-2,7-diamine was chosen as the most suitable core structure of the new HCV NS5A inhibitors. In **Chapter III**, we describe the synthesis of a series of compounds and evaluation of antiviral activity via various

in vitro and *in vivo* assays. We found that compound **III-10b** exhibits excellent inhibitory activity toward the mutated NS5A strains such as those containing L31V, Y93H and even L31V+Y93H.

The second part discusses our approaches toward the design of new fluorophores for novel bioimaging studies. In **Chapter IV**, our efforts to design the new NIR fluorophore, **DVM-1**, are reported. Because **DVM-1** showed no emission in aqueous media, an encapsulated form (**DVM-1L**) was made for application to bioimaging. **DVM-1L** showed good water solubility and strong emission peak was recorded at the NIR region. In addition, it exhibited bright fluorescence signal within the cytosol of cells. In **Chapter V**, our studies are described on the articulated structure of D-A type dipolar dye with AIEgen. Fluorophores (**DA-AIE-M** and **DA-AIE-D**) linked between D-A type dipolar dye and an AIEgen via sp^3 bond were synthesized. Their photophysical properties were characterized by the D-A type fluorophore, because HOMO and LUMO structures were dictated by the D-A type dipolar dye. In **Chapter VI**, our efforts to develop AIE-based ATP sensing probe are described. **TPE-TA** was designed based on AIEgen (**TPE**) and triamine moiety because the triamine moiety can bind triphosphate group selectively. Contrary to our expectation, **TPE-TA** existed as an aggregated form (**AAP-1**) in aqueous media and **AAP-1** was applied successfully to the sensing and imaging of ATP in biological media and even in cancer cells and human embryonic stem cells.

Keywords: Mutagenicity, NS5A inhibitor, Fluorescent probes, NIR probe, Aggregation-induced emission.

Student Number: 2017-26933

Table of Contents

Abstract	1
Table of Contents	3
List of Figures	6
List of Tables	9
List of Schemes	10
List of Abbreviations	12
Chapter I. Introduction	17
I. Development of New HCV NS5A Inhibitors Embedding Fluorene.....	18
II. Synthesis of New Organic Fluorophores for Bioimaging	21
Chapter II. SAR Studies on the Mutagenic Properties of 2,7-Diaminofluorene and 2,7-Diaminocarbazole Derivatives	24
I. Introduction	25
II. Results and Discussion	27
1. Preparation of diamine compounds.....	27
2. Ames test results of diamine compounds.....	32
III. Conclusion	39
IV. Experimental Section	39

Chapter III. Development of Potent HCV NS5A Inhibitors Containing a Fluorene Skeleton	67
I. Introduction	68
II. Results and Discussion	69
1. Preparation of HCV NS5A inhibitors	69
2. SAR studies	72
3. Biological evaluation of compound III-10b	77
III. Conclusion	82
IV. Experimental Section	82
Chapter IV. Liposomal-Encapsulated NIR Fluorophore Based on π-Extended Dipolar Naphthalene Platform and its Imaging Applications in Human Cancer Cells	88
I. Introduction	89
II. Results and Discussion	90
1. Preparation of DVM-1 and DVM-1L	90
2. Photophysical properties of DVM-1 and DVM-1L	91
3. Bioimaging application of DVM-1L	95
III. Conclusion	97
IV. Experimental Section	97
Chapter V. Articulated Structures of D-A Type Dipolar Dye with AIEgen: Synthesis, Photophysical Properties, and Applications.....	102
I. Introduction	103
II. Results and Discussion	105

1. Material design.....	105
2. Preparation of compounds.....	106
3. Spectroscopic studies	106
4. Quantum chemical calculation.....	109
5. Proposed mechanism.....	111
6. Sensing applications in real water samples	113
III. Conclusion	116
IV. Experimental Section.....	116
Chapter VI. AIEgen-Based Nanoprobe for the ATP Sensing and Imaging in Cancer Cells and Embryonic Stem Cells	121
I. Introduction.....	122
II. Results and Discussion	125
1. Material design.....	125
2. Preparation of TPE-TA	126
3. Sensing properties of AAP-1	126
4. CLSM imaging of ATP in cancer cells	132
5. CLSM imaging of ATP in embryonic stem cells.....	133
III. Conclusion	135
IV. Experimental Section.....	135
Reference	141
Appendix	170
국문초록	207

List of Figures

Chapter II

Figure II-1. Chemical structure of daclatasvir (Compound **II-1**).

Chapter III

Figure III-1. PK profile of Compound **III-10b**.

Figure III-2. Prodrug of Compound **III-10b** (Compound **III-20**).

Figure III-3. PK profile of Compound **III-20**.

Chapter IV

Figure IV-1. Molecular structures of the FDNP, dicyanomethylene-4*H*-pyran (DCMP), and **DVM-1**.

Figure IV-2. Schematic illustration for the preparation of **DVM-1L**.

Figure IV-3. UV/Vis absorption and emission spectra of **DVM-1** in various solvents at 25 °C.

Figure IV-4. UV/Vis absorption and emission spectra of **HyP-1** in various solvents at 25 °C

Figure IV-5. UV/Vis absorption and emission spectra of **HyP-1** and **DVM-1** within various pH buffer solutions at 25 °C.

Figure IV-6. . Photostability assay of **HyP-1** and **DVM-1**.

Figure IV-7. UV/Vis absorption and emission spectra of **DVM-1L** in DI H₂O at 25 °C.

Figure IV-8. Representative CLSM images of HeLa and U87MG cells with the treatment of **DVM-1L**.

Figure IV-9. Schematic illustration for the **DVM-1L** preparation.

Chapter V

Figure V-1. Chemical structures of D-A type naphthalene-based dipolar dye and tetraphenylethylene-based AIEgen.

Figure V-2. Absorption and emission spectra of **DA-AIE-M**, **DA-AIE-D**, **DA** (10 μM), and **AIE-Br**, in various solvents at 25 °C.

Figure V-3. Mean hydrodynamic diameter (intensity distribution) of **DA-AIE-M** and **DA-AIE-D** in DI H₂O at 25 °C.

Figure V-4. Absorption and emission spectra of **DA-AIE-M**, **DA-AIE-D**, **DA**, and **AIE-Br** in DI H₂O and DMSO at 25 °C.

Figure V-5. Quantum chemical calculations for **DA-AIE-M**, **DA-AIE-D**, **DA**, and **TPE**.

Figure V-6. Proposed mechanism for the photophysical properties of **DA-AIE-D** in the aggregated form (in H₂O) and dissolved form (in DMSO).

Figure V-7. Absorbance spectra and emission spectra of **DA-AIE-M**, **DA-AIE-D**, **DA**, and **AIE-Br** in DI H₂O-DMSO mixture.

Figure V-8. Detection limit for the DMSO in real water samples.

Chapter VI

Figure VI-1. ATP sensing approaches.

Figure VI-2. Absorption and emission spectra of **AAP-1** after adding ATP to PBS buffer.

Figure VI-3. Absorption and emission spectra of **AAP-1** in various solvents.

Figure VI-4. Absorption and emission spectra of **AAP-1** in the mixture of pH 7.4 (PBS buffer) and glycerol (0–50% glycerol).

Figure VI-5. The intensity distribution curves derived from the DLS measurement of **AAP-1**.

Figure VI-6. Emission spectra of **AAP-1** after mixing ATP (0.5, 1, 2, 3 mM) with PBS buffer (pH 7.4).

Figure VI-7. CLSM images of HeLa cells co-incubated with **AAP-1**, CCCP, ATP, and MitoTracker Deep Red.

Figure VI-8. Schematic illustration and CLSM images of the ATP imaging in hESC.

List of Tables

Chapter II

Table II-1. Ames test results of 2,7-diaminofluorene derivatives.

Table II-2. Ames test results of 2,7-diaminocarbazole derivatives.

Chapter III

Table III-1. Antiviral activities (EC_{50}) of compounds **III-5a–e**.

Table III-2. Antiviral activities (EC_{50}) of compounds **III-5f–10e**.

Table III-3. Antiviral activities (EC_{50}) of compounds **III-19a–j**.

Table III-4. The results of hERG ligand binding assay.

Table III-5. The results of microsomal stability of compound **III-10b**.

Table III-6. The results of CYP₄₅₀ enzyme inhibition assay.

Table III-7. PK parameters of compound **III-10b**.

Table III-8. PK parameters of compound **III-20**.

List of Schemes

Chapter II

Scheme II-1. Synthesis of compounds **II-6a–f**.

Scheme II-2. Synthesis of compounds **II-8a–10c**.

Scheme II-3. Synthesis of compounds **II-12a–d**.

Scheme II-4. Synthesis of compounds **II-16a–d**.

Scheme II-5. Synthesis of compound **II-20**.

Scheme II-6. Synthesis of compounds **II-23a,b**.

Scheme II-7. Synthesis of compounds **II-27a,b**.

Scheme II-8. Synthesis of compounds **II-30a–e**.

Chapter III

Scheme III-1. Synthesis of compounds **III-5a–k**.

Scheme III-2. Synthesis of compounds **III-10a–e**.

Scheme III-3. Synthesis of compounds **III-19a–j**.

Chapter IV

Scheme. IV-1. Synthesis of compound **DVM-1**.

Chapter V

Scheme V-1. Synthesis of compounds **DA-AIE-M** and **DA-AIE-D**.

Chapter VI

Scheme VI-1. Synthesis of compound **TPE-TA**.

List of Abbreviations

Ac	acetyl
Acedan	6-acetyl-2-(dimethylamino)-naphthalene
ACQ	aggregation-caused quenching
ADP	adenosine diphosphate
AMP	adenosine monophosphate
ATP	adenosine triphosphate
AIE	aggregation-induced emission
AUC	area under the curve
BLQ	below the limit of quantitation
Bn	benzyl
Boc	<i>tert</i> -butoxycarbonyl
CCCC	carbonyl cyanide <i>m</i> -chlorophenyl hydrazone
CLSM	confocal laser scanning microscopy
C _{max}	highest plasma concentration
COMU	(1-Cyano-2-ethoxy-2-oxoethylideneaminoxy)dimethylamino-morpholino-carbenium hexafluorophosphate
CTP	cytidine triphosphate
Cy	cyanine
CYP ₄₅₀	cytochrome P450
Cys	cysteine
DAA	direct-acting antiviral
dba	dibenzylideneacetone

DBU	1,8-diazabicyclo(5.4.0)undec-7-ene
DCM	dichloromethane
DCMP	dicyanomethylene-4 <i>H</i> -pyran
DFT	density functional theory
DI	de-ionized
DIPEA	<i>N,N</i> -diisopropylethylamine
DLS	dynamic light scattering
DME	1,2-dimethoxyethane
DMEM	Dulbecco modified eagle medium
DMF	<i>N,N</i> -dimethylformamide
DMSO	dimethyl sulfoxide
DNA	deoxyribonucleic acid
EC ₅₀	half-maximal effective concentration
ESI	electrospray ionization
FBS	fatal bovine serum
FDA	Food and Drug Administration
FDNP	functionalized dipolar naphthalene platform
Gln	glutamine
GSH	glutathione
GT	genotype
GTP	guanosine triphosphate
HCV	hepatitis C virus
Hcy	homocysteine
HeLa	human cervical cancer cell

hERG	human ether-a-go-go related gene
hESC	human embryonic stem cell
HOMO	highest occupied molecular orbital
HP- β -CD	(2-hydroxypropyl)- β -cyclodextrin
HRMS	high-resolution mass spectrometry
IC ₅₀	half-maximal inhibitory concentration
ICT	intramolecular charge transfer
IFN	interferon
IRES	internal ribosome entry site
IV	intravenous
LC	liquid chromatography
LOD	limit of detection
LOQ	limit of quantitation
LUMO	lowest unoccupied molecular orbital
Lys	lysine
MOM	methoxymethyl
MS	mass spectrometer
NA	not applicable
NBD	7-amino-4-nitro-benzoxadiazole
NIR	near infrared
NMR	nuclear magnetic resonance
NS5A	nonstructural protein 5A
ORF	open reading frame
PBS	phosphate buffered saline

PDI	polydispersity index
PEG	polyethylene glycol
PET	photoinduced electron transfer
Phg	phenylglycine
PK	pharmacokinetics
PO	oral administration (per os)
PPG	poly propylene glycol
Prep-HPLC	preparative high-performance liquid chromatography
Pro	proline
RAS	resistance-associated substitution
RAV	resistance-associated variant
RET	resonance energy transfer
RNA	ribonucleic acid
SAR	structure-activity relationship
SVR	sustained virologic response
TFA	trifluoroacetic acid
THF	tetrahydrofuran
TLC	thin layer chromatography
t_{\max}	time for a drug to reach the C_{\max}
TMS	tetramethylsilane
TOF	time of flight
TPGS	tocopherol polyethylene glycol succinate
TPE	tetraphenyl-ethylene
Tris	tromethamine

Ts	toluenesulfonyl
TTP	thymidine triphosphate
U87MG	human primary glioblastoma cell
UTP	uridine triphosphate
UV	ultraviolet
Val	valine
Vis	visible light
WHO	World Health Organization
XPhos	Dicyclohexyl[2',4',6'-tris(propan-2-yl)[1,1'-biphenyl]-2-yl]phosphane

Chapter I. Introduction

I. Development of New HCV NS5A Inhibitors Embedding Fluorene

Hepatitis C virus (HCV), first identified in 1989, is an enveloped virus that contains a 9.6 kb positive-sense single-stranded RNA genome.¹ Approximately 1% of the world population is known to be infected with HCV.² About 30% of HCV patients get acute hepatitis C, which will not develop to a life-threatening disease.³ However, the remainder patients will develop chronic HCV infection and more serious diseases such as liver cirrhosis and hepatocellular carcinoma.³ HCV strains are classified into 8 genotypes (from GT-1 to GT-8)⁴ and about 90 subtypes.⁵ As numerous genotypes and subtypes have demonstrated, HCV evolves very fast. Because of this fast evolution of HCV, there is no vaccine for hepatitis C contrary to the cases of hepatitis A and B.^{6,7}

HCV viral genome, containing one open reading frame (ORF), is translated to one polyprotein-precursor.⁸ The polyprotein-precursor is cleaved by host and viral proteases and converts to 3 structural proteins and 7 nonstructural proteins.⁸ Non-structural protein 5A (NS5A) is an RNA binding membrane-associated phosphoprotein consisting of three distinct structural domains.⁹ Domain 1 (amino acids 33–213), which was crystalized as a homodimeric structure in two different configurations,^{10,11} is known as well conserved region across the HCV genotypes.¹² Domain 2 and domain 3, which are more varied compared to domain 1, have been revealed their functions but still remain uncharted area.^{13–15} NS5A plays various roles such as viral RNA replication, virion reassembly and virion releasing, although it has no enzymatic activity.^{9,16,17} Therefore, NS5A has been highlighted as an important

therapeutic target for the treatment of hepatitis C.

Treatment using PEGylated interferon- α (PEG-IFN- α) with ribavirin was the first standard of care against chronic HCV infection.¹⁸ However, this prescription revealed apparent limitations of not only low sustained virologic response (SVR, ~50% in patients with HCV GT-1),¹⁹ but also severe side effects such as alopecia, depression, neutropenia, fatigue, lymphopenia, insomnia, and other unexpected drug-drug interactions.²⁰ To surpass drawbacks of interferon-based therapy, direct-acting antivirals (DAAs) have been intensively studied. Daclatasvir, first-in-class NS5A inhibitor, had been reported in 2010 by Bristol-Myers Squibb and was approved in 2015 by the US FDA.²¹ This landmark inhibitor presented excellent efficacy such as two-digit pico molar 50% EC₅₀ value (50 pM and 9 pM against GT-1a and GT-1b, respectively) in *in vitro* assay. It also showed reduced HCV RNA level by an average of 3.3 log₁₀ with a single 100 mg dose treatment in clinical trials.²² Despite this remarkable remedial effect, daclatasvir has a low genetic barrier for resistance-associated variants (RAVs), especially L31V and Y93H in GT-1b.²³ To overcome this resistance issue, many laboratories and pharmaceutical companies have focused on the development of new NS5A inhibitors.²⁴⁻³²

In **Chapter II**, our efforts to find a novel core structure for new class of NS5A inhibitors are described. Our laboratory already reported two kinds of NS5A inhibitors containing benzidine³³ and biaryl sulfate,³⁴ which are surrogates of the biphenyl core structure in daclatasvir, keeping the Pro-Val-carbamate motif. In our continued studies, we started to explore compounds containing fluorene as a next generation NS5A inhibitor for two reasons. First, fluorene is sterically restrained form of biphenyl, thus it is a different flat biphenyl structure spatially. Second, 2,7-

diaminofluorene can easily accommodate the Pro-Val-carbamate motif via consecutive amide couplings. Despite its convenience in synthesis, amide bonds of the fluorene-containing inhibitors can be cleaved easily by amidases and the expected metabolite is well-known mutagen.³⁵ Therefore, we explored derivatives of 2,7-diaminofluorene through structure-activity relationship (SAR) studies to circumvent the expected genotoxicity issue.

In **Chapter III**, our efforts to discover potent NS5A inhibitors to solve existing drug-resistance problem are described. As mentioned earlier, daclatasvir presented highly potent efficacy against GT-1a and GT-1b,²² however, antiviral activity against RAVs such as L31V and Y93H dropped 23-fold and 19-fold, respectively. When L31V and Y93H mutations occur simultaneously, EC₅₀ of daclatasvir increased up to 15,000-fold.^{23,36} Learning from previously reported research results that non-symmetric molecules showed good efficacy against mutated NS5A,^{37,38} we synthesized and examined a series of compounds with 4-substituted proline to make non-symmetric environment, embedding 9,9-dibutyl-9*H*-fluorene-2,7-diamine as a core structure.

II. Synthesis of New Organic Fluorophores for Bioimaging

1. Donor-acceptor type organic fluorophore based on naphthalene platform

From a perspective of organic chemistry, the biological system can be understood by observation and interpretation of molecular interactions. Among lots of analytical methods for bioimaging, fluorescence methods have received tremendous attention due to their high sensitivity and accessibility.³⁹ Fluorescent probes with proper properties such as sensitivity, selectivity, and biocompatibility are powerful tools for the investigation of molecular interactions, therefore, these tools have been used widely.⁴⁰

Among photophysical properties of fluorophore, manipulation of emission and absorption wavelength is crucial. Numerous approaches for adjusting wavelength have been taken and the choice of scientists who are interested in biosystem is developing near-infrared region (NIR) dye.⁴¹ NIR fluorophore have lots of advantage, which have especially used in biosystem. Radiation of NIR area wavelength can penetrate skin and tissue deeper than that of short wavelength does,⁴² and avoid autofluorescence issue because the wavelength of autofluorescent molecules are in the range of 400–600 nm.⁴¹

The fluorophore wavelength is ruled by energy difference between HOMO and LUMO. One of the methods to manipulate energy difference of fluorescent molecule is introducing electron donor-acceptor groups.⁴³ In this push-pull fluorophore, or dipolar fluorophore, excited electron is transferred from donor to acceptor. This intramolecular charge transfer (ICT) process depends on the energies of the HOMO of donor and LUMO of acceptor.⁴³ To maximize this effect, thereby altering the

wavelength of fluorophore from UV-vis to NIR, strong donor and acceptor units need to be connected by π conjugation.⁴³

In **Chapter IV**, our efforts to discover a new NIR fluorophore, which is available in biosystem, are reported. We choose naphthalene as a π -conjugation system because it has multiple sites to manipulate electronic properties and install a chemical moiety.⁴⁴ To synthesize the NIR fluorophore, we introduced a known fluorophore, dicyanomethylene-4*H*-pyran (DCMP) as an electron acceptor.⁴⁵

2. Organic fluorophores based on AIE phenomena

Traditional organic fluorophores suffer from aggregation-caused quenching (ACQ) when their concentration is too high or their solubility in media is too low.⁴⁶ Due to the ACQ problem, the concentration of fluorophores employed to the biological systems has to be limited and leads to some problem: low signal-to-noise ratio, photobleaching, etc.⁴⁶ Many scientists have concentrated their efforts in the development of new organic fluorescent probes like NIR dyes, however, that can not be the fundamental solution.

In 2001, Tang group discovered that a series of silole derivatives emit fluorescence not in a dilute solution but in a concentrated solution.⁴⁷ In a concentrated solution, they form aggregates, therefore, these phenomena were named aggregation-induced emission (AIE).⁴⁷ Even though elucidating the exact mechanism of AIE is still controversial, people agree that restricted intramolecular motion is a key element of its working mechanism.⁴⁸

AIE has lots of advantage compared to the ACQ phenomena. First, AIE luminogens (AIEgens) operate in turn-on manner.⁴⁹ Compared to turn-off or

rationometric type, turn-on type dye possesses highest signal to noise ratio. Due to this characteristic, AIEgens can be utilized as photosensitizer,⁵⁰ free from photobleaching issue⁵¹ relatively.

We first studied articulated structure of AIEgen and traditional dipolar dye (**Chapter V**). Before our study, the physicochemical properties of fluorophores linked by sp^3 bond between AIEgen and dipolar dye have not be fully elucidated. We reported on their synthesis, photophysical properties and applications. Furthermore, we designed a new AIEgen-based nanoprobe (named **AAP-1**) for sensing and imaging of ATP in live cells. We described the design rational and application of **AAP-1** in cancer cells and embryonic stem cells (**Chapter VI**).

**Chapter II. SAR Studies on the Mutagenic Properties
of 2,7-Diaminofluorene and 2,7-Diaminocarbazole
Derivatives**

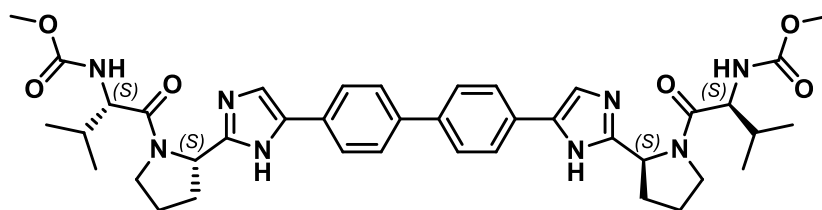
I. Introduction

9*H*-Fluorene (or fluorene), emits a violet fluorescence, is a polycyclic compound. As its name indicates, fluorene has been utilized for the preparation of various organic dyes.⁵² 9*H*-Carbazole (or carbazole) is similar to fluorene except for the nitrogen atom at the 9 position. Like fluorene, carbazole has also been used for various areas such as dyes,⁵³ drugs,^{54,55} and ligands.⁵⁶ Among various derivatives, 2,7-diaminofluorene and 2,7-diaminocarbazole have received most attention because they can be transformed to an excellent scaffold for symmetric or pseudo-symmetric molecules. Chemical applications of 2,7-diaminofluorene and 2,7-diaminocarbazole derivatives are diverse including chemical adsorbent,⁵⁷ nanoparticle for photodynamic therapy,⁵⁸ ATP sensing probe,⁵⁹ and covalent organic frameworks for CO₂ capture.⁶⁰ Among various usage of 2,7-diaminofluorene or 2,7-diaminocarbazole derivatives, we concentrated on their potential as key scaffolds for the synthesise of physiologically active molecules.

Daclatasvir (Compound **II-1** in Figure II-1), which had been reported by Bristol-Myers Squibb in 2010, was approved in 2015 by the US FDA as an effective HCV NS5A inhibitor.²¹ Despite its extremely high antiviral activity, it loses its inhibitory activity against mutated NS5A proteins.²³ To overcome this issue, many pharmaceutical companies and laboratories worldwide have searched for and reported numerous NS5A inhibitors based on the structure of daclatasvir.²⁴⁻³² We had reported a new class of HCV NS5A inhibitors including benzidine³³ and biaryl sulfate³⁴ as core structures, maintaining the Pro-Val-carbamate motif of daclatasvir. In our continued research, we were curious if 2,7-diaminofluorene and 2,7-

diaminocarbazole could be applied as a key scaffold of a drug candidates, particularly in relation with HCV NS5A inhibitors. Compounds embedding these structures showed extremely potent inhibitory activities against a variety of HCV genotype.⁶¹ Even though inhibitors can readily be transformed from 2,7-diaminofluorene or 2,7-diaminocarbazole via a series of amide coupling and exhibit extremely potent inhibitory activities, it is susceptible to cleavage by proteolysis once administered into the body, and the resulting metabolites have potential as mutagens.^{35,62,63} The mutagenicity of 2,7-diaminofluorene and 2,7-diaminocarbazole must be inspected for use in the discovery of new NS5A inhibitors. Therefore, we decided to explore the SAR on the mutagenicity of the 9-substituted 2,7-diaminofluorene and 2,7-diaminocarbazole.

Herein, we reported our systematic approach through Ames test⁶⁴ to circumvent the mutagenicity problems when 2,7-diaminofluorene and 2,7-diaminocarbazole are utilized as core structures of NS5A inhibitors.



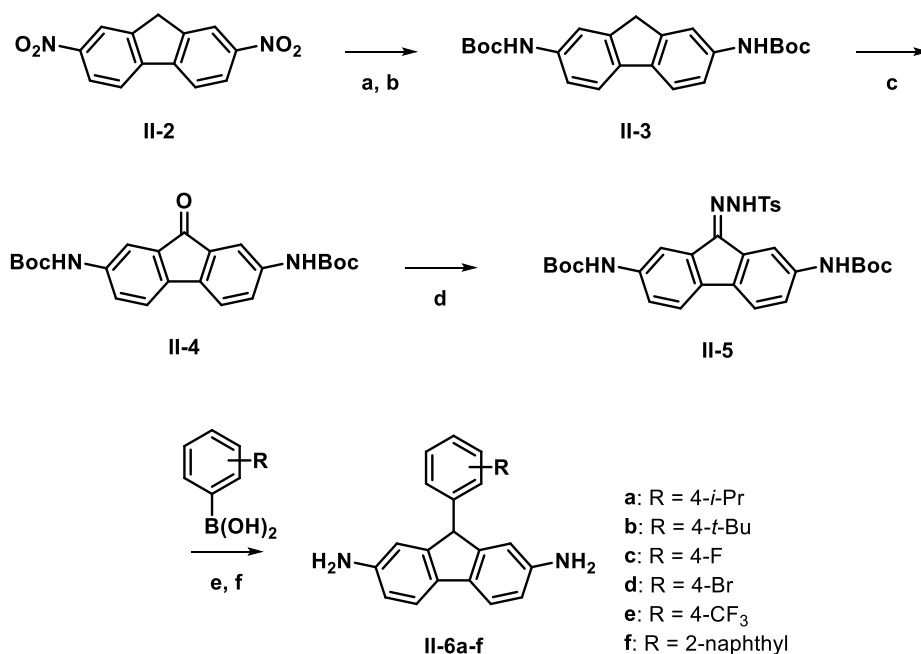
Daclatasvir (II-1)

Figure II-1. Chemical structure of daclatasvir (Compound II-1).

II. Results and Discussion

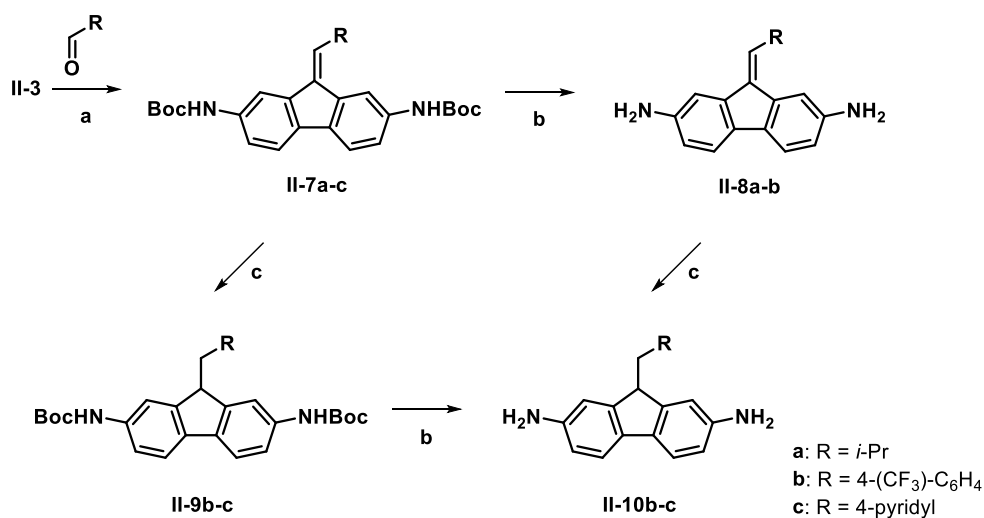
1. Preparation of diamine compounds

We describe the synthesis of 9-aryl substituted fluorene compounds in Scheme II-1. Compound **II-2** was reduced to 2,7-diaminofluorene with the aid of iron oxide nanoparticles and hydrazine as reported in our previous report⁶⁵ and Boc protection of the resulting diamine afforded compound **II-3**. After oxidation at the 9 position, the resulting ketone **II-4** was converted to hydrazone **II-5** from treatment with *p*-TsNHNH₂. Metal-free reductive coupling⁶⁶ of **II-5** with the corresponding arylboronic acid was performed followed by Boc deprotection to give compounds **II-6a-f**.



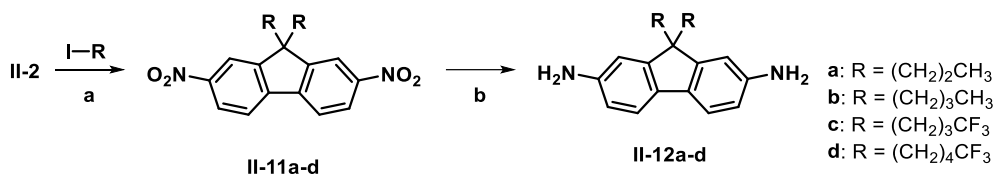
Scheme II-1. Synthesis of compounds **II-6a-f**. Reagents and conditions: (a) Fe₃O₄, hydrazine monohydrate, EtOH, reflux, 2 h; (b) Boc₂O, NaOH, 1,4-dioxane, H₂O, 25 °C, 24 h; (c) Cs₂CO₃, DMSO, 25 °C, 18 h; (d) *p*-TsNHNH₂, MeOH, 60 °C, 4 h; (e) K₂CO₃, 1,4-dioxane, reflux, 2 h; (f) TFA, DCM, 25 °C, 2 h.

Synthesis of 2,7-diaminofluorene derivatives containing 9-alkyl or alkylidene substituents is described in Scheme II-2. Compounds **II-7a–c** were synthesized from compound **II-3** via Knoevenagel condensation with various aldehydes. Compounds **II-7a–c** were converted to diamine through Boc deprotection (**II-8a–b**) or dehydrogenation followed by Boc deprotection (**II-10b–c**).



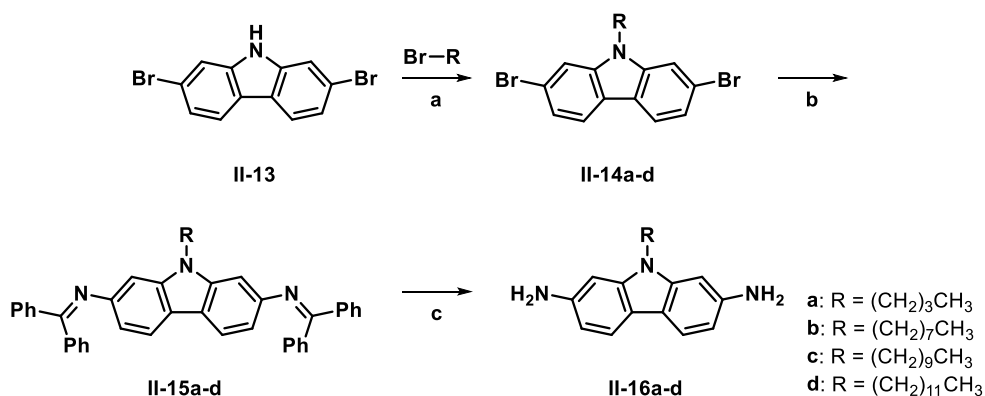
Scheme II-2. Synthesis of compounds **II-8a–10c**. Reagents and conditions: (a) *t*-BuOK, xylene, reflux, 1 h or KOH, DME, reflux, 4 h; (b) TFA, DCM, 25 °C, 2 h; (c) Pd/C, H₂, MeOH, 25 °C, 12 h.

Synthesis of 2,7-diaminofluorene derivatives containing 9,9-dialkyl substituents is described in Scheme II-3. We introduced two alkyl groups through S_N2 reaction of compound **II-2** to obtain compounds **II-11a–d**. Reduction of the nitro groups of **II-11a–d** gave compounds **II-12a–d**.



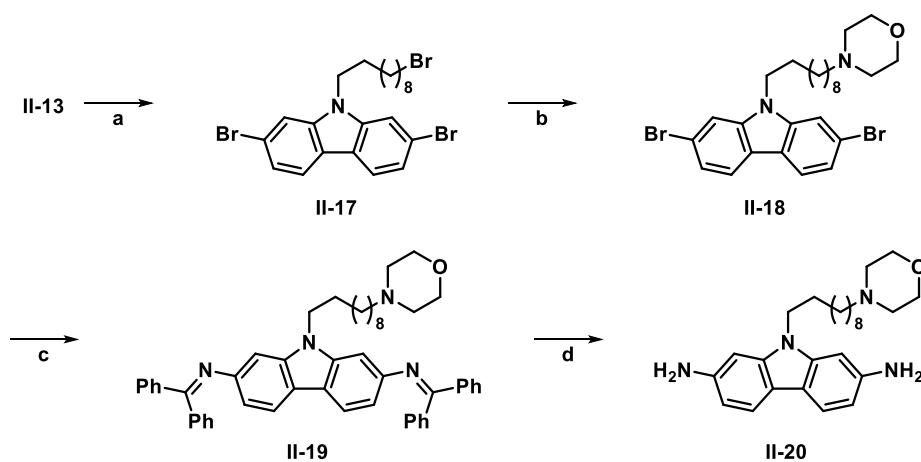
Scheme II-3. Synthesis of compounds **II-12a–12d**. Reagents and conditions: (a) Cs₂CO₃, DMF, 0 °C to 25 °C, 18 h; (b) Fe₃O₄, hydrazine monohydrate, EtOH, reflux, 2 h.

Scheme II-4 describes the preparation of 9-alkyl substituted carbazole derivatives. In the synthesis of 2,7-diaminocarbazole derivatives, 2,7-dibromocarbazole (compound **II-13**) was used as starting material. Compound **II-13** was converted to *N*-alkylated carbazole (**II-14a–d**) from S_N2 reaction with proper alkyl bromides. Buchwald-Hartwig amination of aromatic bromide (**II-14a–d**) with the use of diphenylmethanimine followed by imine hydrolysis afforded **II-16a–d**. Transformation from aryl bromide to diamine via Buchwald-Hartwig amination and imine hydrolysis was repetitive in following schemes (vide infra).



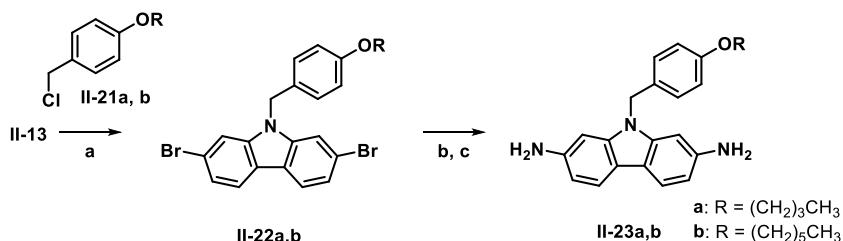
Scheme II-4. Synthesis of compounds **II-16a–d**. Reagents and conditions: (a) NaH, DMF, 25 °C; (b) Pd₂(dba)₃·CHCl₃, *t*-BuXPhos, *t*-BuONa, diphenylmethanimine, toluene, 100 °C, 16 h; (c) 4.0 M HCl/MeOH, 25 °C, 1 h.

Synthesis of 9-(10-morpholinodecyl)-9*H*-carbazole-2,7-diamine (**II-20**) is described in Scheme II-5. Compound **II-17** was prepared via S_N2 reaction of compound **II-13** with 1,10-dibromodecane. Additional S_N2 reaction between compound **II-17** and morpholine gave compound **II-18** albeit in a moderate yield. Following the synthetic procedure mentioned in Scheme II-4, we converted compound **II-18** to compound **II-20**.



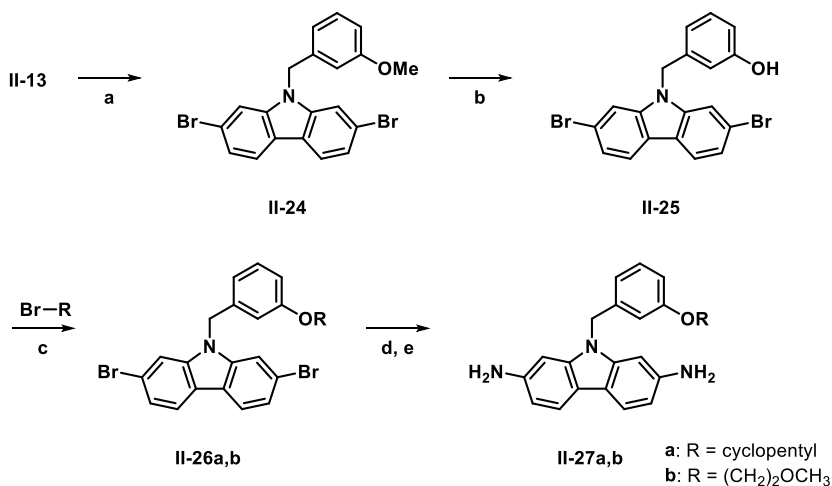
Scheme II-5. Synthesis of compound **II-20**. Reagents and conditions: (a) NaH, 1,10-dibromodecane, DMF, 0 °C to 25 °C, 16 h; (b) K₂CO₃, morpholine, MeCN, reflux, 10 h; (c) Pd₂(dba)₃·CHCl₃, *t*-BuXPhos, *t*-BuONa, diphenylmethanimine, toluene, 100 °C, 16 h; (d) 4.0 M HCl/MeOH, 25 °C, 4 h.

Scheme II-6 describes the synthetic procedure for compounds **II-23a** and **II-23b**, which were prepared from para-alkoxy-substituted benzyl chlorides. S_N2 reaction between compound **II-13** and para-substituted benzyl chloride (**II-21a** and **II-21b**) afforded **II-22a** and **II-22b**, respectively. These compounds were converted to diamine (**II-23a** and **II-23b**) through above-mentioned methods in Scheme II-4.



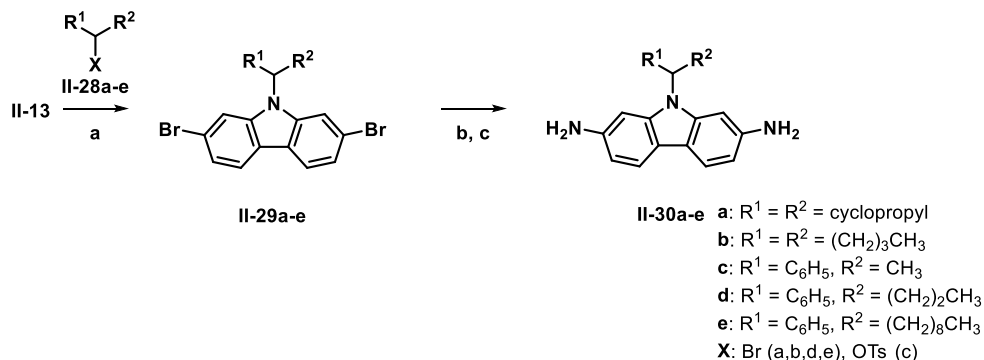
Scheme II-6. Synthesis of compounds **II-23a,b**. Reagents and conditions: (a) NaH, DMF, 0 °C to 25 °C, 12 h; (b) Pd₂(dba)₃·CHCl₃, *t*-BuXPhos, *t*-BuONa, diphenylmethanimine, toluene, 100 °C, 16 h; (c) 4.0 M HCl/MeOH, 25 °C, 1 h.

Scheme II-7 describes the preparation of 2,7-diaminocarbazole derivatives (**II-27a** and **II-27b**) containing meta-substituted benzyl group at the 9 position. *N*-Alkylation of compound **II-13** with 1-(bromomethyl)-3-methoxybenzene afforded compound **II-24** and demethylation of the resulting **II-24** furnished compound **II-25**. After proper *O*-alkylation (**II-26a** and **II-26b**), compounds **II-27a** and **II-27b** were synthesized via the same procedure described in Scheme II-4.



Scheme II-7. Synthesis of compounds **II-27a,b**. Reagents and conditions: (a) NaH, 1-(bromomethyl)-3-methoxybenzene, DMF, 0 °C to 25 °C, 12 h; (b) NaI, TMSCl, MeCN, reflux, 3 h; (c) K₂CO₃, DMF, 90 °C, 5 h; (d) Pd₂(dba)₃·CHCl₃, *t*-BuXPhos, *t*-BuONa, diphenylmethanimine, toluene, 100 °C, 16 h; (e) 4.0 M HCl/MeOH, 25 °C, 2 h.

Compounds **II-30a–e** have similar structure as dialkylated fluorene derivatives (**II-12a–d**). Scheme II-8 describes the preparation of compounds **II-30a–e**. These compounds (**II-30a–e**) were also prepared via the same way as described in Scheme II-4: i) alkylation, ii) Buchwald-Hartwig amination, and iii) imine hydrolysis.



Scheme II-8. Synthesis of compounds **II-30a–e**. Reagents and conditions: (a) NaH, DMF, 0 °C to 25 °C, 12 h; (b) Pd₂(dba)₃·CHCl₃, *t*-BuXPhos, *t*-BuONa, diphenylmethanimine, toluene, 100 °C, 16 h; (c) 4.0 M HCl/MeOH, 25 °C.

2. Ames test results of diamine compounds

The mutagenicity of several 2,7-diaminofluorene derivatives and 2,7-diaminocarbazole derivatives was examined using the Ames test in strains TA98 and TA100, both with and without S9 mix treatment. All compounds were tested at six different concentrations from 4 to 5000 μM. The results are presented in Table II-1 and Table II-2, respectively.

Entry	R ¹	R ²	Ames results ^{a,b}
II-6a	H	4-(<i>i</i> -Pr)-C ₆ H ₄	-,+,,-
II-6b	H	4-(<i>t</i> -Bu)-C ₆ H ₄	-,+,,-
II-6c	H	4-F-C ₆ H ₄	-,+,,-
II-6d	H	4-Br-C ₆ H ₄	-,+,,-
II-6e	H	4-CF ₃ -C ₆ H ₄	-,+,,-
II-6f	H	2-naphthyl	-,+,,-
II-8a			+,+,+,+
II-8b			+,+,,-
II-10b	H		+,+,,-
II-10c	H		-,+,+,+
II-12a	(CH ₂) ₂ CH ₃	(CH ₂) ₂ CH ₃	-,+,,-
II-12b	(CH ₂) ₃ CH ₃	(CH ₂) ₃ CH ₃	-,+,,-
II-12c	(CH ₂) ₃ CF ₃	(CH ₂) ₃ CF ₃	-,+,,-
II-12d	(CH ₂) ₄ CF ₃	(CH ₂) ₄ CF ₃	-,,-,-

Table II-1. Ames test results of 2,7-diaminofluorene derivatives.

^aAmes results means the test result of TA98–S9, TA98+S9, TA100–S9, and TA100+S9, respectively.

^b+: positive, -: negative.

Entry	R ¹	R ²	Ames results ^{a,b}
II-16a	H	(CH ₂) ₂ CH ₃	+,+,+,+
II-16b	H	(CH ₂) ₆ CH ₃	-,+,-,-
II-16c	H	(CH ₂) ₈ CH ₃	-,+,-,-
II-16d	H	(CH ₂) ₁₀ CH ₃	-,,-,-,-
II-20	H		-,,-,-,-
II-23a	H		-,+,-,-
II-23b	H		-,+,-,-
II-27a	H		-,+,-,-
II-27b	H		-,+,-,-
II-30a			-,+,-,+
II-30b	(CH ₂) ₃ CH ₃	(CH ₂) ₃ CH ₃	-,,-,-,-
II-30c	C ₆ H ₅	CH ₃	-,+,-,+
II-30d	C ₆ H ₅	(CH ₂) ₂ CH ₃	-,+,-,-
II-30e	C ₆ H ₅	(CH ₂) ₆ CH ₃	-,,-,-,-

Table II-2. Ames test results of 2,7-diaminocarbazole derivatives.

^aAmes results means the test result of TA98–S9, TA98+S9, TA100–S9, and TA100+S9, respectively.

^b+: positive, -: negative.

Compounds **II-6a–f**, equipped with various aromatic rings at the C9 position of fluorene, were found to be non-mutagenic in TA98 and TA100 strains in the absence of S9 mix. However, in the presence of S9 mix, these compounds turned to be mutagenic in TA98 strain. Compounds containing a double bond at the C9 position (**II-8a** and **II-8b**) were found to be mutagenic regardless of treatment with S9 mix. Compounds with a reduced double bond (**II-10b** and **II-10c**) were mutagenic in TA 98 strain only in the presence of S9 mix. However, compounds possessing dialkyl substituents at the C9 position of fluorene (**II-12a–d**) exhibited varying degrees of mutagenicity depending on the length of the alkyl groups. With dipropyl substituents, compound **II-12a** showed mutagenic activity in TA98 strain treated with S9 mix. In the cases of dibutyl, bis(trifluoromethylpropyl), and bis(trifluoromethylbutyl) substituted compounds **II-12b**, **II-12c**, and **II-12d**, respectively, they were found to be slightly mutagenic in TA98 strain treated with S9 mix only when the concentration was higher than 5 mM. Therefore, it can be concluded that the longer the length of alkyl chain is, the lower the probability of mutation.

In the case of carbazole derivatives, compounds equipped with monoalkyl substituents at the *N*9 position of carbazole (**II-16a–d** and **II-20**) showed a similar mutagenic pattern as in the fluorene derivatives; the mutagenicity was dependent on the length and bulkiness of the alkyl substituent. When the alkyl chains were longer than *n*-decyl, the corresponding carbazole derivatives were non-mutagenic. *N*-Benzyl derivatives with an alkoxy substitution, such as compounds **II-23a**, **II-23b**, **II-27a**, and **II-27b**, were all found to be mutagenic in TA98 strain treated with S9 mix, regardless of the position and type of the alkoxy groups attached to the benzene ring. Bis(cyclopropyl)methyl-substituted derivative (**II-30a**) also showed mutagenic

activity in both TA98 and TA100 strains treated with S9 mix. A compound with a longer substitution such as a 5-nonyl group (**II-30b**) showed no mutagenicity in TA98 and TA100 strains treated with and without S9 mix. In compounds with (1-phenyl)alkyl substitution (**II-30c-e**), the alkyl chain length played a critical role in determining their mutagenicity, regardless of the phenyl group.

According to the precedent research, 2-aminofluorene (2-AF) or *N*-acetyl-2-aminofluorene (2-AAF) is transformed to *N*-hydroxy-2-AF or *N*-hydroxy-2-AAF via CYP₄₅₀ monooxygenase oxidation.⁶² *N*-Hydroxy-2-AF or *N*-hydroxy-2-AAF can be metabolized to electrophilic species, such as *N*-SO₄-2-AF, *N*-acetoxy-2-AF, and *N*-SO₄-2-AAF.⁶² These electrophiles can form DNA adducts through a reaction with the guanine base, which we considered as a major mutation pathway in the aminofluorene case.

Compounds **II-6a-f**, equipped with various aromatic ring substitutions at the C9 position of 2,7-diaminofluorene, were found to be mutagenic in TA98 strain treated with S9 mix. The fact that these compounds did not act as mutagens in TA98 without S9 treatment indicated that the formation of metabolites through DNA adduct can be a cause of mutation. In addition, the negative result for mutation in TA100 strain treated with S9 mixture indicated that the DNA adduct caused a frame-shift mutation rather than a base-pair substitution.⁶⁷ In the case of fluorene derivatives substituted with dialkyl groups at the C9 position (compounds **II-12a-d**), shorter alkyl chain substituents tended to cause mutagenicity. From the results of previous⁶² and current study, we hypothesized that the mutation of 2,7-diaminofluorene can be prevented by introducing sterically bulky dialkyl groups at the C9 position, presumably because they prevent the guanine base from approaching electrophilic metabolites.

In the case of 2,7-diaminofluorene, introduction of dibutyl-, bis(trifluoromethylpropyl)-, or bis(trifluoromethylbutyl)- chains, as in compounds **II-12b**, **II-12c**, and **II-12d**, respectively, diminished mutation propensity. However, the carbazole moiety needed to be substituted with a longer *N*-alkyl chain than an *n*-decyl group (as in **II-16c**, **II-16d** and **II-20**) to avoid mutagenicity issues. These results agree well with our hypothesis because carbazole needed to be substituted with a longer chain monoalkyl group than fluorene with longer-than-propyl dialkyl groups at the C9 position. Therefore, to block the formation of DNA adduct, carbazole has to be substituted with a longer alkyl chain than that of fluorene. In the case of carbazoles substituted with a symmetric secondary alkyl group (**II-30a** and **II-30b**), which mimics the dialkyl group of fluorene derivatives, compounds substituted with a long branched alkyl chain, such as (1-butyl)pentyl substitution (mimicking 9,9-dipentyl groups at the fluorene) (**II-30b**), may avoid mutagenic issues, but not those with a short chain (**II-30a**). The importance of the alkyl chain length in determining the mutagenicity of compounds could be explained by the (1-phenyl)alkyl substitution cases (**II-30c–e**). Regardless of the phenyl group, mutagenicity pattern was consistent with the length of the alkyl chain. With methyl (**II-30c**) or propyl (**II-30d**) substitution, the compounds were found to be mutagenic, but compounds with longer substituent (e.g. nonyl group, **II-30e**) were non-mutagenic. Our hypothesis was also confirmed by the results of *N*-benzyl derivatives with an alkoxy substitution (**II-23a**, **II-23b**, **II-27a** and **II-27b**). In these cases, any changes in the alkoxy group did not affect the Ames results of the four compounds because those variations did not affect the bulkiness of the compounds.

In the case of carbazole derivatives, compounds equipped with monoalkyl substituents at the *N*9 position of carbazole (**II-16a–d** and **II-20**) showed a similar mutagenic pattern as in the fluorene derivatives; the mutagenicity was dependent on the length and bulkiness of the alkyl substituent. When the alkyl chains were longer than *n*-decyl, the corresponding carbazole derivatives were non-mutagenic. *N*-Benzyl derivatives with an alkoxy substitution, such as compounds **II-23a**, **II-23b**, **II-27a**, and **II-27b**, were all found to be mutagenic in TA98 strain treated with S9 mix, regardless of the position and type of the alkoxy groups attached to the benzene ring. Bis(cyclopropyl)methyl-substituted derivative (**II-30a**) also showed mutagenic activity in both TA98 and TA100 strains treated with S9 mix. A compound with a longer substitution such as a 5-nonyl group (**II-30b**) showed no mutagenicity in TA98 and TA100 strains treated with and without S9 mix. In compounds with (1-phenyl)alkyl substitution (**II-30c–e**), the alkyl chain length played a critical role in determining their mutagenicity, regardless of the phenyl group.

III. Conclusion

In this study, using Ames test, we investigated the important factors affecting the mutagenicity of the aniline derivatives 2,7-diaminofluorene and 2,7-diaminocarbazole, which are often employed in drug discovery. Ames test results showed that mutagenicity problems with derivatives of 2,7-diaminofluorene and 2,7-diaminocarbazole can be solved by equipping these derivatives with a long alkyl chain at a proper location. The results imply that 2,7-diaminofluorene and 2,7-diaminocarbazole can successfully be employed in drug discovery as long as they are equipped with proper substituents. In addition, several of the examined compounds showed extremely high antiviral activities,⁶¹ proving that fluorene and carbazole can be used as effective core structures of HCV NS5A inhibitors.

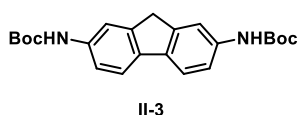
IV. Experimental Section

1. Materials

All commercially available reagents and solvents were obtained from commercial suppliers and used without further purification. All reactions involving reactants, reagents, or intermediates sensitive to air or moisture were conducted under Ar atmosphere. ¹H, ¹³C, and ¹⁹F NMR spectra were obtained on an Agilent NMR system 400 MHz DD2MR400 (400 MHz), a Bruker Ascend 400 MHz (400 MHz), or a Varian NMR System 500 MHz in DMSO-*d*₆, CDCl₃, or CD₃OD, with TMS used as an internal standard. Multiplicities are indicated by s (singlet), d (doublet), t (triplet), q (quartet), dd (doublet of doublet), and ddd (doublet of doublet of doublet). TLC was conducted on pre-coated silica gel plates (60F-254; Merck KGaA, Germany).

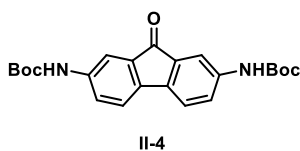
2. Synthesis

The procedures used in the synthesis of compounds are described in Scheme II-1 to II-8, respectively.



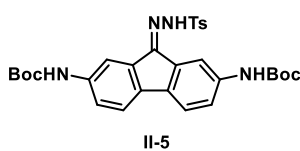
Di-tert-butyl (9H-fluorene-2,7-diyl)dicarbamate

(II-3). To a mixture of **II-2** (5.00 g, 19.5 mmol) and Fe₃O₄ (904 mg, 3.90 mmol) in EtOH (65.0 mL), hydrazine monohydrate (9.5 mL, 195 mmol) was added. The reaction mixture was stirred at 75 °C for 2 h. The crude mixture was filtered through Celite and the filtrates were concentrated in vacuo and diluted with DCM. The organic layer was washed with H₂O, dried over MgSO₄, and concentrated in vacuo. Product (2,7-diaminofluorene, 3.71 g, 96%, dark yellow solid) was isolated without further purification. 2,7-diaminofluorene (3.71 g, 18.9 mmol) was dissolved in 1,4-dioxane (42.0 mL), and H₂O (21.0 mL), 2.0 M NaOH (20.8 mL), and Boc₂O (10.9 mL, 47.2 mmol) were added successively. The reaction mixture was stirred vigorously at room temperature for 24 h. The crude mixture was quenched by the addition of H₂O, acidified to pH 3.0 with 1.0 M KHSO₄, and diluted with DCM. The organic layer was washed with brine, dried over MgSO₄, and concentrated in vacuo. The residue was purified by flash column chromatography (n-hexane/EtOAc = 4:1) to give compound **II-3** (6.28 g, 84%, dark yellow solid). ¹H NMR (400 MHz, DMSO-*d*₆): δ 9.38 (s, 2H), 7.70 (s, 2H), 7.62 (d, *J* = 8.3 Hz, 2H), 7.39 (dd, *J* = 2.0, 8.3 Hz, 2H), 3.81 (s, 2H), 1.49 (s, 18H); ¹³C NMR (100 MHz, DMSO-*d*₆): δ 152.84, 144.35, 137.83, 135.40, 119.25, 115.92, 114.88, 78.94, 36.54, 28.17.



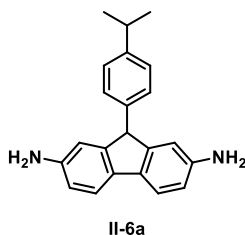
Di-tert-butyl (9-oxo-9H-fluorene-2,7-diyl)dicarbamate (II-4). Compound **II-3** (3.00 g, 7.57 mmol) and Cs₂CO₃ (6.16 g, 18.9 mmol) were dissolved

in DMSO (25.0 mL). The reaction mixture was stirred at room temperature for 18 h under open air. The crude mixture was quenched by the addition of H₂O and diluted with EtOAc. The organic layer was washed with H₂O, dried over MgSO₄, and concentrated in vacuo. The residue was purified by flash column chromatography (n-hexane/EtOAc = 3:2) to give compound **II-4** (1.93 g, 63%, red solid). ¹H NMR (400 MHz, DMSO-*d*₆): δ 9.61 (s, 2H), 7.71 (d, *J* = 2.0 Hz, 2H), 7.59–7.46 (m, 4H), 1.48 (s, 18H); ¹³C NMR (100 MHz, DMSO-*d*₆): δ 193.12, 152.68, 139.98, 137.82, 134.21, 123.66, 120.77, 113.77, 79.52, 28.06.



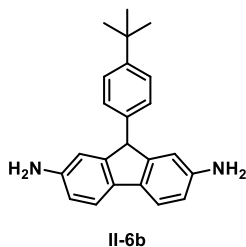
Di-tert-butyl (9-(2-tosylhydrazineylidene)-9H-fluorene-2,7-diyl)dicarbamate (II-5). Compound **II-4** (1.80 g, 4.39 mmol) and *p*-TsNHNH₂ (899 mg, 4.83

mmol) were dissolved in MeOH (4.4 mL). The reaction mixture was stirred at 60 °C for 4 h and the crude mixture was cooled to room temperature. The mixture was filtered and the residue was washed with petroleum ether to give compound **II-5** (2.40 g, 95%, yellow solid). ¹H NMR (400 MHz, DMSO-*d*₆): δ 11.25 (s, 1H), 9.59 (s, 1H), 9.46 (s, 1H), 8.26 (s, 1H), 7.91 (d, *J* = 8.3 Hz, 2H), 7.67 (s, 1H), 7.58 (d, *J* = 8.2 Hz, 1H), 7.51 (s, 3H), 7.44 (d, *J* = 8.1 Hz, 2H), 2.40 (s, 3H), 1.50 (s, 18H); ¹³C NMR (125 MHz, DMSO-*d*₆): 153.32, 153.17, 152.34, 144.06, 139.49, 139.20, 137.09, 136.36, 135.71, 134.25, 130.20, 129.68, 128.72, 121.89, 120.54, 120.31, 120.24, 118.93, 112.00, 79.69, 79.64, 28.60, 28.58, 21.50.



9-(4-Isopropylphenyl)-9H-fluorene-2,7-diamine (II-6a).

Compound **II-5** (100 mg, 0.173 mmol), K₂CO₃ (35.9 mg, 0.260 mmol), and (4-isopropylphenyl)boronic acid (42.6 mg, 0.260 mmol) were dissolved in 1,4-dioxane (0.6 mL). The reaction mixture was refluxed for 2 h. The crude mixture was cooled to room temperature and diluted with DCM. The organic layer was washed with brine, dried over MgSO₄, and concentrated in vacuo. The residue was purified by flash column chromatography (n-hexane/EtOAc = 9:1) to give product (di-*tert*-butyl (9-(4-isopropylphenyl)-9H-fluorene-2,7-diyl)dicarbamate, 66.4 mg, 68%, white solid). To a solution of di-*tert*-butyl (9-(4-isopropylphenyl)-9H-fluorene-2,7-diyl)dicarbamate (162 mg, 0.315 mmol) in DCM (1.0 mL), TFA (1.0 mL, 13.1 mmol) was added. The reaction mixture was stirred at room temperature for 2 h. The crude mixture was concentrated in vacuo and the residue was diluted with DCM. The organic layer was washed with saturated sodium bicarbonate solution, dried over MgSO₄, and concentrated in vacuo. The residue was purified by flash column chromatography (n-hexane/EtOAc = 3:2) to give compound **II-6a** (57 mg, 58%, ivory solid). ¹H NMR (400 MHz, DMSO-*d*₆): δ 7.29 (d, *J* = 8.0 Hz, 2H), 7.14 (d, *J* = 7.9 Hz, 2H), 6.95 (d, *J* = 8.0 Hz, 2H), 6.49 (d, *J* = 8.1 Hz, 2H), 6.40 (s, 2H), 4.91 (s, 4H), 4.78 (s, 1H), 2.83 (p, *J* = 6.9 Hz, 1H), 1.18 (d, *J* = 6.9 Hz, 6H); ¹³C NMR (100 MHz, DMSO-*d*₆): δ 148.12, 146.66, 146.27, 140.41, 130.22, 128.05, 126.36, 118.57, 112.89, 110.92, 52.94, 33.09, 23.96. HRMS (*m/z*): [M+H]⁺ calcd for C₂₂H₂₃N₂, 315.1856; found, 315.1866.

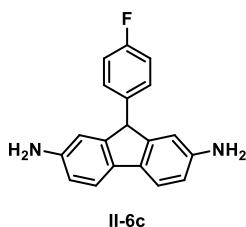


9-(4-(tert-Butyl)phenyl)-9H-fluorene-2,7-diamine (II-6b).

Compound **II-6b** (40.3 mg, 57%, orange solid) was prepared according to the procedure described for the synthesis **II-6a**.

¹H NMR (400 MHz, DMSO-*d*₆): δ 7.30 (d, *J* = 8.1 Hz, 4H), 6.97 (d, *J* = 8.2 Hz, 2H), 6.51 (d, *J* = 8.0 Hz, 2H), 6.42 (s,

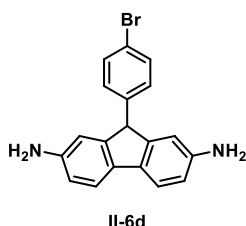
2H), 4.92 (s, 4H), 4.79 (s, 1H), 1.26 (s, 9H); ¹³C NMR (100 MHz, DMSO-*d*₆): δ 148.50, 148.09, 146.65, 140.01, 130.24, 127.78, 125.22, 118.57, 112.90, 110.94, 52.86, 34.12, 31.21. HRMS (*m/z*): [M+H]⁺ calcd for C₂₃H₂₄N₂, 329.2012; found, 329.2018.



9-(4-Fluorophenyl)-9H-fluorene-2,7-diamine (II-6c).

Compound **II-6c** (55.2 mg, 35%, dark brown solid) was prepared according to the procedure described for the synthesis **II-6a**.

¹H NMR (400 MHz, DMSO-*d*₆): δ 7.29 (d, *J* = 8.0 Hz, 2H), 7.13–7.03 (m, 4H), 6.49 (dd, *J* = 2.1, 8.1 Hz, 2H), 6.38 (s, 2H), 4.92 (s, 4H), 4.85 (s, 1H); ¹³C NMR (100 MHz, DMSO-*d*₆): δ 162.12, 159.72, 147.91, 146.76, 139.36, 139.32, 130.12, 129.92, 129.84, 118.65, 115.28, 115.07, 113.03, 110.78, 52.35; ¹⁹F NMR (376 MHz, DMSO-*d*₆): δ -116.82. HRMS (*m/z*): [M+H]⁺ calcd for C₁₉H₁₆FN₂, 291.1292; found, 291.1293.

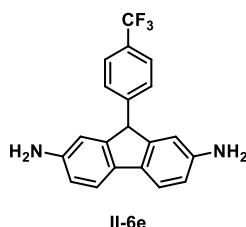


9-(4-Bromophenyl)-9H-fluorene-2,7-diamine (II-6d).

Compound **II-6d** (62.3 mg, 51%, brown solid) was prepared according to the procedure described for the synthesis **II-6a**.

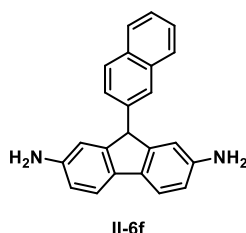
¹H NMR (400 MHz, DMSO-*d*₆): δ 7.46 (d, *J* = 8.4 Hz, 2H), 7.29 (d, *J* = 8.1 Hz, 2H), 6.99 (d, *J* = 8.4 Hz, 2H), 6.50 (dd, *J* = 2.0, 8.0 Hz, 2H), 6.38 (s, 2H), 4.94 (s, 4H), 4.84 (s, 1H); ¹³C NMR (100 MHz, DMSO-*d*₆): δ 147.59,

146.80, 142.75, 131.60, 130.38, 130.17, 119.34, 118.68, 110.76, 52.49. HRMS (m/z): $[M+H]^+$ calcd for $C_{19}H_{16}BrN_2$, 351.0491; found, 351.0495.



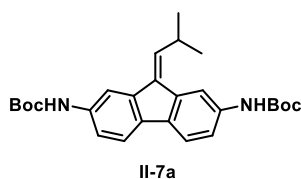
9-(4-(Trifluoromethyl)phenyl)-9H-fluorene-2,7-diamine (**II-6e**). Compound **II-6e** (62.8 mg, 62%, brown solid) was prepared according to the procedure described for the

synthesis **II-6a**. 1H NMR (400 MHz, $DMSO-d_6$): δ 7.65 (d, J = 8.1 Hz, 2H); 7.32 (d, J = 8.1 Hz, 2H), 7.26 (d, J = 8.0 Hz, 2H), 6.52 (dd, J = 2.1, 8.0 Hz, 2H), 6.39 (s, 2H), 4.98 (s, 1H), 4.94 (s, 4H); ^{13}C NMR (100 MHz, $DMSO-d_6$): δ 148.31, 147.35, 146.89, 130.21, 128.96, 125.44, 125.40, 118.77, 113.17, 110.75, 52.81; ^{19}F NMR (376 NMR, $DMSO-d_6$): δ -60.81. HRMS (m/z): $[M+H]^+$ calcd for $C_{20}H_{16}F_3N_2$, 341.1260; found, 341.1266.



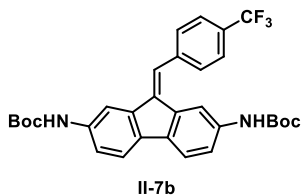
9-(Naphthalen-2-yl)-9H-fluorene-2,7-diamine (**II-6f**).

Compound **II-6f** (57.3 mg, 41%, brown solid) was prepared according to the procedure described for the synthesis **II-6a**. 1H NMR (400 MHz, $DMSO-d_6$): δ 7.92–7.80 (m, 3H), 7.75 (d, J = 8.5 Hz, 1H), 7.53–7.44 (m, 2H), 7.35 (d, J = 8.1 Hz, 2H), 6.86 (dd, J = 1.7, 8.5 Hz, 1H), 6.54 (d, J = 8.1 Hz, 2H), 6.43 (s, 2H), 4.99 (d, J = 13.7 Hz, 5H); ^{13}C NMR (100 MHz, $DMSO$): δ 148.02, 146.67, 140.71, 133.17, 131.95, 130.42, 128.10, 127.47, 127.33, 126.72, 126.36, 126.13, 125.50, 118.71, 113.14, 111.03, 53.42. HRMS (m/z): $[M+H]^+$ calcd for $C_{23}H_{19}N_2$, 323.1543; found, 323.1540.



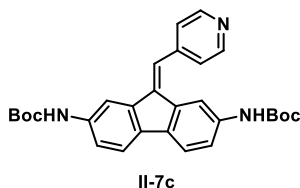
Di-tert-butyl (9-(2-methylpropylidene)-9H-fluorene-2,7-diyl)dicarbamate (**II-7a**). Compound **II-3** (300 mg, 0.757 mmol) and KO^tBu (255 mg, 2.27 mmol) were

dissolved in xylene (7.6 mL). The reaction mixture was refluxed for 30 min. Cooled to room temperature, isobutyraldehyde (139 μ L, 1.51 mmol) was added and refluxed for 10 min. The crude mixture was quenched with saturated ammonium chloride solution and diluted with DCM. The organic layer was washed with brine, dried over MgSO_4 , and concentrated in vacuo. The residue was purified by flash column chromatography (n-hexane/EtOAc = 4:1) to give compound **7a** (218 mg, 66%, bright yellow solid). ^1H NMR (400 MHz, $\text{DMSO-}d_6$): δ 9.37 (d, J = 8.8 Hz, 2H), 8.00 (s, 1H), 7.94 (s, 1H), 7.62 (d, J = 8.2 Hz, 1H), 7.56 (d, J = 8.2 Hz, 2H), 7.24 (dd, J = 1.9, 8.2 Hz, 1H), 6.49 (d, J = 9.4 Hz, 1H), 3.46–3.37 (m, 1H), 1.49 (s, 18H), 1.23 (d, J = 6.6 Hz, 6H); ^{13}C NMR (100 MHz, $\text{DMSO-}d_6$): δ 152.88, 152.82, 139.31, 138.24, 138.13, 137.70, 136.81, 134.56, 133.62, 132.02, 119.36, 119.18, 118.16, 117.68, 114.96, 109.54, 79.00, 28.16, 27.39, 22.54.



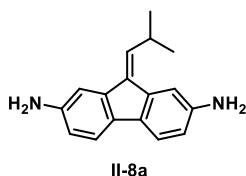
Di-tert-butyl (9-(4-(trifluoromethyl)benzylidene)-9H-fluorene-2,7-diyl)dicarbamate (II-7b). Compound **II-7b** (252 mg, 60%, bright yellow solid) was prepared according to the procedure described for the synthesis

II-7a. ^1H NMR (400 MHz, $\text{DMSO-}d_6$): δ 9.45 (s, 1H), 9.27 (s, 1H), 8.08 (s, 1H), 7.81 (s, 4H), 7.77 (s, 1H), 7.67 (s, 1H), 7.58 (dd, J = 3.5, 8.2 Hz, 2H), 7.36 (d, J = 8.2 Hz, 1H), 7.28 (d, J = 8.1 Hz, 1H), 1.50 (s, 9H), 1.40 (s, 9H); ^{13}C NMR (100 MHz, $\text{DMSO-}d_6$): δ 152.91, 152.57, 143.34, 140.18, 139.22, 138.39, 137.86, 137.20, 135.88, 135.37, 133.36, 129.86, 128.40, 128.08, 125.71, 125.59, 125.55, 123.00, 119.47, 119.39, 119.28, 114.64, 110.68, 79.08, 78.93, 28.16, 27.96; ^{19}F NMR (376 MHz, $\text{DMSO-}d_6$): δ -61.13.



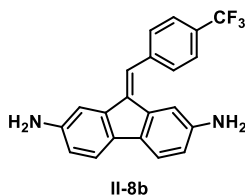
Di-tert-butyl (9-(pyridin-4-ylmethylene)-9H-fluorene-2,7-diyl)dicarbamate (II-7c). Compound **II-7c** (203 mg, 54%, yellow solid) was prepared according to the procedure described for the synthesis **II-7a**. ¹H NMR

(400 MHz, DMSO-*d*₆): δ 9.46 (s, 1H), 9.33 (s, 1H), 8.67 (d, *J* = 6.0 Hz, 2H), 8.06 (s, 1H), 7.67 (s, 1H), 7.54–7.61 (m, 5H), 7.47 (s, 1H), 7.34 (dd, *J* = 1.9, 8.2 Hz, 1H), 1.50 (s, 9H), 1.42 (s, 9H); ¹³C NMR (100 MHz, DMSO-*d*₆): δ 152.84, 152.64, 148.77, 145.06, 138.96, 138.43, 138.16, 137.91, 135.56, 135.51, 133.43, 124.07, 123.79, 119.53, 119.38, 114.73, 110.84, 79.05, 78.94, 28.10, 28.03.

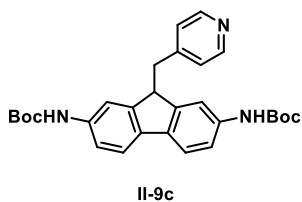


9-(2-Methylpropylidene)-9H-fluorene-2,7-diamine (II-8a).

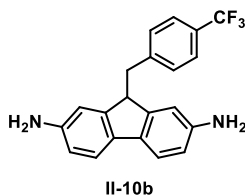
To a solution of compound **II-7a** (188 mg, 0.416 mmol) in DCM (2.0 mL), TFA (2.0 mL, 26.1 mmol) was added. The reaction mixture was stirred at room temperature for 2 h. The crude mixture was concentrated in vacuo and diluted with DCM. The organic layer was washed with saturated sodium bicarbonate solution, dried over MgSO₄, and concentrated in vacuo. The residue was purified by flash column chromatography (n-hexane/EtOAc = 1:1) to give compound **II-8a** (42.5 mg, 41%, orange sticky solid). ¹H NMR (400 MHz, DMSO-*d*₆): δ 7.25 (d, *J* = 8.0 Hz, 1H), 7.20 (d, *J* = 8.0 Hz, 1H), 7.12 (d, *J* = 2.0 Hz, 1H), 6.85 (d, *J* = 2.0 Hz, 1H), 6.52 (ddd, *J* = 1.9, 8.0, 15.8 Hz, 2H), 6.31 (d, *J* = 9.4 Hz, 1H), 5.28 (s, 4H), 3.38 (dd, *J* = 5.3, 8.1 Hz, 1H), 1.19 (d, *J* = 6.5 Hz, 6H); ¹³C NMR (125 MHz, DMSO-*d*₆): δ 146.58, 146.39, 139.52, 137.09, 135.21, 133.78, 130.68, 128.67, 118.47, 118.21, 113.67, 113.54, 111.03, 105.47, 27.07, 22.59. HRMS (*m/z*): [M+H]⁺ calcd for C₁₇H₁₉N₂, 251.1543; found, 251.1539.



9-(4-(Trifluoromethyl)benzylidene)-9H-fluorene-2,7-diamine (II-8b). Compound **II-8b** (92.8 mg, 49%, orange solid) was prepared according to the procedure described for the synthesis **II-8a**. ¹H NMR (400 MHz, DMSO-*d*₆): δ 7.78–7.83 (m, 4H), 7.44 (s, 1H), 7.20 (dd, *J* = 4.1, 8.0 Hz, 2H), 6.97 (d, *J* = 2.0 Hz, 1H), 6.74 (d, *J* = 2.0 Hz, 1H), 6.51 (ddd, *J* = 2.0, 8.0, 17.4 Hz, 2H), 5.01 (s, 2H), 4.87 (s, 2H); ¹³C NMR (100 MHz, CDCl₃): δ 144.94, 144.34, 141.04, 140.36, 138.42, 137.28, 133.96, 131.87, 129.69, 129.65, 126.61, 125.57, 124.18, 122.96, 119.54, 119.44, 116.19, 116.02, 107.48, 111.55; ¹⁹F NMR (376 MHz, DMSO-*d*₆): δ -60.86. HRMS (*m/z*): [M+H]⁺ calcd for C₂₁H₁₆F₃N₂, 353.1260; found, 353.1264.

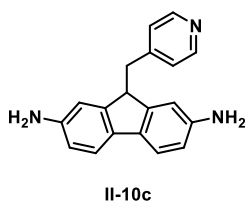


Di-tert-butyl (9-(pyridin-4-ylmethyl)-9H-fluorene-2,7-diyl)dicarbamate (II-9c). Compound **II-7c** (49.0 mg, 0.101 mmol) and palladium on carbon (Pd/C, 10.7 mg, 0.010 mmol) were dissolved in MeOH (2.0 mL). The solution was purged by hydrogen gas balloon and stirred at room temperature for 12 h under hydrogen atmosphere. The crude mixture was filtered through Celite and the filtrate was concentrated in vacuo and the residue was diluted with DCM. The organic layer was washed with H₂O, dried over MgSO₄, and concentrated in vacuo. The residue was purified by flash column chromatography (n-hexane/EtOAc = 6:4) to give compound **II-9c** (25.2 mg, 51%, white solid). ¹H NMR (400 MHz, CDCl₃): δ 8.39 (s, 2H), 7.52–7.39 (m, 4H), 7.19 (dd, *J* = 2.0, 8.2 Hz, 2H), 7.04 (d, *J* = 5.4 Hz, 2H), 6.56 (s, 2H), 4.20 (t, *J* = 6.6 Hz, 1H), 3.23 (d, *J* = 6.6 Hz, 2H), 1.53 (s, 18H); ¹³C NMR (125 MHz, CDCl₃): δ 152.96, 149.35, 148.39, 146.63, 137.04, 136.11, 125.38, 119.96, 118.24, 115.24, 80.75, 47.70, 39.01, 28.54.



9-(4-(Trifluoromethyl)benzyl)-9H-fluorene-2,7-diamine (**II-10b**). Compound **II-8b** (63.7 mg, 0.181 mmol) and palladium on carbon (Pd/C, 19.3 mg, 0.018 mmol) were dissolved in MeOH (1.8 mL). The solution was purged by

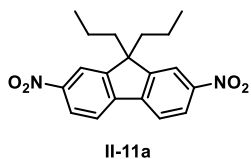
hydrogen gas balloon and stirred at room temperature for 12 h under hydrogen atmosphere. The crude mixture was filtered through Celite and the filtrate was concentrated in vacuo and the residue was diluted with DCM. The organic layer was washed with H₂O, dried over MgSO₄, and concentrated in vacuo. The residue was purified by flash column chromatograph (n-hexane/EtOAc = 6:4) to give compound **II-10b** (37.6 mg, 58%, dark green solid). ¹H NMR (400 MHz, DMSO-*d*₆): δ 7.56 (d, *J* = 7.9 Hz, 2H), 7.35 (d, *J* = 7.9 Hz, 2H), 7.19 (d, *J* = 8.0 Hz, 2H), 6.53–6.43 (m, 4H), 4.89 (s, 4H), 4.04 (t, *J* = 6.5 Hz, 1H), 3.15 (d, *J* = 6.6 Hz, 2H); ¹³C NMR (125 MHz, DMSO-*d*₆): δ 146.24, 146.16, 144.47, 130.29, 129.91, 124.62, 124.59, 118.40, 112.96, 110.47, 46.89, 38.76; ¹⁹F NMR (376 MHz, DMSO-*d*₆): δ -60.62. HRMS (*m/z*): [M+H]⁺ calcd for C₂₁H₁₈F₃N₂, 355.1417; found, 355.1415.



9-(Pyridin-4-ylmethyl)-9H-fluorene-2,7-diamine (**II-10c**). To a solution of compound **II-9c** (77.0 mg, 0.158 mmol) in DCM (1.6 mL), TFA (1.6 mL, 20.9 mmol) was added. The reaction mixture was stirred at room temperature for 2 h. The

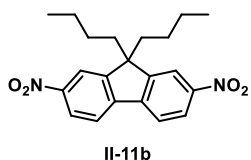
crude mixture was concentrated in vacuo and diluted with DCM. The organic layer was washed with saturated sodium bicarbonate solution, dried over MgSO₄, and concentrated in vacuo. The residue was purified by flash column chromatography (n-hexane/EtOAc = 1:9) to give compound **II-10c** (27.4 mg, 60%, bright orange solid). ¹H NMR (400 MHz, DMSO-*d*₆): δ 8.37 (d, *J* = 6.0 Hz, 2H), 7.19 (d, 7.9 Hz,

2H), 7.13 (d, $J = 6.0$ Hz, 2H), 6.50–6.44 (m, 4H), 4.87 (s, 4H), 4.05 (t, $J = 6.5$ Hz, 1H), 3.07 (d, $J = 6.6$ Hz, 2H); ^{13}C NMR (125 MHz, DMSO- d_6): δ 149.01, 148.39, 146.22, 146.15, 130.26, 124.63, 118.41, 112.96, 110.38, 46.22, 38.22. HRMS (m/z): $[\text{M}+\text{H}]^+$ calcd for $\text{C}_{19}\text{H}_{18}\text{N}_3$, 288.1495; found, 288.1494.



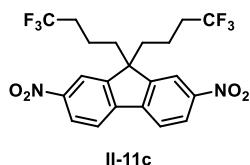
2,7-Dinitro-9,9-dipropyl-9H-fluorene (II-11a). (**II-2**) (300 mg, 1.17 mmol) and Cs_2CO_3 (1.53 g, 3.51 mmol) were dissolved in DMF (3.9 mL). The reaction mixture was stirred

at 0 °C for 30 min and subsequently 1-iodopropane (287 μL , 2.93 mmol) was added. The reaction mixture was stirred at room temperature for 18 h. The crude mixture was quenched by the addition of H_2O and diluted with DCM. The organic layer was washed with H_2O , dried over MgSO_4 , and concentrated in vacuo. The residue was purified by flash column chromatography (n-hexane/EtOAc = 19:1) to give compound **II-11a** (246 mg, 62%, brown solid). ^1H NMR (400 MHz, DMSO- d_6): δ 8.44 (d, $J = 1.6$ Hz, 2H), 8.34–8.27 (m, 4H), 2.20–2.13 (m, 4H), 0.59 (t, $J = 7.2$ Hz, 6H), 0.47 (ddd, $J = 6.2, 9.8, 12.2$ Hz, 4H); ^{13}C NMR (100 MHz, DMSO- d_6): δ 153.18, 148.12, 144.52, 123.50, 122.54, 118.48, 56.34, 40.60, 16.74, 13.98



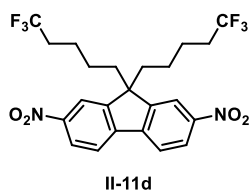
9,9-Dibutyl-2,7-dinitro-9H-fluorene (II-11b). Compound **II-11b** (213 mg, 47%, brown solid) was prepared according to the procedure described for the synthesis **II-11a**. ^1H NMR

(400 MHz, DMSO- d_6): δ 8.44 (d, $J = 1.9$ Hz, 2H), 8.35–8.27 (m, 4H), 2.24–2.16 (m, 4H), 1.06–0.96 (m, 4H), 0.59 (t, $J = 7.3$ Hz, 6H), 0.45–0.37 (m, 4H); ^{13}C NMR (100 MHz, DMSO- d_6): δ 153.20, 148.15, 144.57, 123.52, 122.55, 118.47, 56.16, 38.17, 25.53, 22.23, 13.56.



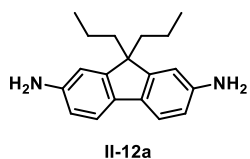
2,7-Dinitro-9,9-bis(4,4,4-trifluorobutyl)-9H-fluorene (II-11c). Compound **II-11c** (223 mg, 40%, brown solid) was prepared according to the procedure described for the

synthesis **II-11a**. ¹H NMR (400 MHz, CDCl₃): δ 8.39 (d, *J* = 8.4 Hz, 2H), 8.27 (s, 2H), 7.98 (d, *J* = 8.3 Hz, 2H), 2.25–2.20 (m, 4H), 1.96–1.84 (m, 4H), 0.84–0.76 (m, 4H); ¹³C NMR (100 MHz, CDCl₃): δ 151.42, 148.87, 144.76, 125.21, 124.57, 123.31, 118.36, 55.89, 38.81, 33.76, 33.48, 16.62; ¹⁹F NMR (376 MHz, CDCl₃): δ -66.21.



2,7-Dinitro-9,9-bis(5,5,5-trifluoropentyl)-9H-fluorene (II-11d). Compound **II-11d** (379 mg, 64%, brown solid) was prepared according to the procedure described for the

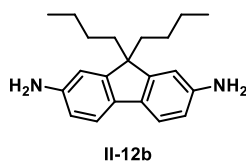
synthesis **II-11a**. ¹H NMR (400 MHz, DMSO-*d*₆): δ 8.49 (d, *J* = 2.0 Hz, 2H), 8.36–8.29 (m, 4H), 2.28–2.24 (m, 4H), 2.02–1.95 (m, 4H), 1.22 (p, *J* = 7.7 Hz, 4H), 0.57–0.49 (m, 4H); ¹³C NMR (100 MHz, DMSO-*d*₆): δ 153.15, 148.67, 144.97, 129.02, 126.82, 124.07, 123.03, 119.17, 56.35, 38.14, 32.38, 32.16, 22.63, 21.82; ¹⁹F NMR (376 MHz, CDCl₃): δ -64.89



9,9-Dipropyl-9H-fluorene-2,7-diamine (II-12a). To a mixture of **II-11a** (222 mg, 0.652 mmol) and Fe₃O₄ (30.2 mg, 0.130 mmol) in EtOH (2.2 mL), hydrazine monohydrate (316

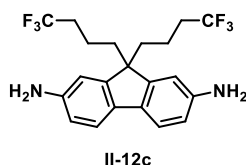
μL, 6.52 mmol) was added. The reaction mixture was stirred at 75 °C for 2 h. The crude mixture was filtered through Celite and the filtrates were concentrated in vacuo and the residue was diluted with DCM. The organic layer washed with H₂O, dried over MgSO₄, and concentrated in vacuo. The residue was purified by flash column chromatography (n-hexane/EtOAc = 7:3) to give compound **II-12a** (70.3 mg, 39%, dark yellow solid). ¹H NMR (400 MHz, DMSO-*d*₆): δ 7.17 (d, *J* = 8.0 Hz, 2H), 6.52

(d, $J = 2.0$ Hz, 2H), 6.44 (dd, $J = 2.0, 8.0$ Hz, 2H), 4.90 (s, 4H), 1.73 (dd, $J = 5.7, 9.7$ Hz, 4H), 0.66–0.55 (m, 10H); ^{13}C NMR (100 MHz, DMSO- d_6): δ 150.24, 146.50, 130.52, 118.33, 112.54, 108.47, 53.86, 42.77, 16.86, 14.30. HRMS (m/z): $[\text{M}+\text{H}]^+$ calcd for $\text{C}_{19}\text{H}_{25}\text{N}_2$, 281.2012; found, 281.2015.



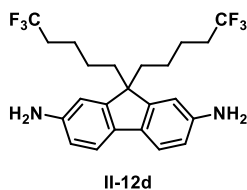
9,9-Dibutyl-9H-fluorene-2,7-diamine (II-12b). Compound **II-12b** (45.6 mg, 28%, dark yellow solid) was prepared according to the procedure described for the synthesis **II-12a**.

^1H NMR (400 MHz, DMSO- d_6): δ 7.17 (d, $J = 8.0$ Hz, 2H), 6.51 (d, $J = 2.0$ Hz, 2H), 6.44 (dd, $J = 2.0, 8.0$ Hz, 2H), 4.90 (s, 4H), 1.77–1.73 (m, 4H), 1.09–1.00 (m, 4H), 0.65 (t, $J = 7.3$ Hz, 6H), 0.58–0.50 (m, 4H); ^{13}C NMR (100 MHz, DMSO- d_6): δ 150.21, 146.48, 130.56, 118.33, 112.56, 108.42, 53.59, 40.30, 25.83, 22.63, 13.90. HRMS (m/z): $[\text{M}+\text{H}]^+$ calcd for $\text{C}_{21}\text{H}_{29}\text{N}_2$, 309.2325; found, 309.2324.

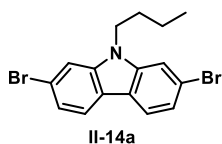


9,9-Bis(4,4,4-trifluorobutyl)-9H-fluorene-2,7-diamine (II-12c). Compound **II-12c** (19.4 mg, 17%, dark yellow solid) was prepared according to the procedure described for the synthesis **II-12a**.

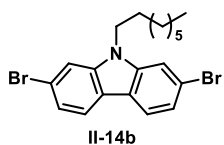
^1H NMR (500 MHz, CDCl_3): δ 7.35 (d, $J = 7.9$ Hz, 2H), 6.65 (dd, $J = 2.2, 8.0$ Hz, 2H), 6.60 (d, $J = 2.1$ Hz, 2H), 3.68 (s, 4H), 1.94–1.91 (m, 4H), 1.86–1.76 (m, 4H), 0.94–0.88 (m, 4H); ^{13}C NMR (125 MHz, CDCl_3): δ 149.58, 145.08, 133.20, 128.24, 126.04, 119.72, 114.74, 109.66, 54.15, 34.07, 33.84, 16.64; ^{19}F NMR (376 MHz, CDCl_3): δ -65.91. HRMS (m/z): $[\text{M}+\text{H}]^+$ calcd for $\text{C}_{21}\text{H}_{23}\text{F}_6\text{N}_2$, 417.1760; found, 417.1759.



9,9-Bis(5,5,5-trifluoropentyl)-9H-fluorene-2,7-diamine (II-12d). Compound **II-12d** (72.2 mg, 23%, dark yellow solid) was prepared according to the procedure described for the synthesis **II-12a**. ¹H NMR (500 MHz, DMSO-*d*₆): δ 7.18 (d, *J* = 8.0 Hz, 2H), 6.53 (d, *J* = 2.0 Hz, 2H), 6.45 (dd, *J* = 2.0, 8.0 Hz, 2H), 4.90 (s, 4H), 2.04–1.93 (m, 4H), 1.82–1.79 (m, 4H), 1.24 (p, *J* = 7.9 Hz, 4H), 0.66–0.60 (m, 4H); ¹³C NMR (125 MHz, DMSO-*d*₆): δ 149.56, 146.55, 130.50, 128.56, 126.36, 118.38, 112.74, 108.37, 53.34, 39.93, 32.30, 32.08, 22.59, 21.77; ¹⁹F NMR (376 MHz, CDCl₃): δ -65.00. HRMS (*m/z*): [M+H]⁺ calcd for C₂₃H₂₇F₆N₂, 445.2073; found, 445.2075.

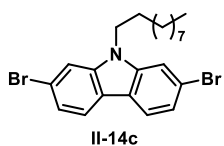


2,7-Dibromo-9-butyl-9H-carbazole (II-14a). **II-13** (3.00 g, 9.23 mmol) and NaH (480 mg, 12.0 mmol) was dissolved in DMF (50.0 mL) at 0 °C. After stirring for 30 min at room temperature, 1-bromobutane (1.19 mL, 11.1 mmol) was added to the mixture and stirred at room temperature for 12 h. The reaction was quenched with addition of H₂O and diluted with EtOAc. The organic layer was washed with brine, dried over MgSO₄, and concentrated in vacuo. The residue was purified by flash column chromatography (n-hexane/EtOAc = 50:1) to give compound **II-14a** (3.52 g, 96%, white solid). ¹H NMR (400 MHz, CDCl₃): δ 7.87 (d, *J* = 8.3 Hz, 2H), 7.54 (d, *J* = 1.5 Hz, 2H), 7.36 (d, *J* = 8.3 Hz, 2H), 4.16 (t, *J* = 7.3 Hz, 2H), 1.87–1.79 (m, 2H), 1.47–1.37 (m, 2H), 0.99 (t, *J* = 7.4 Hz, 3H); ¹³C NMR (100 MHz, CDCl₃) δ 141.32, 122.51, 121.46, 121.25, 119.70, 111.98, 43.13, 30.94, 20.56, 13.89.



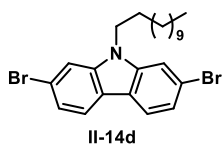
2,7-Dibromo-9-octyl-9H-carbazole (II-14b). Compound **II-14b** (324 mg, 80%, white solid) was prepared according to the procedure described for the synthesis **II-14a**.

^1H NMR (400 MHz, CDCl_3): δ 7.83 (d, $J = 8.2$ Hz, 2H), 7.49 (d, $J = 1.5$ Hz, 2H), 7.31 (dd, $J = 1.6$, 8.3 Hz, 2H), 4.12 (t, $J = 7.4$ Hz, 2H), 1.83–1.76 (m, 2H), 1.33–1.24 (m, 10H), 0.87 (t, $J = 6.9$ Hz, 3H); ^{13}C NMR (100 MHz, CDCl_3): δ 141.36, 122.52, 121.45, 121.29, 119.70, 112.00, 43.33, 31.79, 29.29, 29.17, 28.77, 27.18, 22.63, 14.09.



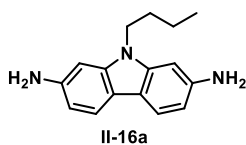
2,7-Dibromo-9-decyl-9H-carbazole (II-14c). Compound **II-14c** (426 mg, 98%, white solid) was prepared according to the procedure described for the synthesis **II-14a**.

^1H NMR (400 MHz, CDCl_3): δ 7.82–7.85 (m, 4H), 7.74 (d, $J = 8.2$ Hz, 2H), 7.55–7.50 (m, 2H), 7.48–7.44 (m, 4H), 7.30–7.26 (m, 6H), 7.25–7.21 (m, 4H), 6.75 (d, $J = 1.2$ Hz, 2H), 6.65 (dd, $J = 1.7$, 8.2 Hz, 2H), 3.96 (t, $J = 7.1$ Hz, 2H), 1.52 (p, $J = 7.4$ Hz, 2H), 1.37–1.21 (m, 14H), 0.93 (t, $J = 5.4$ Hz, 3H); ^{13}C NMR (100 MHz, CDCl_3): δ 167.95, 148.74, 141.24, 140.01, 136.65, 130.69, 129.68, 129.41, 128.58, 128.24, 128.01, 119.70, 119.07, 113.66, 101.47, 42.98, 31.92, 29.67, 29.61, 29.43, 29.36, 28.43, 27.24, 22.72, 14.16.

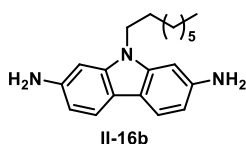


2,7-Dibromo-9-dodecyl-9H-carbazole (II-14d). Compound **II-14d** (312 mg, 69%, white solid) was prepared according to the procedure described for the synthesis **II-14a**.

^1H NMR (400 MHz, CDCl_3): δ 7.87 (d, $J = 8.3$ Hz, 2H), 7.51 (d, $J = 1.6$ Hz, 2H), 7.33 (dd, $J = 1.6$, 8.3 Hz, 2H), 4.16 (t, $J = 7.4$ Hz, 2H), 1.86–1.78 (m, 2H), 1.35–1.24 (m, 18H), 0.87 (t, $J = 6.9$ Hz, 3H); ^{13}C NMR (100 MHz, CDCl_3): δ 141.36, 122.52, 121.49, 121.28, 119.70, 112.02, 43.86, 31.94, 29.63, 29.59, 29.52, 29.35, 28.79, 27.19, 22.72, 14.16.

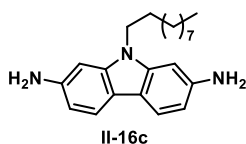


9-Butyl-9H-carbazole-2,7-diamine (II-16a). Compound **II-14a** (500 mg, 1.31 mmol), Pd₂(dba)₃·CHCl₃ (41.0 mg, 0.039 mmol), *t*-BuXPhos (50.0 mg, 0.118 mmol), *t*-BuONa (378 mg, 3.94 mmol) were dissolved in toluene (5.0 mL). Diphenylmethanimine (510 μL, 3.02 mmol) was added and stirred at 100 °C for 16 h. The crude mixture filtered through Celite and the filtrate was concentrated in vacuo and the residue was diluted with DCM. The organic layer was washed with brine, dried over MgSO₄, and concentrated in vacuo. Compound **II-15a** (591 mg, 77%, yellow stick solid) was directly used in the next step without further purification. To a solution of compound **II-15a** (652 mg, 1.12 mmol) in minimum volume of MeOH, 4.0 M HCl in MeOH (11.2 mL, 44.8 mmol) was added and the reaction mixture was stirred at room temperature for 1 h. The crude mixture was concentrated in vacuo and washed with acetone. Compound **II-16a** (290 mg, quantitative yield, yellowish white solid) was isolated without further purification. ¹H NMR (400 MHz, DMSO-*d*₆): δ 10.58 (s, 6H), 8.26 (d, *J* = 8.2 Hz, 2H), 7.66 (d, *J* = 0.9 Hz, 2H), 7.26 (dd, *J* = 1.3, 8.2, Hz, 2H), 4.33 (t, *J* = 6.8 Hz, 2H), 1.75 (p, *J* = 7.2 Hz, 2H), 1.32–1.23 (m, 2H), 0.88 (t, *J* = 7.3 Hz, 3H); ¹³C NMR (100 MHz, DMSO-*d*₆): δ 140.95, 130.70, 122.08, 121.32, 114.68, 104.69, 42.99, 30.81, 22.26, 14.15. HRMS (*m/z*): [M+H]⁺ calcd for C₁₆H₂₀N₃, 254.1652; found, 254.1659.



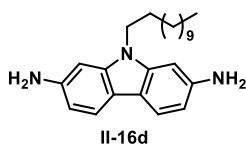
9-Octyl-9H-carbazole-2,7-diamine (II-16b). Compound **II-16b** (312 mg, 69%, white solid) was prepared according to the procedure described for the synthesis **II-16a**. ¹H NMR (400 MHz, DMSO-*d*₆): δ 10.47 (s, 6H), 8.26 (d, *J* = 8.2 Hz, 2H), 7.63 (s, 2H), 7.24 (d, *J* = 8.1 Hz, 2H), 4.35 (t, *J* = 6.4 Hz, 2H), 1.78 (t, *J* = 6.3 Hz, 2H), 1.27–1.19 (m,

10H), 0.82 (t, $J = 6.6$ Hz, 3H); ^{13}C NMR (100 MHz, $\text{DMSO-}d_6$): δ 140.53, 130.67, 121.48, 120.65, 114.18, 103.80, 42.81, 31.11, 28.71, 28.54, 28.19, 26.50, 21.95, 13.87. HRMS (m/z): $[\text{M}+\text{H}]^+$ calcd for $\text{C}_{20}\text{H}_{28}\text{N}_3$, 310.2278; found, 310.2279.



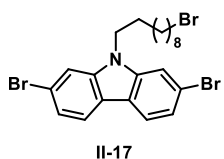
9-Decyl-9H-carbazole-2,7-diamine (II-16c). Compound **II-16c** (441 mg, 86%, yellowish white solid) was prepared according to the procedure described for the synthesis **II-16a**.

^1H NMR (400 MHz, $\text{DMSO-}d_6$): δ 10.25 (s, 6H); 8.24 (d, $J = 8.3$ Hz, 2H), 7.57 (d, $J = 1.3$ Hz, 2H), 7.20 (dd, $J = 1.6, 8.2$, Hz, 2H), 4.35 (t, $J = 7.0$ Hz, 2H), 1.79 (t, $J = 6.7$ Hz, 2H), 1.28–1.20 (m, 14H), 0.85 (t, $J = 6.9$ Hz, 3H); ^{13}C NMR (100 MHz, $\text{DMSO-}d_6$): δ 141.00, 137.47, 133.17, 130.07, 129.05, 104.52, 43.32, 31.72, 29.43, 29.39, 29.30, 29.11, 28.72, 27.03, 22.54, 14.42. HRMS (m/z): $[\text{M}+\text{H}]^+$ calcd for $\text{C}_{22}\text{H}_{32}\text{N}_3$, 338.2591; found, 338.2594.



9-Dodecyl-9H-carbazole-2,7-diamine (II-16d). Compound **II-16d** (82.0 mg, 93%, yellowish white solid) was prepared according to the procedure described for the synthesis **II-16a**.

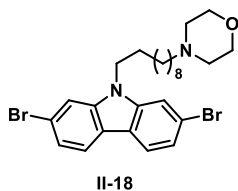
^1H NMR (400 MHz, $\text{DMSO-}d_6$): δ 8.24 (d, $J = 8.2$ Hz, 2H), 7.59 (d, $J = 1.0$ Hz, 2H), 7.21 (dd, $J = 1.3, 8.2$ Hz, 2H), 4.35 (t, $J = 6.8$ Hz, 2H), 1.77 (t, $J = 6.8$ Hz, 2H), 1.26–1.18 (m, 18H), 0.84 (t, $J = 6.8$ Hz, 3H); ^{13}C NMR (100 MHz, $\text{DMSO-}d_6$): δ 141.08, 131.32, 122.01, 121.05, 114.51, 104.08, 43.27, 31.74, 29.45, 29.43, 29.30, 29.14, 28.72, 27.01, 22.54, 14.41. HRMS (m/z): $[\text{M}+\text{H}]^+$ calcd for $\text{C}_{24}\text{H}_{36}\text{N}_3$, 366.2904; found, 366.2912.



2,7-Dibromo-9-(10-bromodecyl)-9H-carbazole (II-17).

Compound **II-17** (82.0 mg, 99%, white solid) was prepared according to the procedure described for the synthesis **II-14a**.

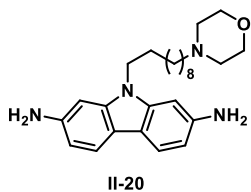
¹H NMR (400 MHz, DMSO-*d*₆): δ 8.11 (d, *J* = 8.3 Hz, 2H), 7.89 (d, *J* = 1.7 Hz, 2H), 7.35 (dd, *J* = 1.6, 8.3 Hz, 2H), 4.38 (t, *J* = 7.1 Hz, 2H), 3.49 (t, *J* = 6.7 Hz, 2H), 1.78–1.66 (m, 4H), 1.35–1.15 (m, 12H); ¹³C NMR (100 MHz, DMSO-*d*₆): δ 141.12, 122.21, 122.11, 120.68, 119.16, 112.45, 42.33, 35.19, 32.21, 28.83, 28.72, 28.59, 28.28, 28.04, 27.48, 26.16.



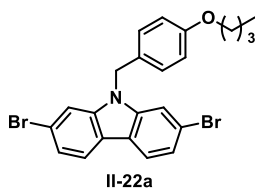
4-(10-(2,7-Dibromo-9H-carbazol-9-yl)decyl)morpholine (II-18).

A mixture of compound **II-17** (715 mg, 1.31 mmol), K₂CO₃ (706 mg, 5.11 mmol), and morpholine (490 μL, 5.11 mmol) in MeCN (6.0 mL) was refluxed for 10 h. After cooling

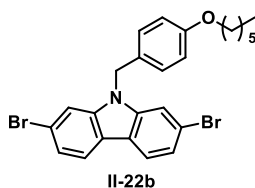
to room temperature, the crude mixture was concentrated in vacuo and diluted with EtOAc. The organic layer was washed with brine, dried over MgSO₄, and concentrated in vacuo. The residue was purified by flash column chromatography (n-hexane/EtOAc = 1:3) to give compound **II-18** (441 mg, 47%, white solid). ¹H NMR (400 MHz, CDCl₃): δ 7.93 (d, *J* = 8.0 Hz, 2H), 7.55 (s, 2H), 7.38 (dd, *J* = 0.8, 8.0 Hz, 2H), 4.24 (m, 2H), 3.75 (t, *J* = 0.8 Hz, 4H), 2.45 (s, 4H), 2.35 (t, *J* = 7.2 Hz, 2H), 1.87 (m, 2H), 1.45 (m, 2H), 1.37 (m, 14H); ¹³C NMR (100 MHz, CDCl₃): δ 141.37, 122.53, 121.50, 121.29, 119.69, 112.01, 66.51, 59.05, 53.50, 43.34, 29.44, 29.42, 29.41, 29.39, 29.28, 28.76, 27.37, 27.14.



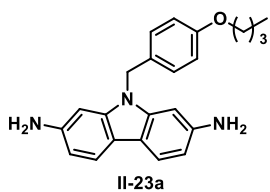
9-(10-Morpholinodecyl)-9H-carbazole-2,7-diamine (II-20). Compound **II-20** (235 mg, 69%, pink solid) was prepared according to the procedure described for the synthesis **II-16a**. ¹H NMR (400 MHz, DMSO-*d*₆): δ 7.46 (d, *J* = 8.1 Hz, 2H), 6.51 (d, *J* = 1.8 Hz, 2H), 6.37 (dd, *J* = 1.8, 8.1 Hz, 2H), 4.93 (s, 4H), 3.99 (t, *J* = 7.2 Hz, 2H), 3.54 (t, *J* = 4.7 Hz, 4H), 2.29 (s, 4H), 2.23–2.18 (m, 2H), 1.68 (t, *J* = 7.1 Hz, 2H), 1.39–1.22 (m, 12H); ¹³C NMR (125 MHz, DMSO-*d*₆): δ 145.77, 141.40, 118.72, 113.90, 107.16, 93.12, 66.15, 58.25, 53.32, 41.99, 28.94, 28.88, 28.85, 28.83, 28.13, 26.81, 26.61, 25.85. HRMS (*m/z*): [M+H]⁺ calcd for C₂₆H₃₉N₄O, 423.3118; found, 423.3114.



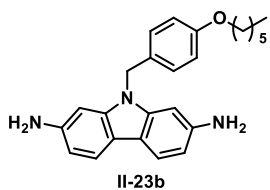
2,7-Dibromo-9-(4-butoxybenzyl)-9H-carbazole (II-22a). 2,7-Dibromocarbazole (**II-13**) (352 mg, 1.08 mmol) and NaH (56.4 mg, 1.41 mmol) was dissolved in DMF (5.4 mL) at 0 °C. After stirring at room temperature for 30 min, compound **II-21a** (280 mg, 1.41 mmol) was added to the mixture and stirred at room temperature for 12 h. The reaction was quenched with addition of H₂O and diluted with EtOAc. The organic layer was washed with brine, dried over MgSO₄, and concentrated in vacuo. The residue was purified by flash column chromatography (n-hexane/EtOAc = 50:1) to give compound **II-22a** (528 mg, 99%, white solid). ¹H NMR (400 MHz, CDCl₃): δ 7.92 (dd, *J* = 0.2, 8.3 Hz, 2H), 7.53 (d, *J* = 1.5 Hz, 2H), 7.39 (dd, *J* = 1.7, 8.3 Hz, 2H), 7.05 (d, *J* = 8.8 Hz, 2H), 6.85–6.82 (m, 2H), 5.33 (s, 2H), 3.93 (t, *J* = 6.5 Hz, 2H), 1.80–1.73 (m, 2H), 1.53–1.48 (m, 2H), 1.00 (t, *J* = 7.4 Hz, 3H); ¹³C NMR (100 MHz, CDCl₃): δ 158.82, 141.55, 127.71, 127.54, 122.96, 121.50, 121.44, 119.92, 114.94, 112.28, 67.73, 46.25, 31.29, 19.25, 13.87.



2,7-Dibromo-9-(4-(hexyloxy)benzyl)-9H-carbazole (II-22b). Compound **II-22b** (1.35 g, 99%, white solid) was prepared according to the procedure described for the synthesis **II-22a**. ¹H NMR (400 MHz, CDCl₃): δ 7.90 (d, *J* = 8.3 Hz, 2H), 7.53 (d, *J* = 1.5 Hz, 2H), 7.39 (dd, *J* = 1.6, 8.3 Hz, 2H), 7.05 (d, *J* = 8.7 Hz, 2H), 6.83 (dd, *J* = 2.0, 6.8 Hz, 2H), 5.29 (s, 2H), 3.91 (t, *J* = 6.6 Hz, 2H), 1.78 (p, *J* = 7.1 Hz, 2H), 1.51–1.41 (m, 2H), 1.39–1.33 (m, 4H), 0.96 (t, *J* = 6.9 Hz, 3H); ¹³C NMR (100 MHz, CDCl₃): δ 158.82, 141.52, 127.72, 127.57, 122.96, 121.50, 121.43, 119.93, 114.93, 112.27, 68.05, 46.22, 31.63, 29.24, 25.76, 22.66, 14.12.

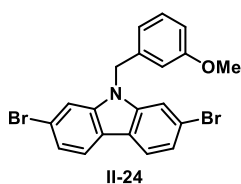


9-(4-Butoxybenzyl)-9H-carbazole-2,7-diamine (II-23a). Compound **II-23a** (336 mg, 91%, yellowish white solid) was prepared according to the procedure described for the synthesis **II-16a**. ¹H NMR (400 MHz, CDCl₃): δ 7.73 (d, *J* = 8.2 Hz, 2H), 7.01 (d, *J* = 8.6 Hz, 2H), 6.75 (d, *J* = 8.7 Hz, 2H), 6.56 (dd, *J* = 1.7, 8.2 Hz, 2H), 6.47 (d, *J* = 1.6 Hz, 2H), 5.09 (s, 2H), 3.85 (t, *J* = 6.5 Hz, 2H), 3.65 (s, 4H), 1.77–1.70 (m, 2H), 1.53–1.33 (m, 2H), 1.00 (t, *J* = 6.7 Hz, 3H); ¹³C NMR (100 MHz, CDCl₃): δ 158.45, 144.33, 142.26, 129.25, 127.60, 119.87, 116.25, 114.75, 108.55, 94.99, 67.74, 45.66, 31.38, 19.33, 13.97. HRMS (*m/z*): [M+H]⁺ calcd for C₂₃H₂₆N₃O, 360.2070; found, 360.2073.



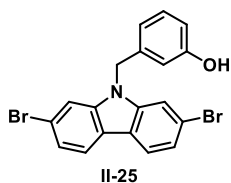
9-(4-(Hexyloxy)benzyl)-9H-carbazole-2,7-diamine (II-23b). Compound **II-23a** (675 mg, 86%, yellowish white solid) was prepared according to the procedure described for the synthesis **II-16a**. ¹H NMR (400 MHz, CDCl₃): δ 7.74 (d, *J* = 8.1 Hz, 2H), 7.08 (d, *J* = 8.6 Hz, 2H), 6.81 (d, *J* = 8.6 Hz, 2H), 6.61–

6.57 (m, 4H), 5.24 (s, 2H), 3.91 (t, $J = 6.5$ Hz, 2H), 3.71 (s, 4H), 1.77 (p, $J = 7.0$ Hz, 2H), 1.48–1.43 (m, 2H), 1.37–1.30 (m, 4H), 0.93 (t, $J = 6.7$ Hz, 3H); ^{13}C NMR (100 MHz, CD_3OD): δ 158.17, 144.50, 142.05, 129.46, 127.39, 119.20, 116.12, 114.12, 108.70, 95.34, 67.53, 44.80, 31.40, 28.95, 25.47, 22.33, 13.18.



2,7-Dibromo-9-(3-methoxybenzyl)-9H-carbazole (II-24).

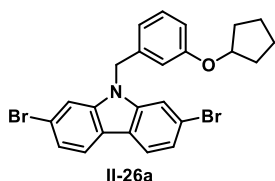
A mixture of 2,7-dibromocarbazole (**II-13**) (200 mg, 0.165 mmol) and NaH (8.6 mg, 0.214 mmol) in DMF (0.8 mL) was stirred at 0°C for 30 min. After 30 min, 1-(bromomethyl)-3-methoxybenzene (100 μL , 0.738 mmol) was added to the mixture and stirred at room temperature for 12 h. The crude mixture was quenched by the addition of H_2O and diluted with EtOAc. The organic layer washed with H_2O , dried over MgSO_4 , and concentrated in vacuo. The residue was purified by flash column chromatography (n-hexane/EtOAc = 50:1) to give compound **II-24** (274 mg, 99%, white solid). ^1H NMR (400 MHz, CDCl_3): δ 7.93 (d, $J = 8.3$ Hz, 2H), 7.52 (d, $J = 1.5$ Hz, 2H), 7.39 (dd, $J = 1.6, 8.3$ Hz, 2H), 7.24 (t, $J = 7.9$ Hz, 1H), 6.83 (dd, $J = 2.1, 8.2$ Hz, 1H), 6.71–6.69 (m, 1H), 6.66 (d, $J = 2.0$ Hz, 1H), 5.39 (s, 2H), 3.76 (s, 3H); ^{13}C NMR (100 MHz, CDCl_3): δ 160.11, 141.62, 137.65, 130.15, 123.09, 121.54, 121.48, 119.97, 118.43, 112.67, 112.36, 112.24, 55.22, 46.63.



3-((2,7-Dibromo-9H-carbazol-9-yl)methyl)phenol (II-25).

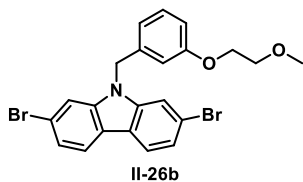
A solution of compound **II-24** (380 mg, 0.854 mmol) and NaI (640 mg, 4.27 mmol) in MeCN (3.0 mL), TMSCl (867 μL , 6.83 mmol) was added dropwise. The reaction mixture was refluxed for 3 h. The crude mixture was quenched by the addition of H_2O and diluted with EtOAc. The organic layer washed with H_2O , dried over MgSO_4 , and

concentrated in vacuo. The residue was purified by flash column chromatography (n-hexane/EtOAc = 5:1) to give compound **II-25** (205 mg, 56%, white solid). ¹H NMR (400 MHz, acetone-*d*₆): δ 8.40 (s, 1H), 8.08 (d, *J* = 8.3 Hz, 2H), 7.78 (d, *J* = 1.5 Hz, 2H), 7.39 (dd, *J* = 1.7, 8.3 Hz, 2H), 7.16 (t, *J* = 7.9 Hz, 1H), 6.78–6.75 (m, 1H), 6.74–6.71 (m, 1H), 6.58 (t, *J* = 1.9 Hz, 1H), 5.60 (s, 2H); ¹³C NMR (100 MHz, acetone-*d*₆): δ 157.84, 141.77, 138.59, 129.92, 122.77, 121.87, 121.40, 119.56, 117.66, 114.60, 113.13, 112.59, 45.96.



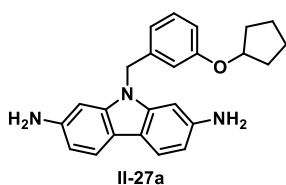
2,7-Dibromo-9-(3-(cyclopentyloxy)benzyl)-9H-carbazole (II-26a). A suspension of compound **II-25** (400 mg, 0.928 mmol), bromocyclopentane (150 μL, 1.39 mmol), and K₂CO₃ (256 mg, 1.86 mmol) in DMF (4.0 mL)

was stirred at 90 °C for 5 h. The crude mixture was cooled to room temperature and diluted with EtOAc. The organic layer was washed with H₂O, dried over MgSO₄, and concentrated in vacuo. The residue was purified by flash column chromatography (n-hexane/EtOAc = 50:1) to give compound **II-26a** (169 mg, 37%, white solid). ¹H NMR (400 MHz, CDCl₃): δ 7.91 (d, *J* = 8.3 Hz, 2H), 7.52 (d, *J* = 1.5 Hz, 2H), 7.39 (dd, *J* = 1.6, 8.3 Hz, 2H), 7.21 (t, *J* = 7.9 Hz, 1H), 6.81 (dd, *J* = 2.0, 8.2 Hz, 1H), 6.67 (dd, *J* = 0.7, 7.6 Hz, 1H), 6.63 (d, *J* = 1.9 Hz, 1H), 5.34 (s, 2H), 4.69–4.65 (m, 1H), 1.90–1.74 (m, 6H), 1.66–1.58 (m, 2H); ¹³C NMR (100 MHz, CDCl₃): δ 158.68, 141.63, 137.52, 130.01, 123.04, 121.51, 121.47, 119.95, 117.98, 114.39, 113.77, 112.30, 79.25, 46.68, 32.80, 24.09.



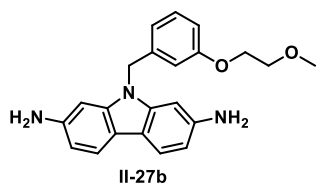
2,7-Dibromo-9-(3-(2-methoxyethoxy)benzyl)-9H-carbazole (II-26b). Compound **II-26b** (388 mg, 92%, white solid) was prepared according to the procedure

described for the synthesis **II-26a**. ^1H NMR (400 MHz, CDCl_3): δ 7.87 (d, $J = 8.3$ Hz, 2H), 7.47 (d, $J = 1.5$ Hz, 2H), 7.37 (dd, $J = 1.6, 8.3$ Hz, 2H), 7.22 (t, $J = 7.9$ Hz, 1H), 6.82 (dd, $J = 2.1, 8.2$ Hz, 1H), 6.71 (d, $J = 7.6$ Hz, 1H), 6.66–6.65 (m, 1H), 5.27 (s, 2H), 4.04–4.02 (m, 2H), 3.70–3.68 (m, 2H), 3.43 (s, 3H); ^{13}C NMR (100 MHz, CDCl_3): δ 159.33, 141.53, 137.68, 130.10, 123.07, 121.53, 121.43, 119.98, 118.75, 113.13, 112.20, 70.91, 67.17, 59.23, 46.53.



9-(3-(Cyclopentyloxy)benzyl)-9H-carbazole-2,7-diamine (II-27a). Compound **II-27a** (68.0 mg, 71%, yellowish white solid) was prepared according to the procedure described for the synthesis **II-16a**. ^1H NMR

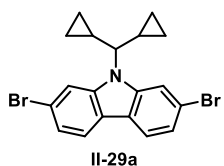
(400 MHz, $\text{DMSO}-d_6$): δ 7.51 (d, $J = 8.2$ Hz, 2H), 7.17 (t, $J = 7.9$ Hz, 1H), 6.74 (dd, $J = 2.5, 8.2$ Hz, 1H), 6.68 (d, $J = 7.7$ Hz, 1H), 6.50–6.47 (m, 3H), 6.40 (dd, $J = 1.8, 8.2$ Hz, 2H), 5.22 (s, 2H), 4.94 (s, 4H), 4.71–4.62 (m, 1H), 1.88–1.78 (m, 2H), 1.65–1.45 (m, 6H); ^{13}C NMR (100 MHz, $\text{DMSO}-d_6$): δ 157.79, 146.01, 141.64, 139.67, 129.57, 118.92, 118.20, 113.92, 113.80, 112.88, 107.54, 93.31, 78.42, 45.07, 32.21, 23.58. HRMS (m/z): $[\text{M}+\text{H}]^+$ calcd for $\text{C}_{24}\text{H}_{26}\text{N}_3\text{O}$, 372.2070; found, 372.2071.



9-(3-(2-Methoxyethoxy)benzyl)-9H-carbazole-2,7-diamine (II-27b). Compound **II-27b** (153 mg, 82%, yellowish white solid) was prepared according to the procedure described for the synthesis **II-16a**. ^1H NMR

(400 MHz, $\text{DMSO}-d_6$): δ 10.53 (s, 6H), 8.27 (d, $J = 8.2$ Hz, 2H), 7.63 (d, $J = 1.4$ Hz, 2H), 7.27 (dd, $J = 1.6, 8.3$ Hz, 2H), 7.18 (t, $J = 7.9$ Hz, 1H), 6.81 (dd, $J = 8.2, 2.2$ Hz, 1H), 6.70–6.66 (m, 2H), 5.58 (s, 2H), 4.02–3.99 (m, 2H), 3.58–3.55 (m, 2H), 3.23 (s, 3H); ^{13}C NMR (100 MHz, $\text{DMSO}-d_6$): δ 159.20, 141.16, 138.84, 131.16,

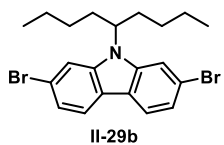
130.46, 122.16, 121.38, 119.18, 115.21, 113.60, 113.34, 104.62, 70.73, 67.25, 58.55, 46.32. HRMS (m/z): $[M+H]^+$ calcd for $C_{22}H_{24}N_3O_2$, 362.1863; found, 362.1865.



2,7-Dibromo-9-(dicyclopropylmethyl)-9H-carbazole (**II-**

29a). 2,7-Dibromocarbazole (**II-13**) (1.54 g, 4.74 mmol) and NaH (246 mg, 6.16 mmol) was dissolved in DMF (23.7 mL) at

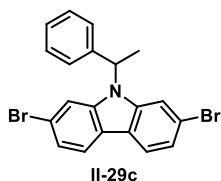
0 °C. After stirring at room temperature for 30 min, compound (bromomethylene)dicyclopropane (**II-28a**) (1.66 g, 9.48 mmol) was added to the mixture and stirred at room temperature for 12 h. The reaction was quenched with addition of H_2O and diluted with EtOAc. The organic layer was washed with brine, dried over $MgSO_4$, and concentrated in vacuo. The residue was purified by flash column chromatography (n-hexane/EtOAc = 50:1) to give compound **II-29a** (1.56 g, 79%, white solid). 1H NMR (400 MHz, $CDCl_3$): δ 7.87 (d, $J = 6.2$ Hz, 2H), 7.54 (d, $J = 0.9$ Hz, 2H), 7.36 (dd, $J = 1.0, 6.2$ Hz, 2H), 5.45–5.35 (m, 1H), 5.05–4.99 (m, 1H), 4.21–4.18 (m, 2H), 2.52–2.47 (m, 2H), 1.36–1.28 (m, 1H), 0.69–0.62 (m, 2H), 0.26–0.23 (m, 2H); ^{13}C NMR (100 MHz, $CDCl_3$): δ 141.23, 137.42, 123.15, 122.52, 121.37, 121.18, 119.68, 112.13, 43.37, 31.72, 13.58, 6.52.



2,7-Dibromo-9-(nonan-5-yl)-9H-carbazole (**II-29b**).

Compound **II-29b** (656 mg, 95%, white solid) was prepared according to the procedure described for the synthesis **II-29a**.

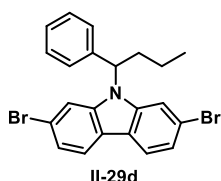
1H NMR (400 MHz, $CDCl_3$): δ 7.93 (d, $J = 7.8$ Hz, 2H), 7.73 (d, $J = 6.8$ Hz, 1H), 7.58 (d, $J = 7.0$ Hz, 1H), 7.39–7.36 (m, 2H), 4.48–4.41 (m, 1H), 2.25–2.22 (m, 2H), 1.99–1.92 (m, 2H), 1.32–1.19 (m, 6H), 1.00–0.97 (m, 2H), 0.81 (t, $J = 7.2$ Hz, 6H); ^{13}C NMR (100 MHz, $CDCl_3$): δ 122.59, 122.35, 121.44, 119.74, 114.49, 112.11, 57.07, 33.28, 28.95, 22.42, 13.84.



2,7-Dibromo-9-(1-phenylethyl)-9H-carbazole (II-29c).

Compound **II-29c** (754 mg, 91%, white solid) was prepared according to the procedure described for the synthesis **II-29a**.

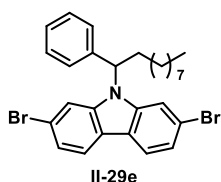
^1H NMR (400 MHz, CDCl_3): δ 7.95 (d, $J = 8.3$ Hz, 2H), 7.46 (d, $J = 1.5$ Hz, 2H), 7.42–7.36 (m, 5H), 7.33–7.29 (m, 2H), 6.00 (q, $J = 7.1$ Hz, 1H), 2.03 (d, $J = 7.2$ Hz, 1H); ^{13}C NMR (100 MHz, CDCl_3): δ 140.85, 139.57, 128.96, 127.88, 126.39, 122.86, 121.93, 121.47, 119.66, 113.47, 52.86, 17.51.



2,7-Dibromo-9-(1-phenylbutyl)-9H-carbazole (II-29d).

Compound **II-29d** (573 mg, 82%, white solid) was prepared according to the procedure described for the synthesis **II-29a**.

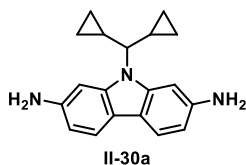
^1H NMR (400 MHz, CDCl_3): δ 7.89 (d, $J = 8.3$ Hz, 2H), 7.46 (d, $J = 1.3$ Hz, 2H), 7.33–7.24 (m, 7H), 5.74 (q, $J = 5.2$ Hz, 1H), 2.61–2.51 (m, 1H), 2.48–2.40 (m, 1H), 1.34–1.22 (m, 1H), 1.06–1.04 (m, 1H), 0.89 (t, $J = 7.2$ Hz, 3H); ^{13}C NMR (100 MHz, CDCl_3): δ 141.27, 139.26, 128.86, 127.79, 126.55, 122.82, 121.71, 121.42, 119.65, 113.50, 57.65, 33.61, 20.07, 13.94.



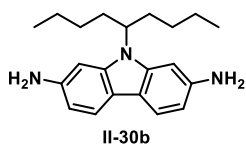
2,7-Dibromo-9-(1-phenyldecyl)-9H-carbazole (II-29e).

Compound **II-29e** (317 mg, 38%, white solid) was prepared according to the procedure described for the synthesis **II-29a**.

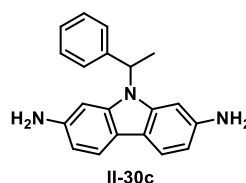
^1H NMR (400 MHz, CDCl_3): δ 7.78 (d, $J = 8.3$ Hz, 2H), 7.48 (d, $J = 1.2$ Hz, 2H), 7.26 (dd, $J = 1.6, 8.3$ Hz, 2H), 7.20–7.09 (m, 5H), 5.65 (q, $J = 5.2$ Hz, 1H), 2.57–2.47 (m, 1H), 2.43–2.35 (m, 1H), 1.36–0.99 (m, 13H), 0.97–0.88 (m, 1H), 0.82 (t, $J = 7.1$ Hz, 3H); ^{13}C NMR (100 MHz, CDCl_3): δ 141.44, 139.46, 128.95, 127.90, 126.71, 122.99, 121.87, 121.56, 119.89, 113.66, 58.01, 32.02, 31.57, 29.62, 29.50, 29.49, 29.41, 26.76, 22.87, 14.37.



9-(Dicyclopropylmethyl)-9H-carbazole-2,7-diamine (**II-30a**). Compound **II-30a** (139 mg, 56%, yellowish white solid) was prepared according to the procedure described for the synthesis **II-16a**. ¹H NMR (400 MHz, DMSO-*d*₆): δ 10.63 (s, 6H), 8.24 (d, *J* = 6.2 Hz, 2H), 7.67–7.64 (m, 2H), 7.25 (dd, *J* = 1.2, 6.2 Hz, 2H), 5.51–5.44 (m, 1H), 4.91–4.85 (m, 1H), 4.35–4.31 (m, 2H), 2.46–2.41 (m, 2H), 1.28–1.19 (m, 1H), 0.53–0.48 (m, 2H), 0.08–0.05 (m, 2H); ¹³C NMR (100 MHz, DMSO-*d*₆): δ 140.89, 137.16, 130.69, 123.58, 121.99, 121.29, 114.83, 104.79, 43.25, 31.59, 13.70, 6.56. HRMS (*m/z*): [M+H]⁺ calcd for C₁₉H₂₂N₃, 292.1808; found, 292.1817.

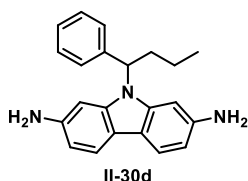


9-(Nonan-5-yl)-9H-carbazole-2,7-diamine (**II-30b**). Compound **II-30b** (71.0 mg, 69%, yellowish white solid) was prepared according to the procedure described for the synthesis **II-16a**. ¹H NMR (400 MHz, CDCl₃): δ 7.71–7.66 (m, 2H), 6.77 (s, 1H), 6.59–6.53 (m, 3H), 4.33–4.26 (m, 1H), 3.72 (s, 4H), 2.24–2.14 (m, 2H), 1.88–1.79 (m, 2H), 1.31–1.12 (m, 6H), 1.09–0.97 (m, 2H), 0.77 (t, *J* = 7.2 Hz, 6H); ¹³C NMR (100 MHz, CDCl₃): δ 143.89, 143.52, 143.24, 119.78, 119.58, 117.34, 115.96, 108.05, 97.75, 94.93, 56.21, 33.26, 29.13, 22.63, 14.00. HRMS (*m/z*): [M+H]⁺ calcd for C₂₁H₃₀N₃, 324.2434; found, 324.2439.



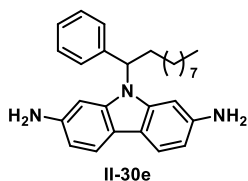
9-(1-Phenylethyl)-9H-carbazole-2,7-diamine (**II-30c**). Compound **II-30c** (62.5 mg, 48%, yellowish white solid) was prepared according to the procedure described for the synthesis **II-16a**. ¹H NMR (400 MHz, DMSO-*d*₆): δ 7.51 (d, *J* = 8.2 Hz, 2H), 7.31 (dd, *J* = 6.6, 8.1 Hz, 2H), 7.27–7.19 (m, 3H), 6.47 (d, *J* = 1.9 Hz, 2H), 6.39 (dd, *J* = 1.8 Hz, 8.1 Hz, 2H), 5.81 (q, *J* = 7.1 Hz, 1H), 4.89 (s, 4H),

1.91 (d, $J = 7.1$ Hz, 3H); ^{13}C NMR (100 MHz, DMSO- d_6): δ 145.58, 141.50, 140.88, 128.42, 126.88, 126.16, 118.78, 114.45, 107.42, 94.82, 51.33, 17.48. HRMS (m/z): $[\text{M}+\text{H}]^+$ calcd for $\text{C}_{20}\text{H}_{20}\text{N}_3$, 302.1652; found, 302.1651.



9-(1-Phenylbutyl)-9H-carbazole-2,7-diamine (**II-30d**).

Compound **II-30d** (122 mg, 93%, yellowish white solid) was prepared according to the procedure described for the synthesis **II-16a**. ^1H NMR (400 MHz, DMSO- d_6): δ 10.23 (s, 6H), 8.28–8.23 (m, 2H), 7.77–7.55 (m, 2H), 7.37–7.29 (m, 5H), 7.21–7.15 (m, 2H), 6.02 (d, $J = 4.9$ Hz, 1H), 2.63–2.60 (m, 2H), 1.21–0.86 (m, 2H), 0.88 (t, $J = 5.3$ Hz, 3H); ^{13}C NMR (100 MHz, DMSO- d_6): δ 140.84, 140.02, 131.04, 129.23, 128.05, 126.98, 122.04, 121.63, 115.04, 105.74, 57.66, 33.13, 19.87, 14.07. HRMS (m/z): $[\text{M}+\text{H}]^+$ calcd for $\text{C}_{22}\text{H}_{24}\text{N}_3$, 330.1965; found, 330.1967.



9-(1-Phenyldecyl)-9H-carbazole-2,7-diamine (**II-30e**).

Compound **II-30e** (53 mg, 67%, yellowish white solid) was prepared according to the procedure described for the synthesis **II-16a**. ^1H NMR (400 MHz, CD_3OD): δ 8.37 (d, $J = 7.7$ Hz, 2H), 7.77–7.66 (m, 2H), 7.36–7.29 (m, 7H), 6.15–6.11 (m, 1H), 2.70–2.66 (m, 2H), 1.38–1.14 (m, 13H), 0.93–0.89 (m, 1H), 0.84 (t, $J = 6.8$ Hz, 3H); ^{13}C NMR (100 MHz, CD_3OD): δ 142.58, 140.79, 130.26, 130.02, 128.90, 127.86, 124.07, 123.43, 115.69, 106.92, 59.44, 32.96, 32.47, 30.52, 30.43, 30.41, 30.24, 27.81, 23.64, 14.44. HRMS (m/z): $[\text{M}+\text{H}]^+$ calcd for $\text{C}_{28}\text{H}_{36}\text{N}_3$, 414.2904; found, 414.2911.

3. Mutagenicity assay

Mutagenicity assay was conducted using a commercial assay kit (XEA10-210-1-S1-P; Xenometrix, Switzerland). The bacterial strains used were histidine-requiring frame-shift mutants (TA98) or base-pair substitution mutants (TA100) of *Salmonella typhimurium* LT-2.⁶⁸ The bacteria were exposed twice to six different concentrations (4 to 5000 μ M) of the test samples, once with S9 mix, which was obtained from rat liver for metabolic activation purpose, and the other without S9, for 90 min in a medium containing sufficient amount of histidine to support approximately two cell divisions. As positive controls, the bacteria were treated with 2-aminoanthracene (2-AA) in the presence of S-9 mix or with 4-nitroquinoline *N*-oxide (4-NQO) and 2-nitrofluorene (2-NF) in the absence of S9.⁶⁷ As a negative control, the bacteria were treated with DMSO. After exposure, the cultures were diluted in a pH indicator medium lacking histidine, and aliquoted into 48 wells of a 384-well plate. Within two days, cells that have undergone reversion to histidine prototrophy would grow into colonies. Bacterial metabolism reduces the pH of the medium, changing the color of that well. The number of wells containing revertant colonies were counted for each dose and compared with that in the negative control. Assays for each dose were performed in triplicate to allow statistical analysis. If the ratio of the number of revertant colonies in a sample to that in the negative control is more than 3, the sample is regarded mutagenic.

Chapter III. Development of Potent HCV NS5A Inhibitors Containing a Fluorene Skeleton

I. Introduction

The HCV is a major pathogen of humans worldwide. Infection with HCV can become chronic in 60–80% of patients, and a significant number of them develop liver cirrhosis or even hepatocellular carcinoma.^{1,2} An estimated 71 million people are chronically infected with hepatitis C globally, and every year approximately 0.4 million people die from it.^{1,2}

Currently, no vaccine is available for hepatitis C, however, treatment with DAAs that directly target HCV viral proteins have achieved >95% SVR rate without noticeable side effects.⁶⁹ The WHO aims to eliminate HCV by 2030, but this task is challenging. First, DAAs do not induce protective immunity, so after patients are cured, they can be re-infected.⁷⁰ Second, only an estimated 20% of patients are aware of their infection, so the number of patients to be treated is huge.⁷¹ Most importantly, treatment using DAAs is not always applicable; its effectiveness can be limited to specific HCV genotypes, restricted by the patient's treatment history, and useless for patients who have developed cirrhosis.

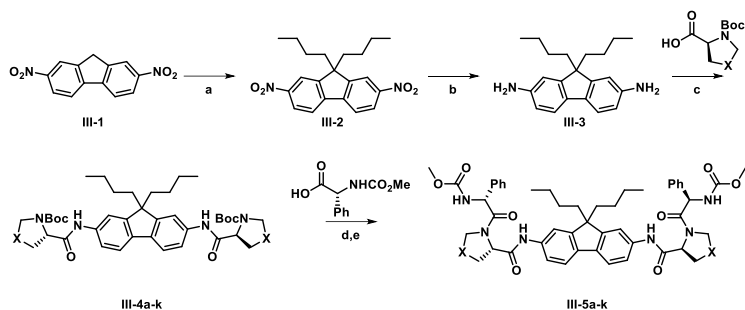
Recently, we reported several fluorene compounds as potent NS5A inhibitors containing a proline residue showing remarkable antiviral activities against HCV GT-1b and GT-3a.⁶¹ Through *in vitro* assays, we revealed that introducing (*R*)-OH group at C4 position of the proline residue could enhance inhibitory effect on mutated proteins. This enhancement seems to be the result of additional hydrogen bonding between the (*R*)-OH group and mutated NS5A according to *in silico* studies. Despite excellent antiviral activities, a representative compound displayed poor oral bioavailability and toxicity during PK study (see details in Appendix), therefore, we

have explored to develop new fluorene compounds equipped with not only high efficacy in *in vitro* assays, but also adequate *in vivo* properties. Herein, we describe our studies toward development of a series of NS5A inhibitors embedding the fluorene core structure connected with 4-substituted proline or imidazole.

II. Results and Discussion

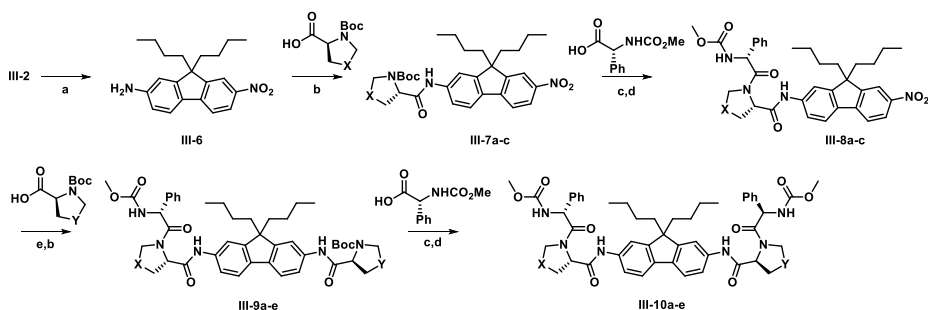
1. Preparation of HCV NS5A inhibitors

For the development of potent NS5A inhibitor, a total of 25 fluorene containing molecules were synthesized. Synthetic routes for compounds **III-2–6** are depicted in Scheme III-1. Two butyl groups were introduced through S_N2 reaction on compound **III-1** to give compound **III-2**. The nitro groups of compound **III-2** was converted to amino groups from treatment with hydrazine in the presence of iron oxide nanoparticles as published in our previous report³⁴ to afford compound **III-3**. Amide coupling of compound **III-3** with the corresponding *N*-Boc-4-X-L-Pro gave compounds **III-4a–4k**. Compounds **III-5a–5k** were obtained through Boc deprotection followed by amide coupling between the proline residue and phenylglycine-carbamate (Phg cap).



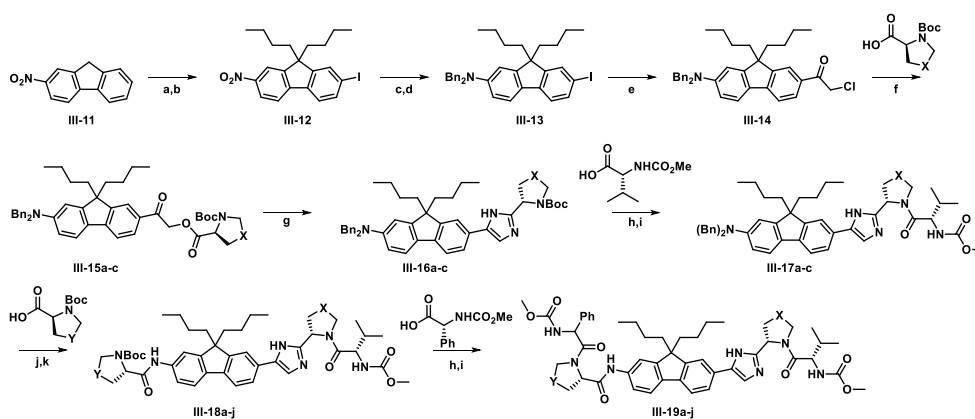
Scheme III-1. Synthesis of compounds **III-5a-k**. Reagents and conditions: (a) Cs_2CO_3 , 1-iodobutane, DMF, 0 °C to 25 °C, 18 h; (b) Fe_3O_4 , hydrazine monohydrate, EtOH, reflux, 2 h; (c) COMU, DIPEA, DMF, 25 °C, 12 h; (d) TFA, DCM, 25 °C, 1 h; (e) COMU, DIPEA, DCM, 25 °C, 12 h.

A series of non-symmetric molecules embedding diamide structure were synthesized according to Scheme III-2. Only one nitro group of compound **III-2** was reduced by treatment with Pd/C under H_2 atmosphere to afford compound **III-6**. As shown in the Scheme III-1, *N*-Boc-4-X-L-Pro and Phg cap were introduced sequentially to give compounds **III-8a-8c**. The remaining nitro group was converted to an amino group and the resulting amine compounds were converted to compounds **III-9a-9e** via amide coupling with *N*-Boc-4-Y-L-Pro. After Boc deprotection, introducing Phg cap gave compounds **III-10a-10e**.



Scheme III-2. Synthesis of compounds **III-10a-e**. Reagents and conditions: (a) Pd/C, H_2 MeOH, 25 °C, 2 h; (b) COMU, DIPEA, DMF, 25 °C, 12 h; (c) TFA, DCM, 25 °C, 1 h; (d) COMU, DIPEA, DCM, 25 °C, 12 h; (e) Fe_3O_4 , hydrazine monohydrate, EtOH, reflux, 2 h.

Synthesis of imidazole-containing inhibitors are described in Scheme III-3. Compound **III-11** was converted to compound **III-12** via alkylation and iodination. Transformation of the nitro group of **III-12** through reduction and benzyl protection gave compound **III-13**. α -Chloro group was introduced from the treatment of Grignard reagents (**III-14**) and the resulting compound was converted to **III-15a–15c** via S_N2 reaction with 4-substituted proline. Imidazole ring construction (**III-16a–16c**) was performed from the treatment of NH_4OAc , and resulting compounds were transformed to **III-17a–17c** via Boc deprotection and amide coupling sequentially. After benzyl deprotection of **III-17a–17c**, amide coupling of the resulting free amine gave **III-18a–18j** and introducing Phg cap was carried out via Boc deprotection and amide coupling (**III-19a–19j**).

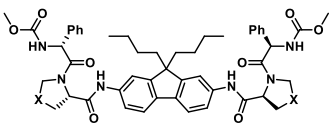


Scheme III-3. Synthesis of compounds **III-19a–j**. Reagents and conditions: (a) Cs_2CO_3 , 1-iodobutane, DMF, 0 °C to 25 °C, 18 h; (b) I_2 , $NaNO_2$, conc. H_2SO_4 , $AcOH$, 25 °C to reflux, 1 h; (c) Fe_3O_4 , hydrazine monohydrate, $EtOH$, reflux, 2 h; (d) $NaHCO_3$, $BnBr$, sodium dodecyl sulfate, H_2O , 80 °C, 1 h; (e) $i\text{-PrMgCl}$, 2-chloro- N -methoxy- N -methylacetamide, THF , 0 °C to 25 °C, 2 h; (f) $DIPEA$, DMF , 35 °C, 14 h; (g) NH_4OAc , toluene, reflux, 12 h; (h) TFA , DCM , 25 °C, 1 h; (i) $COMU$, $DIPEA$, DCM , 25 °C, 12 h; (j) Pd/C , H_2 , $MeOH$, 25 °C, 1 h; (k) $COMU$, $DIPEA$, DMF , 25 °C, 12 h.

2. SAR studies

2.1. Introducing 4-substituted proline with hydrogen bonding donor

According to our previous report,⁶¹ the (*R*)-OH group at C4 position of the proline residue (**III-5a**) acts as hydrogen bonding donor and this additional interaction appears to be the basis for the efficacy enhancement. From our continued efforts to develop more potent NS5A inhibitor, we introduced another hydrogen bonding donor at the C4 position of proline. The antiviral activities (EC₅₀) of several compounds containing potential hydrogen bonding donor, against HCV GT-1b, GT-2a, GT-3a, and GT-1b containing RAVs such as L31V, Y93H, and L31V+Y93H are listed in Table III-1. Introducing (*S*)-OH group at the C4 position of proline (**III-5b**) gave similar inhibitory activities against GT-1b, GT-2a, and GT-3a. However, inhibition was lowered on RAV L31V+Y93H. Therefore, we explored another hydrogen bonding donor containing a nitrogen atom with (*R*) configuration. Unfortunately, (*R*)-NH₂ group (**III-5c**) showed very low antiviral activities, and other inhibitors containing a nitrogen group at the C4 position of proline (**III-5d,e**) didn't show their effectiveness. From low antiviral activity of inhibitors, which contain hydrogen bonding donor at C4 position, we presumed that hydrogen bond might not be a crucial factor to increase antiviral activity.



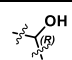
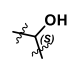
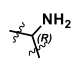
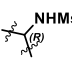
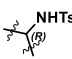
EC ₅₀ ^a (nM)							
Entry	X	GT-1b	GT-2a	GT-3a	RAV of GT-1b		
					L31V	Y93H	L31V+Y93H
III-5a		0.029	3.5	0.13	0.025	0.029	0.058
III-5b		0.034	1.5	0.35	0.0062	0.26	10
III-5c		> 00	>100	>1.0			
III-5d		0.088	0.77	0.17	0.15	1.3	>2.0
III-5e		1.0	17	2.1			

Table III-1. Antiviral activities (EC₅₀) of compounds **III-5a–e**.

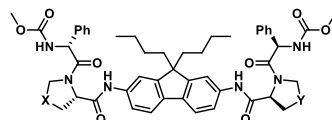
^aThe EC₅₀ values were measured in triplicate and display mean.

2.2. Introducing 4-substituted proline regardless of hydrogen bonding donor and configuration

We proceeded further SAR studies with 4-substituted proline regardless of hydrogen bonding donor property and configuration. Table III-2 showed other inhibitors' inhibitory results. As with compounds **III-5a–5e**, compounds **III-5f–5k** have a symmetric structure. Despite the absence of hydrogen bonding donor, compounds showed around 1 digit nanomolar potency. Compound **III-5k** showed strong inhibition against RAV L31V+Y93H, however, their potencies are definitely lower compared to compound **III-5a**.

Domain I of NS5A is known as well conserved region across the HCV genotype and the precedent studies revealed that this region is involved in the binding to NS5A inhibitor.¹² Due to the homodimeric structure of the domain I, many researchers have searched C₂ symmetric or pseudo-symmetric molecules like daclatasvir. Unfortunately, structural mechanistic basis for RAVs such as L31V, Y93H or L31V+Y93H still remains unclear. Several models with symmetric binding modes were suggested,^{12,72-74} however, those models can't fully explain strong inhibitory effects of nonsymmetrical inhibitors. Numerous reports have been introduced toward explaining how inhibitors interact with NS5A and certain researches have claimed asymmetric binding mode between inhibitor and NS5A.^{37,75}

We synthesized a series of inhibitors, which have asymmetric structure with various substituted prolines. Compound **III-10b**, bearing (*S*)-methoxymethyl group and (*R*)-OH group respectively, was the most potent compound, whose EC₅₀ value is 33 pM against RAV L31V+Y93H.



Entry	X	Y	EC ₅₀ ^a (nM)			RAV of GT-1b		
			GT-1b	GT-2a	GT-3a	L31V	Y93H	L31V+Y93H
			III-5f			0.015	18	1.0
III-5g			0.16	28	1.5	0.031	0.030	6.5
III-5h			0.0036	3.3	0.028	<0.10	1.2	
III-5i			0.0033	0.49	0.034	0.10	9.6	89
III-5j			0.0075	34	0.047	0.0038	0.077	> 100
III-5k			0.0033	0.14	0.010	0.00030	0.0078	0.22
III-10a			0.0026	0.50	0.012	<0.010	0.024	2.0
III-10b			0.0079	0.61	0.037	<0.010	0.0048	0.033
III-10c						0.0076	8.3	74
III-10d						0.0064	9.4	≈100
III-10e			0.0033	28	0.024	0.00060	>10	>10

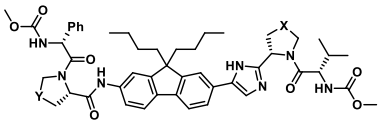
Table III-2. Antiviral activities (EC₅₀) of compounds III-5f–10e.

^aThe EC₅₀ values were measured in triplicate and display mean.

2.3. Introducing imidazole ring as a spacer and bioisostere of amide

Strong inhibitory effects of nonsymmetric inhibitors prompted us to design a new class of inhibitors, which embed a spacer to break the C₂ symmetry. One amide bond

was substituted to imidazole, which plays a role as not only a spacer but also a bioisostere. Although compounds containing the imidazole structure exhibited relatively weak antiviral activities against RAVs, there was a tremendous increasing in inhibitory potency against GT-2a, e.g. from nanomolar to 2-digit picomolar range. This remarkable change was a meaningful result because the genotype 2 is prevalent in East Asia especially South Korea and Japan.⁷⁶






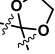

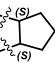
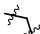
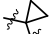
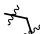
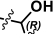
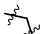
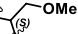
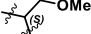

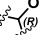


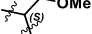
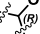
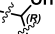
Entry	X	Y	EC ₅₀ ^a (nM)			RAV of GT-1b		
			GT-1b	GT-2a	GT-3a	L31V	Y93H	L31V+Y93H
III-19a			0.0066	0.036	0.045	0.049	0.081	190
III-19b			0.0075	0.042	0.058	0.0032	0.0083	2.4
III-19c			0.0018	0.014	0.032	0.0081	0.13	170
III-19d			0.0048	0.013	0.046	0.010	0.10	190
III-19e			0.023	0.055	0.36	0.16	0.053	14
III-19f			0.0098	0.056	0.12	0.0091	0.026	42
III-19g			0.016	0.028	0.47	0.0074	0.016	>10
III-19h			0.081	0.094	0.36	0.25	0.17	0.44
III-19i			0.011	0.022	0.27	0.0056	0.012	≈10
III-19j			0.19	1.5	0.52	0.21	0.060	0.39

Table III-3. Antiviral activities (EC₅₀) of compounds III-19a-j.

^aThe EC₅₀ values were measured in triplicate and display mean.

3. Biological evaluation of compound **III-10b**

We choose compound **III-10b** because it has the most strong inhibitory effect (EC₅₀: 7.9 pM (GT-1b), 610 pM (GT-2a), 37 pM (GT-3a), <10 pM (L31V-GT-1b), 4.8 pM (Y93H-GT-1b), 33 pM (L31V+Y93H-GT-1b)). Herein, we report several biological evaluation of compound **III-10b**.

3.1. hERG ligand binding assay

To assess potential cardiac toxicity of compound **III-10b**, we performed the hERG ligand binding assay, identifying inhibition of potassium ion channel encoded by hERG gene (Table III-4).⁷⁷ Compared to E-4031 control (IC₅₀ = 370 nM),⁷⁸ compound **III-10b** (IC₅₀ = >10 μM) was proved to poorly bind to the hERG membrane. In this assay, general criteria of IC₅₀ value to provoke cardiac toxicity is 10 μM. Therefore, compound **III-10b** has rare chance to cause cardiac toxicity.

Compounds	IC ₅₀ ^a
19b	>10 μM
E-4031	37 nM

Table III-4. The results of hERG ligand binding assay.

^aInhibition of hERG channel binding relative to DMSO control.

3.2. Microsomal stability

Next, we examine human and rat microsomal stability of compound **III-10b** (Table III-5). Microsomal stability⁷⁹ data enable to predict pharmacokinetics properties or *in vivo* efficacy. Compound **III-10b** showed good stability in microsomal stability.

Microsomal stability (%) ^a		
Human	Rat	Mouse
77.8	93.2	91.4

Table III-5. The results of microsomal and plasma stability of compound **III-10b**.

^aRemaining after 30 min of incubation with each human or rat liver microsomal fractions.

3.3. CYP₄₅₀ enzyme inhibition assay

We displayed CYP₄₅₀ inhibitory profiles of compound **III-10b** to evaluate potential drug–drug interaction⁸⁰ (Table III-6). Among five CYP₄₅₀ isozyme, CYP2C9 was exhibited strong inhibitory activity (IC₅₀ <2 μM) by **III-10b**, therefore, drug–drug interaction between **III-10b** and drug what is metabolized by CYP2C9 have to be considered.

Compound	CYP ₄₅₀ enzyme activity (%) ^a				
	CYP1A2	CYP2C9	CYP2C19	CYP2D6	CYP3A4
10b (μM) ^a	>20	<2	>20	>20	>20
Ketoconazole (%) ^{b,c}	>100	>100	>100	>100	31.2

Table III-6. The results of CYP₄₅₀ enzyme inhibition assay.

^aIC₅₀ of compound for each CYP₄₅₀ isozymes

^b% of control activity for each CYP₄₅₀ isozymes.

^cReference compound.⁸¹

3.5. PK properties of compound III-10b

PK study⁸² of compound **III-10b** was performed in rats with the vehicles consisting of 10% DMSO and 90% of mixture (70% of Pececol, 20% of TPGS, and 10% of PEG400). Compound was administered via IV and PO. However, we could not achieve the meaningful PO data (see details in Appendix) because values of plasma concentration at each time point were located at below of LOQ. We concluded that extreme low plasma concentration in PO administration is formulation problem, therefore we conducted another PK study in rats with the vehicles consisting of 10% DMSO, 5% Cremophor EL, 85% HP- β -CD (20% in H₂O, w/v). In second PK study, PO data were not very clear, but it gave meaningful data (Figure III-1 and Table III-8).

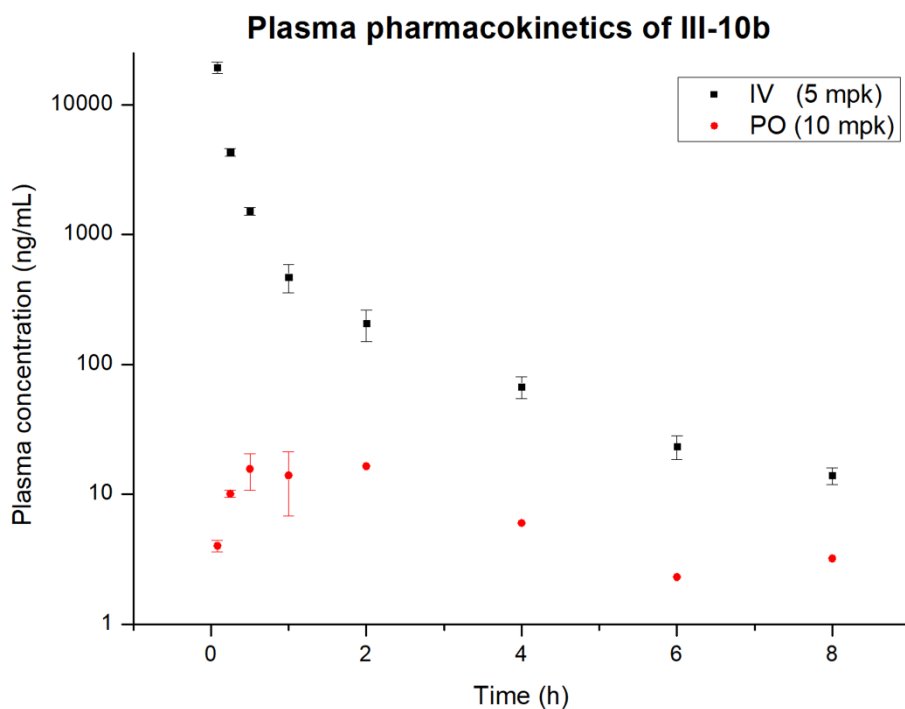


Figure III-1. PK profile of compound **III-10b**.

Parameter	IV (5 mg/kg)	PO (10 mg/kg)
t_{\max} (h) ^a		0.6
C_{\max} (ng/mL) ^b		16.3
$AUC_{(0-\infty)}$ (h*ng/mL) ^c	6435.5	83.0
F (%) ^d		0.2

Table III-7. PK parameters of compound **III-10b**.

^aThe t_{\max} values were measured in triplicate and display mean.

^bThe C_{\max} values were measured in triplicate and display mean.

^cThe AUC values were measured in triplicate and display mean.

^dThe oral bioavailability was ratio of AUC value for IV and PO.

3.6. PK study of prodrug of Compound **III-10b**

From PK data of Compound **III-5a** and **III-10b**, we concluded that problem of PK studies such as toxicity and low oral bioavailability are result from low solubility in biological media. Therefore, we synthesized prodrug of Compound **III-10b** (Compound **III-20**)

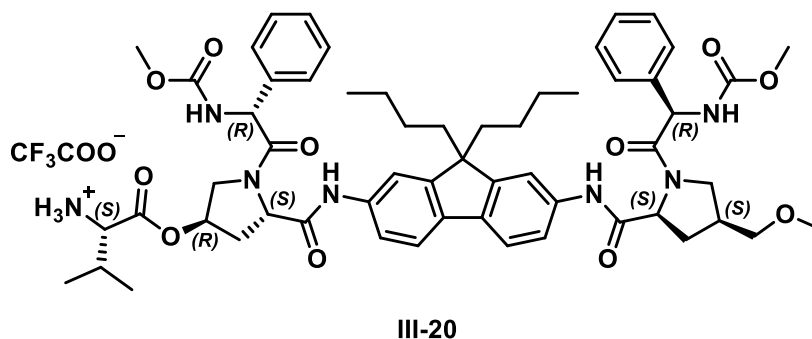


Figure III-2. Prodrug of Compound **III-10b** (Compound **III-20**).

PK study of prodrug also performed in rats and vehicles condition was changed to 5% EtOH, 45% PEG400, 50% (50 mM citrate buffer (pH = 3.0)). We tracked

concentration of Compound **III-10b** and achieved PK data (Figure III-3 and Table III-8). Prodrug of **III-10b** exhibited still low oral bioavailability ($F = 4.44\%$), PK study of **III-20** implies that improvement of solubility in aqueous media is strongly related to higher oral bioavailability.

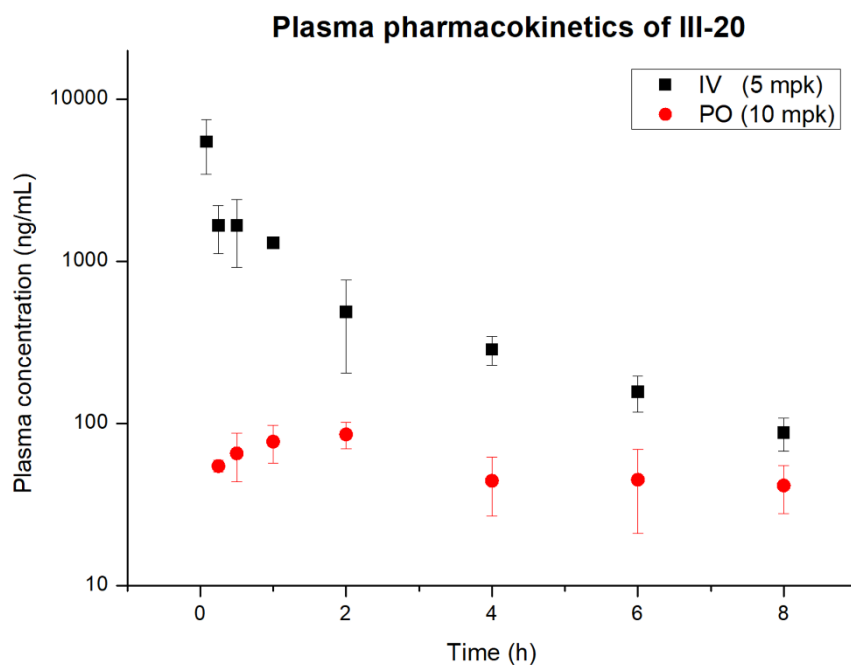


Figure III-3. PK profile of compound **III-20**.

Parameter	IV (5 mg/kg)	PO (10 mg/kg)
t_{\max} (h) ^a		2.0
C_{\max} (ng/mL) ^b		85.4
$AUC_{(0-\infty)}$ (h*ng/mL) ^c	4936.0	832.0
F (%) ^d		4.4

Table III-8. PK parameters of compound **III-20**.

^aThe t_{\max} values were measured in triplicate and display mean.

^bThe C_{\max} values were measured in triplicate and display mean.

^cThe AUC values were measured in triplicate and display mean.

^dThe oral bioavailability was ratio of AUC value for IV and PO.

III. Conclusion

From our precedent study, we synthesized 25 compounds equipped with 4-substituted proline. The antiviral potencies of the compounds were tested against wild-type NS5A and mutated NS5A. Among them, nonsymmetric inhibitor **III-10b** exhibited the highest potency against RAV L31V+Y93H. Compound **III-10b** showed no cardiotoxicity, moderate microsomal stability, and low drug-drug interaction possibility. In PK studies, however, **III-10b** showed extremely low oral bioavailability (0.2%) even when various formulations were tried. We concluded that low oral bioavailability issue comes from low solubility of **III-10b** in aqueous media, therefore, we synthesized prodrug of **III-10b** (**III-20**) and performed another PK study. The PK study with **III-20** exhibited better oral bioavailability (4.4%) but still on the low side. Based on these results, further investigations are in progress to find more potent inhibitors not only in *in vitro*, but also *in vivo* assays.

IV. Experimental Section

1. Materials

All commercially available reagents and solvents were obtained from commercial suppliers and used without further purification. All reactions involving reactants, reagents, or intermediates sensitive to air or moisture were conducted under Ar atmosphere. ¹H, ¹³C, and ¹⁹F NMR spectra were obtained on an Agilent NMR system 400 MHz DD2MR400 or a Varian NMR System 500 MHz in DMSO-*d*₆, CDCl₃, or CD₃OD, with TMS used as an internal standard. Multiplicities are indicated by s

(singlet), d (doublet), t (triplet), q (quartet), p (pentet), dd (doublet of doublet), dt (doublet of triplet), and ddd (doublet of doublet of doublet). TLC was conducted on pre-coated silica gel plates (60F-254; Merck KGaA, Germany).

2. Synthesis

Compounds used in this experiment are prepared according to our previous report⁸³ and also characteristic data are included.

3. Cell culture system

The Huh7.5.1 cells were cultured at 37 °C in DMEM (Gibco) containing 10% FBS (PEAK) and antibiotics (100 U/mL penicillin, 10 µg/mL streptomycin), under humidified 5% CO₂ conditions.⁸⁴ G418 (AG scientific) was added at a final concentration of 300 mg/mL to cell lines carrying HCV replicons.

4. Subgenomic replicon cell lines

Genotype 1b (NK5.1-Gluc) and 3a (S52-Fluc) subgenomic replicons, described in precedent research,⁶¹ were modified by addition of Gaussia luciferase which flanked by 2A peptide or firefly luciferase next to HCV IRES. Genotype 2a (JFH1-Gluc) subgenomic replicons were generated by replacing NSP region (NS3-NS5B) from NK5.1-Gluc to 2a NSP. Replicon DNAs were linearized by *XbaI* and *in vitro* transcribed. The transcribed mixtures were treated with Ambion™ DNase I (Introgen) and cleaned by using RNeasy kit (RNeasy Mini Kit) according to the

manufacturer's instructions. A prepared RNA was introduced into Huh7.5.1 cells as followed reference.⁸⁵ These cells were selected for 2 weeks in DMEM supplemented with 500 µg/mL of G418. After selection, survived colonies were picked to 96 well plate and keep transferred to large scale.

5. Western blot analysis for NS5A expression test

Replicon cell line or replicon RNA transfected Huh7.5.1 cells were washed with PBS and then lysed with RIPA lysis buffer (50 mM Tris, 150 mM NaCl, 0.5% sodium deoxycholate (SDS), 0.1%, 1% Triton X-100), 1 mM phenylmethylsulfonyl fluoride) for 10 min at 4 °C. Lysates were transferred to e-tube and centrifuged for 10 min (12,000 rpm, 4 °C). Supernatants were separated on 10% SDS-PAGE gel and gel was transferred to PVDF membrane (Merck millipore), and blocked with 5% (w/v) dialyzed skim milk and 0.1% Tween-20 in Tris-buffered saline (TBST) for 30 min at room temperature. Membrane was then incubated with primary antibody (rabbit-anti-NS5A, mouse-anti- α -actin and mouse-anti-GAPDH) in blocking buffer over night at 4 °C, and washed three times with TBST buffer before incubation with secondary antibody (anti-rabbit and anti-mouse) in blocking buffer for 2 h at room temperature. The membrane was washed 3 times again with TBST buffer and developed by using EZ-Western Lumi Pico Kit (Dogen) according to the manufacturer's instrument. Luminescence was detected using in AmershamTM Imager 680 (GE healthcare).

6. Measurement of *in vitro* antiviral activity using replicon cell line

The replicon cells were seeded into 12-well plate (5×10^4 cells per well) one day before compound treatment. 5 different concentration of compounds, which serially diluted with DMSO and same amount of DMSO (0.1%) were added to DMEM containing 10% FBS or 5% FBS and 40% human plasma (Sigma Aldrich). Medium from the seeded replicon cells was changed to the one containing compounds or DMSO. 3 days later, *Gaussia* and *Firefly* luciferase activities were measured by using *Renilla* luciferase assay system (Promega) and luciferase assay system (Promega) each from culture supernatant of cell lysate luminescence were measured in GloMax™ 20/20 Luminometer (Promega) according to manufacturer's instructions. Each obtained luciferase activity was normalized to mock-treated (DMSO) cells. The EC₅₀ was calculated by four parameter logistic of the SigmaPlot program (Systat Software).

7. *In vitro* activity against resistance variants

RASs conferring significant fold change to NS5A inhibitors were prepared as followed reference.⁸⁶ Known RASs in NS5A were introduced into the GT-1b (NK5.1) replicon using the site-directed mutagenesis. Presence of mutation was confirmed by sequencing analysis (Solgent). The procedures, used for replicon RNA preparation and introduction to cell were conducted same as described as above. Transiently transfected cells were seeded into 12 well plate and treated with compounds after one day. EC₅₀ was calculated from the luciferase activity as described above.

8. Microsomal stability assay

The two different liver microsomes (Human, Rat, 0.5 mg/mL), 0.1 M PBS and 1 μ M of compound mixture was pre-incubated in 37 °C for 5 min. NADPH regeneration system solution was then added to mixture and incubated in 37 °C for 30 min. The reaction was terminated by adding chlorpropamide containing acetonitrile solution and centrifuged (14,000 rpm, 4 °C) for 5 min. The compounds in the supernatant was analyzed by LC-MS/MS.

9. hERG channel binding assay

The experiment conducted by using hERG Fluorescence Polarization Assay kit (Invitrogen) according to manufacturer's instruction. Each 10 μ M of compound and 3-fold serially diluted E-4031 (Positive control) were mixed with the hERG channel containing membrane and fluorescence tracer. 4 h later, dose dependent polarization levels were measured by Synergy Neo (BioTek) and determined IC₅₀.

10. CYP₄₅₀ inhibition assay

0 and 10 μ M of compounds were mixed with human liver microsomes (0.25 mg/mL), 0.1 M PBS and cocktail of 5 different substrates for drug metabolic enzymes (Phenacetin 50 μ M, Diclofenac 10 μ M, S-mephenytoin 100 μ M, Dextromethorphan 5 μ M and Midazolam 2.5 μ M) and incubated for 5 mins in 37 °C. NADPH generation system solution was added to mixture and incubated for 15 mins

in 37 °C. Reaction was terminated by adding acetonitrile solution containing terfenadine and centrifuged (14,000 rpm, 4 °C) for 5 mins. Supernatant was injected to LC-MS/MS system to evaluate inhibitory effect of compound on drug metabolizing enzyme.

11. PK test

The plasma PK profile and oral bioavailability of compound were studied in male SD rats following a single IV and PO, respectively. Five rats for each dose route were used in the study. Five rats in Group 1 were dosed intravenously at 1 mg/kg and the rats in Group 2 were dosed orally at 10 mg/kg. Blood samples were collected from all animals up to 8 hour post-dose. Concentration of compound in the plasma samples were determined by using LC-MS/MS methodologies

**Chapter IV. Liposomal-Encapsulated NIR
Fluorophore Based on π -Extended Dipolar
Naphthalene Platform and its Imaging Applications
in Human Cancer Cells**

I. Introduction

NIR area has received much attention in the area of fluorescence detection and bioimaging due to its advantages: less background signal, higher signal-to-noise ratio, deeper penetration of tissue, etc.^{47,87-91} From these reasons, several NIR emitting dyes have been developed for the labeling of biomolecules (peptides, proteins, and others), sensing of biologically important species (metal ions, microenvironments, biomarkers, and others) and bioimaging of specific organs (tumor site, blood vessel, and others).⁹²⁻⁹⁴

Recently, we have focused on the development of new fluorophores and molecular sensing probes based on the functionalized dipolar naphthalene platform (FDNP) (Figure IV-1).⁴⁴ The naphthalene-based push-pull type (electron donor-acceptor; D-A) FDNP has shown unique photophysical properties with advantages in the molecular sensing and bio-imaging.⁹⁵⁻⁹⁸ In our recent work, a hydrazine sensing probe based on FDNP was developed, which has a MOM that enhances the hydrazine sensing ability.⁹⁶

In this work, we disclose a new NIR fluorophore (**DVM-1**) based on the hybridization of FDNP with DCMP,⁹⁹⁻¹⁰¹ which has been widely used in the development of NIR-emitting fluorescent probes (Figure IV-1). We also prepared a liposomal-encapsulated formulation of **DVM-1** (named **DVM-1L**) for the bioimaging application within cancer cells.

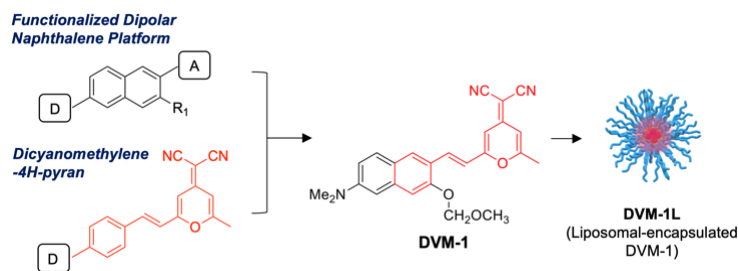
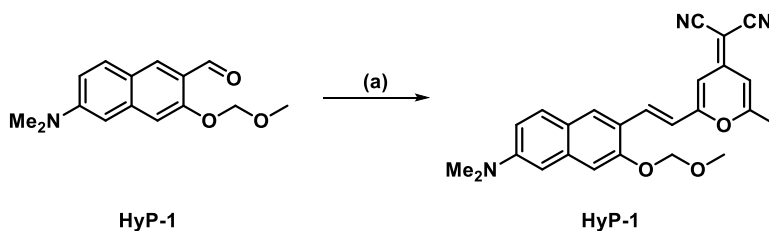


Figure IV-1. Molecular structures of the FDNP, DCMP, and **DVM-1**. D: electron donating group, A: electron withdrawing (accepting) group, R_1 = functional groups. **DVM-1L** is prepared from the **DVM-1** through liposomal-encapsulation protocol.

II. Results and Discussion

1. Preparation **DVM-1** and **DVM-1L**

The **DVM-1** was prepared via Knoevenagel condensation reaction between (6-dimethylamino)-3-(methoxymethylether)-2-naphthaldehyde (**HyP-1**)⁹⁶ and 2-(2,6-dimethyl-4*H*-pyran-4-ylidene)-malononitrile in the presence of piperidine and acetic acid (Scheme IV-1).



Scheme. IV-1. Synthesis of compound **DVM-1**. Reagents and conditions: (a) 2-(2,6-dimethyl-4*H*-pyran-4-ylidene)-malononitrile, piperidine, AcOH, toluene, reflux, 8 h.

For the bioimaging applications of **DVM-1**, we prepared a liposomal-encapsulated formulation of **DVM-1** by using Pluronic F127 (generic name, poloxamer 407),^{102,103} which is a well-known amphiphilic triblock co-polymer containing poly-(ethylene glycol) and poly-(propylene glycol) (PEG-PPG-PEG) (Figure IV-2). **DVM-1** and F127 were firstly dissolved in DCM (both substances are soluble, stock solution: **DVM-1** (2 mg/400 μ L) and F127 (20 vol %/vol %), and mixed for the final concentration as a 0.5 mg/100 μ L **DVM-1** within DCM-F127 mixture (9:1, v/v). Through the solvent evaporation under ultrasonication, **DVM-1** was encapsulated within the F127 liposome (**DVM-1 L**) (see the details in Experimental Section).

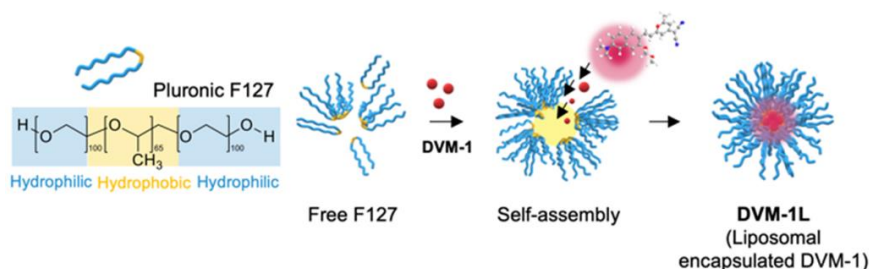


Figure IV-2. Schematic illustration for the preparation of **DVM-1L**.

2. Photophysical Properties of **DVM-1** and **DVM-1L**

First, we measured the absorption and emission spectra of **DVM-1** in various solvents (Figure IV-3). The maximum absorption and emission wavelength range of **DVM-1** is displayed at the 400–550 nm and 550–750 nm, respectively. Due to the π -extended character, the **DVM-1** exhibited emission at a longer wavelength in most of the solvents compared with **HyP-1** (Figure IV-4). However, **DVM-1** showed no emission in DI H₂O and pH buffers (pH 3–12) (Figure IV-5), which appears to be

caused by low water solubility and its aggregation in aqueous media even in the presence of the water-soluble MOM moiety. In the photostability assay, both **HyP-1** and **DVM-1** showed no significant emission changes that represent no light-induced decomposition of compounds (Figure IV-6).

A broad absorption peak of **DVM-1L** was observed in the DI H₂O ($\lambda_{\text{abs-max}}$: 450 nm), and a strong emission peak was recorded at the NIR region (600–800 nm, $\lambda_{\text{emi-max}}$: 700 nm) (Figure IV-7).

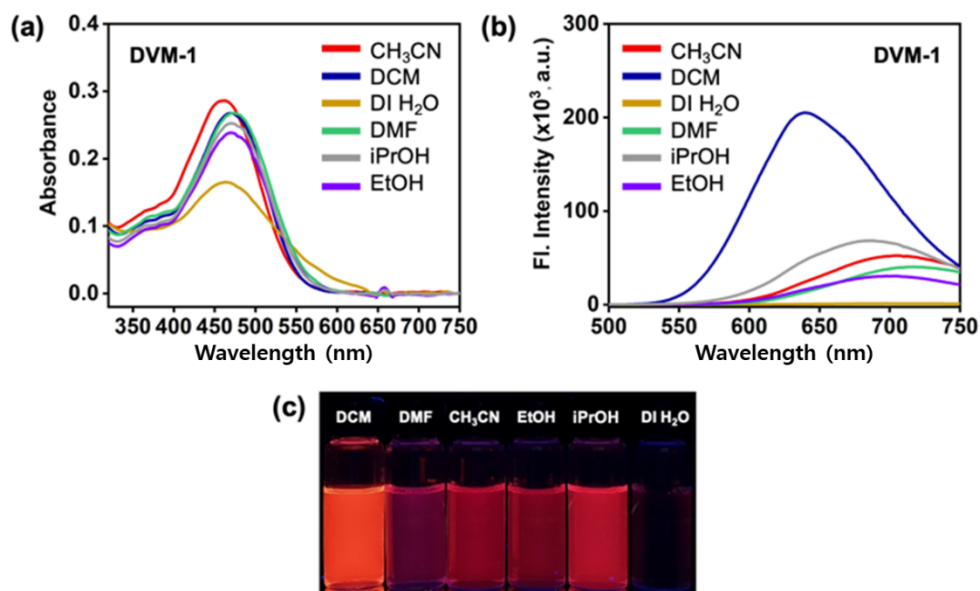


Figure IV-3. (a) UV-Vis absorption and (b) emission spectra of **DVM-1** (10 μM) in various solvents at 25 °C. The emission spectra were obtained in each solvent under excitation at the maximum absorption wavelength. (c) A photo for **DVM-1** (10 μM) in various solvents under UV light (365 nm).

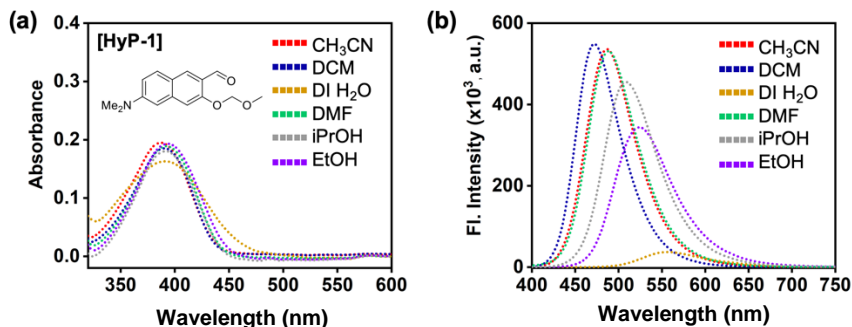


Figure IV-4. (a) UV-Vis absorption and (b) emission spectra of **HyP-1** (10 μM) in various solvents at 25 $^{\circ}\text{C}$.

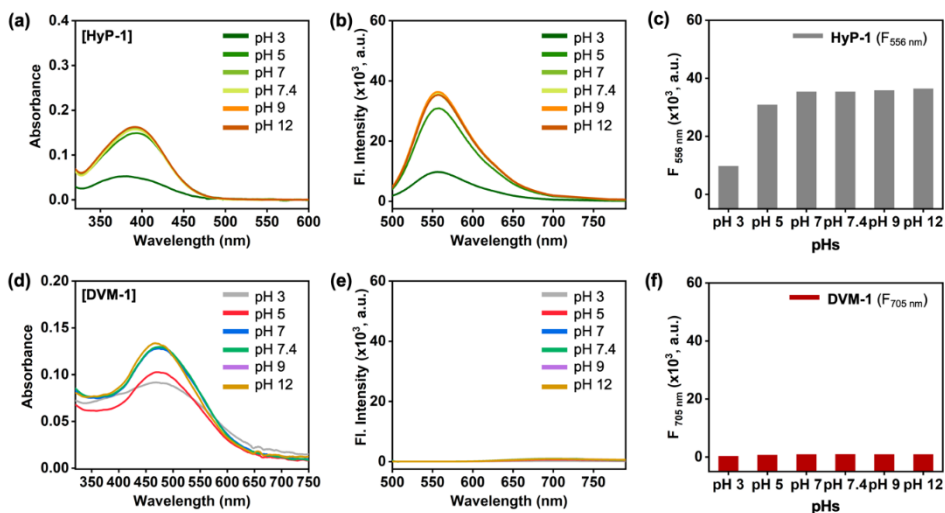


Figure IV-5. (a, d) UV-Vis absorption and (b, e) emission spectra of **HyP-1** (10 μM , top) and **DVM-1** (10 μM , bottom) within various pH buffer solutions (pH 3, 5, 7, 7.4, 9, 12) at 25 $^{\circ}\text{C}$. The emission was measured under excitation at the maximum absorption wavelength. (c, f) Emission intensity plot of **HyP-1** and **DVM-1** from panel Figure IV-5b and IV-5e, respectively.

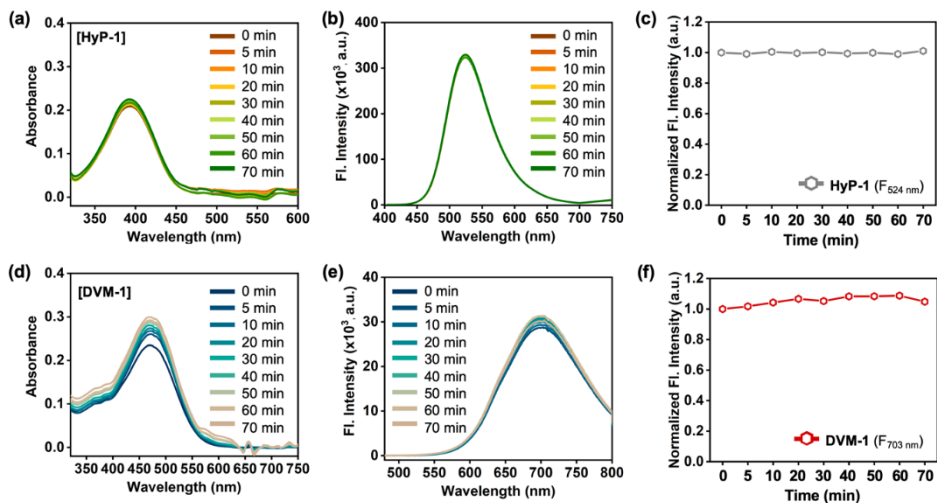


Figure IV-6. Photostability assay of **HyP-1** and **DVM-1**. (a, d) UV-Vis absorption and (b, e) emission spectra of **HyP-1** (10 μM , top) and **DVM-1** (10 μM , bottom) in EtOH under continuous UV light (3W, 365 nm) exposure for 70 min at 25 $^{\circ}\text{C}$. The emission was measured under excitation at the maximum absorption wavelength. (c, f) Emission intensity plot of **HyP-1** and **DVM-1** from panel Figure IV-6b and IV-6e, respectively. The emission intensity scale in the y-axis of Figure IV-6e is smaller (10 times) than the Figure IV-6b.

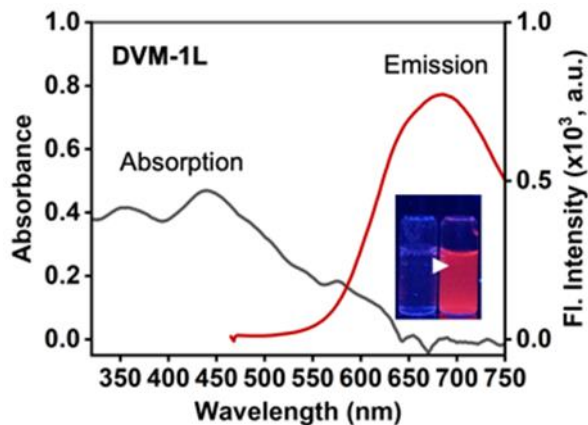


Figure IV-7. UV-Vis absorption and emission spectra of **DVM-1L** in DI H_2O at 25 $^{\circ}\text{C}$. Inset photo: **DVM-1L** (in DI H_2O) under UV light (365 nm). The emission spectra were obtained under excitation at the maximum absorption wavelength (443 nm).

3. Bioimaging application of DVM-1L

To explore the bioimaging application of **DVM-1L**, we performed a CLSM imaging of cancer cell lines (HeLa, U87MG). As shown in Figures IV-8, each cell treated with **DVM-1L** exhibited a bright fluorescence signal in the red channel within the cytosol of cells. A specifically targeted imaging ability of **DVM-1L** toward cellular suborganelles such as mitochondria, endoplasmic reticulum, and lysosome was not observed. Given that the different kinds of two cells were well stained, we confirmed that the liposomal encapsulated **DVM-1L** could enter the cells, which warrants promising further applications of this formulation within bioimaging as well as drug-delivery system.

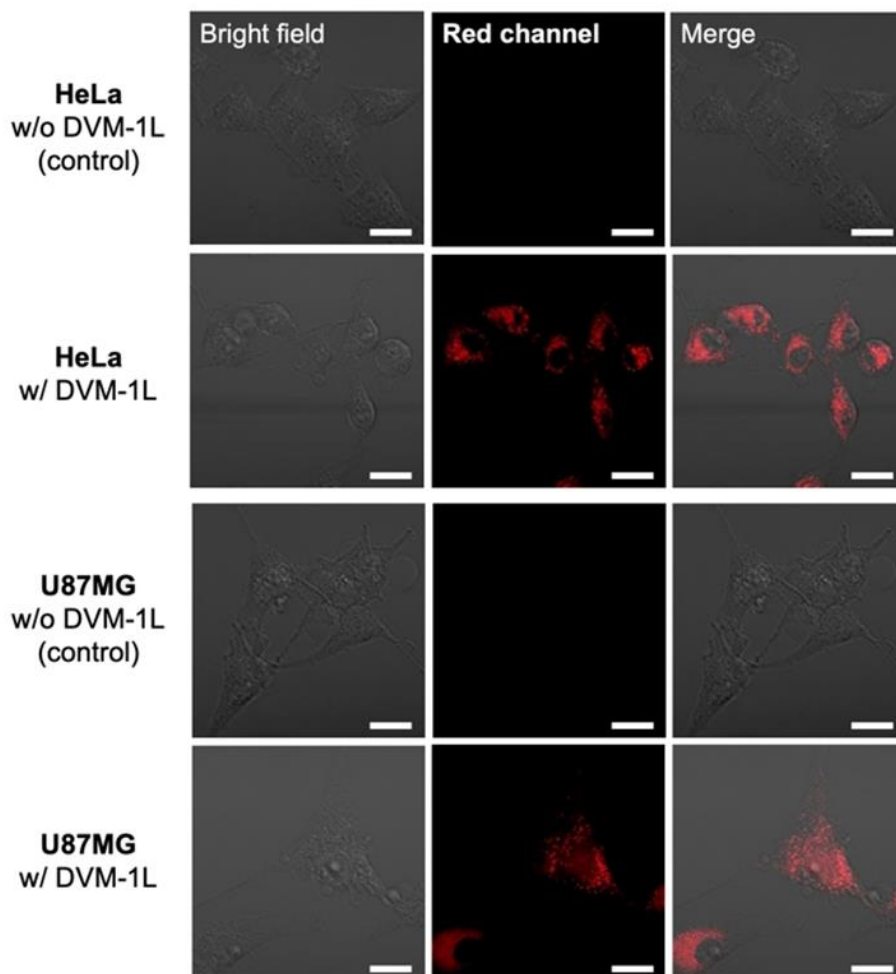


Figure IV-8. Representative CLSM images of HeLa (top two rows) and U87MG (bottom two rows) cells with the treatment of **DVM-1L**. Cell images were obtained after treating **DVM-1L** (0.1%, final concentration within total media volume) to each cell at 37 °C, 5% incubator for 3 h. Excitation wavelength $\lambda_{\text{ex}} = 488$ nm, detection band filter = 545–700 nm, scale bar = 20 μm .

III. Conclusion

In this study, we disclosed a new NIR-emitting fluorophore (**DVM-1**) based on a π -extended FDNP and their liposomal-encapsulated nanoformulation (**DVM-1L**) for the application in bioimaging. The photophysical properties were systematically analyzed, and a method for the preparation of nano-formulation with F127 polymer was optimized. CLSM imaging results within human cancer cell lines suggested that the **DVM-1L** has potentials in further applications for *in vivo* imaging of biologically important species as well as disease-site (cancer, brain, etc.) targeted drug-delivery system in clinical.

IV. Experimental Section

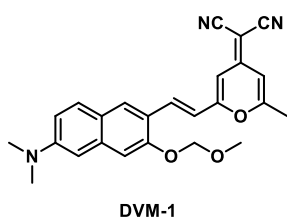
1. Materials and Methods

The chemical reagents were purchased from Aldrich (US), TCI (Japan), Alfa Aesar (US), and Acros Organics (US). Commercially available reagents and anhydrous solvents were used without further purification. DMEM and FBS for cell culture (U87MG, HeLa) were purchased from Hyclone (Utah, US). Penicillin-streptomycin for U87MG, HeLa cell line was purchased from Gibco Industries Inc. (Auckland, NZ). PBS were purchased from Sigma-Aldrich (St Louis, MO, USA). The pH range was 3–12, including biological pH (7.4) for the pH screening. The pH buffers were purchased from Daejung Chemicals & Metals co., LTD (Rep. of Korea). The cell culture dish (SPL Life Science, #20060, Rep. of Korea) was purchased for the applications. Chemical reactions were performed under an argon atmosphere. TLC was performed using pre-coated silica gel 60F-254 glass plates (Merck KGaA,

Germany). ^1H and ^{13}C NMR spectra were obtained on an Agilent 400-MR DD2 (400 MHz). In the NMR spectra, the chemical shifts (δ) are reported in ppm with TMS used as an internal standard; multiplicities are indicated by s (singlet), d (doublet), t (triplet), dd (doublet of doublets), and m (multiplet). HRMS analysis of the compounds was conducted using an Ultra High-Resolution ESI Q-TOF mass spectrometer (Bruker, MA, USA) from the Organic Chemistry Research Center at Sogang University, Seoul, Korea. LCMS spectra were measured on an Agilent HP 1260 system (Agilent Technologies, Santa Clara, US). Fluorescence images were visualized by a CLSM (LSM-800, Carl Zeiss, Germany). The hydrodynamic size and zeta-potential were measured using Malvern Instruments Zetasizer Nano ZS90 (Worcester-shire, UK).

2. Synthesis

The procedures used in the synthesis of compounds are described in Scheme IV-1.



(E)-2-(2-(2-(6-(dimethylamino)-3-(methoxymethoxy)naphthalen-2-yl)vinyl)-6-methyl-4H-pyran-4-ylidene)malononitrile (**DVM-1**). **HyP-1** was prepared according to the reported procedure.¹⁰⁸ **HyP-1**

(259.3 mg, 1.00 mmol) and 2-(2,6-dimethyl-4H-pyran-4-ylidene)-malononitrile (309.9 mg, 1.80 mmol) were dissolved in toluene (10 mL). Piperidine (167 μL , 1 mol%) and AcOH (83 μL , 1 mol%) was added to the solution. The reaction mixture was refluxed for 8 h. The crude mixture was concentrated in vacuo and diluted with

EtOAc. The organic layer was washed with brine and dried over by using MgSO₄. The resulting EtOAc solution was concentrated in vacuo. The residue was purified by flash column chromatography (*n*-hexane/EtOAc = 7:3) to give **DVM-1** (163.8 mg, 40%). ¹H NMR (400 MHz, CDCl₃): δ 7.93 (s, 1H), 7.80–7.75 (m, 2H), 7.40 (s, 1H), 7.25–7.20 (m, 2H), 7.00 (d, *J* = 16.1 Hz, 1H), 6.72 (d, *J* = 2.1 Hz, 1H), 6.55 (s, 1H), 5.42 (s, 2H), 3.58 (s, 3H), 3.17 (s, 6H), 2.43 (s, 3H). ¹³C NMR (100 MHz, Acetone-*d*₆): δ 163.44, 160.69, 156.64, 154.00, 150.02, 137.41, 133.90, 129.29, 129.18, 122.21, 121.21, 117.60, 115.02, 114.73, 108.03, 106.14, 105.59, 104.62, 94.63, 55.53, 55.51, 39.61, 18.88. HRMS (*m/z*): [M+H]⁺ calcd for C₂₅H₂₄N₃O₃, 414.1812; found, 414.1813.

2.1. Preparation of DVM-1L

(I) Solution preparation: 0.5 mg of **DVM-1** was dissolved in 100 μL of DCM. Individually, 40% F127 stock solution was prepared by liquefying 400 mg of F127 powder in 1 mL of DCM as well.

(II) Liposome formation: 100 μL of 40% F127 solution was added to 0.5 mg/100 μL of **DVM-1** in 4 mL vial. The vial was sealed with parafilm, and the mixture was immediately sonicated for 1 h at 25 °C. After complete removal of DCM during the ultrasonication, the crude mixture was washed with DI H₂O (1 mL, 3 times). The resulting supernatant (**DVM-1** in DI H₂O) was collected and analyzed by following the absorbance and emission. See details in Figure IV-9.

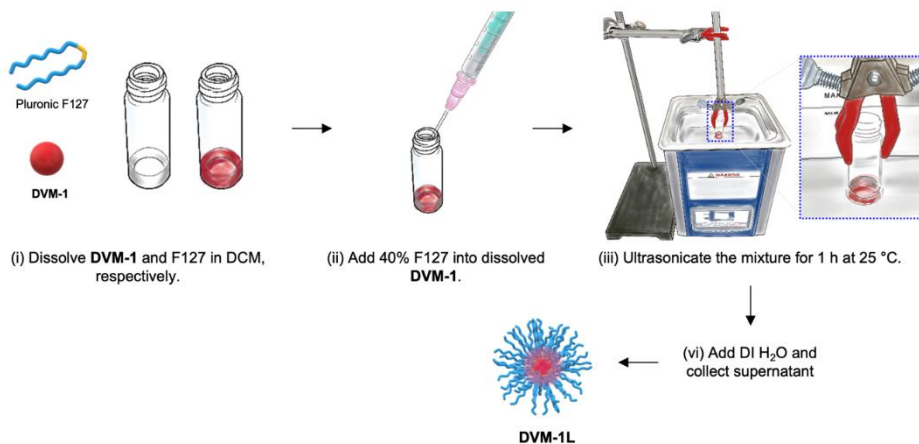


Figure IV-9. Schematic illustration for the **DVM-1L** preparation.

3. UV-Vis and fluorescence spectroscopic analysis

UV-Vis absorption spectra were measured using a spectrophotometer (Agilent Technologies Cary 8454, US). Fluorescence emission spectra were obtained by a spectro-fluorophotometer (SHIMADZU CORP. RF-6000, Japan) with a 1 cm standard quartz cell (internal volume of 0.1 mL, Hellma Analytics, Jena, Germany). DVM-1 was stored in DMSO (10 mM) as a stock solution. All analysis spectra were recorded at a concentration of 10 μM . The photophysical property of DVM-1L was evaluated in aqueous media (DI H₂O).

4. Cell culture

U87MG cell line and HeLa cell line were obtained from the Korean Cell Line Bank (Rep. of Korea). Cells were cultured in DMEM (Hyclone, US) supplemented with 10% FBS (Hyclone) and 1% penicillin-streptomycin (Gibco). Cell lines were kept under humidified air condition, containing 5% CO₂ at 37 °C.

5. CLSM imaging

Approximately 2×10^5 cells were seeded on 35-mm glass confocal dishes (SPL Life Science, Rep. of Korea) and incubated for 24 h. At 80% confluency, media was changed to serum-free media. After 2 h, **DVM-1L** (0.1% and 1% of 1 mg/mL supernatant in 1× PBS) was treated to cells for 3 h at 37 °C in an incubator under 5% CO₂. Incubated media was washed three times using DPBS (Dulbecco's PBS). After the washing, 4% PFA was added to cells and incubated for 15 min at 4 °C. Then, the PFA was removed by suctioning and washing with PBS (3 times). CLSM images were obtained from the prepared samples.

**Chapter V. Articulated Structures of D-A Type
Dipolar Dye with AIEgen: Synthesis, Photophysical
Properties, and Applications**

I. Introduction

Donor-bridge-acceptor (D- π -A, D-A) type dipolar fluorophores have been widely used as molecular probes and biological tags due to their unique photophysical properties, such as high quantum yield, environment sensitive emission, high biocompatibility with photostability, and multi-photon absorption capability.^{97, 104–108} To date, many D-A type dipolar dyes have been introduced, including acedan, 4-amino (or hydroxy)-1,8-naphthalimide, NBD, coumarin, and Cy^{87,109–114}. The photophysical properties of these fluorophores could be readily tunable by changing (i) the functional group at donor and acceptor site, (ii) the size of the bridge linker, and (iii) the physical property; aggregation/disaggregation.

Typically, D-A type fluorophores emit fluorescence in aqueous media and their fluorescence emission wavelengths depend significantly on the solvent polarity, due to the ICT character in the excited state.^{104,115} In an aggregated form of D-A type fluorophore (solid state), it generally shows no emission, although the emission characteristics do change depending on the molecular arrangements in the aggregated form.¹¹⁶

Unlike the D-A type fluorophores, AIEgens show strong emissions in an aggregated form (solid state), but no emission is observed in a dissolved form (solution state).¹¹² This unique property of AIEgen has been applied in various research fields and industries.¹¹⁷ Recently, it showcased in a few cases that the photophysical properties of AIEgens are manageable, like D-A type fluorophores, by introducing electron donating and accepting moieties to the AIEgen backbones through π -conjugation.^{49,118,119} However, the synthesis, photophysical properties, and

practical applications of the articulated structures (no π -conjugation), between D-A type fluorophore and AIEGen have yet to be fully investigated.

Herein, we have comprehensively studied two compounds; the DA-AIE series (**DA-AIE-M**, **DA-AIE-D**), which have articulated structures of 6-(dimethylamino)-2-naphthaldehyde (**DA**) and **TPE**, as a representative D-A type fluorophore and AIEGen, respectively (Figure V-1). The **DA** was linked to **TPE** via a C-C bond in a non-conjugated manner; **DA-AIE-M**: mono-DA-substituted TPE, **DA-AIE-D**: bis-DA-substituted TPE. In this study, the photophysical properties of these two compounds were experimentally characterized within various environments and in conjunction with quantum chemical calculations. Its unique properties were demonstrated for the detection of residual DMSO in real water samples with high sensitivity.

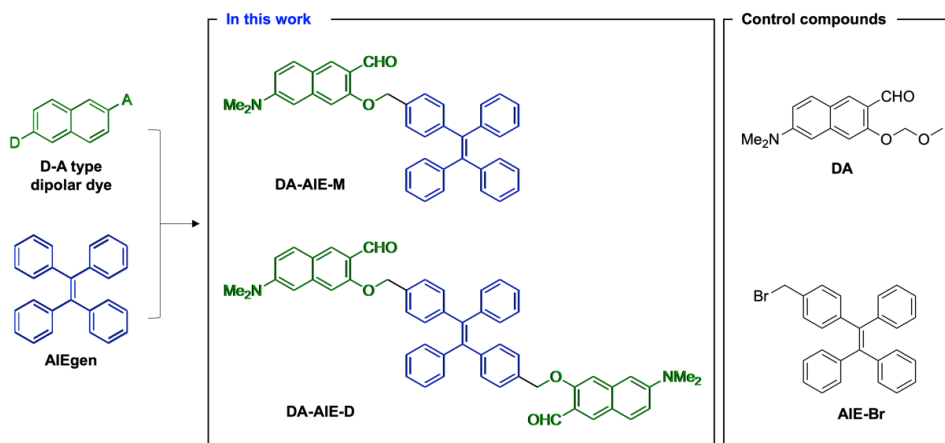
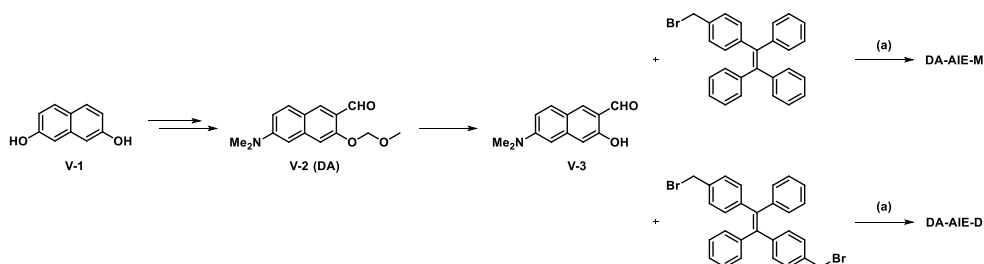


Figure V-1. Chemical structures of D-A type naphthalene-based dipolar dye and tetraphenylethylene-based AIEGen.

II. Results and Discussion

1. Material design

First, we chose 6-(dimethylamino)-3-hydroxy-2-naphthaldehyde (Compound **V-3**) as a representative D-A type fluorophore, because its hydroxy moiety could be linked with AIEgen material without disturbing the character of dipolar backbone. The synthesis and distinguishable applications of Compound **V-3** have been presented by our research group.^{96,120–124} For an AIEgen material, we chose bromomethyl-functionalized TPE because it showed a typical property of AIEgen and has been widely used throughout various research fields.^{125–127} D-A type fluorophore and AIEgen have shown to exhibit opposite photophysical properties. Compound **V-3** and TPE were directly linked via sp^3 carbon linker (-CH₂-) to give **DA-AIE-M** (mono-DA-conjugated), **DA-AIE-D** (bis-DA-conjugated) (Figure V-1).



Scheme V-1. Synthesis of compounds **DA-AIE-M** and **DA-AIE-D**. Reagents and conditions: (a) NaH, DMF, 0 °C to 25 °C, 1 h.

2. Preparation of compounds

The D-A type dipolar fluorophore (Compound **V-3**) was prepared from 2,7-dihydroxy-naphthalene (compound **V-1**) via four-step synthesis¹²⁸ (Scheme V-1); (i) Bucherer reaction, (ii) MOM protection, (iii) directed lithiation using *t*-BuLi (resulting product: Compound **V-2**), and (iv) MOM deprotection in acidic solution. Then, the DA-AIE series were produced through the reaction between compound **V-3** and bromomethyl-TPE in the presence of NaH; mono-bromomethyl TPE affording **DA-AIE-M** (yield: 58%), bis-bromomethyl TPE affording **DA-AIE-D** (yield: 30%). As control compounds, non-conjugated compound **DA** and **AIE-Br** were used (Figure V-1).

3. Spectroscopic studies

The UV-vis absorption and emission spectra of synthesized DA-AIE series were measured in various solvents, and were compared with those of the control compounds, as represented in Figure V-2.

Firstly, we observed the maximum absorption and emission wavelengths of DA-AIE series at 300-450 nm and 400-600 nm (Figure V-2a, V-2b). These optical properties were similar to a typical feature of D-A type fluorophore; (i) solvent polarity dependent wavelength shift, (ii) relatively lower emission intensity in polar solvents, (iii) negligible emission intensity in aqueous media compared with that of organic solvents, and it was correlated with control compound **DA** (Figure V-2c). Both **DA-AIE-M** and **DA-AIE-D** showed a strong emission in aprotic solvents,

including EtOAc, toluene, THF, and DMSO, but negligibly weak emissions in protic polar solvents, DI H₂O, and PBS. As we expected, the control compound AIE-Br showed emission in aqueous media (DI H₂O, PBS), in an aggregated form, and no emissions were observed in organic solvents, in a dissolved form (Figure V-2d). The emission intensity of aggregated **AIE-Br** in aqueous media was slightly lower than that of **DA** in organic solvents.

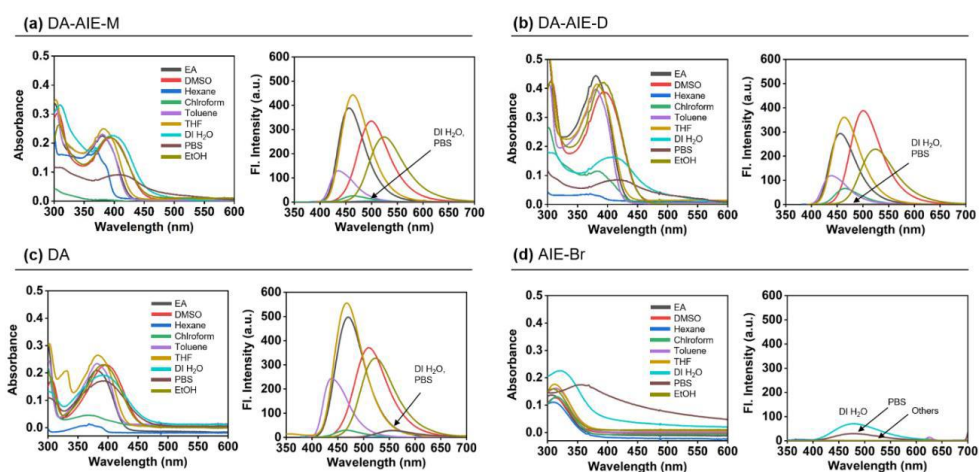


Figure V-2. Absorption (left) and emission (right) spectra of (a) **DA-AIE-M** (10 μ M), (b) **DA-AIE-D** (10 μ M), (c) **DA** (10 μ M), (d) **AIE-Br** (10 μ M), in various solvents at 25 $^{\circ}$ C. The emission spectra were obtained in each solvent under excitation at the maximum absorption wavelength.

The DA-AIE series exhibited optical features that are very similar to D-A type dipolar dye, not to AIEgen. In addition, we confirmed their aggregate formation by DLS analysis. The DA-AIE series formed relatively uniformed aggregates, whose sizes are on a nanometer length scale ($d = 248.9$ nm and PDI = 0.102 for **DA-AIE-M** and $d = 403.5$ nm and PDI = 0.593 nm for **DA-AIE-D**) in DI H₂O (Figure V-3), but they were fully dissolved in organic solvents. From the emission property

monitoring with DLS analysis, we concluded that the DA-AIE series produced an aggregated form in aqueous media, but the packing of TPE moieties in the aggregates was not efficient enough to inhibit the rotation-induced non-radiative relaxation of phenyl rings. In addition, TPE emission of DA-AIE series in the aggregated form could be quenched in the excited state by closely attaching the DA moieties via a RET,¹²⁹ followed by subsequent non-radiative decays of the DA moieties.

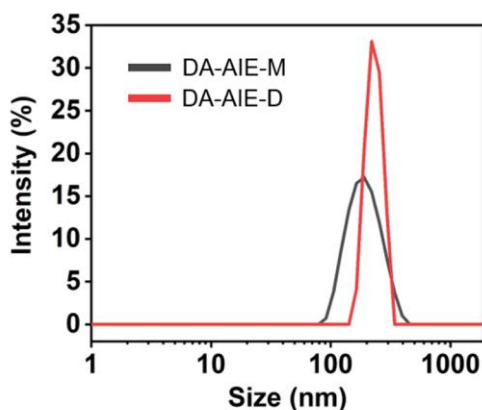
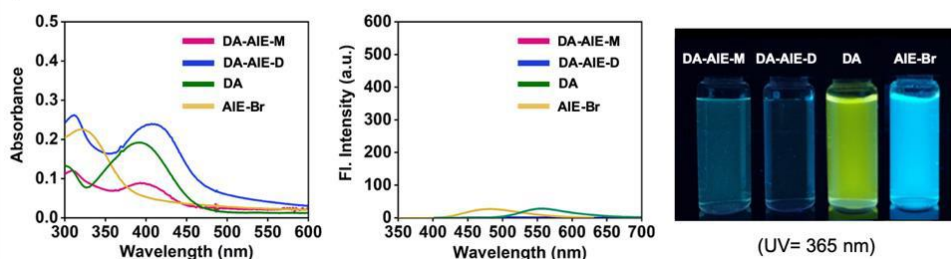


Figure V-3. Mean hydrodynamic diameter (intensity distribution) of **DA-AIE-M** (black line) and **DA-AIE-D** (red line) in DI H₂O at 25 °C.

The emission properties of the compounds were summarized in two representative solvents; (i) DI H₂O: no emission from the DA-AIE series (aggregated), emission from **AIE-Br** (aggregated), and emission from **DA** (dissolved), (ii) DMSO: emission from the DA-AIE series (dissolved, emission from DA moiety), no emission from **AIE-Br** (dissolved), emission from **DA** (dissolved) (Figure V-4). The UV-vis absorption intensity of **DA-AIE-D** (0.26) in water was higher than that of **DA-AIE-M** (0.12) at 310 nm due to the two DA moieties in **DA-AIE-D**.

(a) DI H₂O



(b) DMSO

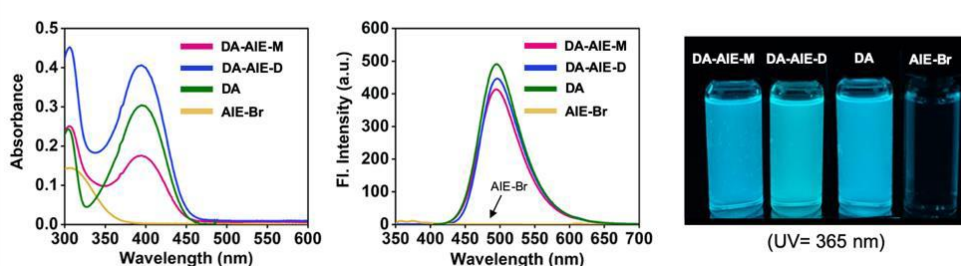


Figure V-4. Absorption and emission spectra of **DA-AIE-M** (10 μ M), **DA-AIE-D** (10 μ M), **DA** (10 μ M), and **AIE-Br** (10 μ M) in (a) DI H₂O, (b) DMSO at 25 °C. Inset photos: each compound (10 μ M) is dissolved in DI H₂O and DMSO under UV light (365 nm). The emission spectra were produced in each solvent under excitation at the maximum absorption wavelength.

4. Quantum chemical calculation

To understand the molecular conformations and optical properties of the DA-AIE series, we conducted theoretical calculations for the optimized structures and the HOMO and LUMO energies (Figure V-5). In the optimized structures, the DA moieties were folded, so that the DA and TPE moieties were located close to each other. The side view images clearly showed that the DA moiety was vertically located in the plane of TPE moiety (Figure V-5b). In such molecular conformations, DA moieties could disturb the packing of TPE moieties in the aggregates, and thus the AIE of TPE moieties would not be turned on in aqueous media.

The optimized molecular structures and the HOMO and LUMO of compounds were produced (Figure V-5b). In **DA-AIE-M** and **DA-AIE-D**, the DA and TPE moieties are directly linked via sp^3 carbon linker (-CH₂-), and thus the two moieties individually contributed to the molecular orbitals and the optical properties of **DA-AIE-M** and **DA-AIE-D**. The HOMO and LUMO of **DA-AIE-M** and **DA-AIE-D** are dictated by the DA moieties, and the absorption and emission spectra measured with **DA-AIE-M** and **DA-AIE-D** within various solvents were shown to be very similar to those of **DA** (Figure V-2 and Figure V-4). In **DA**, a relatively large electron density in the HOMO is located in the donor part (-N(Me)₂), and in the LUMO, it is located in the acceptor part (-CHO). **DA** exhibits the ICT characteristics in the absorption and emission transitions. **DA**, **DA-AIE-M**, and **DA-AIE-D** showed almost the same bathochromic shifts in polar solvents (Figure V-2).

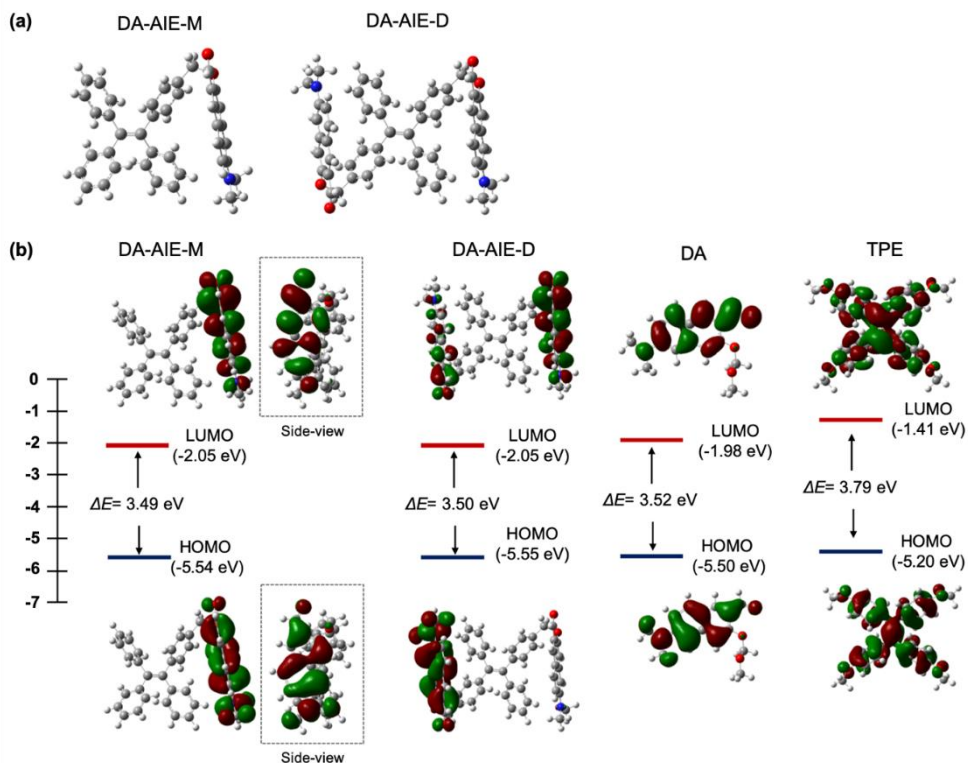


Figure V-5. Quantum chemical calculations for **DA-AIE-M**, **DA-AIE-D**, **DA**, and **TPE**. (a) Optimized structures of **DA-AIE-M**, **DA-AIE-D** calculated using the DFT calculations. (b) The HOMO and LUMO orbitals and their energies for the compounds.

5. Proposed mechanism

From the analysis of UV-vis absorption and emission spectra and quantum chemical calculation, we proposed a mechanism to explain the photophysical properties of **DA-AIE-M** and **DA-AIE-D** with a schematic illustration (Figure V-6). AIE was not observed in the aggregated form of the DA-AIE series in aqueous media. That is because the DA moieties could disturb the close packing of TPE moieties, and thus allowing the phenyl groups in TPE to rotate or vibrate. Additionally, it is

feasible that the RET from TPE to DA moieties occurs. The emission from the **DA** was also found to be quenched and significantly red-shifted because of the hydrogen bonding interactions in aqueous media (Figure V-4a). The DA-AIE series were found to form aggregates in aqueous media but show no emission.

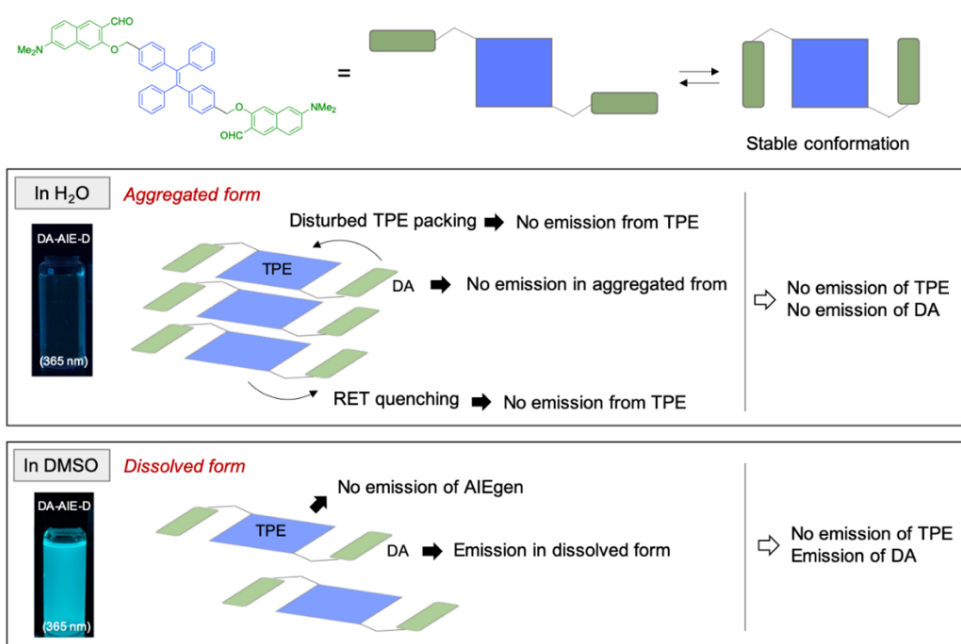


Figure V-6. Proposed mechanism for the photophysical properties of **DA-AIE-D** in the aggregated form (in H₂O) and dissolved form (in DMSO).

6. Sensing applications in real water samples

Given that the DA-AIE series exhibit a strong emission in DMSO, we have evaluated its sensing ability for the detection of residual DMSO in aqueous media (Figure V-7). First, we monitored the UV-vis absorption change and emission enhancement of the DA-AIE series in a mixture of DMSO-DI H₂O (0–100% DMSO) (Figure V-7a, V-7b). Significant UV-vis absorption shifts were not observed in the given media. In the emission spectra, the DA-AIE series showed a strong emission and hypsochromic shift in the solutions with 70% and 100% DMSO content. The emission maximum of the DA-AIE series shifted to 527 nm for 70% DMSO and 509 nm for 100% DMSO, which is a representative feature of D-A type dipolar dye. The large emission intensity was only observed from high contents of DMSO (>70%) in aqueous media, similar to turn-on fluorescence probes, and it represented that the quenching effect of DA moiety could be diminished in a certain ratio of organic solvent. In the low content of DMSO (0–30%), a significant emission enhancement was also observed from 1% DMSO, and the enhancement factor of **DA-AIE-D** was more effective than **DA-AIE-M**, due to the completely quenched emission properties of **DA-AIE-D** at 0% DMSO media (Figure V-7C). The detection limit of the DA-AIE series was 1.3 ppb for **DA-AIE-M** and 0.4 ppb for **DA-AIE-D**, according to the signal-to-noise ratio above 3 (Figure V-7D). The control compound **DA** showed a similar property with the DA-AIE series, but the emission gradually increased depending on the DMSO ratio with hypsochromic shift (Figure V-7c). As expected, the control compound **AIE-Br** showed emission in the mixtures with 0–70% DMSO due to the aggregate formation, and no emission was observed at 100% DMSO solution (Figure V-7d).

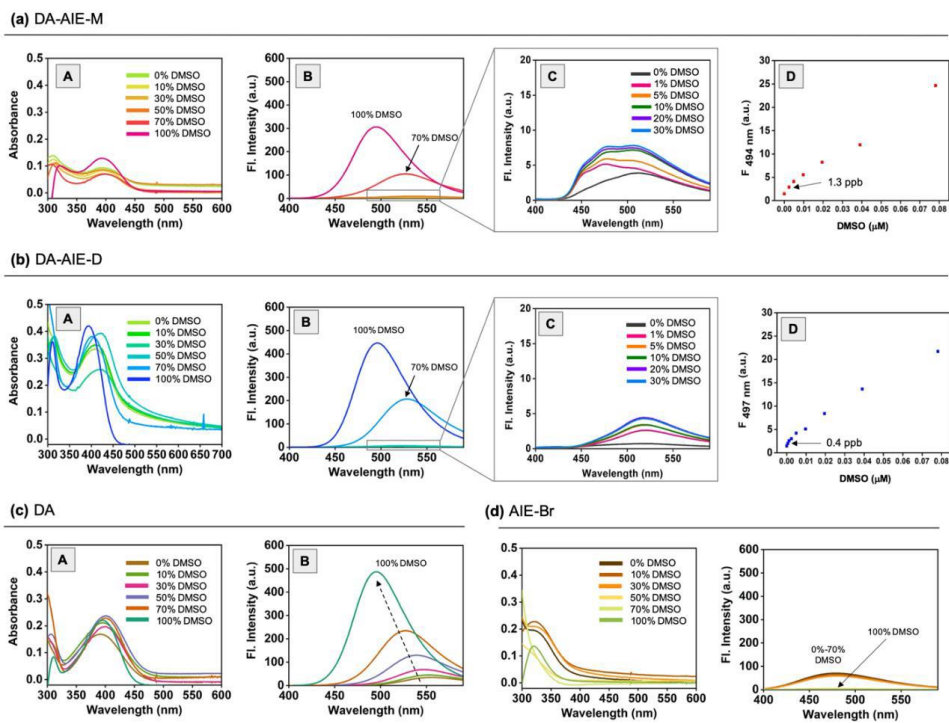


Figure V-7. Absorbance spectra (A) and emission spectra (B) of (a) **DA-AIE-M** (10 μM), (b) **DA-AIE-D** (10 μM), (c) **DA** (10 μM), and (d) **AIE-Br** (10 μM) in DI H_2O -DMSO mixture (0–100%). (C) Enlarged emission spectra of **DA-AIE-M** and **DA-AIE-D** in the 0–30% range of DMSO. (D) The plot of emission intensity of **DA-AIE-M** (at 501 nm) and **DA-AIE-D** (at 513 nm), in contrast to the concentration of DMSO (0–0.08 μM) in DI H_2O , and measured at 25 $^\circ\text{C}$. The emission spectra were measured under excitation at the maximum absorption wavelength. The mean value of detection limit (ppb unit) was represented and derived from triplicate measurement.

In order to further explore the potential use of the DA-AIE series for detecting a trace of DMSO, we measured the LOD values for DMSO in real water samples; tap water, bottled water (commercial drinking water), purified water, sea water, river water, and lake water, by using **DA-AIE-D**, which was found to be more sensitive than **DA-AIE-M** (Figure V-8). The water samples were spiked with a small amount of DMSO (0-0.625 μM) and then **DA-AIE-D** was added to monitor the detection

limit. **DA-AIE-D** showed a low detection limit (<1.9 ppb) in tap water, bottled water, and purified water. In the water samples from environmental sources (sea, river, and lake), **DA-AIE-D** showed slightly higher LOD values for DMSO (<30.7 ppb), but the LOD values were still small enough to monitor a trace of DMSO in real water samples.

LOD of DA-AIE-D

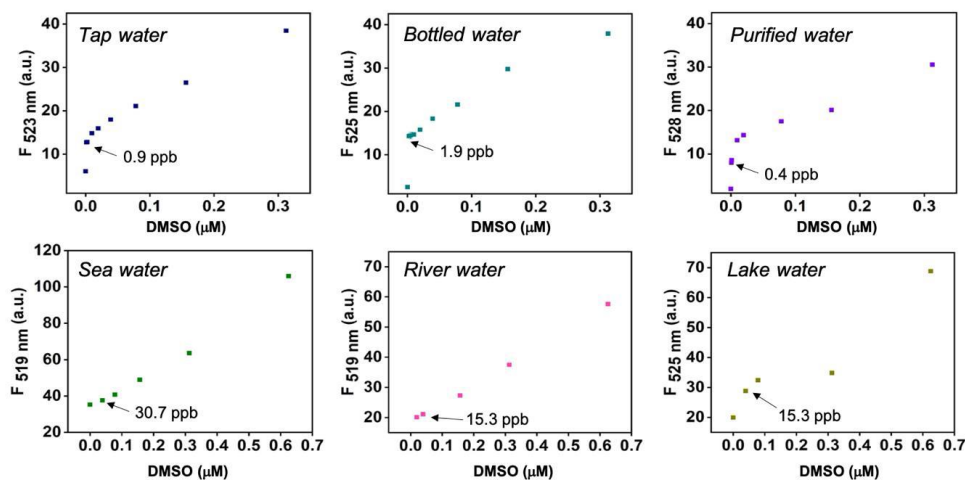


Figure V-8. Detection limit for the DMSO in real water samples. A plot of emission intensity of **DA-AIE-D** ($10 \mu\text{M}$) in tap water, bottled water, purified water, sea water, river water, and lake water, in the presence of DMSO ($0\text{--}0.625 \mu\text{M}$) at 25°C . The emission spectra was measured excitation at the maximum absorption wavelength. The mean value of detection limit (ppb unit) was represented and derived from triplicate measurement.

III. Conclusion

In conclusion, for the first time, we prepared articulated structures of D-A type dipolar dye with AIEgen. The DA-AIE series were prepared by connecting a naphthalene-based dipolar dye to a tetraphenylethylene backbone; **DA-AIE-M** (mono-DA-substitute), **DA-AIE-D** (bis-DA-substitute). We systematically analyzed the photophysical properties of the DA-AIE series with quantum chemical calculation, and demonstrated its optical properties for detecting a trace of DMSO in real water samples. We believe our current fundamental study will provide a foundation for correlated studies on DA type dipolar dyes and AIEgens, and encourage further applications in various research areas.

IV. Experimental Section

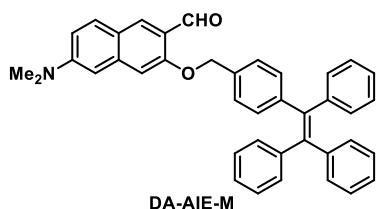
1. Materials

The chemical reagents were purchased from Aldrich (USA), TCI (Japan), and Alfa Aesar (USA), and Acros Organics (USA). Species used to perform the screening of metal ions, and amino acid, and hydrazine; AuCl₃, FeCl₂, FeCl₃, CaCl₂, CuCl₂, HgCl₂, (C₂H₅)₃PAuCl, CdCl₂, NiCl₂, NaCl₂, PdCl₂, KCl, L-Cys, L-GSH, L-Lys, DL-HCys, and N₂H₄. Commercially available reagents and anhydrous solvents were used without further purification. Chemical reactions were performed under an argon atmosphere. TLC was performed on the pre-coated silica gel 60F-254 glass plates (Merck KgaA, Germany). ¹H NMR spectra were recorded on an Agilent 400-MR DD2 (400MHz) and ¹³C NMR spectra were recorded on a Varian/Oxford As-500 (125 MHz) in the indicated solvent. In the NMR spectra, the chemical shifts (δ) are

reported in parts per million (ppm) and TMS was used as an internal standard. Multiplicities are indicated by s (singlet), d (doublet), dd (doublet of doublet), and m (multiplet). Coupling constants were reported in Hz. HRMS of the final compounds were further confirmed by Ultra High Resolution ESI Q-TOF mass spectrometer (Bruker, USA), from the Organic Chemistry Research Center at Sogang University, Rep. of Korea.

2. Synthesis

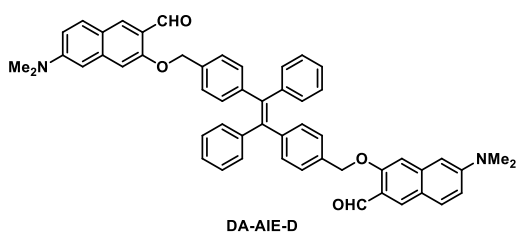
The procedures used in the synthesis of compounds are described in Scheme V-1. Compound **V-3** was prepared by following the existing methods (4 step synthesis from naphthalene-2,7-diol).¹²⁸



6-(dimethylamino)-3-((4-(1,2,2-triphenylvinyl)benzyl)oxy)-2-naphthaldehyde
(**DA-AIE-M**). NaH (13.9 mg, 0.348 mmol) and compound **V-3** (50.0 mg, 0.232 mmol) were

dissolved in DMF (0.77 mL). The reaction mixture was stirred for 30 min at 0 °C. Then, (2-(4-(bromomethyl)phenyl)ethene-1,1,2-triyl)-tribenzene (108.6 mg, 0.255 mmol) was added, and the mixture was stirred for an additional 1 h at 25 °C. The crude reaction mixture was quenched by adding DI H₂O and diluted with EtOAc. The organic layer was washed with DI H₂O, dried MgSO₄, and concentrated in vacuo. The residue was purified by flash column chromatography (*n*-hex/EtOAc = 9:1) to produce the **DA-AIE-M** (75.2 mg, 58%, yellowish green solid). ¹H NMR (400 MHz, DMSO-*d*₆): δ 10.32 (s, 1H), 8.15 (s, 1H), 7.82 (d, *J* = 9.1 Hz, 1H), 7.32 (*J* = 8.0 Hz,

2H), 7.22 (s, 1H), 7.14–7.09 (m, 10H), 7.05–6.96 (m, 8H), 6.80 (d, $J = 2.5$ Hz, 1H), 5.20 (s, 2H), 3.07 (s, 6H); ^{13}C NMR (125 MHz, CDCl_3): δ 189.66, 157.74, 150.86, 143.75, 143.73, 143.71, 143.70, 141.46, 140.63, 139.94, 134.74, 131.68, 131.44, 131.41, 131.38, 130.84, 130.82, 127.83, 127.77, 126.72, 126.64, 126.62, 126.58, 122.39, 120.96, 114.53, 105.50, 104.22, 70.18, 40.42. HRMS (m/z): $[\text{M}+\text{Na}]^+$ calcd for $\text{C}_{40}\text{H}_{33}\text{NNaO}_2$, 582.2404; found, 582.2404.



(E)-3,3'-((((1,2-diphenylethene-1,2-diyl)bis(4,1-phenylene))bis(methylene))bis(oxy))-bis(6-(dimethylamino)-2-

naphthaldehyde) (**DA-AIE-D**). **DA-AIE-D** (22.5 mg, 30%, 115 yellowish green solid) was prepared according to the procedure described for the synthesis **DA-AIE-M**. ^1H NMR (400 MHz, $\text{DMSO}-d_6$): δ 10.31 (d, $J = 3.2$ Hz, 2H), 8.14 (d, $J = 3.5$ Hz, 2H), 7.81 (dd, $J = 6.1, 9.2$ Hz, 2H), 7.31 (d, $J = 7.9$ Hz, 4H), 7.21 (s, 2H), 7.15–6.97 (m, 16H), 6.80 (s, 2H), 5.17 (d, $J = 12.0$ Hz, 4H), 3.05 (d, $J = 8.2$ Hz, 12H); ^{13}C NMR (125 MHz, CDCl_3): δ 189.71, 157.77, 150.89, 143.60, 141.00, 139.97, 134.82, 131.69, 131.45, 131.39, 130.87, 130.78, 127.93, 127.86, 126.84, 126.75, 122.41, 112.96, 105.60, 105.53, 104.24, 70.19, 40.45. HRMS (m/z): $[\text{M}+\text{Na}]^+$ calcd for $\text{C}_{54}\text{H}_{46}\text{N}_2\text{NaO}_4$, 809.3350; found, 809.3348.

3. UV-Vis absorption and fluorescence assay

UV-Vis absorption spectra were obtained using a spectrophotometer (Agilent Technologies Cary 8454, USA). Fluorescence emission spectra were recorded on a spectro-fluorophotometer (SHIMADZU CORP. RF-6000, Japan), with a 1-cm standard quartz cell (internal volume of 1 mL, 108-000-10-40 (10 mm), 108-F-10-40 (10 x 4 mm); Hellma Analytics, Germany). The stock solution of each compound (10 mM) was prepared by dissolving it in DMSO. Absorption and emission spectra were recorded with 10 μ M of each compound, in various solvents at 25 °C. To measure the emission spectrum, the sample solution was excited at the maximum absorption wavelength.

4. Quantum chemical calculations

All calculations were carried out using the DFT and time-dependent DFT methods with the B3LYP-D3 functional and 6-31G(d) basis set that is implemented in the Gaussian 16 package¹³⁰. We calculated the optimized structures, electronic energies, frontier orbitals (HOMO and LUMO), natural transition orbitals (NTOs), electronic absorption spectrum, and emission spectrum. For solvation, we used the integral equation formalism polarizable continuum (IEF-PCM) model.

5. Sensing applications in real water samples

Real water samples were collected: (i) tap water (Kyung Hee University, College of Medicine Building, Seoul, Rep. of Korea), (ii) commercial bottled drinking water (Jeju Samdasoo, 500 mL bottle, Rep. of Korea), (iii) purified drinking water (Kyung Hee University, College of Medicine Building, Seoul, Rep. of Korea), (iv) sea water (Oido, Yellow Sea, Gyeonggi-do, Rep. of Korea), (v) river water (Han-river, Seoul, Rep. of Korea), and (vi) lake water (Jemyoung lake, Seoul, Rep. of Korea). The real water samples were spiked with DMSO and used for the analysis without further purification.

**Chapter VI. AIEgen-Based Nanoprobe for the ATP
Sensing and Imaging in Cancer Cells and
Embryonic Stem Cells**

I. Introduction

ATP is a biological molecule that plays essential roles in cells such as the primary carrier of energy, intracellular signaling, DNA/RNA synthesis, amino acid activation in protein synthesis, immune response, and etc.^{131–133} ATP is produced in the mitochondria, and the change of ATP concentration leads to the critical influence of mitochondrial function. Previous studies have disclosed the close correlation between ATP and diseases such as cancer, neurodegenerative diseases, ischemia, and hypoglycemia.^{134–136}

Due to the importance of ATP, several analytical methods to monitor ATP have been developed based on mass spectrophotometry, Raman scattering, and optical response.^{137–143} Among them, luminescence-/fluorescence-based sensing systems have gained great attention because of their simple operation process, intuitive signal response, high sensitivity, selectivity, and biocompatibility.^{124,144–147} Currently, several ATP monitoring systems, based on luminescence (luciferin-luciferase)^{148–150} and fluorescence (genetically-encoded fluorescent sensors),^{151–153} are actively used in biological studies, and some of these are commercially available.^{154,155} Although such systems are efficient and useful, developing a small organic fluorescence probe for the ATP is needed in terms of ease-of-use and for a wide range of applications.

The development of fluorescence sensing systems (probes) for ATP is a very challenging task because there are numerous molecules with similar structures in the biological system, such as AMP and ADP. To develop a new fluorescent probe without the selectivity issue, scientists have proposed several approaches targeting the components of ATP (Figure VI-1a); (i) Electrostatic interaction: negatively-

charged triphosphate moiety could allow for an interaction with a positively-charged one such as triamine. The triamine-functionalized rhodamine derivatives showed an off-on emission change by electrostatic interaction-induced spirolactam ring-opening.¹⁵⁶⁻¹⁶³ (ii) π - π stacking interactions: aromatic molecules could interact with the adenine base. Some aromatic fluorophores-containing probes have been reported.¹⁶⁴⁻¹⁶⁸ (iii) Chemical bond formation: arylboronic acid could make a chemical bond with vicinal diols in the ribose. Arylboronic acid-containing fluorescent probes were also reported.¹⁶⁹⁻¹⁷¹ Hybrid approaches based on the metal-fluorophore complex, using electrostatic interaction and π - π stacking interaction were also proposed.¹⁷²⁻¹⁷⁷ The fluorescence is quenched by metal ion and recovered via metal-ATP interaction.

Recently, new ATP sensing approaches based on AIE have been reported.¹⁷⁸⁻¹⁸² AIEgen is non-emissive in a dissolved form due to the free rotation-induced non-radiative decay pathway, and the emission is recovered in an aggregated-form, which produces restrictive motions of the intramolecular.^{48,183-185} The AIEgen-based approaches for the ATP sensing could be categorized into two (Figure VI-1b); (i) Emission enhancement via aggregation of single AIE molecules (dissolved-form) by electrostatic interaction with ATP in aqueous media.^{178,179,181} (ii) Emission enhancement via metal ion or aptamer displacement from AIE-metal/aptamer complex to ATP-metal/aptamer complex.^{180,182,186} Notably, and to the best of our knowledge, the AIEgen based nanoprobe that senses ATP without supporting metal ions or aptamer has yet to be reported.

In this study, we disclose a new ATP sensing rationale based on AIEgen nanoprobe for the first time (Figure VI-1c). The newly synthesized molecule **TPE-TA** forms an

aggregated formulation in the buffer (pH 7.4) as a nanoprobe, named **AAP-1**, which shows turn-on type fluorescence response toward ATP with (i) a high sensitivity (0.275 ppb) and selectivity, (ii) fast signal response (<10 s), (iii) mitochondria-targeted ATP sensing, and (iv) applicability in cancer cells and embryonic stem cells. We believe that such properties of the fluorescent nanoprobe could be used within ATP-related biological studies and for clinical applications.

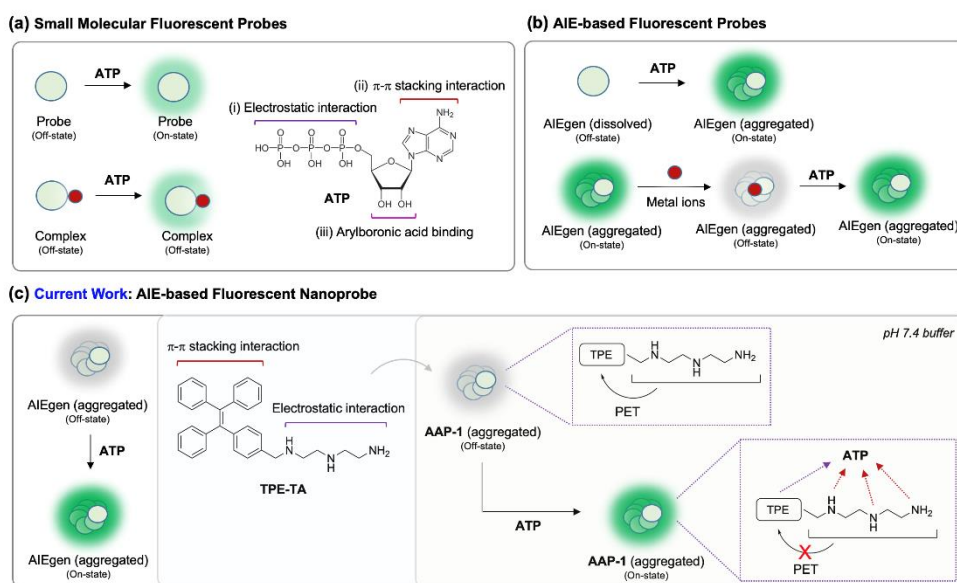


Figure VI-1. ATP sensing approaches using (a) small molecular fluorescent probes and (b) AIE-based fluorescent probes. (c) Current work: AIE-based fluorescent nanoprobe, **TPE-TA** (aggregation form: **AAP-1**), and its schematic illustration of the working mechanism. Purple arrow: π - π stacking interactions. Red arrow: electrostatic interactions.

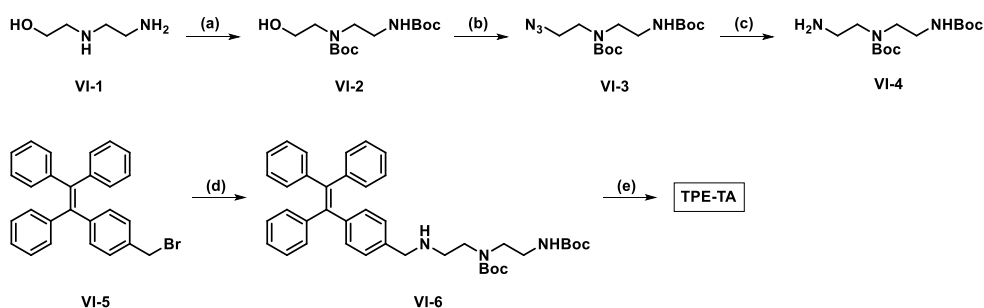
II. Results and Discussion

1. Material design

The ATP sensing probe (**TPE-TA**) was designed based on a propeller-shaped TPE luminogen and triamine moiety. Generally, such TPE luminogen showed an off-emission when dissolved in organic solvents, and an on-emission when aggregated in aqueous media. In the probe designing step, we expected that **TPE-TA** had no emission in aqueous media because it could be dissolved in the aqueous media, due to the triamine moiety with PET quenching, and the emission was recovered after making an aggregation with ATP via electrostatic interaction (triphosphate and triamine) and π - π stacking interaction (TPE and adenine). During the characterization of **TPE-TA**, however, we found that **TPE-TA** existed as a nano-aggregate in aqueous media like liposome (hydrophobic TPE inside, hydrophilic triamine outside, see DLS measurement below), and had an off-emission of TPE due to the PET quenching from the triamine moiety. The nano-aggregate was named **AAP-1**, a fluorescent nanoprobe, and was applied to the sensing and imaging of ATP.

2. Preparation of TPE-TA

Compound **VI-6**, a precursor of **TPE-TA**, was prepared from the reaction between compound **VI-4** and commercially available compound **VI-5** (Scheme VI-1). The Boc deprotection of compound **VI-6** under acidic conditions (TFA) gave **TPE-TA**.



Scheme VI-1. Synthesis of compound **TPE-TA**. Reagent and conditions: (a) Boc_2O , THF, 0 °C to 25 °C, 14 h; (b) diphenylphosphoryl azide, DBU, NaN_3 , THF, 0 °C to reflux, 2 d; (c) PPh_3 , H_2O , Et_2O , 0 °C to 25 °C, 14 h; (d) Compound **VI-4**, NaH, DMF, 0 °C to 25 °C 1 h; (e) TFA, DCM, 25 °C, 1 h.

3. Sensing properties of AAP-1

The sensing properties of **AAP-1** (10 mM of **TPE-TA**, aggregated form) were demonstrated in pure PBS buffer (pH 7.4). **AAP-1** displayed a major absorption peak in the wavelengths 300–350 nm (Figure VI-2a) with a negligible emission (Figure VI-2b, bottom). A negligible fluorescence of **TPE-TA** (dissolved form) was observed in various organic solvents (Figure VI-3). A viscosity-induced fluorescence enhancement was not observed (Figure VI-4). Generally, the emission intensity of the TPE fluorophore is enhanced as viscosity increases, due to the reduced rotational freedom, but such a tendency did not appear in **TPE-TA**. This result indicates significant PET quenching of the triamine moiety toward the TPE fluorophore.

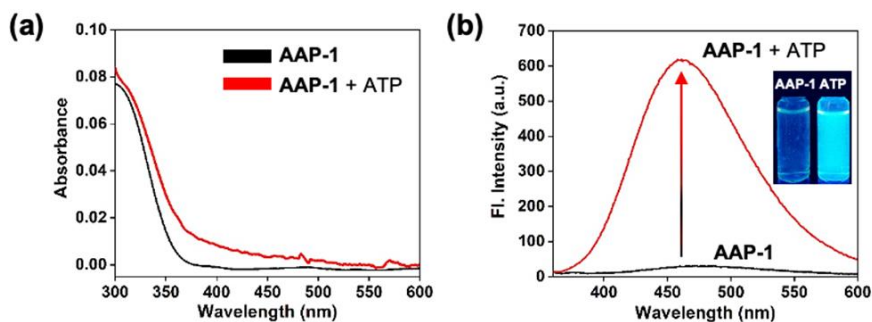


Figure VI-2. (a) Absorption and (b) emission spectra of **AAP-1** (10 μM of **TPE-TA**) after adding **ATP** (3 mM) to **PBS** buffer (pH 7.4). The spectra were recorded within 10 s after mixing at 25 $^{\circ}\text{C}$ under excitation at 315 nm. Inset: photos of **AAP-1** in the solution before and after treatment with **ATP** under UV light (365 nm).

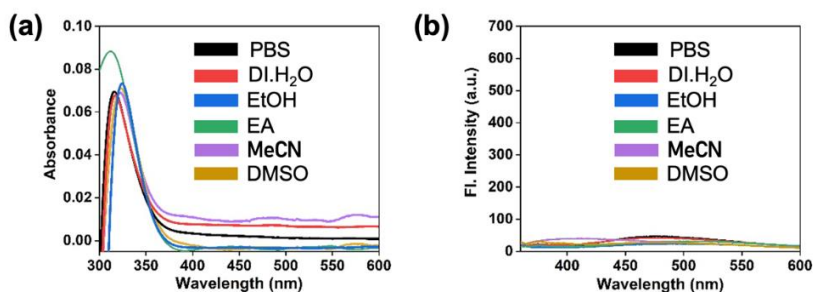


Figure VI-3. (a) Absorption and (b) emission spectra of **AAP-1** (10 μM) in various solvents. The absorption and emission spectra were recorded within 10 s after mixing of **AAP-1** at 25 $^{\circ}\text{C}$. The emission spectra were measured under excitation at the maximum absorption wavelength in each solvent.

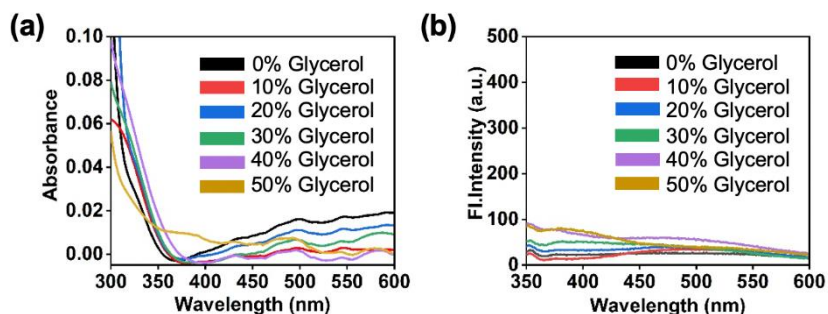


Figure VI-4. (a) Absorption and (b) emission spectra of **AAP-1** (10 μM) in the mixture of pH 7.4 (**PBS** buffer) and glycerol (0–50% glycerol). The absorption and emission spectra were recorded within 10 s after mixing of **AAP-1** at 25 $^{\circ}\text{C}$. The emission spectra were measured under excitation at 315 nm.

Next, we demonstrated the sensing ability of **AAP-1** toward ATP. ATP (3 mM) was added into a solution (PBS buffer, pH 7.4) containing **AAP-1** (10 mM of **TPE-TA**, aggregated-form), which showed a significant fluorescence enhancement at 464 nm (21-fold) (Figure VI-2b). This result indicated that the PET quenching effect was reduced due to the interaction between **AAP-1** and ATP, and the DLS measurement was then conducted to confirm these interactions (Figure VI-5a). In the DLS analysis, the hydrodynamic diameter of **AAP-1** ($d = 359.5$ nm and $PDI = 0.209$) was enlarged ($d = 729.5$ nm and $PDI = 0.275$) when it formed a complex (**AAP-1**+ATP). The size analysis data indicate that **TPE-TA** formed homogeneous nano-aggregates in the sensing solution whose size increased when ATP was bound via electrostatic interaction and π - π stacking interaction. The interaction of **AAP-1** and ATP was also confirmed by monitoring zeta-potential changes after adding the ATP into the **AAP-1** containing solution. **AAP-1** itself has a positive value around +13.76 mV due to the amine moiety, and it decreased as the ATP concentration increases (Fig. VI-5b). To investigate the specificity of **AAP-1**, the emission responses of **AAP-1** towards other anions and biomolecules were monitored under the same conditions, and it only showed an enhanced emission towards ATP sensing (B in Figure VI-5c) with no disturbance by structurally similar species such as ADP and AMP. Other nucleosides (GTP, TTP, UTP, CTP, adenine) did not induce the fluorescence enhancement of **AAP-1**. The ATP sensing ability of **AAP-1** has been maintained in the various pHs and a high salt concentration (Fig. VI-5d). We believe that the better ATP-sensing performance of **AAP-1** is derived from the better ATP complex formation than ADP and AMP via electrostatic interaction (triphosphate in ATP toward triamine) with π - π stacking interaction (TPE and adenine).

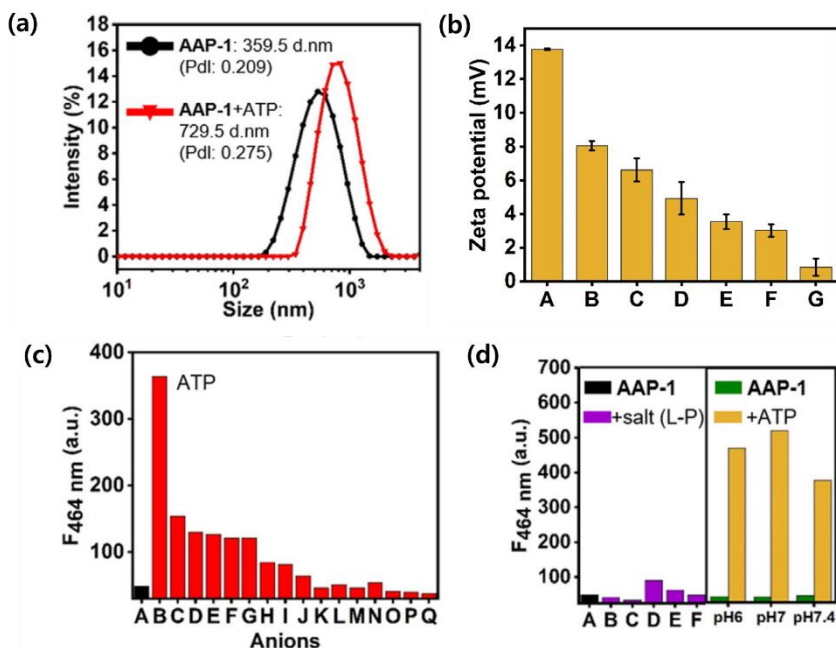


Figure VI-5. (a) The intensity distribution curves derived from the DLS measurement of **AAP-1** (50 μM of **TPE-TA**) after mixing ATP (3 mM) with PBS buffer (pH 7.4). (b) Zeta-potential value of **AAP-1**, **AAP-1**+ATP in PBS buffer (pH 7.4). Each mean and standard deviation was calculated in triplicate. (A) **AAP-1** (50 μM), (B) **AAP-1** (50 μM)+ATP (30 μM), (C) **AAP-1** (50 μM)+ATP (50 μM), (D) **AAP-1** (50 μM)+ATP (70 μM), (E) **AAP-1** (50 μM)+ATP (90 μM), (F) **AAP-1** (50 μM)+ATP (100 μM), and (G) **AAP-1** (50 μM)+ATP (120 μM). The zeta-potential was recorded within 30 s after mixing at 25 $^{\circ}\text{C}$. (c) Emission intensity plot (peak height at 464 nm) of **AAP-1** (10 mM of **TPE-TA**) after adding various substrates (1 mM) to PBS buffer (pH 7.4). (A) **AAP-1** (10 mM of **TPE-TA**), (B) ATP, (C) pyrophosphate, (D) CTP, (E) AMP, (F) TTP, (G) GTP, (H) phosphate, (I) chloride, (J) ADP, (K) dihydrogen phosphate, (L) UTP, (M) acetate, (N) sulfate, (O) nitrate, (P) bicarbonate, (Q) adenosine. (d) Emission intensity plot (peak height at 464 nm) of **AAP-1** (10 μM) in various pHs (pH 6, 7, 7.4) in the presence of salts (M–P in Fig. 3d) and ATP (1 mM). The intensity were measured under excitation at 315 nm. The intensity was recorded within 10 s after mixing at 25 $^{\circ}\text{C}$.

In the concentration-dependent assay with ATP (0–3 mM), the fluorescence intensity of **AAP-1** increased, in proportion to the concentration with the detection limit at around 5 mM (0.275 ppb, Figure VI-6a and 6b). The detection limit was slightly higher in comparison with any known ATP sensing systems,^{156–182} but it has

reliable sensitivity within repeated experiments. Given the higher biological concentration of ATP (1–10 mM) compared with ADP (1–10 μ M), AMP (1–10 μ M), GTP (1–500 μ M),^{187,188} the detection limit of **AAP-1** toward ATP is sufficient to conduct biological studies. Time-course fluorescence changes of **AAP-1**, in the presence of ATP, were monitored in a PBS buffer (pH 7.4) with excitation at 315 nm. Significant fluorescence enhancement of **AAP-1** was observed within a few seconds (<10 s) after adding ATP, and the signal was retained (Figure VI-6c). Before the bio-imaging applications, we conducted an additional ATP sensing demonstration within a cell lysate solution. We prepared the cell lysate solution using HeLa cells following the protocol.¹⁸⁹ The emission spectra change of **AAP-1** was monitored after adding the cell lysate solution (30%) in a PBS buffer (pH 7.4) with/without ATP (3 mM, 5 mM). We observed an enhanced emission of **AAP-1** in the cell lysate containing solution (cell lysate: 6.6-fold, cell lysate with ATP: 7.2-fold (3 mM), 8.0-fold (5 mM)) (Figure VI-6d). The solution was transparent, and an auto-fluorescence issue of the cell lysate was not observed. Considering the biological concentration of ATP (1–10 mM), the cell lysate contained below 3 mM of ATP, and the nanoprobe was able to sense the ATP concentration changes within millimolar concentration ranges.

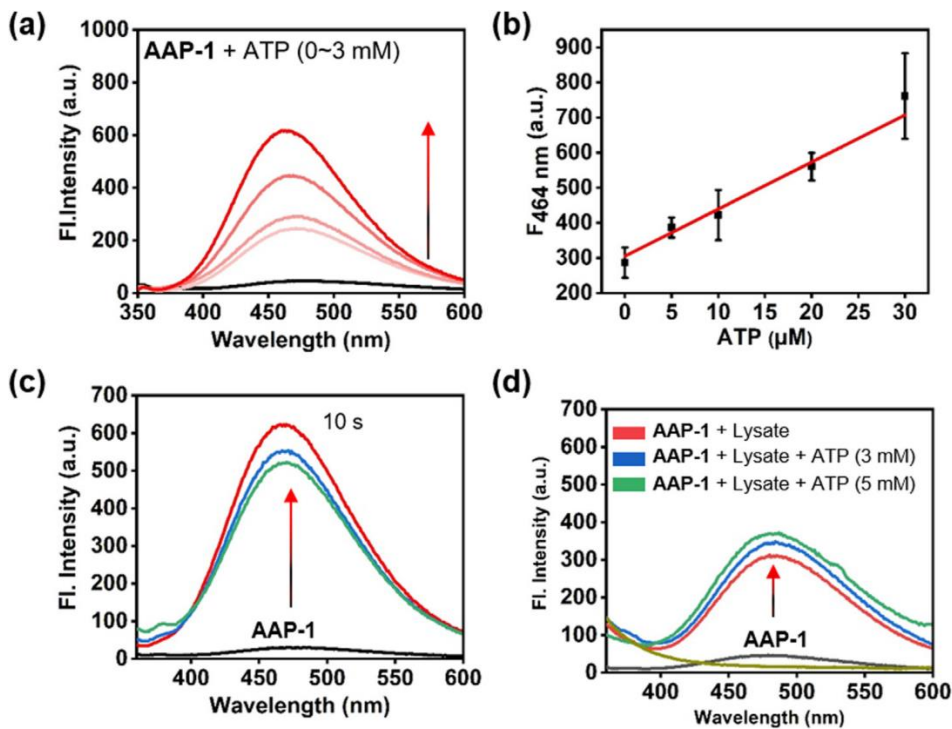


Figure VI-6. (a) Emission spectra of **AAP-1** (10 μM of **TPE-TA**) after mixing ATP (0.5, 1, 2, 3 mM) with PBS buffer (pH 7.4). The spectra were recorded within 10 s at 25 $^{\circ}\text{C}$ under excitation at 315 nm. (b) A fluorescence intensity plot (peak height at 464 nm) of **AAP-1** (10 μM of **TPE-TA**) with ATP (0–30 μM) in PBS buffer (pH 7.4). Means and standard deviations were calculated from triplicate measurements. (c) Time-dependent emission spectra of **AAP-1** (10 μM of **TPE-TA**) after adding ATP (3 mM) to PBS buffer (pH 7.4), measured at 10 s (red), 20 s (blue), and 30 s (green). (d) Emission spectra of **AAP-1** (10 μM of **TPE-TA**) after adding it into the cell lysate solution (30%) with/without ATP (3 mM, 5 mM) in PBS buffer (pH 7.4). Red: **AAP-1**+Lysate. Blue: **AAP-1**+Lysate+ATP (3 mM). Green: **AAP-1**+Lysate+ATP (5 mM). Olive: Lysate.

4. CLSM imaging of ATP in cancer cells

With the promising ATP sensing property of **AAP-1**, we demonstrated the fluorescence imaging of ATP within human cancer cells (HeLa cell line in this study). **AAP-1** was treated to the cells with MitoTracker-Red (mitochondria-specific staining reagent) as we expected that the positively-charged **AAP-1** could target mitochondria and show an enhanced fluorescence producing an ATP complex.

In the **AAP-1** treated set, a bright fluorescence was observed from the cell's cytosol in the blue channel (353 nm excitation, 400–600 nm detection channel) under CLSM (Figure VI-7a, left). As a negative control set, **AAP-1** was added to the CCCP pre-treated (50 μ M, 30 min incubation) HeLa cells. The CCCP is a chemical inhibitor of oxidative phosphorylation, which interferes with the functions of mitochondria.¹⁹⁰ A significantly reduced fluorescence signal was observed when compared with the CCCP non-treated set (4-fold, Figure VI-7b), which shows that **AAP-1** could follow the reduced cellular ATP level (Figure VI-7a, middle). As a positive control set, **AAP-1** was added to the HeLa cells pre-treated with ATP (3 mM, 30 min incubation), and a significantly increased signal (1.5-fold) was observed (Figure VI-7a, right). The fluorescence signal of MitoTracker-Red in the red channel (646 nm excitation, 650–700 nm detection channel) and the blue channel was closely overlapping (Figure VI-7c, intensity profiles collected along lines A and B), which represents that **AAP-1** could sense the mitochondrial ATP. In the cell viability analysis, **AAP-1** showed negligible cytotoxicity at concentration ranges of up to 10 mM, but it was far more significant at higher concentrations above 30 μ M, possibly due to the interference of the ATP cycle and mitochondria functions.

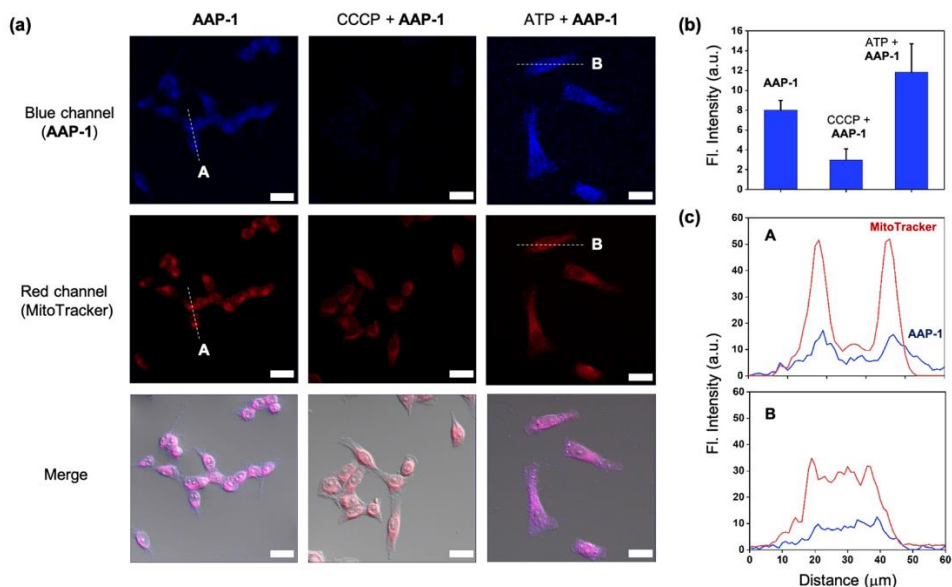


Figure VI-7. (a) CLSM images of HeLa cells co-incubated with **AAP-1** (50 μM of **TPE-TA**), CCCP (50 μM), ATP (3 mM), and MitoTracker Deep Red (25 nM). [**AAP-1**]: incubated with **AAP-1** (50 μM) for 30 min at 37 °C; [**CCCP+AAP-1**]: CCCP (50 μM) was pretreated and incubated for 30 min at 37 °C, and then incubated with **AAP-1** (50 μM) for 30 min at 37 °C; [**3 mM ATP+AAP-1**]: ATP (3 mM) was pretreated and incubated for 30 min at 37 °C, and then incubated with **AAP-1** (50 μM) for 30 min at 37 °C. MitoTracker Deep Red (25 nM) was incubated for 15 min at 37 °C. The scale bar is 20 μm. Excitation wavelength and detection channel: blue (353 nm, 400–600 nm), red (646 nm, 645–700 nm). (b) The relative fluorescence intensity plot of cells in panel (a). The intensity in cells was measured using Image-J by drawing the ROI over the entire cells based on the fluorescence images. (c) Fluorescence intensity along the white dotted line (A, B) on the images in panel (a).

5. CLSM imaging of ATP in embryonic stem cells

Further bioimaging applications of **AAP-1** were conducted in the H9 hESC. As the ATP level could affect the differentiation of the embryonic stem cells,¹⁹¹ the monitoring systems of its level is essential for stem cell-related basic research as well as translational applications. **AAP-1** (50 μM) was treated to the embryonic stem cells (passage 48), and the CCCP and ATP were used for the negative and positive controls,

respectively. Similar to the cancer cell imaging results, a bright fluorescence signal was mainly observed in the cytosol, and the different signal intensities after adding the CCCP or ATP were correlated in each set (Figure VI-8). This is the first demonstration of ATP imaging within hESC using a fluorescent probe, and it holds potential applicability for further studies.

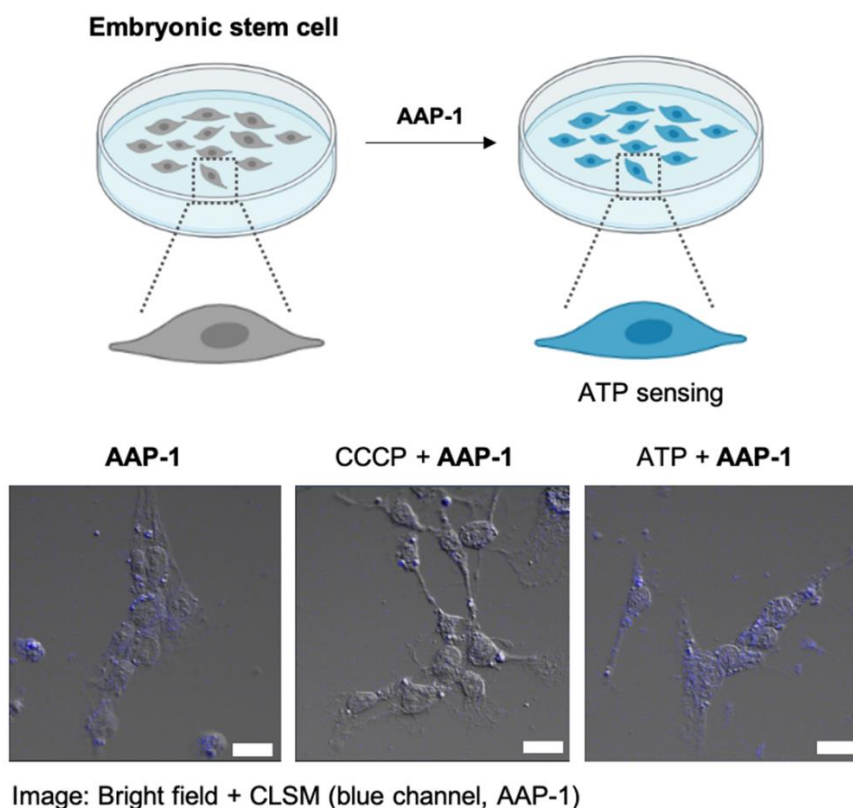


Figure VI-8. Schematic illustration (top) and CLSM images (bottom) of the ATP imaging in hESC. hESC was incubated with **AAP-1** (50 μ M), CCCP (50 μ M, pretreated), and ATP (3 mM, pretreated). [**AAP-1**]: incubated with **AAP-1** (50 μ M) for 30 min at 37 $^{\circ}$ C; [**CCCP+AAP-1**]: CCCP (50 μ M) was pretreated and incubated for 30 min at 37 $^{\circ}$ C, and then incubated with **AAP-1** (50 μ M) for 30 min at 37 $^{\circ}$ C; [**3 mM ATP+AAP-1**]: ATP (3 mM) was pretreated and incubated for 30 min at 37 $^{\circ}$ C, and then incubated with **AAP-1** (50 μ M) for 30 min at 37 $^{\circ}$ C. The scale bar is 20 μ m. Excitation wavelength and detection channel: 353 nm, 400–600 nm.

III. Conclusion

A new turn-on type fluorescent nanoprobe, **AAP-1**, has been presented for the sensing and imaging of ATP in biological media and cell lines, particularly in human cancer cells and embryonic stem cells. The nanoprobe was designed based on the TPE AIEgen and triamine moiety for the targeting of ATP via electrostatic interaction and π - π stacking interaction. It showed a highly effective ATP sensing ability with high selectivity, reliable sensitivity, with a detection limit around 0.275 ppb, an ultrafast response time (signal within 10 s), and mitochondria-targeted imaging. The synthesis, in vitro sensing property analysis, and bio-imaging applications were systematically conducted, which also provided useful information. We believe that this novel fluorescent nanoprobe can serve as a powerful tool for the exploration of ATP's behaviors within biological and pathological processes and we encourage further studies for ATP-related diseases and stem-cell related clinical applications.

IV. Experimental Section

1. Materials

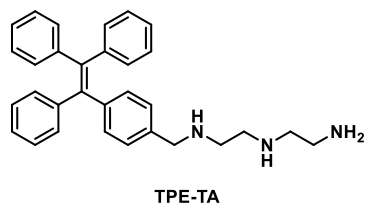
Chemicals from Aldrich (St. Louis, USA), Acros Organics (Morris Plains, USA), TCI (Tokyo, Japan), and Alfa Aesar (Ward Hill, USA) were used. Anions (purchased from Aldrich, Oriental Chemicals, Samchun Chemicals, and Duksan Chemicals): ATP, ADP, AMP, pyrophosphate, CTP, phosphate, dihydrogen phosphate, nitrate, bicarbonate, sulfate, acetate, chloride, UTP, TTP, GTP, and adenosine. Biomolecules (metal ion, amino acid) were purchased from Aldrich and Alfa Aesar: NaCl, MgCl₂, CaCl₂, KCl, biothiols (Cys, Hcy and GSH), L-Gln, L-Lys. CCCP was purchased

from Aldrich (St. Louis, USA). Commercially available reagents were used without further purification. Organic reactions were performed within an inert (argon) atmosphere. Precoated silica gel glass plates (60F-254, Merck KGaA, Germany) were used for TLC. $^1\text{H}/^{13}\text{C}$ NMR spectra were obtained using NMR instruments (Agilent, 400-MR DD2, 400 MHz). In the NMR spectra, a ppm unit was used for the chemical shifts (d) [multiplicities are indicated by s (singlet), d (doublet), and m (multiplet)]. TMS was used as an internal standard. HRMS of newly synthesized compounds was analyzed using Ultra High-Resolution ESI Q-TOF mass spectrometer (Bruker, MA, USA) at the Sogang University (Organic Chemistry Research Center, Seoul, Rep. of Korea). prep-HPLC isolation was performed using Agilent 1260 Infinity system (Agilent Technologies, Santa Clara, USA) with Zorbax C18 column (Agilent Technology, 5 mM, 80 Å, 21.2 x 150 mm). Malvern Instruments Zetasizer Nano ZS90 (Worcester-shire, UK) was used for DLS and zeta-potential analysis.

2. Synthesis

The procedures used in the synthesis of compounds are described in Scheme IV-

1. Compound **VI-4** was synthesized using the following reference.¹⁹²⁻¹⁹⁴



N^1 -(2-aminoethyl)- N^2 -(4-(1,2,2-triphenylvinyl)benzyl)ethane-1,2-diamine. (**TPE-TA**). NaH (6.1 mg, 0.153 mmol) and Compound **VI-4** (43.1 mg, 0.142 mmol) were mixed in DMF

under anhydrous condition. The mixture was stirred at 0 °C for 30 min, and then

Compound **VI-5** (50.0 mg, 0.118 mmol) was added. The resulting mixture was warmed up to 25 °C and then stirred for 30 min. The crude mixture was quenched by the addition of H₂O and diluted with EtOAc. The organic layer was washed with H₂O, dried over MgSO₄, and concentrated in vacuo. The residue was used in the next step without further purification. The crude compound **VI-6** was dissolved in DCM (0.5 mL) and treated with TFA (0.5 mL). After 1 h of stirring, the crude mixture was concentrated in vacuo and dissolved in MeCN. **TPE-TA** was purified by prep-HPLC (H₂O/MeCN with TFA, 35.7 mg, 35% for 2 steps). The purity of the resulting **TPE-TA** was confirmed using NMR and HRMS. ¹H NMR (400 MHz, CD₃OD): δ 7.26 (d, J = 8.2 Hz, 2H), 7.13–7.07 (m, 11H), 7.04–6.96 (m, 6H), 4.17 (s, 2H), 3.27 (d, J = 5.9 Hz, 2H), 3.22–3.12 (m, 6H). ¹³C NMR (101 MHz, CD₃OD): δ 146.81, 144.78, 144.62, 144.60, 143.47, 141.35, 133.16, 132.29, 132.25, 132.21, 130.44, 130.29, 128.91, 128.89, 128.78, 127.77, 52.14, 46.59, 45.33. HRMS (m/z): [M+H]⁺ calcd. for C₃₁H₃₃N₃, 448.2747; found, 448.2746

3. UV-vis and fluorescence spectroscopic methods

A spectrophotometer (Agilent Technologies Cary 8454, USA) was used to obtain the UV-Vis absorption spectra. A spectrofluorophotometer (SHIMADZU CORP. RF-6000, Japan) with a 1-cm standard quartz cell was used for emission spectra acquisition. The **TPE-TA** stock solution was prepared in DMSO, 10 mM). Photophysical properties of **AAP-1** were acquired in PBS buffer (pH 7.4) after adding ATP (0–5 mM). The emission spectra were recorded at 25 °C under excitation at the maximum absorbance. The intensity plot of the absorption and emission is

derived from the value of mean \pm SD (number of replicates: 3).

4. Management of cells

The HeLa cell line was acquired from Korean Cell Line Bank (Rep. of Korea), and cultured within DMEM (Hyclone, USA) supplemented with 1% penicillin-streptomycin (Hyclone, USA) and 10% FBS (Hyclone, USA). [Stem Cell; undifferentiated H9 hESC, passage 48] The stem cells were cultured on a mitotically inactivated SNL 76/7 feeder layer (Cell Biolabs, Inc.) in hESC medium, consisting of DMEM/F12, 0.1 mM MEM-NEAA, 2 mM L-glutamine, 55 μ M β -mercaptoethanol (Life Technologies, Carlsbad, USA), 10 ng/mL FGF2 (R&D Systems, Minneapolis, USA), and 20% knockout serum replacement following the protocol for the hESC culture.¹⁹⁵ All cell lines were maintained at 37 °C and 5% CO₂ (humidified incubator).

5. CLSM imaging

HeLa cells (2×10^5) were seeded on 35-mm glassbottom confocal dishes (SPL Life Science, Rep. of Korea) and incubated for 24 h. Cells were treated with **TPE-TA** (50 μ M, 30 min incubation), CCCP (50 μ M, 30 min incubation), and ATP (3 mM, 30 min incubation) at 37 °C in 5% CO₂ (humidified incubator). [Stem cell]. hESCs were isolated into single cells with Accutase (Life Technologies, Carlsbad, USA) and replated onto recombinant E8 fragments of human laminin 511-coated (iMatrix-511 silk; Matrixome, Inc., Osaka, Japan) confocal dish (SPL Life Sciences, Rep. of Korea)

at a density of 135 cells/mm² with StemFit® Basic 04 medium (Ajinomoto, Chuo, Japan). After 24 h incubation, cells were treated with **TPE-TA** (50 μM, 30 min incubation), CCCP (50 μM, 30 min incubation), and ATP (3 mM, 30 min incubation) at 37 °C in 5% CO₂ (humidified incubator). A CLSM (Carl-Zeiss LSM 700 Exciter, Germany) was used for fluorescence cellular images. Wavelength information (excitation wavelength, emission channel); blue (353 nm, 400–600 nm), red (646 nm, 645–700 nm).

6. Cell viability analysis

Cell viability analysis was conducted using Vybrant® MTT Cell Proliferation Assay Kit (ThermoFisher Scientific, USA) following the manufacturer's instructions. HeLa cells (5 x 10⁴ per well) were placed on a well-plate (96-well, SPL Life Science, Rep. of Korea) and incubated for 24 h in DMEM media containing 1% PS (penicillin-streptomycin) and 10% FBS. The absorbance (at 550 nm) was analyzed using a microplate reader (SpectraMax Gemini EM, Molecular Devices, USA). Cell viability value is expressed as a relative percentage of the untreated control. The data represent the mean ± SD (number of replicates: 3).

7. Cell lysate experiment

HeLa cells (2.1×10^5 in 15 mL microcentrifuge tube) were centrifuged at 1300 rpm for 3 min. After removing the supernatant, the residues were rinsed with PBS buffer (pH 7.4). Next, lysis buffer (0.5 mL, Boster Bio, AR0105, Pleasanton, USA) was added to the tube and vortexed for 1 min. The tube was incubated in an ice-bath (0 °C) for 30 min and centrifuged at 14,000 rpm for 10 min [Cell lysate solution preparation] The supernatant was collected and added to the DMEM media (2 mL, 1% penicillin-streptomycin, 10% FBS without phenol red). [Experimental set] (i) **AAP-1** (10 μ M) in PBS buffer (pH 7.4), (ii) **AAP-1** (10 μ M) in PBS buffer (pH 7.4) containing 30% cell lysate, (iii) **AAP-1** (10 μ M) in PBS buffer (pH 7.4) containing 30% cell lysate with ATP (3 mM, 5 mM), and (iv) 30% Cell lysate solution. The emission spectra were recorded within 10 s after mixing at 25 °C under excitation at 315 nm.

References

1. Bukh, J. The history of hepatitis C virus (HCV): Basic research reveals unique features in phylogeny, evolution and the viral life cycle with new perspectives for epidemic control. *J Hepatol* **2016**, *65* (1 Suppl), S2–S21.
2. Spearman, C. W.; Dusheiko, G. M.; Hellard, M.; Sonderup, M. Hepatitis C. *The Lancet* **2019**, *394* (10207), 1451–1466.
3. Millman, A. J.; Nelson, N. P.; Vellozzi, C. Hepatitis C: Review of the Epidemiology, Clinical Care, and Continued Challenges in the Direct Acting Antiviral Era. *Curr Epidemiol Rep* **2017**, *4* (2), 174–185.
4. Borgia, S. M.; Hedskog, C.; Parhy, B.; Hyland, R. H.; Stamm, L. M.; Brainard, D. M.; Subramanian, M. G.; McHutchison, J. G.; Mo, H.; Svarovskaia, E.; et al. Identification of a Novel Hepatitis C Virus Genotype From Punjab, India: Expanding Classification of Hepatitis C Virus Into 8 Genotypes. *J Infect Dis* **2018**, *218* (11), 1722–1729.
5. Hedskog, C.; Parhy, B.; Chang, S.; Zeuzem, S.; Moreno, C.; Shafran, S. D.; Borgia, S. M.; Asselah, T.; Alric, L.; Abergel, A.; et al. Identification of 19 Novel Hepatitis C Virus Subtypes-Further Expanding HCV Classification. *Open Forum Infect Dis* **2019**, *6* (3), ofz076.
6. Randal, J. Hepatitis C vaccine hampered by viral complexity, many technical restraints. *J Natl Cancer Inst* **1999**, *91* (11), 906–908.
7. Inchauspé, G.; Honnet, G.; Bonnefoy, J. Y.; Nicosia, A.; Strickland, G. T.

Hepatitis C vaccine: supply and demand. *The Lancet Infectious Diseases* **2008**, *8* (12), 739–740.

8. Kumthip, K.; Maneekarn, N. The role of HCV proteins on treatment outcomes. *Virology* **2015**, *12*, 217.

9. Fridell, R. A.; Qiu, D.; Valera, L.; Wang, C.; Rose, R. E.; Gao, M. Distinct functions of NS5A in hepatitis C virus RNA replication uncovered by studies with the NS5A inhibitor BMS-790052. *J Virol* **2011**, *85* (14), 7312–7320.

10. Lindenbach, B. D.; Rice, C. M. Unravelling hepatitis C virus replication from genome to function. *Nature* **2005**, *436* (7053), 933–938.

11. Love, R. A.; Brodsky, O.; Hickey, M. J.; Wells, P. A.; Cronin, C. N. Crystal structure of a novel dimeric form of NS5A domain I protein from hepatitis C virus. *J Virol* **2009**, *83* (9), 4395–4403.

12. Ascher, D. B.; Wielens, J.; Nero, T. L.; Doughty, L.; Morton, C. J.; Parker, M. W. Potent hepatitis C inhibitors bind directly to NS5A and reduce its affinity for RNA. *Sci Rep* **2014**, *4*, 4765.

13. Hanouille, X.; Badillo, A.; Verdegem, D.; Penin, F.; Lippens, G. The domain 2 of the HCV NS5A protein is intrinsically unstructured. *Protein Pept Lett* **2010**, *17* (8), 1012–1018.

14. Ross-Thriepland, D.; Amako, Y.; Harris, M. The C terminus of NS5A domain II is a key determinant of hepatitis C virus genome replication, but is not required for virion assembly and release. *J Gen Virol* **2013**, *94* (Pt 5), 1009–1018.

15. Appel, N.; Zayas, M.; Miller, S.; Krijnse-Locker, J.; Schaller, T.; Friebe, P.; Kallis, S.; Engel, U.; Bartenschlager, R. Essential role of domain III of nonstructural protein 5A for hepatitis C virus infectious particle assembly. *PLoS Pathog* **2008**, *4* (3), e1000035.
16. Huang, Y.; Staschke, K.; De Francesco, R.; Tan, S. L. Phosphorylation of hepatitis C virus NS5A nonstructural protein: a new paradigm for phosphorylation-dependent viral RNA replication? *Virology* **2007**, *364* (1), 1–9.
17. Masaki, T.; Suzuki, T. NS5A phosphorylation: its functional role in the life cycle of hepatitis C virus. *Future Virology* **2015**, *10* (6), 751–762.
18. Bryan-Marrugo, O. L.; Ramos-Jiménez, J.; Barrera-Saldaña, H.; Rojas-Martínez, A.; Vidaltamayo, R.; Rivas-Estilla, A. M. History and progress of antiviral drugs: From acyclovir to direct-acting antiviral agents (DAAs) for Hepatitis C. *Medicina Universitaria* **2015**, *17* (68), 165–174.
19. Poordad, F.; Dieterich, D. Treating hepatitis C: current standard of care and emerging direct-acting antiviral agents. *J Viral Hepat* **2012**, *19* (7), 449–464.
20. Hoofnagle, J. H.; Seeff, L. B. Peginterferon and ribavirin for chronic hepatitis C. *N Engl J Med* **2006**, *355* (23), 2444–2451.
21. Gao, M.; Nettles, R. E.; Belema, M.; Snyder, L. B.; Nguyen, V. N.; Fridell, R. A.; Serrano-Wu, M. H.; Langley, D. R.; Sun, J. H.; O'Boyle, D. R., 2nd; et al. Chemical genetics strategy identifies an HCV NS5A inhibitor with a potent clinical effect. *Nature* **2010**, *465* (7294), 96–100.

22. Herbst, D. A.; Reddy, K. R. NS5A inhibitor, daclatasvir, for the treatment of chronic hepatitis C virus infection. *Expert Opin Investig Drugs* **2013**, *22* (10), 1337–1346.
23. Fridell, R. A.; Wang, C.; Sun, J. H.; O'Boyle, D. R., 2nd; Nower, P.; Valera, L.; Qiu, D.; Roberts, S.; Huang, X.; Kienzle, B.; et al. Genotypic and phenotypic analysis of variants resistant to hepatitis C virus nonstructural protein 5A replication complex inhibitor BMS-790052 in humans: in vitro and in vivo correlations. *Hepatology* **2011**, *54* (6), 1924–1935.
24. Coburn, C. A.; Meinke, P. T.; Chang, W.; Fandozzi, C. M.; Graham, D. J.; Hu, B.; Huang, Q.; Kargman, S.; Kozlowski, J.; Liu, R.; et al. Discovery of MK-8742: an HCV NS5A inhibitor with broad genotype activity. *ChemMedChem* **2013**, *8* (12), 1930–1940.
25. DeGoey, D. A.; Randolph, J. T.; Liu, D.; Pratt, J.; Hutchins, C.; Donner, P.; Krueger, A. C.; Matulenko, M.; Patel, S.; Motter, C. E.; et al. Discovery of ABT-267, a pan-genotypic inhibitor of HCV NS5A. *J Med Chem* **2014**, *57* (5), 2047–2057.
26. Link, J. O.; Taylor, J. G.; Xu, L.; Mitchell, M.; Guo, H.; Liu, H.; Kato, D.; Kirschberg, T.; Sun, J.; Squires, N.; et al. Discovery of ledipasvir (GS-5885): a potent, once-daily oral NS5A inhibitor for the treatment of hepatitis C virus infection. *J Med Chem* **2014**, *57* (5), 2033–2046.
27. Link, J. O.; Taylor, J. G.; Trejo-Martin, A.; Kato, D.; Katana, A. A.; Krygowski, E. S.; Yang, Z. Y.; Zipfel, S.; Cottell, J. J.; Bacon, E. M.; et al. Discovery of velpatasvir (GS-5816): A potent pan-genotypic HCV NS5A inhibitor in the single-

tablet regimens Vosevi((R)) and Epclusa((R)). *Bioorg Med Chem Lett* **2019**, *29* (16), 2415–2427.

28. Meanwell, N. A. 2015 Philip S. Portoghese Medicinal Chemistry Lectureship. Curing Hepatitis C Virus Infection with Direct-Acting Antiviral Agents: The Arc of a Medicinal Chemistry Triumph. *J Med Chem* **2016**, *59* (16), 7311–7351.

29. Tong, L.; Yu, W.; Chen, L.; Selyutin, O.; Dwyer, M. P.; Nair, A. G.; Mazzola, R.; Kim, J. H.; Sha, D.; Yin, J.; et al. Discovery of Ruzasvir (MK-8408): A Potent, Pan-Genotype HCV NS5A Inhibitor with Optimized Activity against Common Resistance-Associated Polymorphisms. *J Med Chem* **2017**, *60* (1), 290–306.

30. Wagner, R.; Randolph, J. T.; Patel, S. V.; Nelson, L.; Matulenko, M. A.; Keddy, R.; Pratt, J. K.; Liu, D.; Krueger, A. C.; Donner, P. L.; et al. Highlights of the Structure-Activity Relationships of Benzimidazole Linked Pyrrolidines Leading to the Discovery of the Hepatitis C Virus NS5A Inhibitor Pibrentasvir (ABT-530). *J Med Chem* **2018**, *61* (9), 4052–4066.

31. Walker, J.; Crosby, R.; Wang, A.; Woldu, E.; Vamathevan, J.; Voitenleitner, C.; You, S.; Remlinger, K.; Duan, M.; Kazmierski, W.; et al. Preclinical characterization of GSK2336805, a novel inhibitor of hepatitis C virus replication that selects for resistance in NS5A. *Antimicrob Agents Chemother* **2014**, *58* (1), 38–47.

32. Zhong, M.; Peng, E.; Huang, N.; Huang, Q.; Huq, A.; Lau, M.; Colonno, R.; Li, L. Discovery of ravidasvir (PPI-668) as a potent pan-genotypic HCV NS5A inhibitor. *Bioorg Med Chem Lett* **2016**, *26* (18), 4508–4512.

33. Bae, I. H.; Kim, H. S.; You, Y.; Chough, C.; Choe, W.; Seon, M. K.; Lee, S. G.; Keum, G.; Jang, S. K.; Moon Kim, B. Novel benzidine and diaminofluorene prolinamide derivatives as potent hepatitis C virus NS5A inhibitors. *Eur J Med Chem* **2015**, *101*, 163–178.
34. You, Y.; Kim, H. S.; Bae, I. H.; Lee, S. G.; Jee, M. H.; Keum, G.; Jang, S. K.; Kim, B. M. New potent biaryl sulfate-based hepatitis C virus inhibitors. *Eur J Med Chem* **2017**, *125*, 87–100.
35. Bomhard, E. M.; Herbold, B. A. Genotoxic activities of aniline and its metabolites and their relationship to the carcinogenicity of aniline in the spleen of rats. *Crit Rev Toxicol* **2005**, *35* (10), 783–835.
36. Manolakopoulos, S.; Zacharakis, G.; Zissis, M.; Giannakopoulos, V. Safety and efficacy of daclatasvir in the management of patients with chronic hepatitis C. *Ann Gastroenterol* **2016**, *29* (3), 282–296.
37. Nettles, J. H.; Stanton, R. A.; Broyde, J.; Amblard, F.; Zhang, H.; Zhou, L.; Shi, J.; McBrayer, T. R.; Whitaker, T.; Coats, S. J.; et al. Asymmetric binding to NS5A by daclatasvir (BMS-790052) and analogs suggests two novel modes of HCV inhibition. *J Med Chem* **2014**, *57* (23), 10031–10043.
38. Nakamura, H.; Fujioka, S.; Terui, T.; Okuda, S.; Kondo, K.; Tamatani, Y.; Akagi, Y.; Komoda, Y.; Kinoshita, W.; Ito, S.; et al. Orally bioavailable HCV NS5A inhibitors of unsymmetrical structural class. *Bioorg Med Chem Lett* **2020**, *30* (17), 127361.

39. Li, X.; Gao, X.; Shi, W.; Ma, H. Design strategies for water-soluble small molecular chromogenic and fluorogenic probes. *Chem Rev* **2014**, *114* (1), 590–659.
40. Berezin, M. Y.; Achilefu, S. Fluorescence lifetime measurements and biological imaging. *Chem Rev* **2010**, *110* (5), 2641–2684.
41. Escobedo, J. O.; Rusin, O.; Lim, S.; Strongin, R. M. NIR dyes for bioimaging applications. *Curr Opin Chem Biol* **2010**, *14* (1), 64–70.
42. Luo, S.; Zhang, E.; Su, Y.; Cheng, T.; Shi, C. A review of NIR dyes in cancer targeting and imaging. *Biomaterials* **2011**, *32* (29), 7127–7138.
43. Fu, Y.; Finney, N. S. Small-molecule fluorescent probes and their design. *RSC Adv* **2018**, *8* (51), 29051–29061.
44. An, J. M.; Kim, S. H.; Kim, D. Recent advances in two-photon absorbing probes based on a functionalized dipolar naphthalene platform. *Org Biomol Chem* **2020**, *18* (23), 4288–4297.
45. Hou, T. T.; Cai, Y.; Zhang, Z. Y.; Wang, C. Y.; Tang, Y. H.; Zhu, M. Q.; Wang, Y. L. Progress of Dicyanomethylene-4H-Pyran Derivatives in Biological Sensing Based on ICT Effect. *Front Chem* **2022**, *10*, 903253.
46. Zhang, K.; Liu, J.; Zhang, Y.; Fan, J.; Wang, C.-K.; Lin, L. Theoretical Study of the Mechanism of Aggregation-Caused Quenching in Near-Infrared Thermally Activated Delayed Fluorescence Molecules: Hydrogen-Bond Effect. *The Journal of Physical Chemistry C* **2019**, *123* (40), 24705–24713.

47. Luo, J.; Xie, Z.; Lam, J. W.; Cheng, L.; Chen, H.; Qiu, C.; Kwok, H. S.; Zhan, X.; Liu, Y.; Zhu, D.; et al. Aggregation-induced emission of 1-methyl-1,2,3,4,5-pentaphenylsilole. *Chem Commun (Camb)* **2001**, (18), 1740–1741.
48. Chen, Y.; Lam, J. W. Y.; Kwok, R. T. K.; Liu, B.; Tang, B. Z. Aggregation-induced emission: fundamental understanding and future developments. *Materials Horizons* **2019**, 6 (3), 428–433.
49. Liang, J.; Tang, B. Z.; Liu, B. Specific light-up bioprobes based on AIEgen conjugates. *Chem Soc Rev* **2015**, 44 (10), 2798–2811.
50. Feng, G.; Liu, B. Aggregation-Induced Emission (AIE) Dots: Emerging Theranostic Nanolights. *Acc Chem Res* **2018**, 51 (6), 1404–1414.
51. Li, D.; Qin, W.; Xu, B.; Qian, J.; Tang, B. Z. AIE Nanoparticles with High Stimulated Emission Depletion Efficiency and Photobleaching Resistance for Long-Term Super-Resolution Bioimaging. *Adv Mater* **2017**, 29 (43).
52. Kurdyukova, I. V.; Ishchenko, A. A. Organic dyes based on fluorene and its derivatives. *Russian Chemical Reviews* **2012**, 81 (3), 258–290.
53. Chamberlain, T. Dioxazine Violet Pigments. In *High Performance Pigments*, 2001; pp 185–194.
54. Eaton, M. J.; Lookingland, K. J.; Moore, K. E. The σ ligand rimcazole activates noradrenergic neurons projecting to the paraventricular nucleus and increases corticosterone secretion in rats. *Brain Research* **1996**, 733 (2), 162–166.

55. Bostrom, I. M.; Nyman, G. C.; Lord, P. E.; Haggstrom, J.; Jones, B. E.; Bohlin, H. P. Effects of carprofen on renal function and results of serum biochemical and hematologic analyses in anesthetized dogs that had low blood pressure during anesthesia. *Am J Vet Res* **2002**, *63* (5), 712–721.
56. Rowland, C. A.; Yap, G. P. A.; Bloch, E. D. Novel syntheses of carbazole-3,6-dicarboxylate ligands and their utilization for porous coordination cages. *Dalton Trans* **2020**, *49* (45), 16340–16347.
57. Mokhtari, N.; Afshari, M.; Dinari, M. Synthesis and characterization of a novel fluorene-based covalent triazine framework as a chemical adsorbent for highly efficient dye removal. *Polymer* **2020**, *195*.
58. Yin, H. Q.; Cao, P. P.; Wang, X. Y.; Li, Y. H.; Yin, X. B. Computed Tomography Imaging-Guided Tandem Catalysis-Enhanced Photodynamic Therapy with Gold Nanoparticle Functional Covalent Organic Polymers. *ACS Appl Bio Mater* **2020**, *3* (4), 2534–2542.
59. Ye, R.; Cui, Q.; Yao, C.; Liu, R.; Li, L. Tunable fluorescence behaviors of a supramolecular system based on a fluorene derivative and cucurbit[8]uril and its application for ATP sensing. *Phys Chem Chem Phys* **2017**, *19* (46), 31306–31315.
60. An, S.; Xu, T.; Peng, C.; Hu, J.; Liu, H. Rational design of functionalized covalent organic frameworks and their performance towards CO₂ capture. *RSC Adv* **2019**, *9* (37), 21438–21443.
61. Kim, H. S.; You, Y.; Mun, J.; Gadhe, C. G.; Moon, H.; Lee, J. S.; Pae, A. N.;

Kohara, M.; Keum, G.; Kim, B. M.; et al. Structure-activity relationships of fluorene compounds inhibiting HCV variants. *Antiviral Res* **2020**, *174*, 104678.

62. Heflich, R. H.; Neft, R. E. Genetic toxicity of 2-acetylaminofluorene, 2-aminofluorene and some of their metabolites and model metabolites. *Mutation Research/Reviews in Genetic Toxicology* **1994**, *318* (2), 73–174.

63. Purohit, V.; Basu, A. K. Mutagenicity of nitroaromatic compounds. *Chem Res Toxicol* **2000**, *13* (8), 673–692.

64. Ames, B. N.; McCann, J.; Yamasaki, E. Methods for detecting carcinogens and mutagens with the salmonella/mammalian-microsome mutagenicity test. *Mutation Research/Environmental Mutagenesis and Related Subjects* **1975**, *31* (6), 347–363.

65. Kim, S.; Kim, E.; Kim, B. M. Fe₃O₄ nanoparticles: a conveniently reusable catalyst for the reduction of nitroarenes using hydrazine hydrate. *Chem Asian J* **2011**, *6* (8), 1921–1925.

66. Barluenga, J.; Tomas-Gamasa, M.; Aznar, F.; Valdes, C. Metal-free carbon-carbon bond-forming reductive coupling between boronic acids and tosylhydrazones. *Nat Chem* **2009**, *1* (6), 494–499.

67. Flückiger-Isler, S.; Kamber, M. The Ames II and Ames MPF Penta I Assay: A Liquid Microplate Format Modification of the Classic Ames Test. In *Genotoxicity and DNA Repair*, Methods in Pharmacology and Toxicology, 2014; pp 23–41.

68. Mortelmans, K.; Zeiger, E. The Ames Salmonella/microsome mutagenicity assay. *Mutation Research/Fundamental and Molecular Mechanisms of Mutagenesis* **2000**,

455 (1-2), 29–60.

69. Falade-Nwulia, O.; Suarez-Cuervo, C.; Nelson, D. R.; Fried, M. W.; Segal, J. B.; Sulkowski, M. S. Oral Direct-Acting Agent Therapy for Hepatitis C Virus Infection: A Systematic Review. *Ann Intern Med* **2017**, *166* (9), 637–648.

70. Cox, A. L. MEDICINE. Global control of hepatitis C virus. *Science* **2015**, *349* (6250), 790–791.

71. Lombardi, A.; Mondelli, M. U.; Hepatitis, E. S. G. f. V. Hepatitis C: Is eradication possible? *Liver Int* **2019**, *39* (3), 416–426.

72. O'Boyle Ii, D. R.; Sun, J. H.; Nower, P. T.; Lemm, J. A.; Fridell, R. A.; Wang, C.; Romine, J. L.; Belema, M.; Nguyen, V. N.; Laurent, D. R.; et al. Characterizations of HCV NS5A replication complex inhibitors. *Virology* **2013**, *444* (1-2), 343–354.

73. Lambert, S. M.; Langley, D. R.; Garnett, J. A.; Angell, R.; Hedgethorpe, K.; Meanwell, N. A.; Matthews, S. J. The crystal structure of NS5A domain 1 from genotype 1a reveals new clues to the mechanism of action for dimeric HCV inhibitors. *Protein Sci* **2014**, *23* (6), 723–734.

74. Barakat, K. H.; Anwar-Mohamed, A.; Tuszynski, J. A.; Robins, M. J.; Tyrrell, D. L.; Houghton, M. A Refined Model of the HCV NS5A protein bound to daclatasvir explains drug-resistant mutations and activity against divergent genotypes. *J Chem Inf Model* **2015**, *55* (2), 362–373.

75. Berger, C.; Romero-Brey, I.; Radujkovic, D.; Terreux, R.; Zayas, M.; Paul, D.;

Harak, C.; Hoppe, S.; Gao, M.; Penin, F.; et al. Daclatasvir-like inhibitors of NS5A block early biogenesis of hepatitis C virus-induced membranous replication factories, independent of RNA replication. *Gastroenterology* **2014**, *147* (5), 1094–1105.

76. Blach, S.; Zeuzem, S.; Manns, M.; Altraif, I.; Duberg, A.-S.; Muljono, D. H.; Waked, I.; Alavian, S. M.; Lee, M.-H.; Negro, F.; et al. Global prevalence and genotype distribution of hepatitis C virus infection in 2015: a modelling study. *The Lancet Gastroenterology & Hepatology* **2017**, *2* (3), 161–176.

77. Priest, B. T.; Bell, I. M.; Garcia, M. L. Role of hERG potassium channel assays in drug development. *Channels (Austin)* **2008**, *2* (2), 87–93.

78. Spector, P. S.; Curran, M. E.; Keating, M. T.; Sanguinetti, M. C. Class III antiarrhythmic drugs block HERG, a human cardiac delayed rectifier K⁺ channel. Open-channel block by methanesulfonanilides. *Circ Res* **1996**, *78* (3), 499–503.

79. Lubberstedt, M.; Muller-Vieira, U.; Mayer, M.; Biemel, K. M.; Knospel, F.; Knobloch, D.; Nussler, A. K.; Gerlach, J. C.; Zeilinger, K. HepaRG human hepatic cell line utility as a surrogate for primary human hepatocytes in drug metabolism assessment in vitro. *J Pharmacol Toxicol Methods* **2011**, *63* (1), 59–68.

80. Obach, R. S.; Walsky, R. L.; Venkatakrishnan, K.; Gaman, E. A.; Houston, J. B.; Tremaine, L. M. The utility of in vitro cytochrome P450 inhibition data in the prediction of drug-drug interactions. *J Pharmacol Exp Ther* **2006**, *316* (1), 336–348.

81. Martin, P.; Gillen, M.; Millson, D.; Oliver, S.; Brealey, C.; Grossbard, E. B.; Baluom, M.; Lau, D.; Sweeny, D.; Mant, T.; et al. Effects of CYP3A4 Inhibitors

Ketoconazole and Verapamil and the CYP3A4 Inducer Rifampicin on the Pharmacokinetic Parameters of Fostatinib: Results from In Vitro and Phase I Clinical Studies. *Drugs R D* **2016**, *16* (1), 81–92.

82. Urso, R.; Bardi, P.; Giorgi, G. A short introduction to pharmacokinetics. *Eur Rev Med Pharmacol Sci* **2002**, *6* (2-3), 33–44.

83. Kim, B. M.; Jang, S. K.; You, Y. S.; Bae, I. H.; Moon, H.; Kim, B. W.; Kim, H. S.; Mun, J. Fluorene derivative or pharmaceutically acceptable salt thereof, preparation method therefor, and pharmaceutical composition comprising same as effective ingredient for preventing or treating HCV-related disease. KR patent WO2019059687, September 20, 2018.

84. Zhong, J.; Gastaminza, P.; Cheng, G.; Kapadia, S.; Kato, T.; Burton, D. R.; Wieland, S. F.; Uprichard, S. L.; Wakita, T.; Chisari, F. V. Robust hepatitis C virus infection in vitro. *Proc Natl Acad Sci U S A* **2005**, *102* (26), 9294–9299.

85. Lohmann, V.; Korner, F.; Koch, J.; Herian, U.; Theilmann, L.; Bartenschlager, R. Replication of subgenomic hepatitis C virus RNAs in a hepatoma cell line. *Science* **1999**, *285* (5424), 110–113.

86. Gottwein, J. M.; Pham, L. V.; Mikkelsen, L. S.; Ghanem, L.; Ramirez, S.; Scheel, T. K. H.; Carlsen, T. H. R.; Bukh, J. Efficacy of NS5A Inhibitors Against Hepatitis C Virus Genotypes 1-7 and Escape Variants. *Gastroenterology* **2018**, *154* (5), 1435–1448.

87. Guo, Z.; Park, S.; Yoon, J.; Shin, I. Recent progress in the development of near-

infrared fluorescent probes for bioimaging applications. *Chem Soc Rev* **2014**, *43* (1), 16–29.

88. Li, J. B.; Liu, H. W.; Fu, T.; Wang, R.; Zhang, X. B.; Tan, W. Recent Progress in Small-Molecule Near-IR Probes for Bioimaging. *Trends Chem* **2019**, *1* (2), 224–234.

89. Pansare, V.; Hejazi, S.; Faenza, W.; Prud'homme, R. K. Review of Long-Wavelength Optical and NIR Imaging Materials: Contrast Agents, Fluorophores and Multifunctional Nano Carriers. *Chem Mater* **2012**, *24* (5), 812–827.

90. Kenry; Duan, Y.; Liu, B. Recent Advances of Optical Imaging in the Second Near-Infrared Window. *Adv Mater* **2018**, *30* (47), e1802394.

91. Hemmer, E.; Benayas, A.; Legare, F.; Vetrone, F. Exploiting the biological windows: current perspectives on fluorescent bioprobes emitting above 1000 nm. *Nanoscale Horiz* **2016**, *1* (3), 168–184.

92. Han, H.; Wang, H.; Chen, Y.; Li, Z.; Wang, Y.; Jin, Q.; Ji, J. Theranostic reduction-sensitive gemcitabine prodrug micelles for near-infrared imaging and pancreatic cancer therapy. *Nanoscale* **2016**, *8* (1), 283–291.

93. Li, D. H.; Schreiber, C. L.; Smith, B. D. Sterically Shielded Heptamethine Cyanine Dyes for Bioconjugation and High Performance Near-Infrared Fluorescence Imaging. *Angew Chem Int Ed Engl* **2020**, *59* (29), 12154–12161.

94. Huang, J.; Huang, J.; Cheng, P.; Jiang, Y.; Pu, K. Near-Infrared Chemiluminescent Reporters for In Vivo Imaging of Reactive Oxygen and Nitrogen

Species in Kidneys. *Advanced Functional Materials* **2020**, *30* (39).

95. An, J. M.; Moon, H.; Kim, Y.; Kang, S.; Kim, Y.; Jung, Y.; Park, S.; Verwilt, P.; Kim, B. M.; Kang, J. S.; et al. Visualizing mitochondria and mouse intestine with a fluorescent complex of a naphthalene-based dipolar dye and serum albumin. *J Mater Chem B* **2020**, *8* (34), 7642–7651.

96. Jung, Y.; Ju, I. G.; Choe, Y. H.; Kim, Y.; Park, S.; Hyun, Y. M.; Oh, M. S.; Kim, D. Hydrazine Expose: The Next-Generation Fluorescent Probe. *ACS Sens* **2019**, *4* (2), 441–449.

97. Moon, H.; Jung, Y.; Kim, Y.; Kim, B. W.; Choi, J. G.; Kim, N. H.; Oh, M. S.; Park, S.; Kim, B. M.; Kim, D. High Stability of a Donor-Acceptor Type Oxazepine-Containing Fluorophore and Its Applications in Cellular Imaging and Two-Photon Deep Tissue Imaging. *Org Lett* **2019**, *21* (11), 3891–3894.

98. Kim, N. H.; Lee, J.; Park, S.; Jung, J.; Kim, D. A Schiff Base Fluorescence Enhancement Probe for Fe(III) and Its Sensing Applications in Cancer Cells. *Sensors (Basel)* **2019**, *19* (11).

99. Li, H.; Yao, Q.; Fan, J.; Du, J.; Wang, J.; Peng, X. A two-photon NIR-to-NIR fluorescent probe for imaging hydrogen peroxide in living cells. *Biosens Bioelectron* **2017**, *94*, 536–543.

100. Guo, Z.; Zhu, W.; Tian, H. Dicyanomethylene-4H-pyran chromophores for OLED emitters, logic gates and optical chemosensors. *Chem Commun (Camb)* **2012**, *48* (49), 6073–6084.

101. Guo, Z.; Zhu, W.; Tian, H. Hydrophilic Copolymer Bearing Dicyanomethylene-4H-pyran Moiety As Fluorescent Film Sensor for Cu²⁺ and Pyrophosphate Anion. *Macromolecules* **2009**, *43* (2), 739–744.
102. Chandaroy, P.; Sen, A.; Hui, S. W. Temperature-controlled content release from liposomes encapsulating Pluronic F127. *Journal of Controlled Release* **2001**, *76* (1-2), 27–37.
103. Chen, D.; Xia, D.; Li, X.; Zhu, Q.; Yu, H.; Zhu, C.; Gan, Y. Comparative study of Pluronic((R)) F127-modified liposomes and chitosan-modified liposomes for mucus penetration and oral absorption of cyclosporine A in rats. *Int J Pharm* **2013**, *449* (1-2), 1–9.
104. Singha, S.; Kim, D.; Roy, B.; Sambasivan, S.; Moon, H.; Rao, A. S.; Kim, J. Y.; Joo, T.; Park, J. W.; Rhee, Y. M.; et al. A structural remedy toward bright dipolar fluorophores in aqueous media. *Chem Sci* **2015**, *6* (7), 4335–4342.
105. Kim, D.; Ryu, H. G.; Ahn, K. H. Recent development of two-photon fluorescent probes for bioimaging. *Org Biomol Chem* **2014**, *12* (26), 4550–4566.
106. Ipuý, M.; Liao, Y.-Y.; Jeanneau, E.; Baldeck, P. L.; Bretonnière, Y.; Andraud, C. Solid state red biphotonic excited emission from small dipolar fluorophores. *Journal of Materials Chemistry C* **2016**, *4* (4), 766–779.
107. Kim, H. M.; Cho, B. R. Small-molecule two-photon probes for bioimaging applications. *Chem Rev* **2015**, *115* (11), 5014–5055.
108. Yang, Z.; Cao, J.; He, Y.; Yang, J. H.; Kim, T.; Peng, X.; Kim, J. S. Macro-

/micro-environment-sensitive chemosensing and biological imaging. *Chem Soc Rev* **2014**, *43* (13), 4563–4601.

109. Kim, D.; Moon, H.; Baik, S. H.; Singha, S.; Jun, Y. W.; Wang, T.; Kim, K. H.; Park, B. S.; Jung, J.; Mook-Jung, I.; et al. Two-Photon Absorbing Dyes with Minimal Autofluorescence in Tissue Imaging: Application to in Vivo Imaging of Amyloid-beta Plaques with a Negligible Background Signal. *J Am Chem Soc* **2015**, *137* (21), 6781–6789.

110. Chen, X.; Wang, F.; Hyun, J. Y.; Wei, T.; Qiang, J.; Ren, X.; Shin, I.; Yoon, J. Recent progress in the development of fluorescent, luminescent and colorimetric probes for detection of reactive oxygen and nitrogen species. *Chem Soc Rev* **2016**, *45* (10), 2976–3016.

111. Tang, Y.; Ma, Y.; Yin, J.; Lin, W. Strategies for designing organic fluorescent probes for biological imaging of reactive carbonyl species. *Chem Soc Rev* **2019**, *48* (15), 4036–4048.

112. Hu, R.; Leung, N. L.; Tang, B. Z. AIE macromolecules: syntheses, structures and functionalities. *Chem Soc Rev* **2014**, *43* (13), 4494–4562.

113. Cao, D.; Liu, Z.; Verwilt, P.; Koo, S.; Jangjili, P.; Kim, J. S.; Lin, W. Coumarin-Based Small-Molecule Fluorescent Chemosensors. *Chem Rev* **2019**, *119* (18), 10403–10519.

114. Shindy, H. A. Fundamentals in the chemistry of cyanine dyes: A review. *Dyes and Pigments* **2017**, *145*, 505–513.

115. Slama-Schwok, A.; Blanchard-Desce, M.; Lehn, J. M. Intramolecular charge transfer in donor-acceptor molecules. *The Journal of Physical Chemistry* **2002**, *94* (10), 3894–3902.
116. Moon, H.; Xuan, Q. P.; Kim, D.; Kim, Y.; Park, J. W.; Lee, C. H.; Kim, H.-J.; Kawamata, A.; Park, S. Y.; Ahn, K. H. Molecular-Shape-Dependent Luminescent Behavior of Dye Aggregates: Bent versus Linear Benzocoumarins. *Crystal Growth & Design* **2014**, *14* (12), 6613–6619.
117. Mei, J.; Leung, N. L.; Kwok, R. T.; Lam, J. W.; Tang, B. Z. Aggregation-Induced Emission: Together We Shine, United We Soar! *Chem Rev* **2015**, *115* (21), 11718–11940.
118. Wu, W.; Mao, D.; Xu, S.; Ji, S.; Hu, F.; Ding, D.; Kong, D.; Liu, B. High performance photosensitizers with aggregation-induced emission for image-guided photodynamic anticancer therapy. *Materials Horizons* **2017**, *4* (6), 1110–1114.
119. Zhang, Y.; Wang, Y.; Wang, J.; Liang, X.-J. Improved pharmaceutical research and development with AIE-based nanostructures. *Materials Horizons* **2018**, *5* (5), 799–812.
120. Jung, Y.; Kim, Y.; Kim, N. H.; Lee, J.; Kim, K.-H.; Jung, J.; Huh, Y.; Jang, H.-J.; Joo, J.; Park, S.; et al. A wavelength-tunable and facilely functionable D-A type naphthalene core skeleton: Synthesis, photophysical property, and bio-imaging applications for cells and tissues. *Dyes and Pigments* **2019**, *162*, 104–111.
121. Kim, D.; Baik, S. H.; Kang, S.; Cho, S. W.; Bae, J.; Cha, M. Y.; Sailor, M. J.;

Mook-Jung, I.; Ahn, K. H. Close Correlation of Monoamine Oxidase Activity with Progress of Alzheimer's Disease in Mice, Observed by in Vivo Two-Photon Imaging. *ACS Cent Sci* **2016**, *2* (12), 967–975.

122. Jung, Y.; Park, N. K.; Kang, S.; Huh, Y.; Jung, J.; Hur, J. K.; Kim, D. Latent turn-on fluorescent probe for the detection of toxic malononitrile in water and its practical applications. *Anal Chim Acta* **2020**, *1095*, 154–161.

123. Jung, Y.; Kim, D. A Selective Fluorescence Turn-On Probe for the Detection of DCNP (Nerve Agent Tabun Simulant). *Materials (Basel)* **2019**, *12* (18).

124. Jung, Y.; Park, N. K.; Kang, J. S.; Kim, D. Hydrazine-Selective Fluorescent Turn-On Probe Based on Ortho-Methoxy-Methyl-Ether (o-MOM) Assisted Retro-aza-Henry Type Reaction. *Sensors (Basel)* **2019**, *19* (20).

125. La, D. D.; Bhosale, S. V.; Jones, L. A.; Bhosale, S. V. Tetraphenylethylene-Based AIE-Active Probes for Sensing Applications. *ACS Appl Mater Interfaces* **2018**, *10* (15), 12189–12216.

126. Zhang, Z.; Yu, Y.; Zhao, Y.; Ng, K. M. A fluorescent nanoparticle probe based on sugar-substituted tetraphenylethene for label-free detection of galectin-3. *J Mater Chem B* **2019**, *7* (43), 6737–6741.

127. Lin, N.; Ren, W.; Hu, J.; Gao, B.; Yuan, D.; Wang, X.; Fu, J. A novel tetraphenylethene-based fluorescent sensor for uranyl ion detection with aggregation-induced emission character. *Dyes and Pigments* **2019**, *166*, 182–188.

128. Kim, D.; Xuan, Q. P.; Moon, H.; Jun, Y. W.; Ahn, K. H. Synthesis of

Benzocoumarins and Characterization of Their Photophysical Properties. *Asian Journal of Organic Chemistry* **2014**, 3 (10), 1089–1096.

129. Jones, G. A.; Bradshaw, D. S. Resonance Energy Transfer: From Fundamental Theory to Recent Applications. *Frontiers in Physics* **2019**, 7.

130. Frisch, M. J.; Schlegel, H. B.; Scuseria, G. E.; Robb, M. A.; Cheeseman, J. R.; Scalmani, G.; Barone, V.; Petersson, G. A.; Nakatsuji, H.; Li, X.; et al. *Gaussian 16, Revision B.01*; Gaussian, Inc.: Wallingford, CT, USA, 2016.

131. Chivasa, S. Insights into Plant Extracellular ATP Signaling Revealed by the Discovery of an ATP-Regulated Transcription Factor. *Plant Cell Physiol* **2020**, 61 (4), 673–674.

132. Jin, M. Unique roles of tryptophanyl-tRNA synthetase in immune control and its therapeutic implications. *Exp Mol Med* **2019**, 51 (1), 1–10.

133. Trautmann, A. Extracellular ATP in the immune system: more than just a "danger signal". *Sci Signal* **2009**, 2 (56), pe6

134. Bennett, N. K.; Nguyen, M. K.; Darch, M. A.; Nakaoka, H. J.; Cousineau, D.; Ten Hoeve, J.; Graeber, T. G.; Schuelke, M.; Maltepe, E.; Kampmann, M.; et al. Defining the ATPome reveals cross-optimization of metabolic pathways. *Nat Commun* **2020**, 11 (1), 4319.

135. Camandola, S.; Mattson, M. P. Brain metabolism in health, aging, and neurodegeneration. *EMBO J* **2017**, 36 (11), 1474–1492.

136. Depaoli, M. R.; Karsten, F.; Madreiter-Sokolowski, C. T.; Klec, C.; Gottschalk, B.; Bischof, H.; Eroglu, E.; Waldeck-Weiermair, M.; Simmen, T.; Graier, W. F.; et al. Real-Time Imaging of Mitochondrial ATP Dynamics Reveals the Metabolic Setting of Single Cells. *Cell Rep* **2018**, *25* (2), 501-512 e503.
137. Yin, S.; Loo, J. A. Elucidating the site of protein-ATP binding by top-down mass spectrometry. *J Am Soc Mass Spectrom* **2010**, *21* (6), 899–907.
138. Tian, Y.-F.; Zhou, W.; Yin, B.-C.; Ye, B.-C. Highly sensitive surface-enhanced Raman scattering detection of adenosine triphosphate based on core–satellite assemblies. *Analytical Methods* **2017**, *9* (42), 6038–6043.
139. Rajendran, M.; Dane, E.; Conley, J.; Tantama, M. Imaging Adenosine Triphosphate (ATP). *Biol Bull* **2016**, *231* (1), 73–84.
140. Hattori, K.; Kajimura, M.; Hishiki, T.; Nakanishi, T.; Kubo, A.; Nagahata, Y.; Ohmura, M.; Yachie-Kinoshita, A.; Matsuura, T.; Morikawa, T.; et al. Paradoxical ATP elevation in ischemic penumbra revealed by quantitative imaging mass spectrometry. *Antioxid Redox Signal* **2010**, *13* (8), 1157–1167.
141. Shi, C. A.; Zhang, X.; Yin, H. J.; Fang, H.; Zhao, Y. M.; Liu, L.; Wu, Z. L.; Xu, H. J. A novel ATP quantification method combining glucose phosphorylation with surface-enhanced Raman scattering. *Sensors and Actuators B: Chemical* **2017**, *241*, 855–859.
142. Karrasch, S.; Walker, J. E. Novel features in the structure of bovine ATP synthase. *J Mol Biol* **1999**, *290* (2), 379–384.

143. Saha, B.; Chatterjee, A.; Reja, A.; Das, D. Condensates of short peptides and ATP for the temporal regulation of cytochrome c activity. *Chem Commun (Camb)* **2019**, *55* (94), 14194–14197.
144. Lee, M. H.; Kim, J. S.; Sessler, J. L. Small molecule-based ratiometric fluorescence probes for cations, anions, and biomolecules. *Chem Soc Rev* **2015**, *44* (13), 4185–4191.
145. Chen, X.; Pradhan, T.; Wang, F.; Kim, J. S.; Yoon, J. Fluorescent chemosensors based on spiroring-opening of xanthenes and related derivatives. *Chem Rev* **2012**, *112* (3), 1910–1956.
146. Wu, X.; Li, Z.; Chen, X. X.; Fossey, J. S.; James, T. D.; Jiang, Y. B. Selective sensing of saccharides using simple boronic acids and their aggregates. *Chem Soc Rev* **2013**, *42* (20), 8032–8048.
147. An, J. M.; Kang, S.; Huh, E.; Kim, Y.; Lee, D.; Jo, H.; Joung, J. F.; Kim, V. J.; Lee, J. Y.; Dho, Y. S.; et al. Penta-fluorophenol: a Smiles rearrangement-inspired cysteine-selective fluorescent probe for imaging of human glioblastoma. *Chem Sci* **2020**, *11* (22), 5658–5668.
148. Morciano, G.; Sarti, A. C.; Marchi, S.; Missiroli, S.; Falzoni, S.; Raffaghello, L.; Pistoia, V.; Giorgi, C.; Di Virgilio, F.; Pinton, P. Use of luciferase probes to measure ATP in living cells and animals. *Nat Protoc* **2017**, *12* (8), 1542–1562.
149. Nguyen, D. T.; Kim, H. R.; Jung, J. H.; Lee, K.-B.; Kim, B. C. The development of paper discs immobilized with luciferase/D-luciferin for the detection of ATP from

airborne bacteria. *Sensors and Actuators B: Chemical* **2018**, *260*, 274–281.

150. Lee, M. S.; Park, W. S.; Kim, Y. H.; Ahn, W. G.; Kwon, S. H.; Her, S. Intracellular ATP assay of live cells using PTD-conjugated luciferase. *Sensors (Basel)* **2012**, *12* (11), 15628–15637.

151. Kitajima, N.; Takikawa, K.; Sekiya, H.; Satoh, K.; Asanuma, D.; Sakamoto, H.; Takahashi, S.; Hanaoka, K.; Urano, Y.; Namiki, S.; et al. Real-time in vivo imaging of extracellular ATP in the brain with a hybrid-type fluorescent sensor. *Elife* **2020**, *9*.

152. Berg, J.; Hung, Y. P.; Yellen, G. A genetically encoded fluorescent reporter of ATP:ADP ratio. *Nat Methods* **2009**, *6* (2), 161–166.

153. Lobas, M. A.; Tao, R.; Nagai, J.; Kronschlager, M. T.; Borden, P. M.; Marvin, J. S.; Looger, L. L.; Khakh, B. S. A genetically encoded single-wavelength sensor for imaging cytosolic and cell surface ATP. *Nat Commun* **2019**, *10* (1), 711.

154. Paciello, L.; Falco, F. C.; Landi, C.; Parascandola, P. Strengths and weaknesses in the determination of *Saccharomyces cerevisiae* cell viability by ATP-based bioluminescence assay. *Enzyme Microb Technol* **2013**, *52* (3), 157–162.

155. Kaur, J.; Singh, P. ATP selective acridone based fluorescent probes for monitoring of metabolic events. *Chem Commun (Camb)* **2011**, *47* (15), 4472–4474.

156. Tan, K. Y.; Li, C. Y.; Li, Y. F.; Fei, J.; Yang, B.; Fu, Y. J.; Li, F. Real-Time Monitoring ATP in Mitochondrion of Living Cells: A Specific Fluorescent Probe for ATP by Dual Recognition Sites. *Anal Chem* **2017**, *89* (3), 1749–1756.

157. Jun, Y. W.; Wang, T.; Hwang, S.; Kim, D.; Ma, D.; Kim, K. H.; Kim, S.; Jung, J.; Ahn, K. H. A Ratiometric Two-Photon Fluorescent Probe for Tracking Lysosomal ATP: Direct In Cellulo Observation of Lysosomal Membrane Fusion Processes. *Angewandte Chemie* **2018**, *130* (32), 10299–10304.
158. de la Fuente-Herreruela, D.; Gonzalez-Charro, V.; Almendro-Vedia, V. G.; Moran, M.; Martin, M. A.; Lillo, M. P.; Natale, P.; Lopez-Montero, I. Rhodamine-based sensor for real-time imaging of mitochondrial ATP in living fibroblasts. *Biochim Biophys Acta Bioenerg* **2017**, *1858* (12), 999–1006.
159. Ren, T. B.; Wen, S. Y.; Wang, L.; Lu, P.; Xiong, B.; Yuan, L.; Zhang, X. B. Engineering a Reversible Fluorescent Probe for Real-Time Live-Cell Imaging and Quantification of Mitochondrial ATP. *Anal Chem* **2020**, *92* (6), 4681–4688.
160. Tang, J. L.; Li, C. Y.; Li, Y. F.; Zou, C. X. A ratiometric fluorescent probe with unexpected high selectivity for ATP and its application in cell imaging. *Chem Commun (Camb)* **2014**, *50* (97), 15411–15414.
161. Tikum, A. F.; Kim, G.; Nasirian, A.; Ko, J. W.; Yoon, J.; Kim, J. Rhodamine-based near-infrared probe for emission detection of ATP in lysosomes in living cells. *Sensors and Actuators B: Chemical* **2019**, *292*, 40–47.
162. Liu, Y.; Lee, D.; Wu, D.; Swamy, K. M. K.; Yoon, J. A new kind of rhodamine-based fluorescence turn-on probe for monitoring ATP in mitochondria. *Sensors and Actuators B: Chemical* **2018**, *265*, 429–434.
163. Li, C. Y.; Zou, C. X.; Li, Y. F.; Kong, X. F.; Zhou, Y.; Wu, Y. S.; Zhu, W. G.

A colormetric and fluorescent chemosensor for adenosine-5'-triphosphate based on rhodamine derivative. *Anal Chim Acta* **2013**, 795, 69–74.

164. Farshbaf, S.; Anzenbacher, P. Fluorimetric sensing of ATP in water by an imidazolium hydrazone based sensor. *Chem Commun (Camb)* **2019**, 55 (12), 1770–1773.

165. Huang, B. H.; Geng, Z. R.; Ma, X. Y.; Zhang, C.; Zhang, Z. Y.; Wang, Z. L. Lysosomal ATP imaging in living cells by a water-soluble cationic polythiophene derivative. *Biosens Bioelectron* **2016**, 83, 213–220.

166. Srivastava, P.; Razi, S. S.; Ali, R.; Srivastav, S.; Patnaik, S.; Srikrishna, S.; Misra, A. Highly sensitive cell imaging "Off-On" fluorescent probe for mitochondria and ATP. *Biosens Bioelectron* **2015**, 69, 179–185.

167. Xu, Z.; Singh, N. J.; Lim, J.; Pan, J.; Kim, H. N.; Park, S.; Kim, K. S.; Yoon, J. Unique sandwich stacking of pyrene-adenine-pyrene for selective and ratiometric fluorescent sensing of ATP at physiological pH. *J Am Chem Soc* **2009**, 131 (42), 15528–15533.

168. Xu, Z.; Song, N. R.; Moon, J. H.; Lee, J. Y.; Yoon, J. Bis- and tris-naphthoimidazolium derivatives for the fluorescent recognition of ATP and GTP in 100% aqueous solution. *Org Biomol Chem* **2011**, 9 (24), 8340–8345.

169. Wang, L.; Yuan, L.; Zeng, X.; Peng, J.; Ni, Y.; Er, J. C.; Xu, W.; Agrawalla, B. K.; Su, D.; Kim, B.; et al. A Multisite-Binding Switchable Fluorescent Probe for Monitoring Mitochondrial ATP Level Fluctuation in Live Cells. *Angewandte*

Chemie **2016**, *128* (5), 1805–1808.

170. Liu, L.; Zhao, L.; Cheng, D.; Yao, X.; Lu, Y. Highly Selective Fluorescence Sensing and Imaging of ATP Using a Boronic Acid Groups-Bearing Polythiophene Derivate. *Polymers (Basel)* **2019**, *11* (7).

171. Kanekiyo, Y.; Naganawa, R.; Tao, H. Fluorescence detection of ATP based on the ATP-mediated aggregation of pyrene-appended boronic acid on a polycation. *Chem Commun (Camb)* **2004**, (8), 1006–1007.

172. Rao, A. S.; Kim, D.; Nam, H.; Jo, H.; Kim, K. H.; Ban, C.; Ahn, K. H. A turn-on two-photon fluorescent probe for ATP and ADP. *Chem Commun (Camb)* **2012**, *48* (26), 3206–3208.

173. Kurishita, Y.; Kohira, T.; Ojida, A.; Hamachi, I. Organelle-localizable fluorescent chemosensors for site-specific multicolor imaging of nucleoside polyphosphate dynamics in living cells. *J Am Chem Soc* **2012**, *134* (45), 18779–18789.

174. Patra, C.; Sen, C.; Mahapatra, A. D.; Chattopadhyay, D.; Mahapatra, A.; Sinha, C. Pyridylthioether-hydroxycoumarin Schiff base as selective Zn²⁺ fluorescence sensor, application in life cell imaging and uses of resulting complex as secondary probe for ATP sensing. *Journal of Photochemistry and Photobiology A: Chemistry* **2017**, *341*, 97–107.

175. Jose, D. A.; Mishra, S.; Ghosh, A.; Shrivastav, A.; Mishra, S. K.; Das, A. Colorimetric sensor for ATP in aqueous solution. *Org Lett* **2007**, *9* (10), 1979–1982.

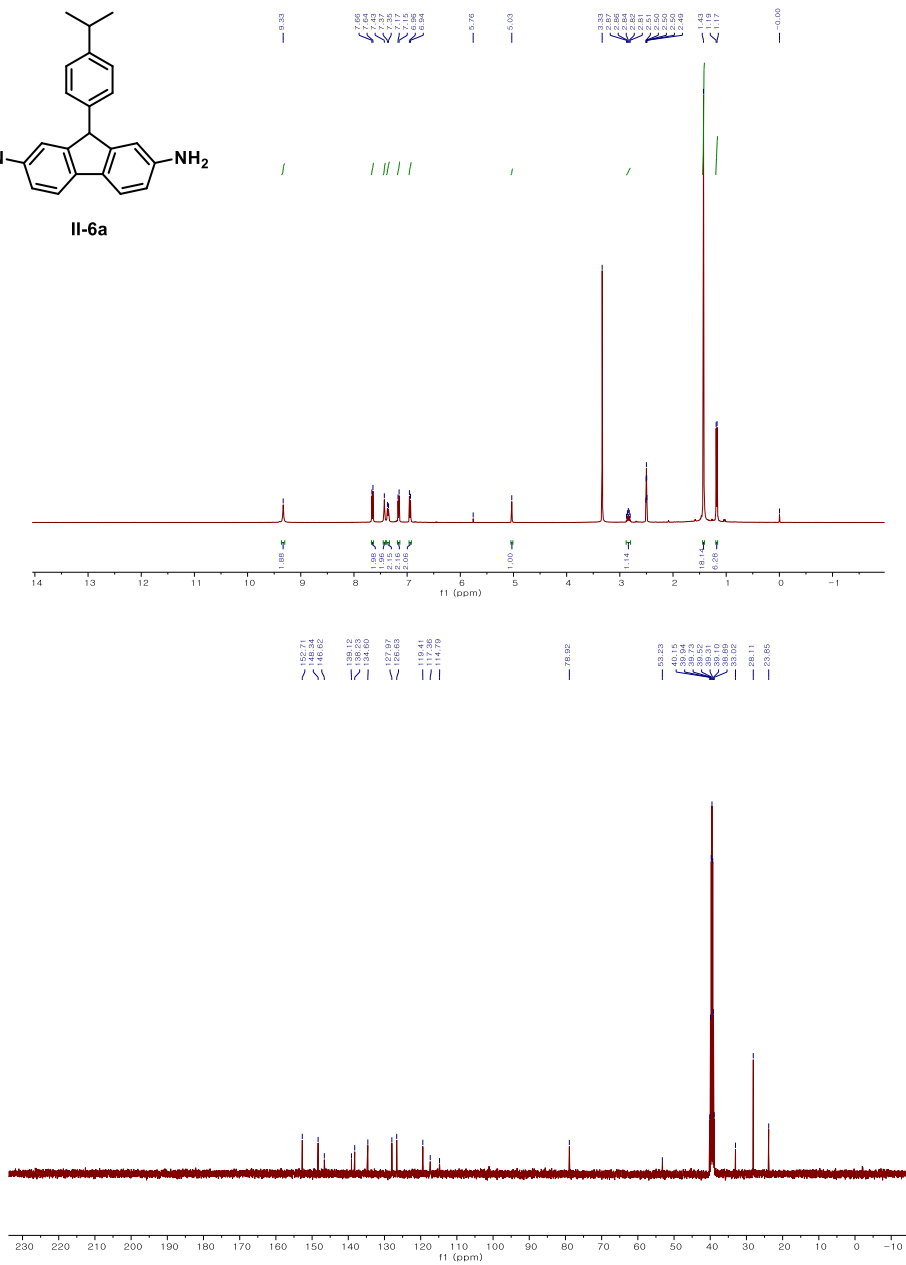
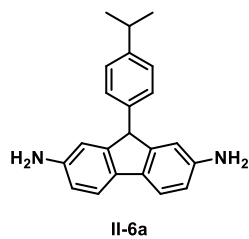
176. Leung, K. H.; Lu, L.; Wang, M.; Mak, T. Y.; Chan, D. S.; Tang, F. K.; Leung, C. H.; Kwan, H. Y.; Yu, Z.; Ma, D. L. A label-free luminescent switch-on assay for ATP using a G-quadruplex-selective iridium(III) complex. *PLoS One* **2013**, *8* (10), e77021.
177. Zhang, X.; Jiang, Y.; Xiao, N. Monitoring ADP and ATP in vivo using a fluorescent Ga(III)-probe complex. *Chem Commun (Camb)* **2018**, *54* (91), 12812–12815.
178. Ma, H.; Yang, M.; Zhang, C.; Ma, Y.; Qin, Y.; Lei, Z.; Chang, L.; Lei, L.; Wang, T.; Yang, Y. Aggregation-induced emission (AIE)-active fluorescent probes with multiple binding sites toward ATP sensing and live cell imaging. *J Mater Chem B* **2017**, *5* (43), 8525–8531.
179. Tao, H.; He, L.; Cheng, G.; Cao, Q.-Y. Linear tetraphenylethene-appended bis-imidazolium salts for sensing of ATP. *Dyes and Pigments* **2019**, *166*, 233–238.
180. Ding, A.-X.; Shi, Y.-D.; Zhang, K.-X.; Sun, W.; Tan, Z.-L.; Lu, Z.-L.; He, L. Self-assembled aggregation-induced emission micelle (AIE micelle) as interfacial fluorescence probe for sequential recognition of Cu²⁺ and ATP in water. *Sensors and Actuators B: Chemical* **2018**, *255*, 440–447.
181. Noguchi, T.; Shiraki, T.; Dawn, A.; Tsuchiya, Y.; Lien le, T. N.; Yamamoto, T.; Shinkai, S. Nonlinear fluorescence response driven by ATP-induced self-assembly of guanidinium-tethered tetraphenylethene. *Chem Commun (Camb)* **2012**, *48* (65), 8090–8092.

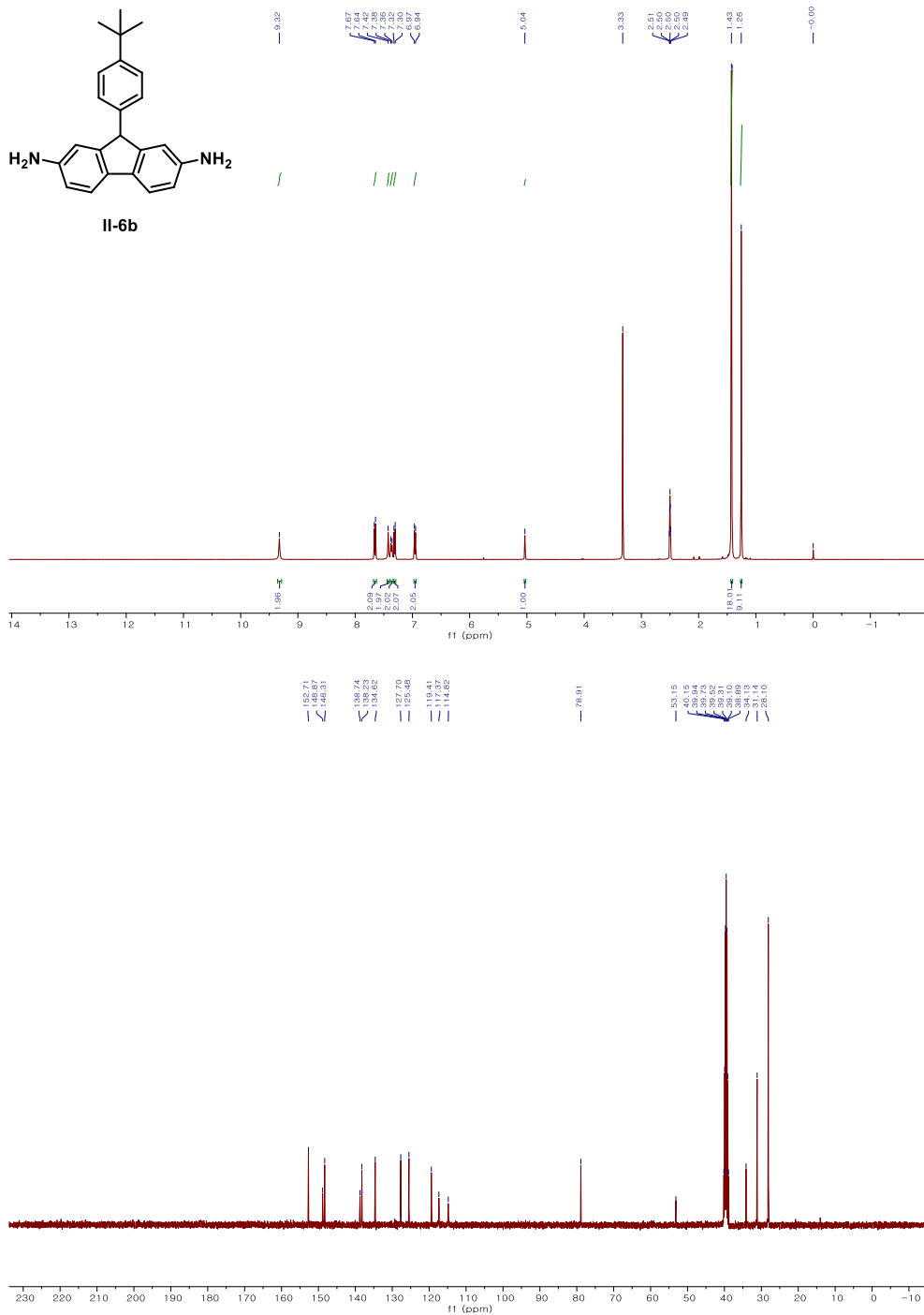
182. Jiang, S.; Qiu, J.; Chen, S.; Guo, H.; Yang, F. Double-detecting fluorescent sensor for ATP based on Cu(2+) and Zn(2+) response of hydrazono-bis-tetraphenylethylene. *Spectrochim Acta A Mol Biomol Spectrosc* **2020**, *227*, 117568.
183. Kim, N. H.; Won, M.; Kim, J. S.; Huh, Y.; Kim, D. A highly sensitive and fast responsive fluorescent probe for detection of Gold(III) ions based on the AIEgen disaggregation. *Dyes and Pigments* **2019**, *160*, 647–653.
184. Hong, Y.; Lam, J. W.; Tang, B. Z. Aggregation-induced emission. *Chem Soc Rev* **2011**, *40* (11), 5361–5388.
185. Liu, B.; Tang, B. Z. Themed Issue on Aggregation-Induced Emission (AIE). *Chem Asian J* **2019**, *14* (6), 672–673.
186. Li, H.; Guo, Z.; Xie, W.; Sun, W.; Ji, S.; Tian, J.; Lv, L. A label-free fluorometric aptasensor for adenosine triphosphate (ATP) detection based on aggregation-induced emission probe. *Anal Biochem* **2019**, *578*, 60–65.
187. Storer, A. C.; Cornish-Bowden, A. Concentration of MgATP²⁻ and other ions in solution. Calculation of the true concentrations of species present in mixtures of associating ions. *Biochem J* **1976**, *159* (1), 1–5.
188. Traut, T. W. Physiological concentrations of purines and pyrimidines. *Mol Cell Biochem* **1994**, *140* (1), 1–22.
189. Worby, C. A.; Simonson-Leff, N.; Dixon, J. E. RNA interference of gene expression (RNAi) in cultured Drosophila cells. *Sci STKE* **2001**, *2001* (95), p11.

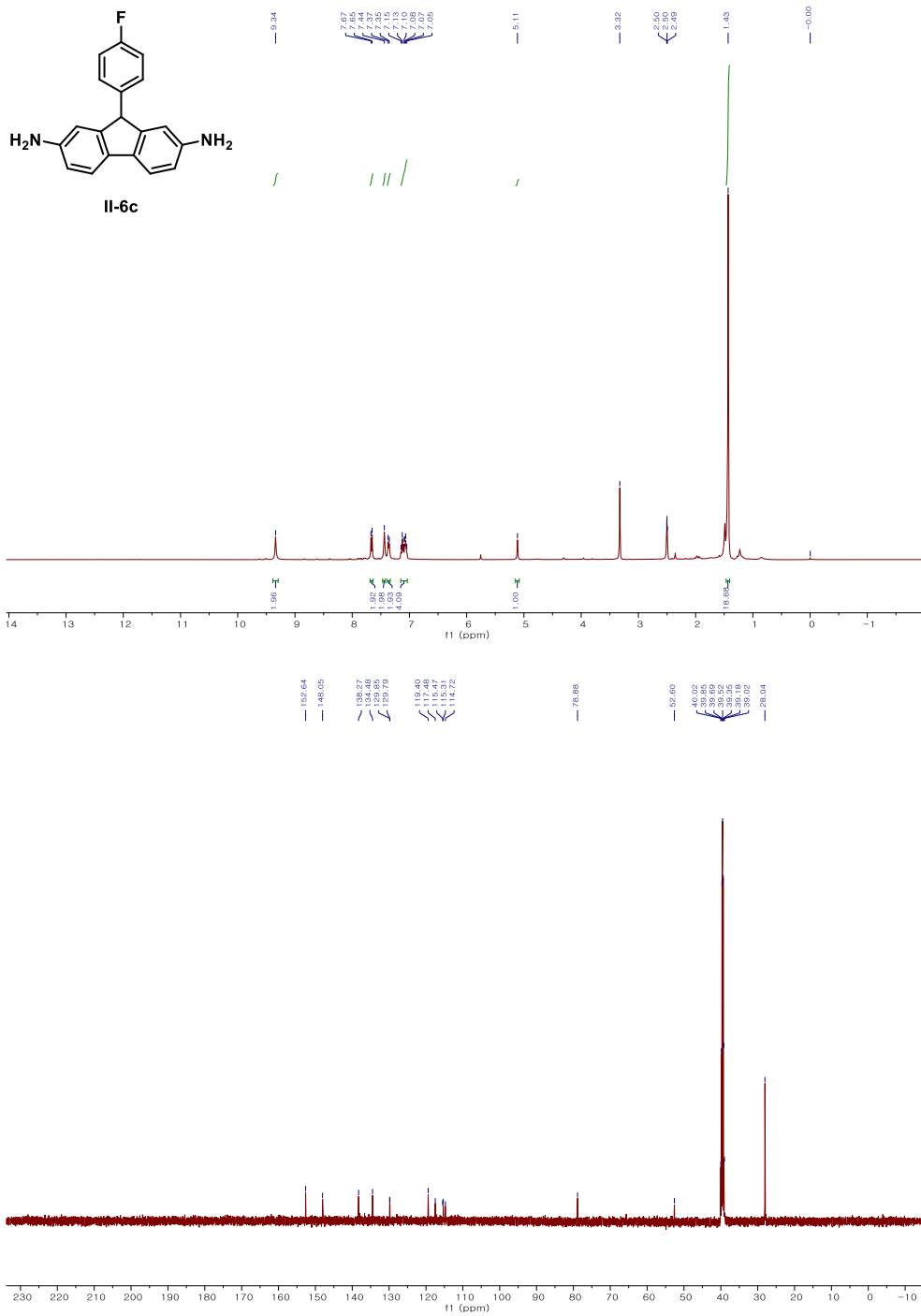
190. Koo, M. J.; Rooney, K. T.; Choi, M. E.; Ryter, S. W.; Choi, A. M.; Moon, J. S. Impaired oxidative phosphorylation regulates necroptosis in human lung epithelial cells. *Biochem Biophys Res Commun* **2015**, *464* (3), 875-880.
191. Gatie, M. I.; Kelly, G. M. Metabolic profile and differentiation potential of extraembryonic endoderm-like cells. *Cell Death Discov* **2018**, *4*, 42.
192. Allam, A.; Dupont, L.; Behr, J.-B.; Plantier-Royon, R. Convenient Synthesis of a Galacturonic Acid Based Macrocyclic with Potential Copper-Complexation Ability. *European Journal of Organic Chemistry* **2012**, *2012* (4), 817–823.
193. Peng, Y.; Zhang, M. M.; Chen, Z. F.; Hu, K.; Liu, Y. C.; Chen, X.; Liang, H. Synthesis, Characterization, and Interaction with Biomolecules of Platinum(II) Complexes with Shikimic Acid-Based Ligands. *Bioinorg Chem Appl* **2013**, *2013*, 565032.
194. Springer, J. B.; Chang, Y. H.; Koo, K. I.; Colvin, O. M.; Colvin, M. E.; Dolan, M. E.; Delaney, S. M.; Flowers, J. L.; Ludeman, S. M. 1,3- vs 1,5-intramolecular alkylation reactions in isophosphoramidate and phosphoramidate mustards. *Chem Res Toxicol* **2004**, *17* (9), 1217–1226.
195. Oh, Y.; Cho, G. S.; Li, Z.; Hong, I.; Zhu, R.; Kim, M. J.; Kim, Y. J.; Tampakakis, E.; Tung, L.; Haganir, R.; et al. Functional Coupling with Cardiac Muscle Promotes Maturation of hPSC-Derived Sympathetic Neurons. *Cell Stem Cell* **2016**, *19* (1), 95-106.

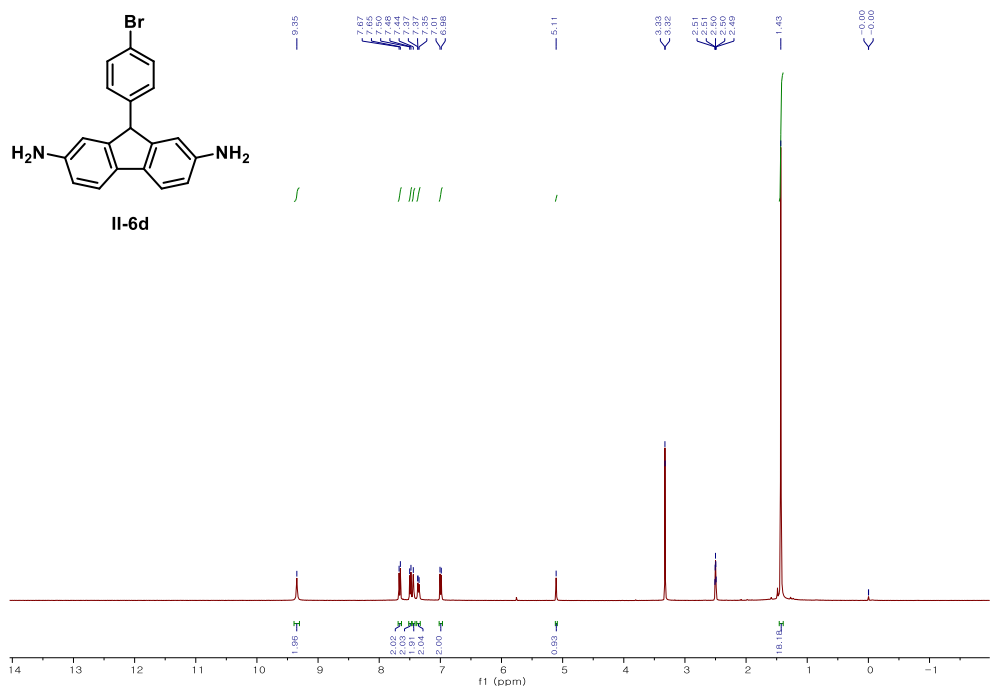
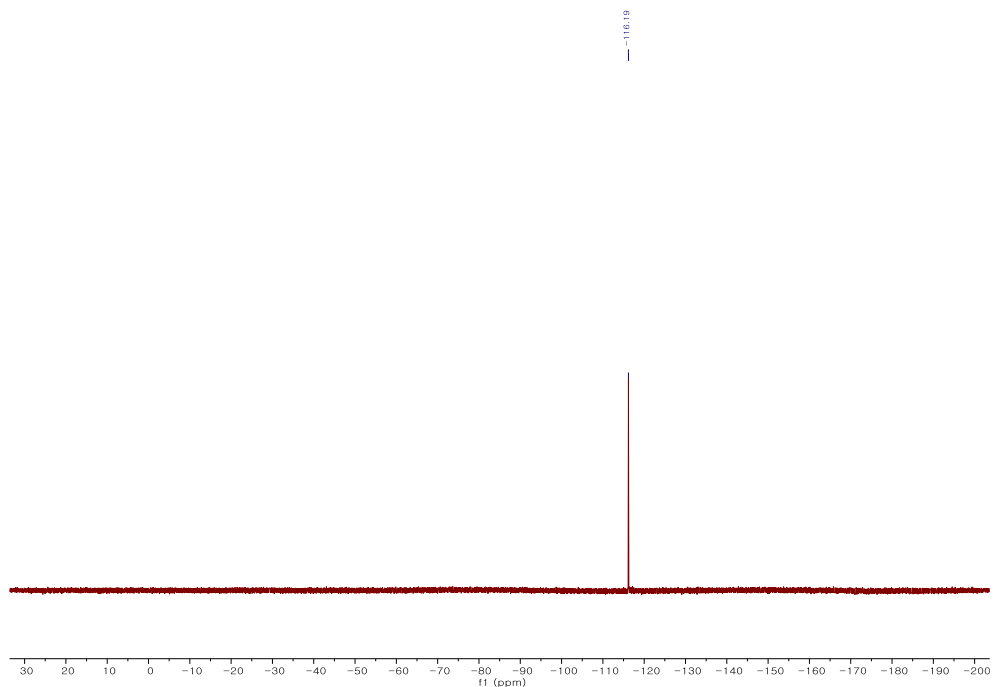
Appendix

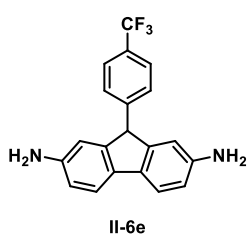
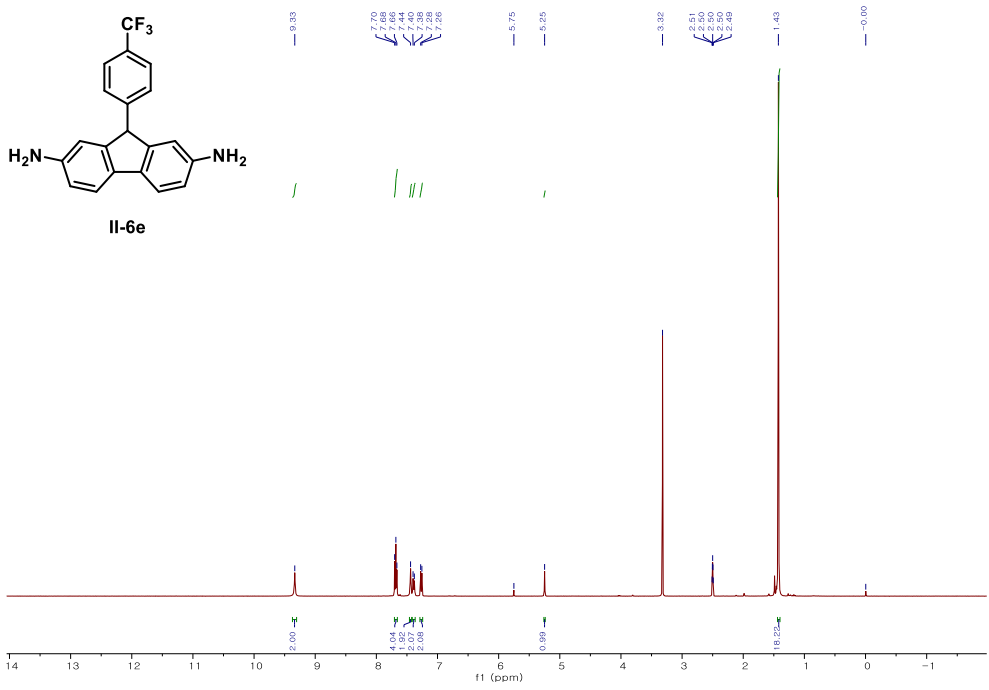
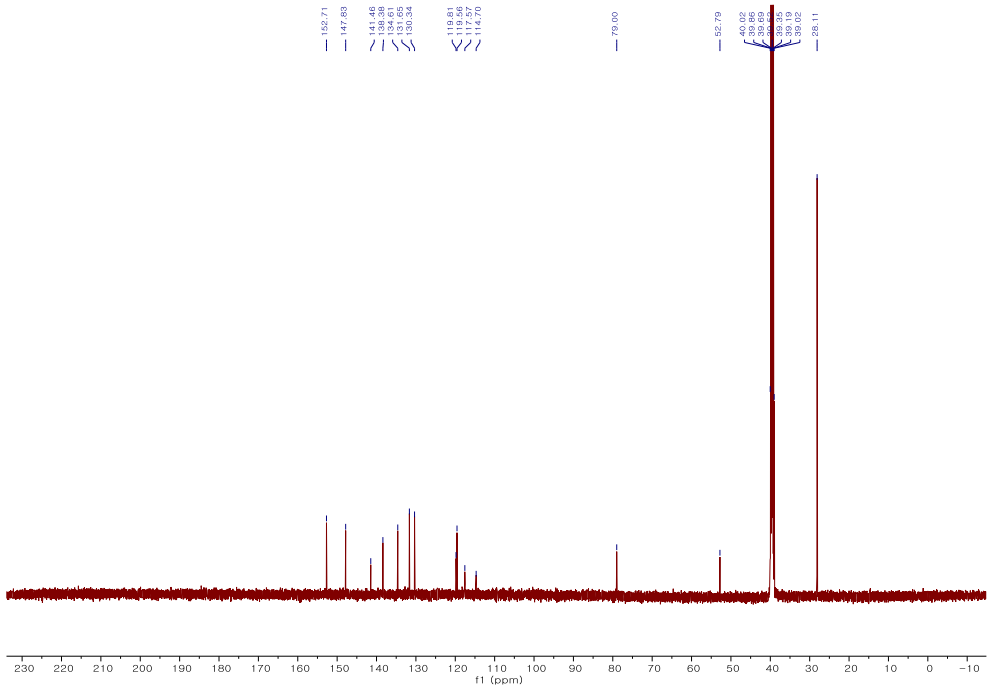
Chapter II

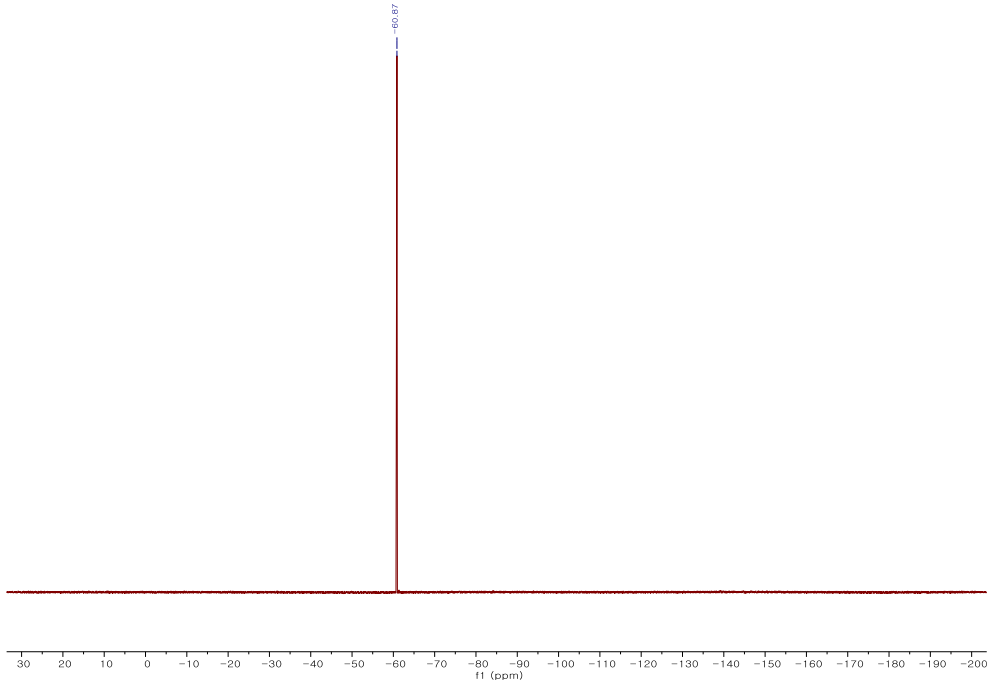
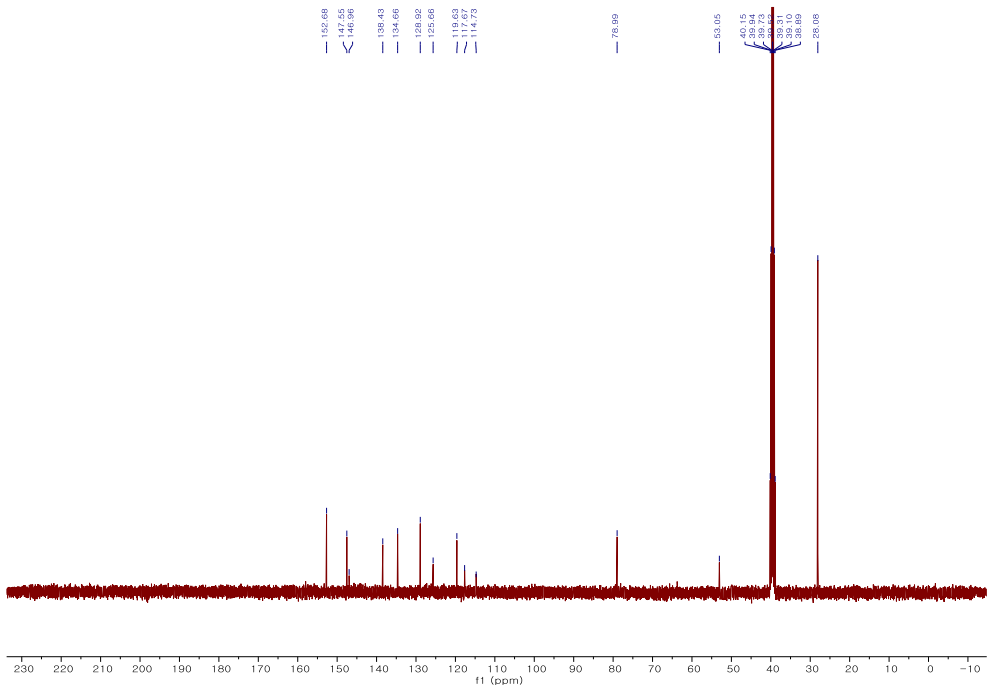


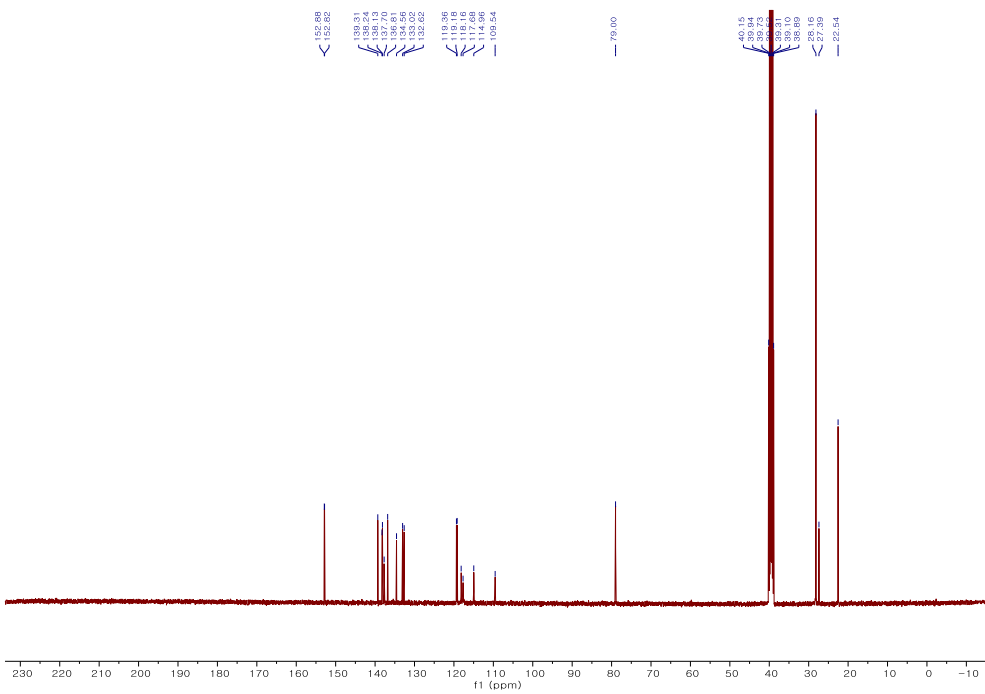
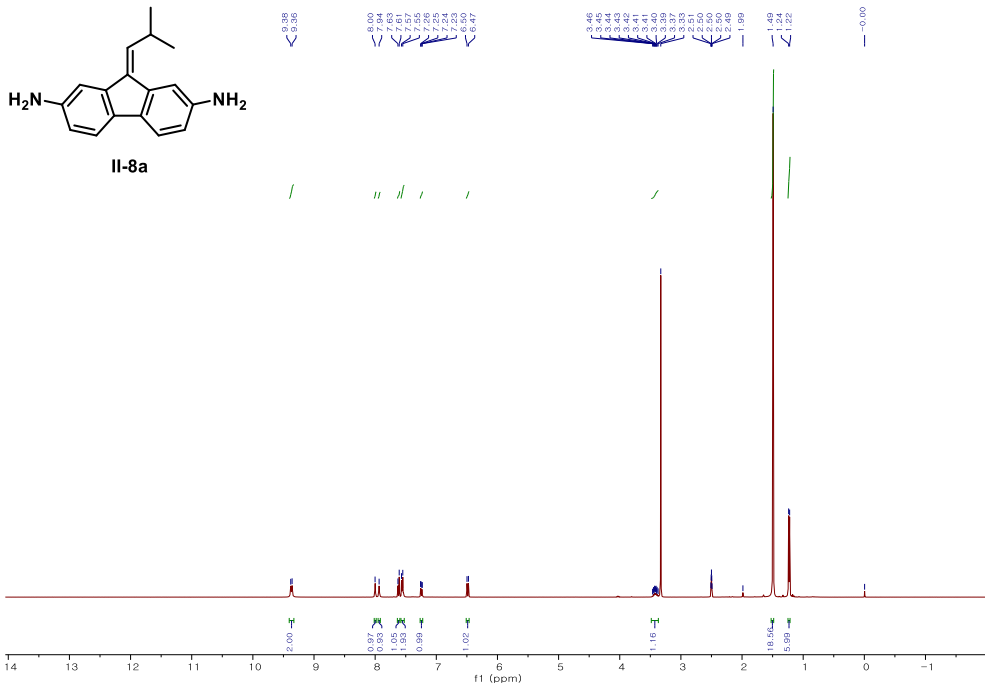


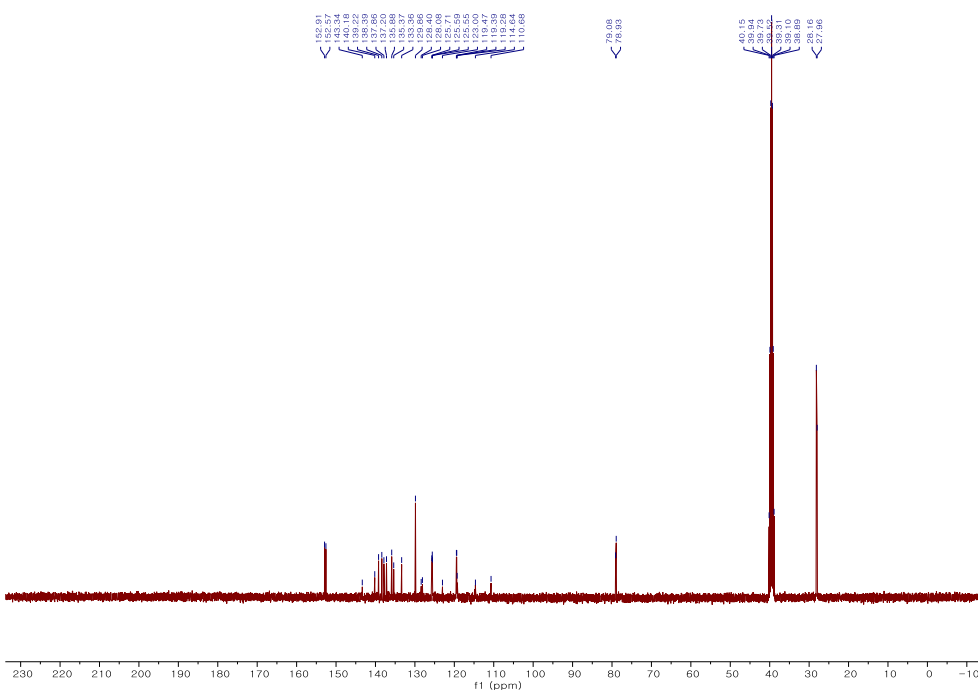
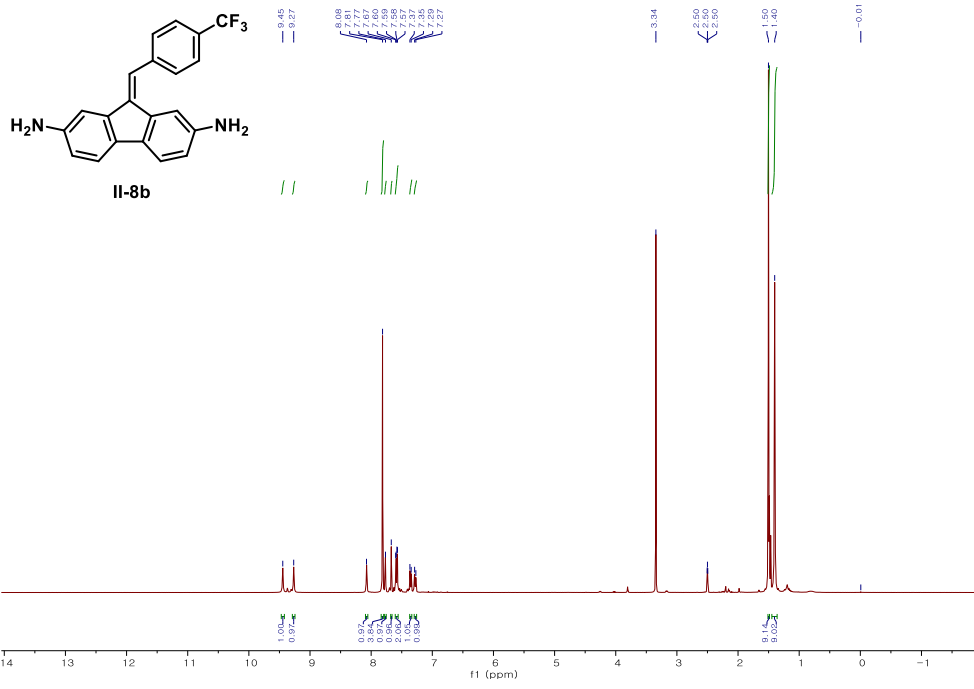


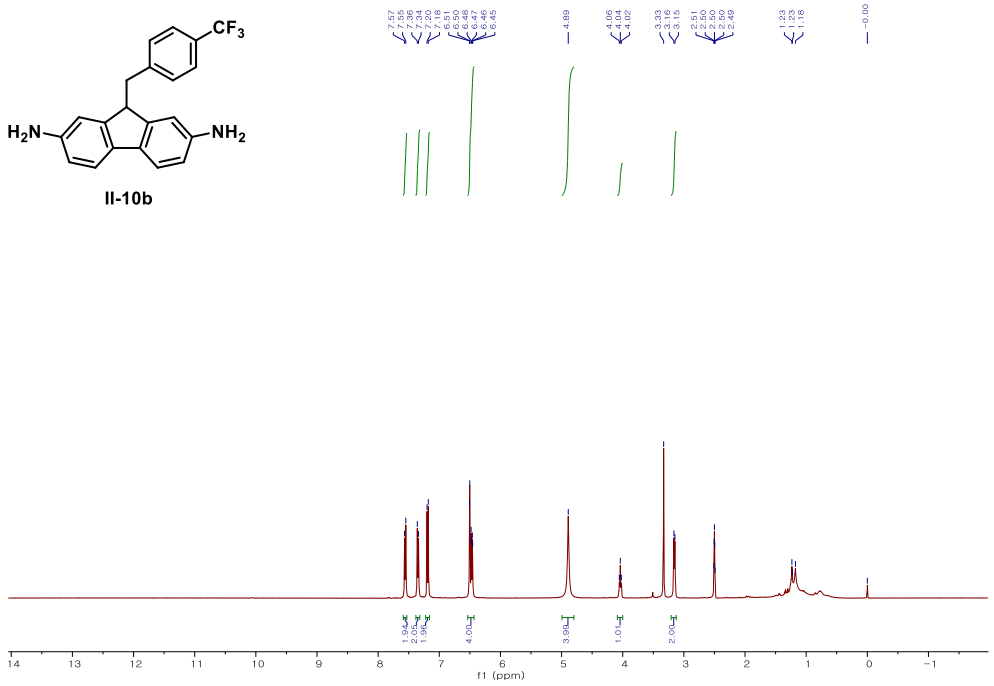
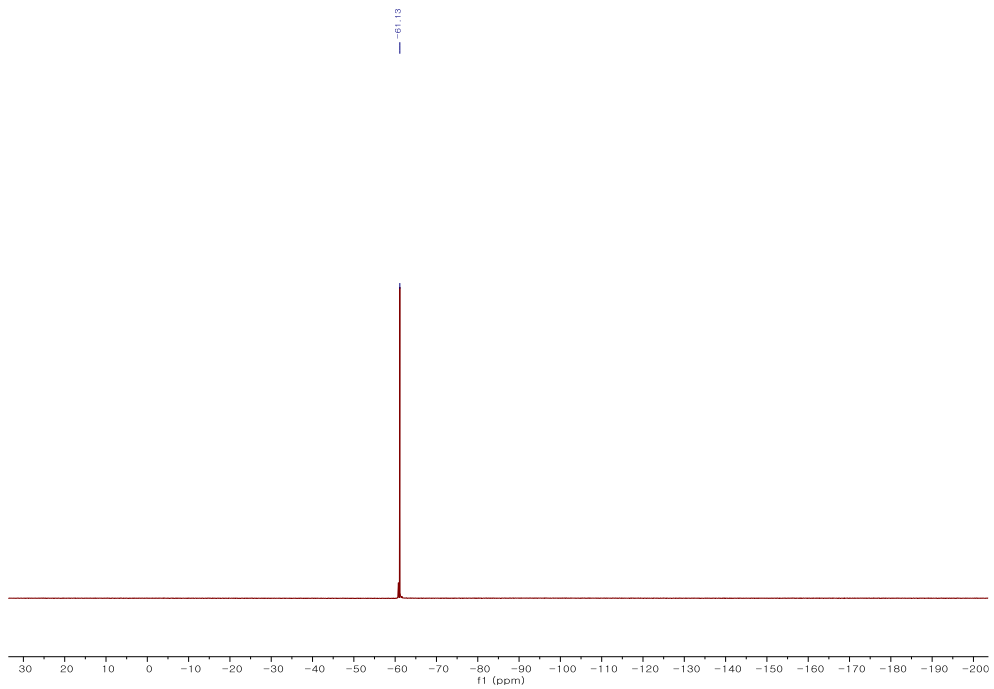


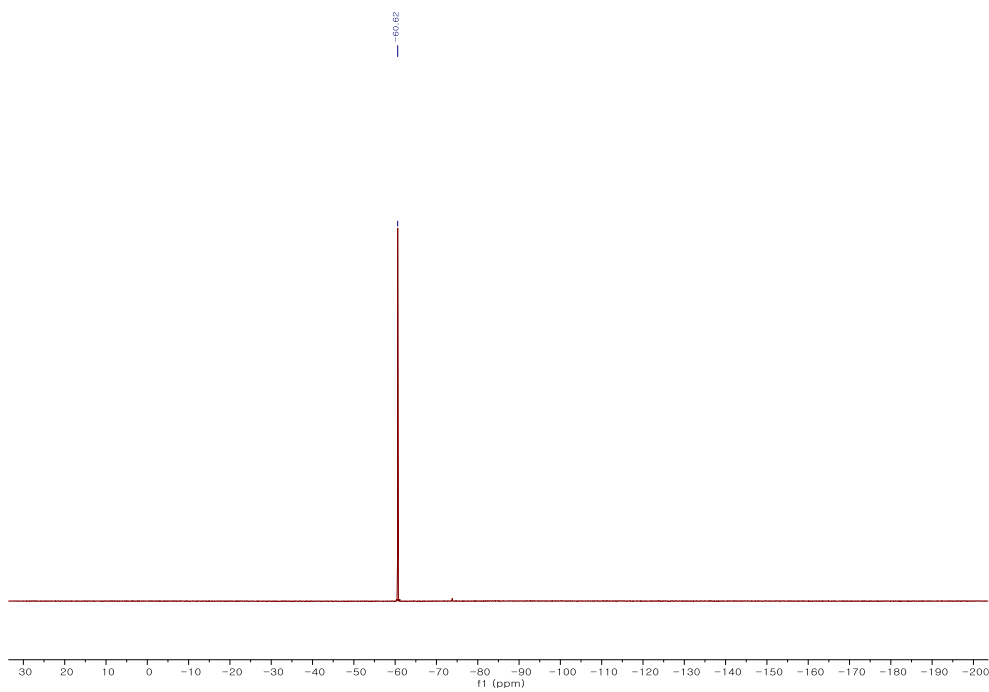
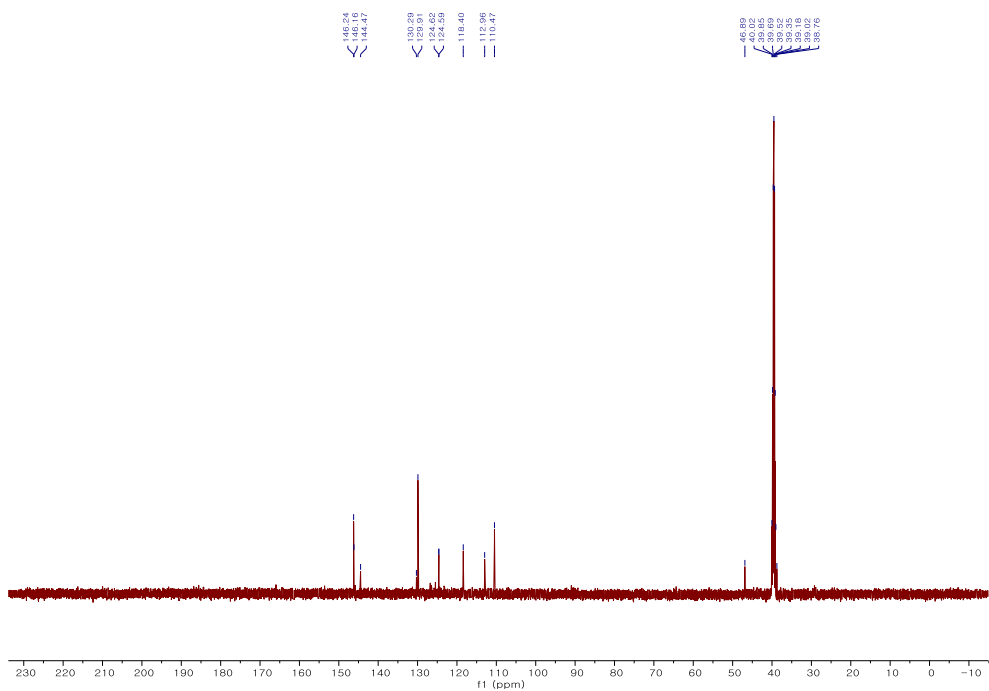


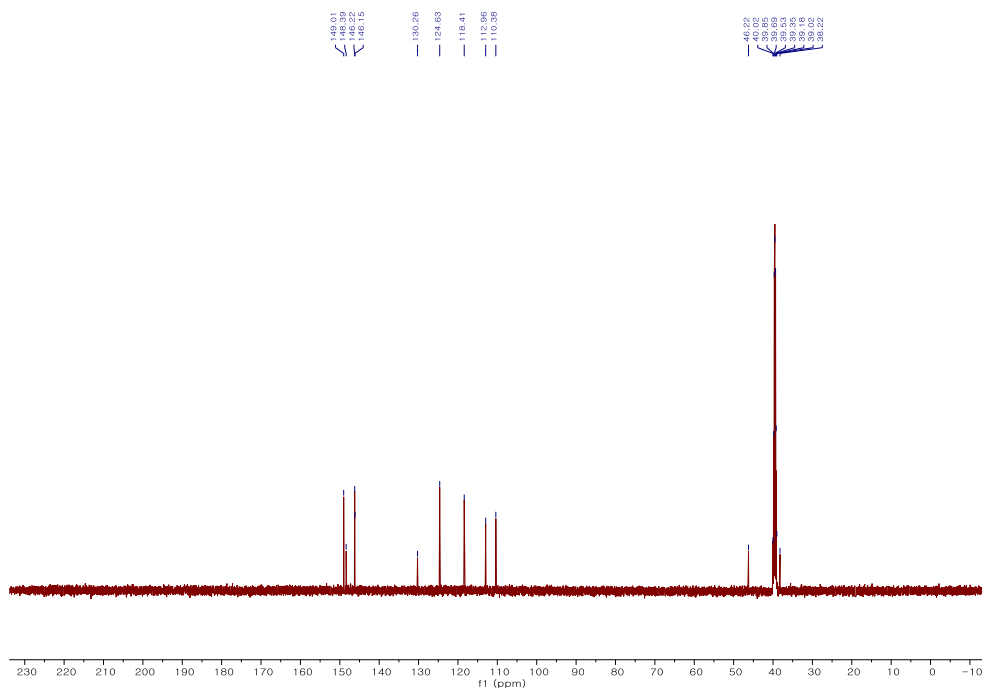
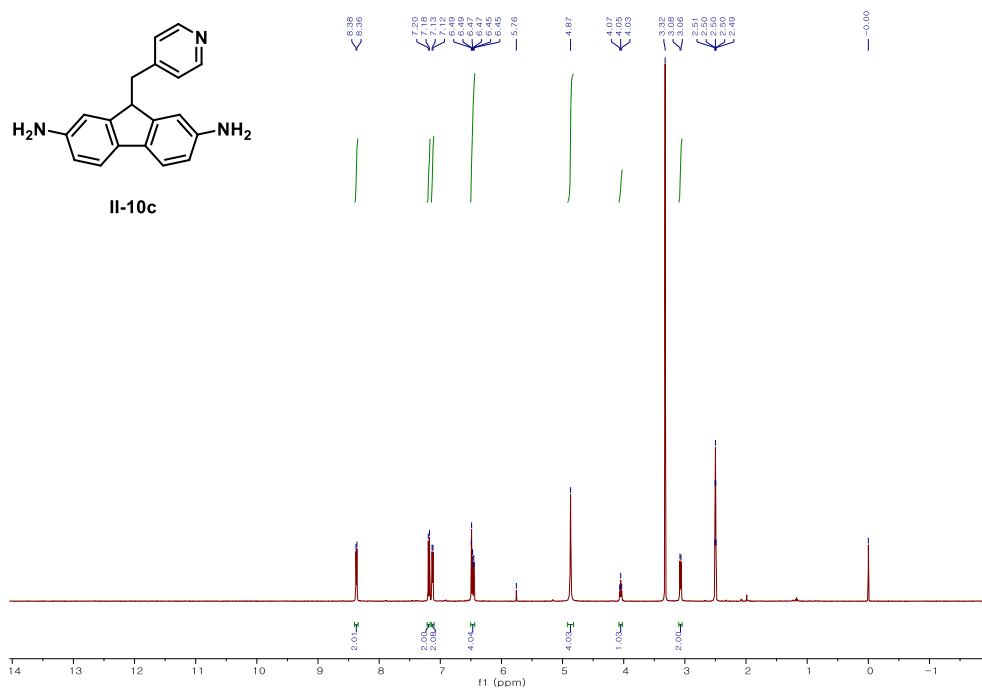
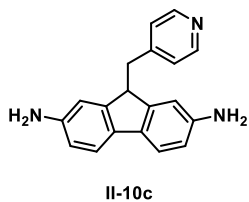


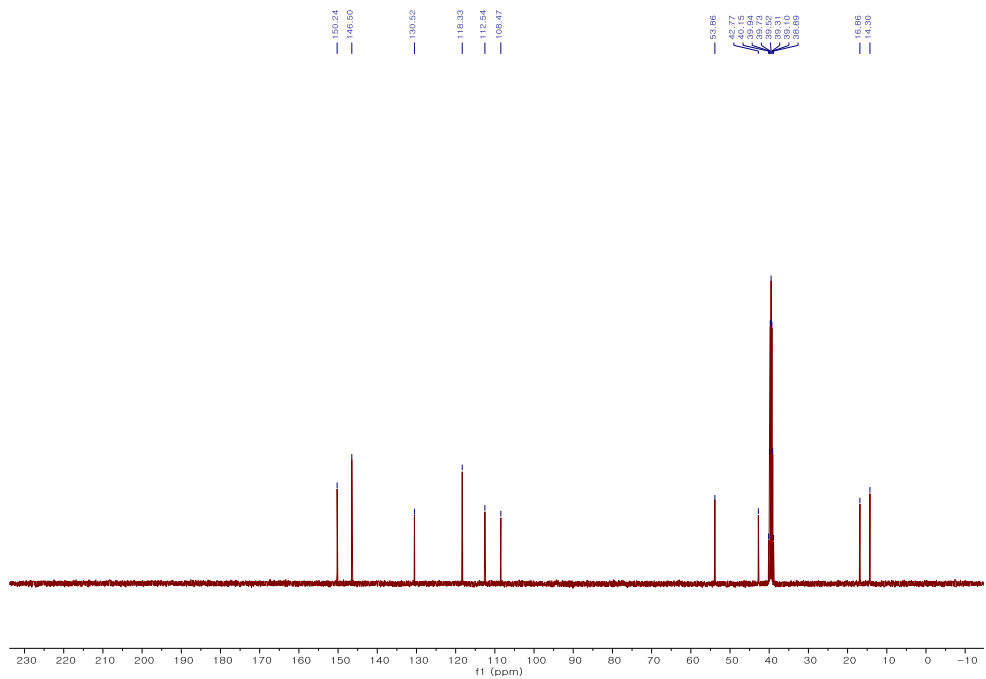
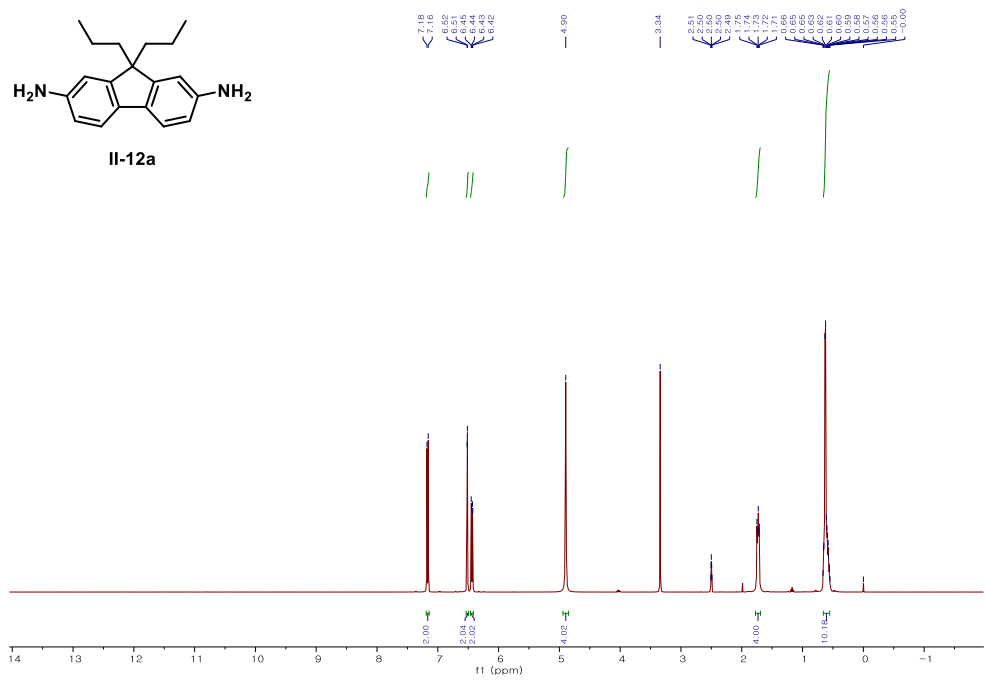
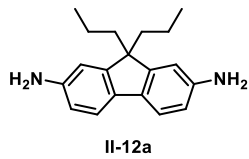


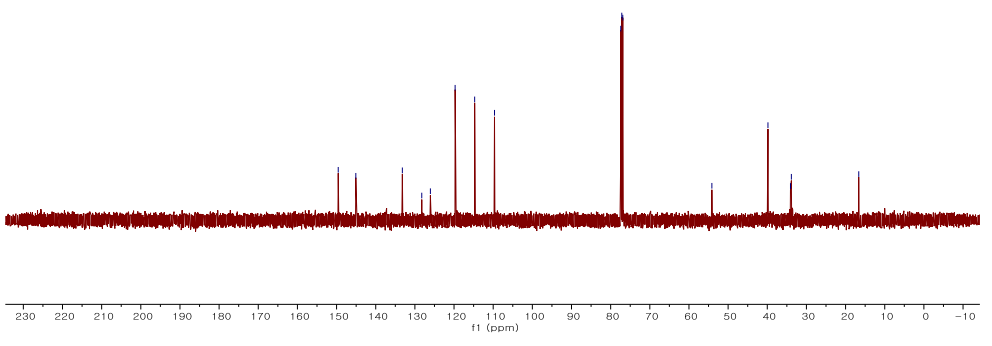
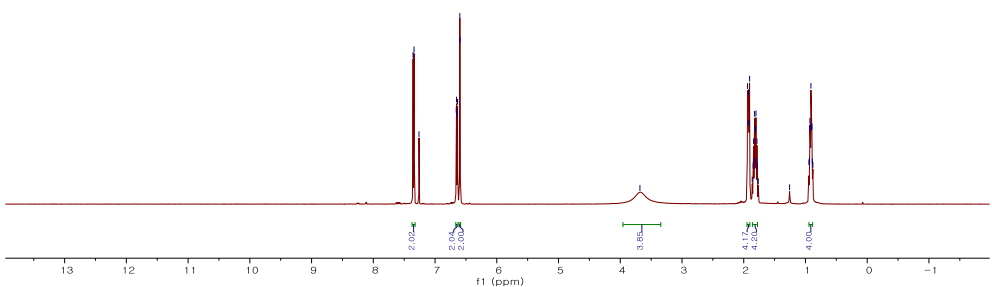
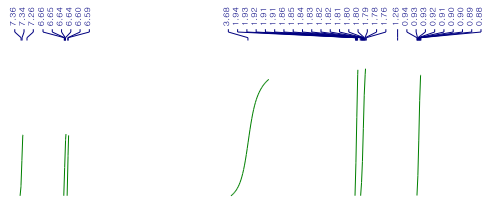
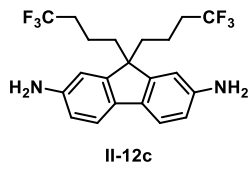


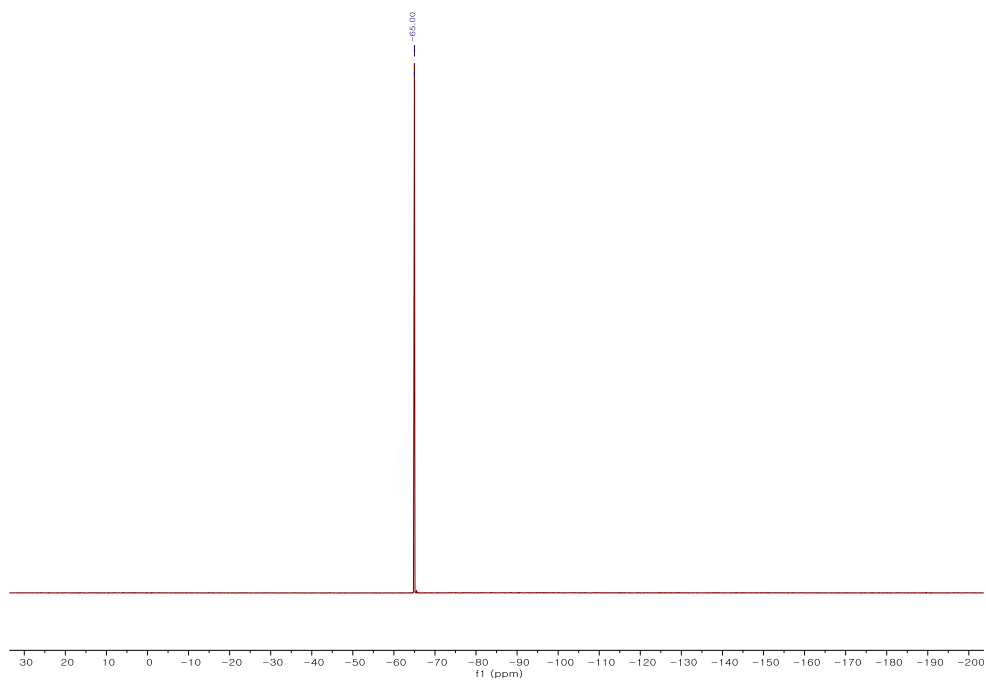
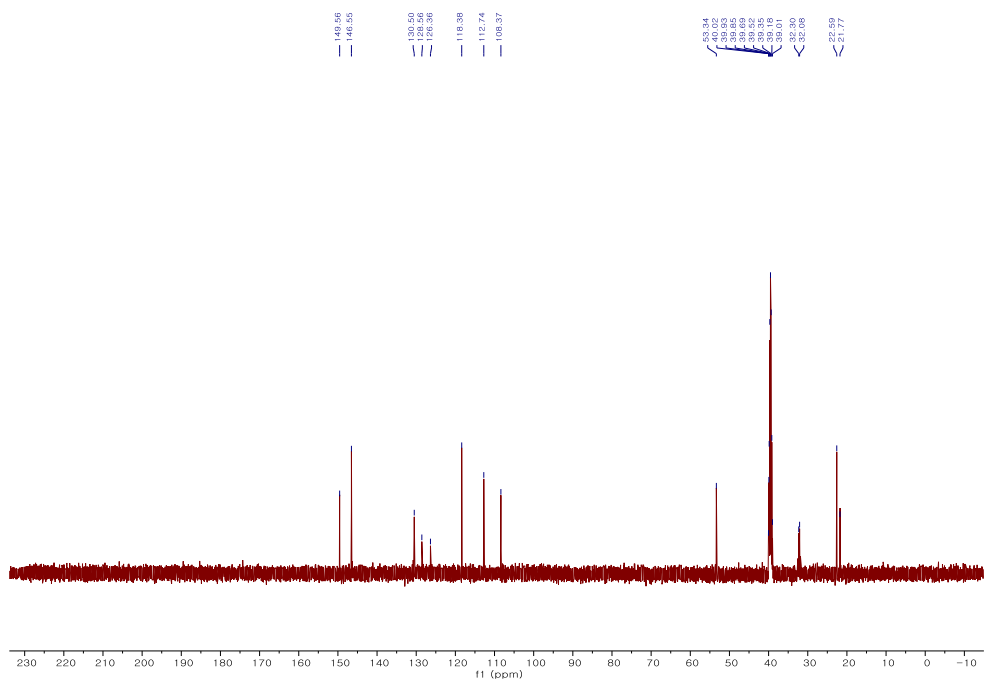


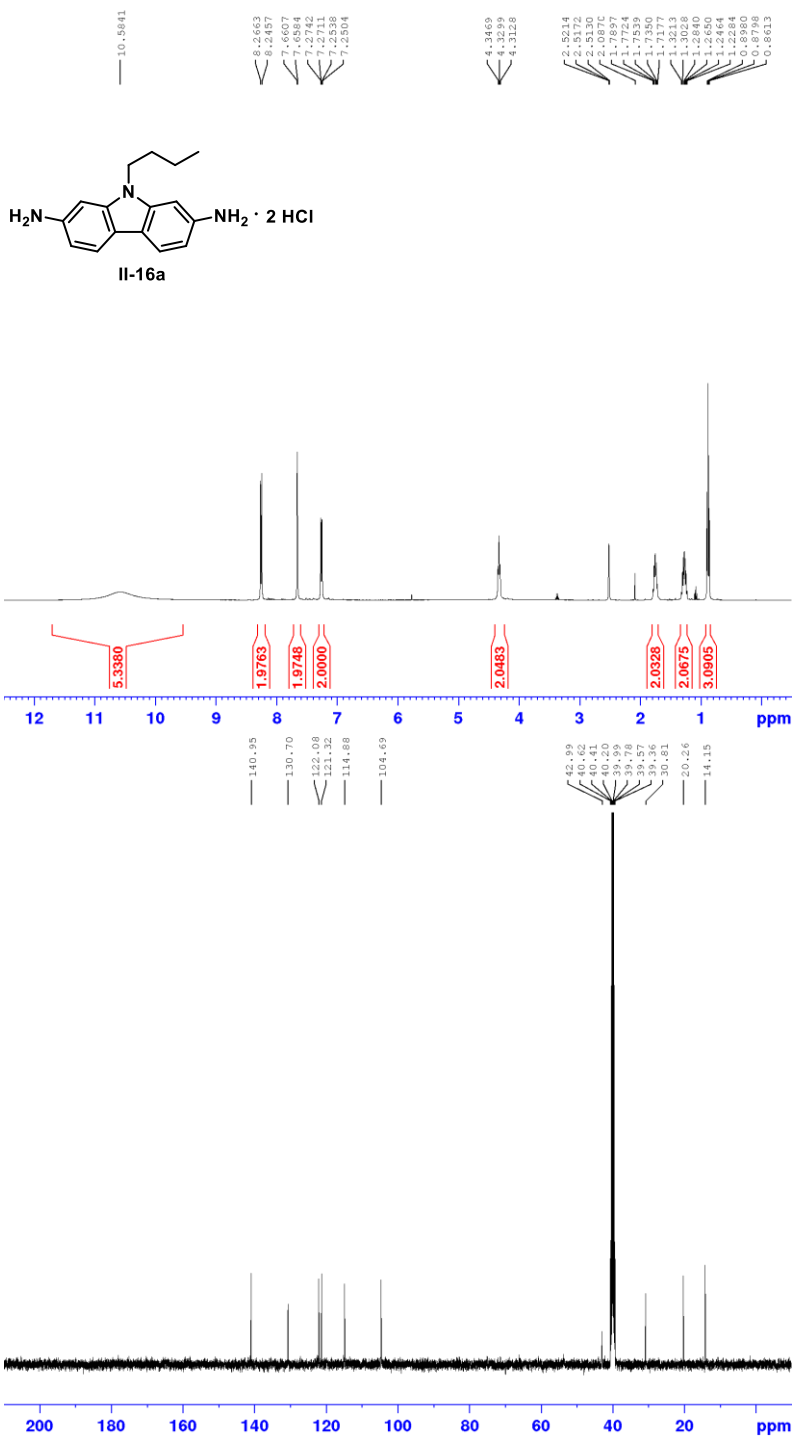


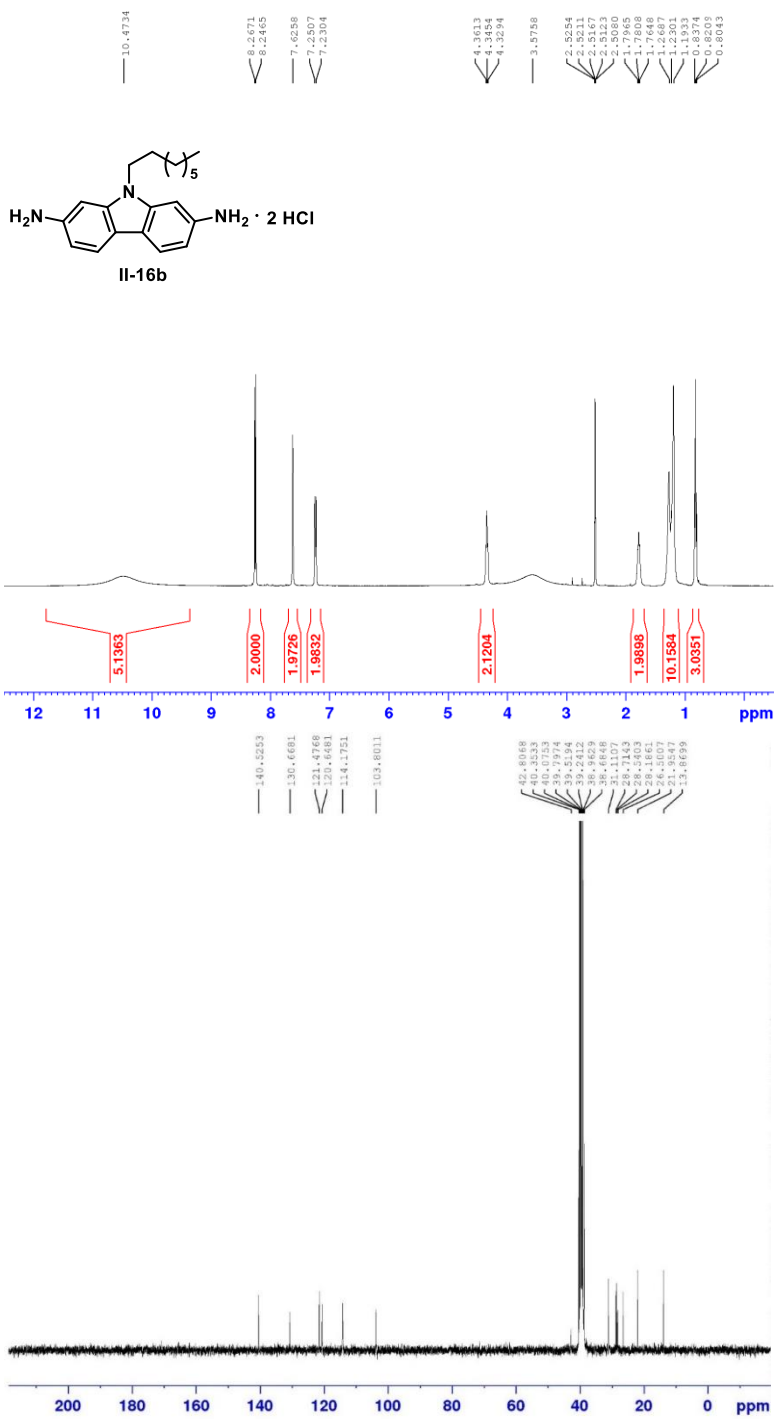


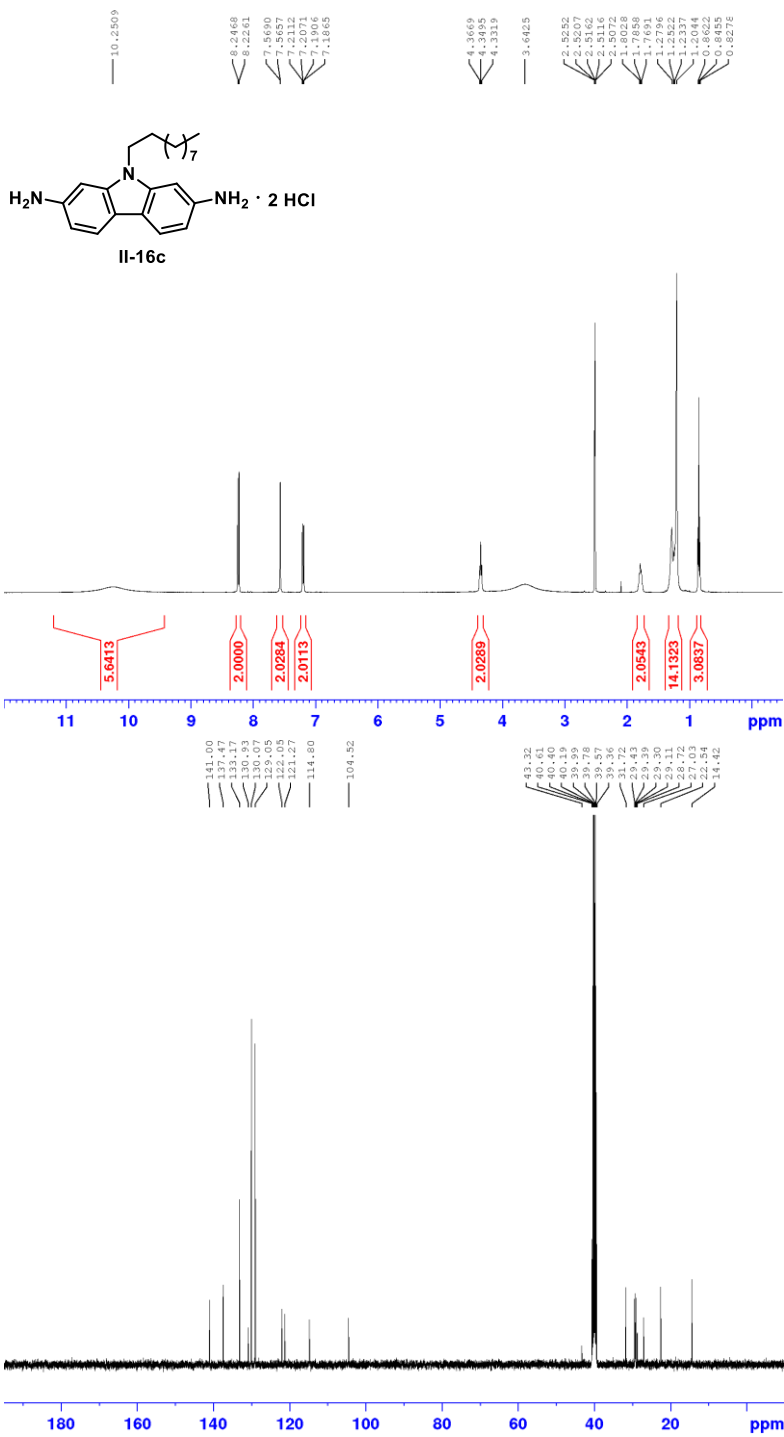


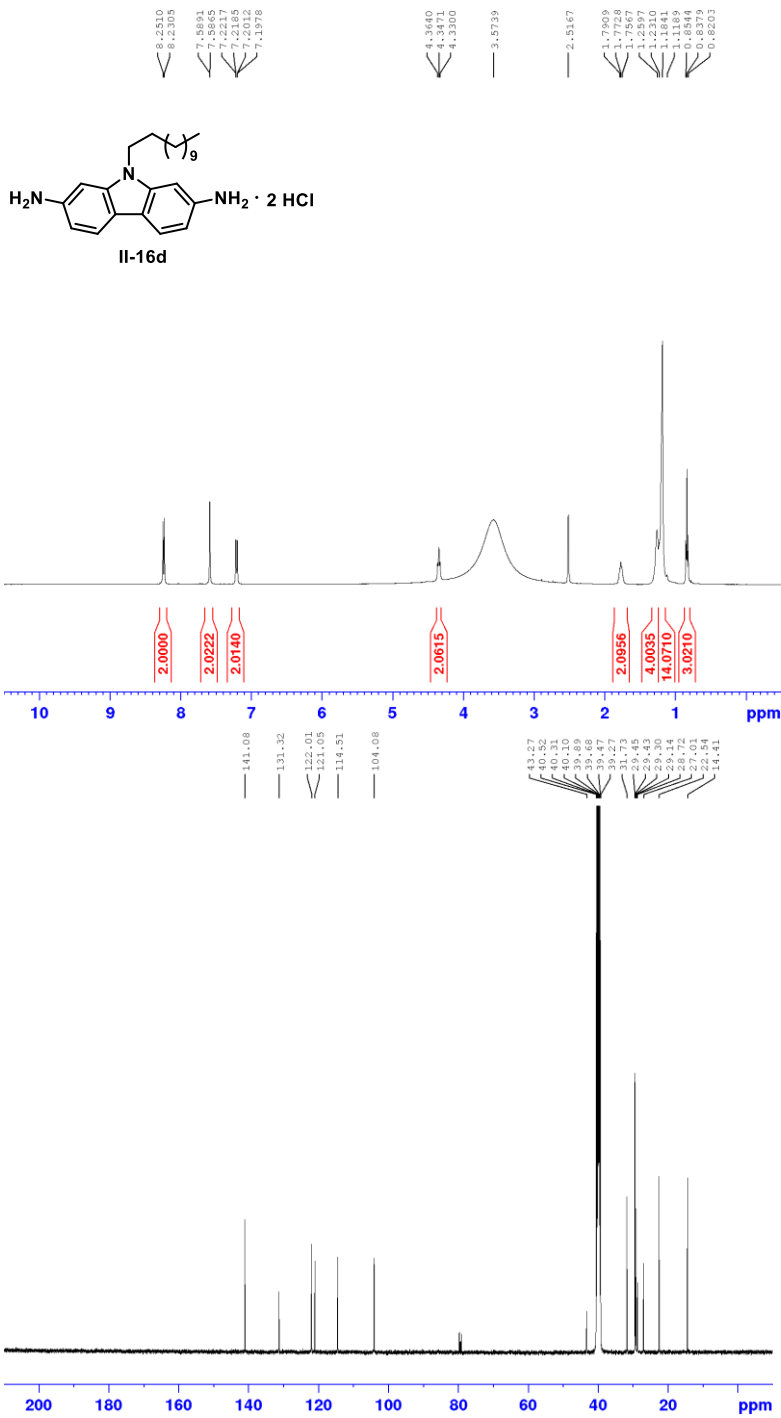


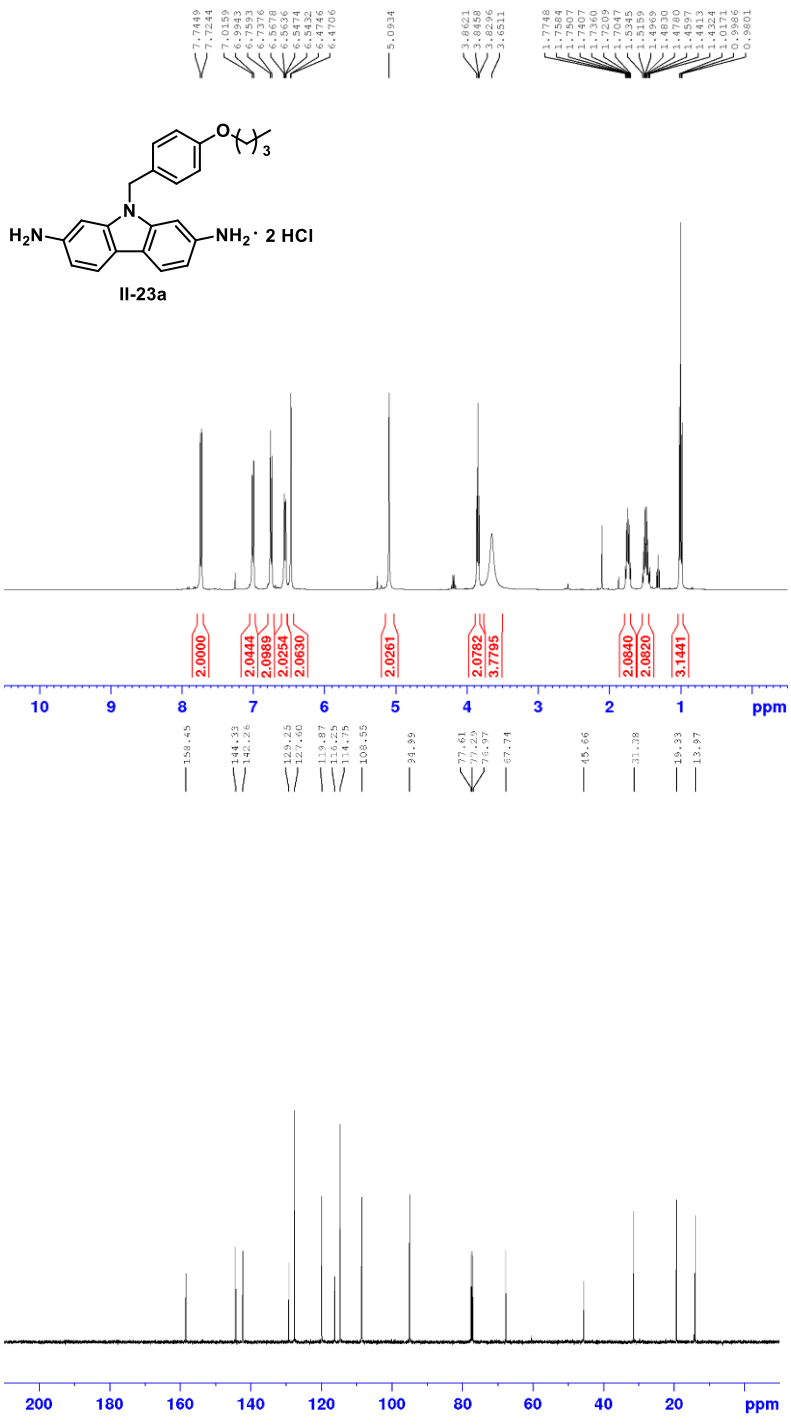


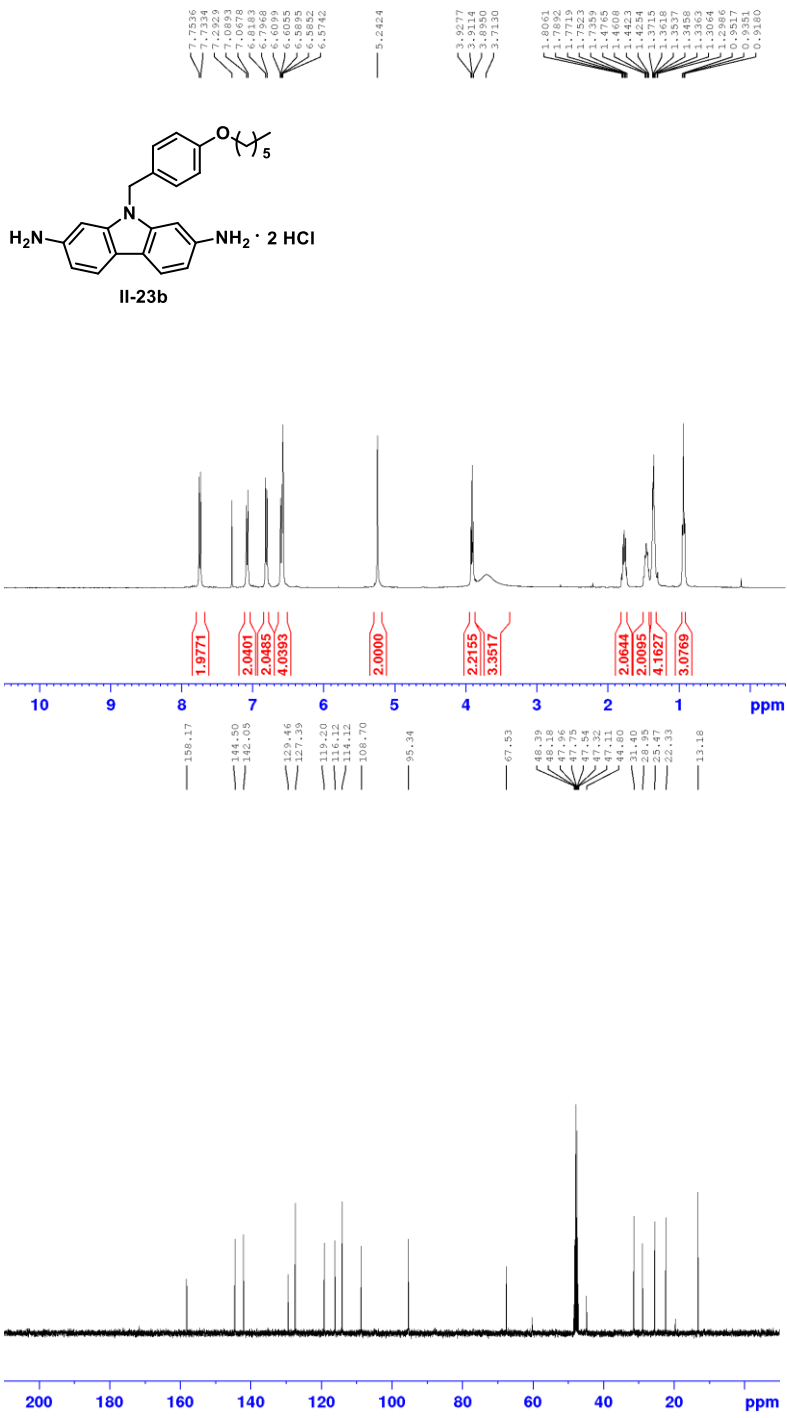


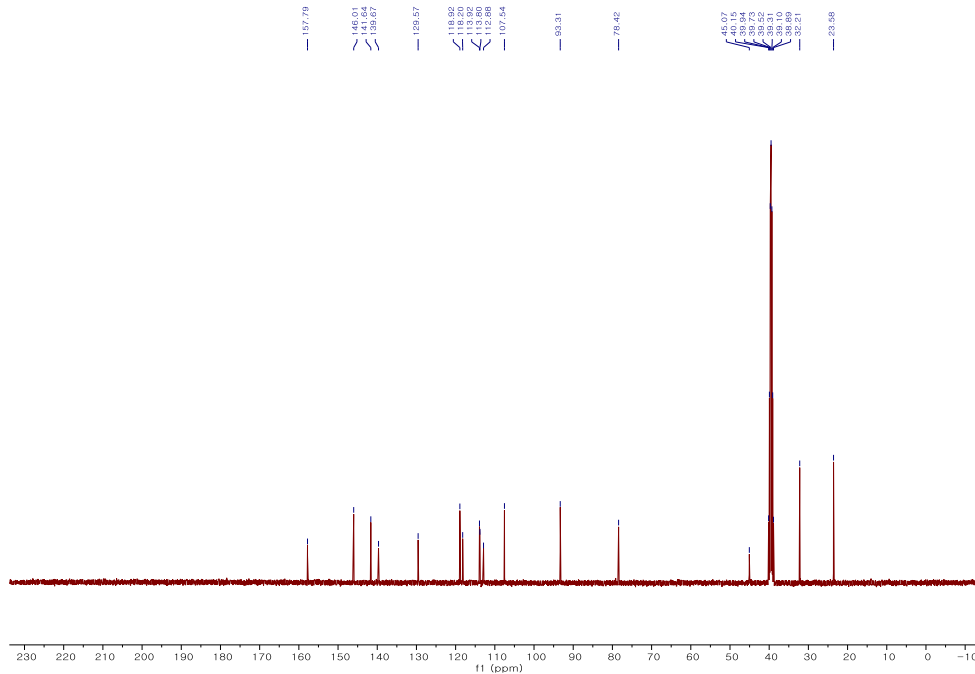
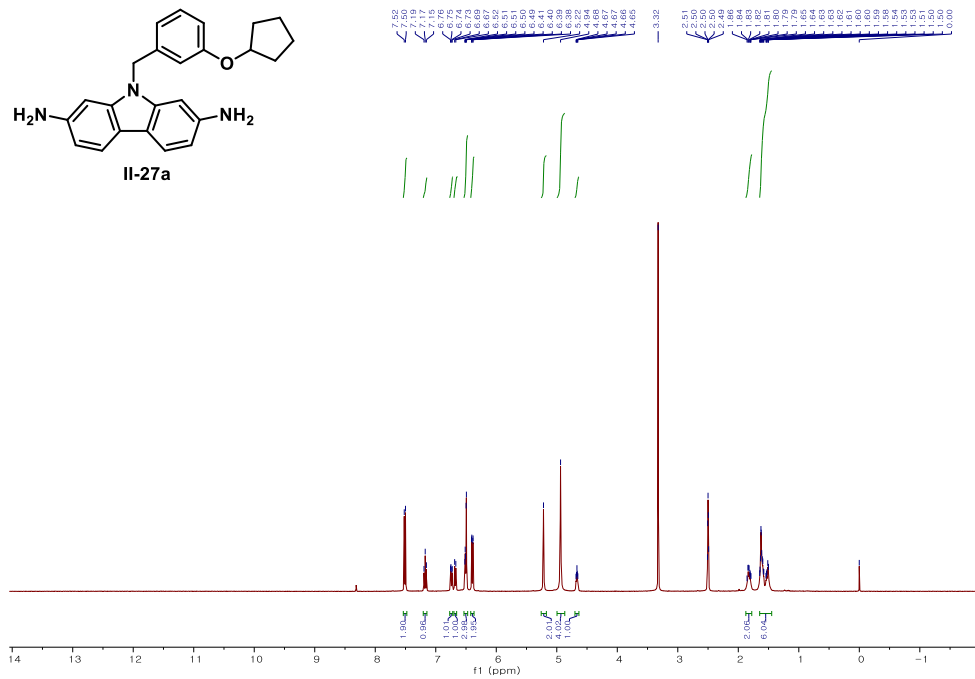
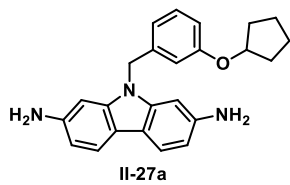


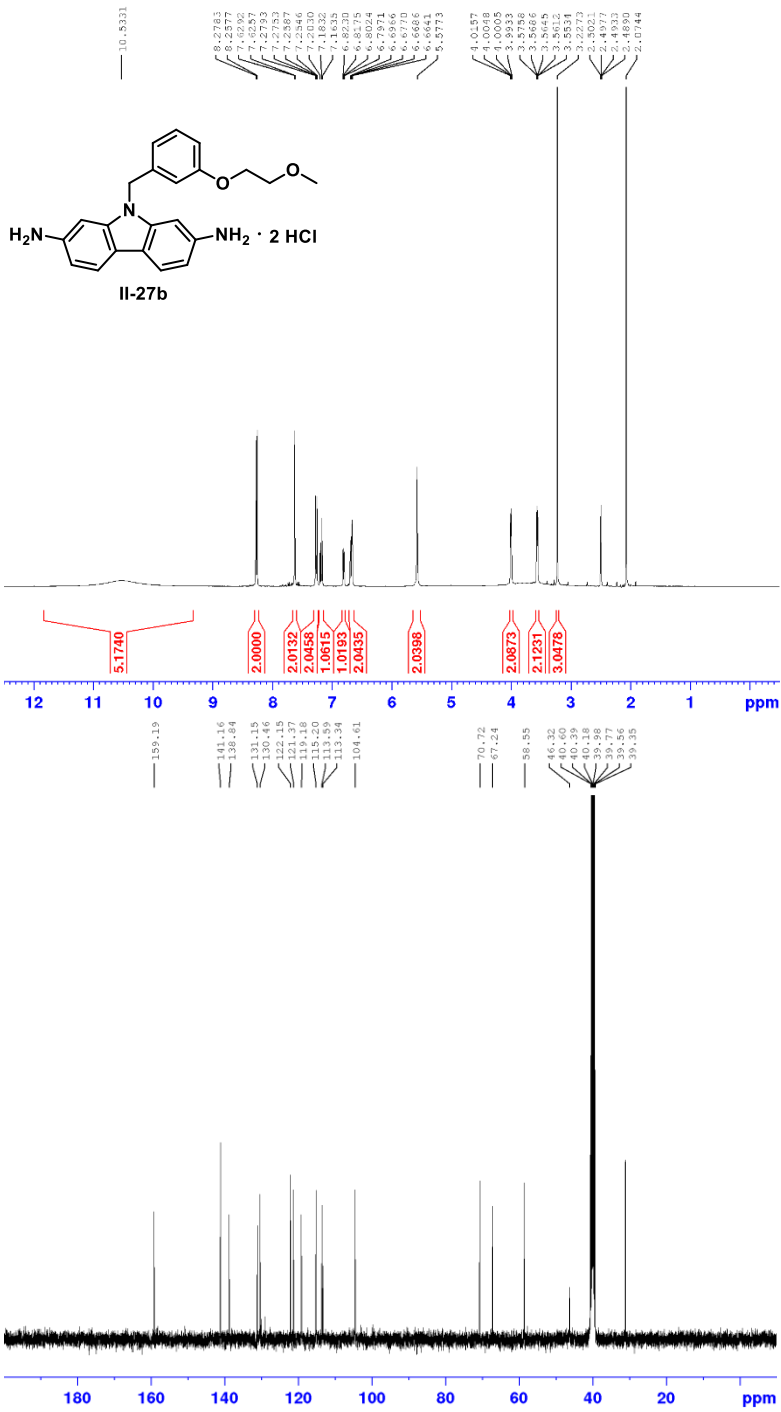


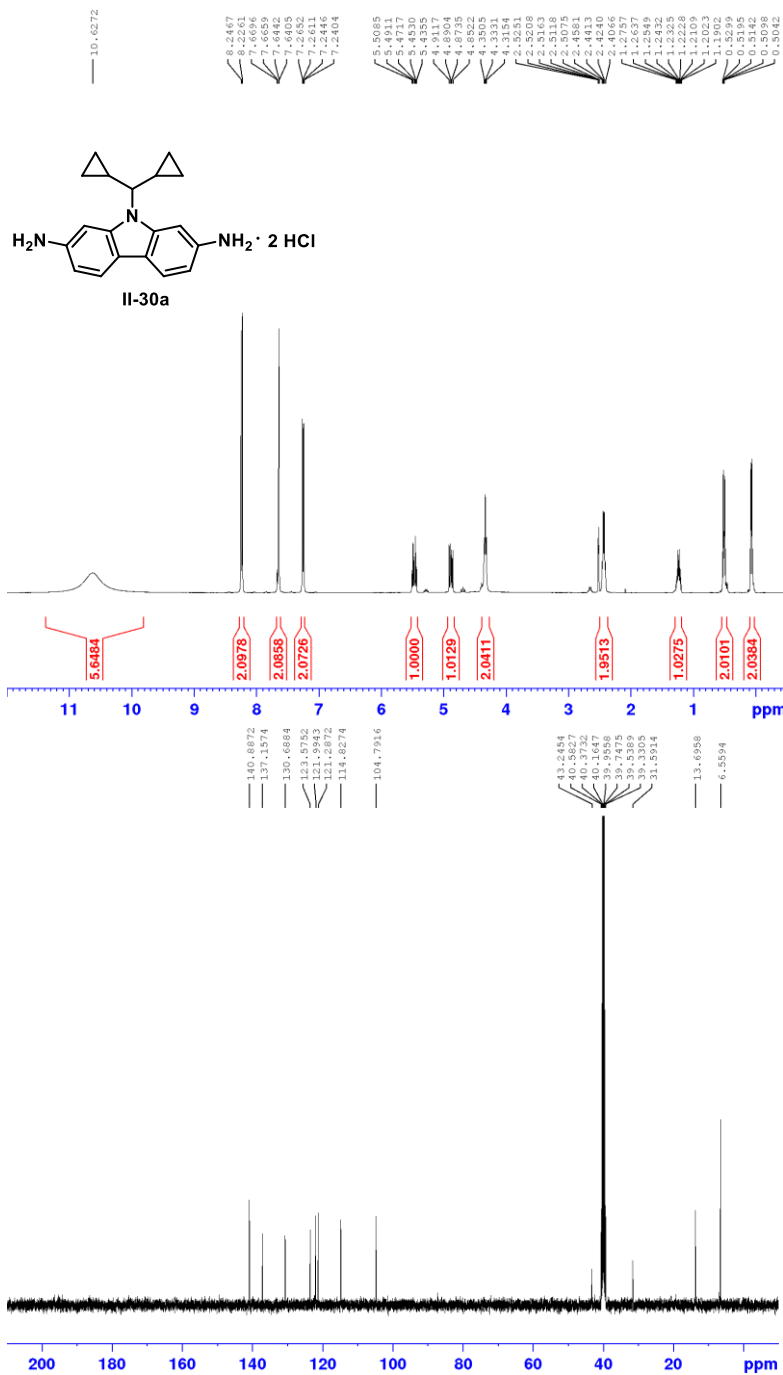


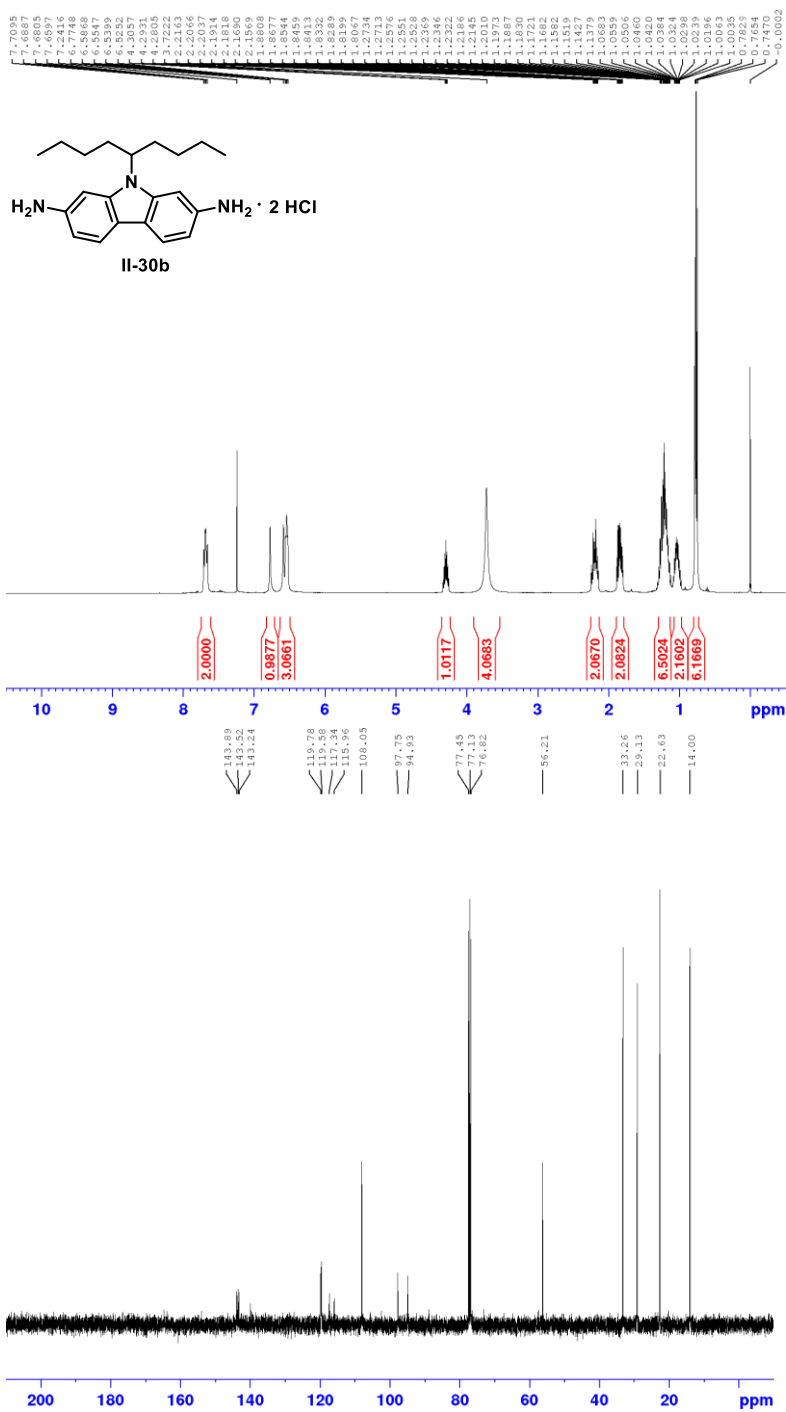


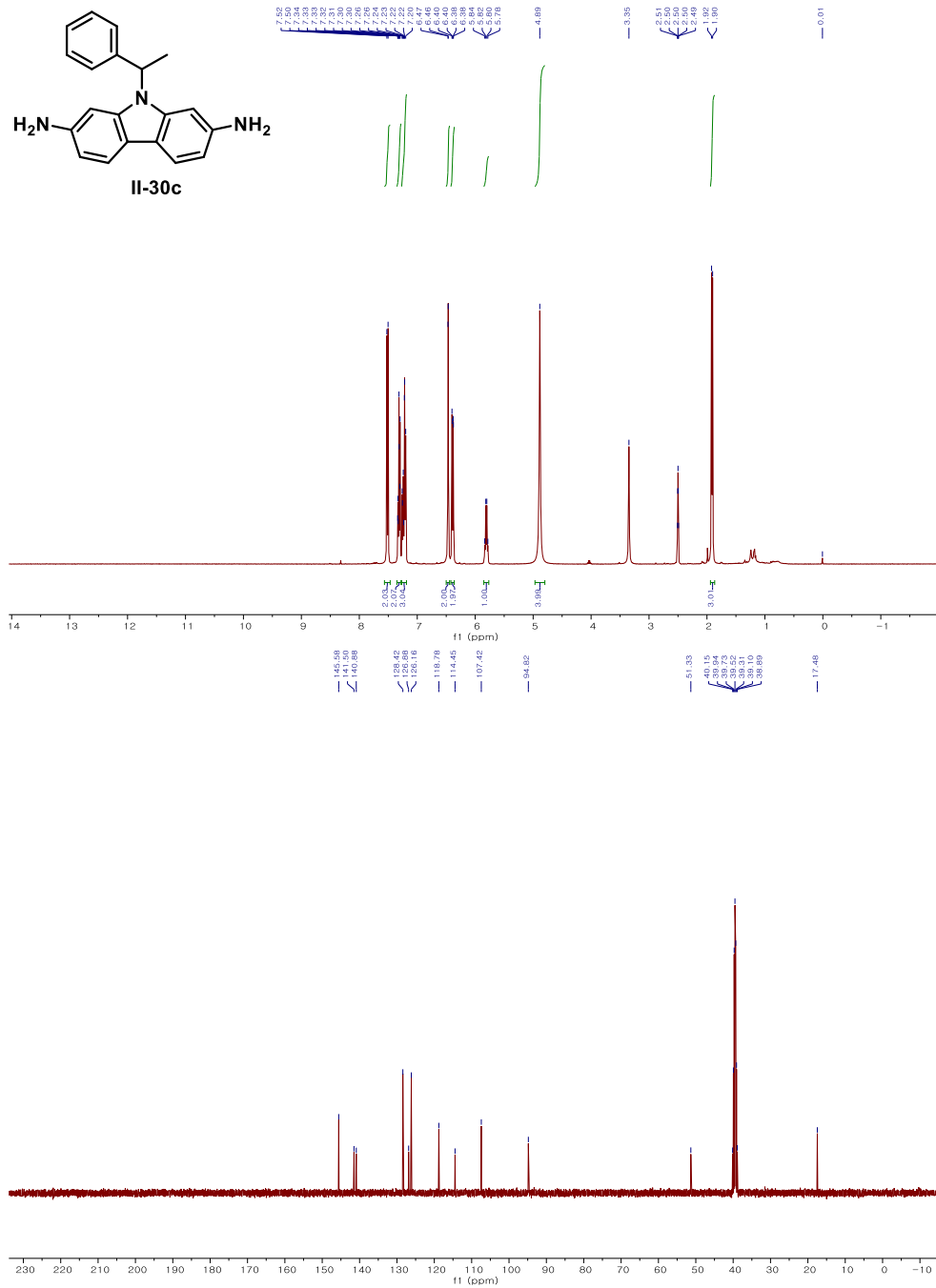
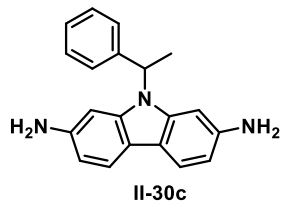


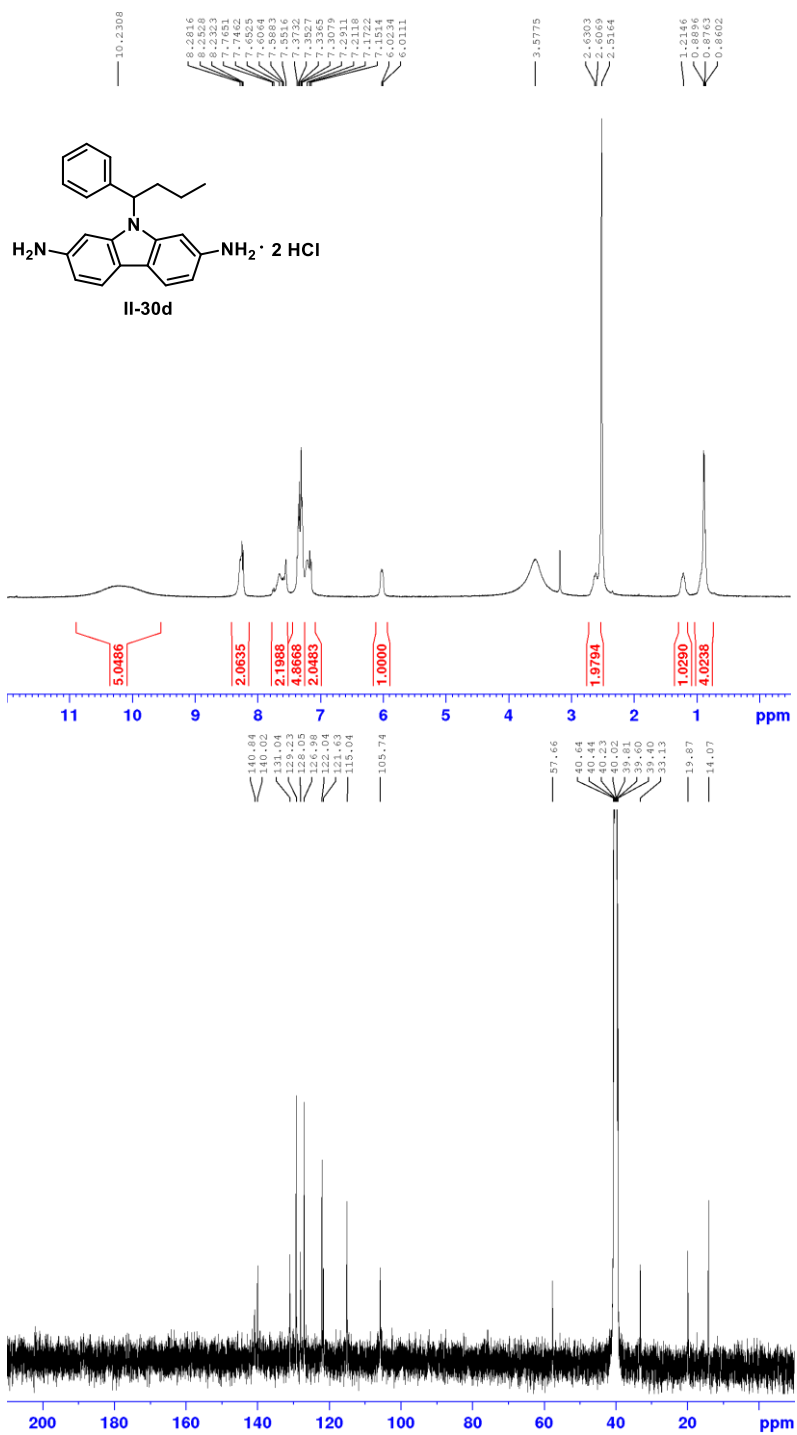


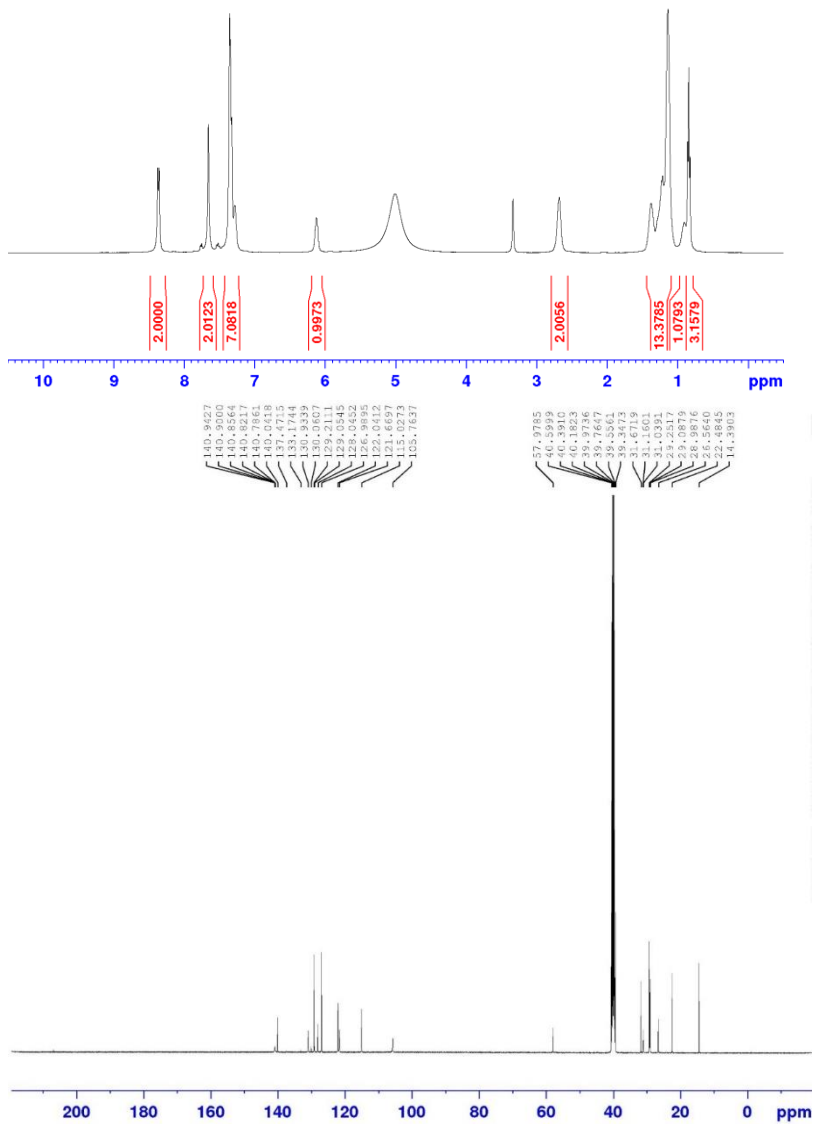
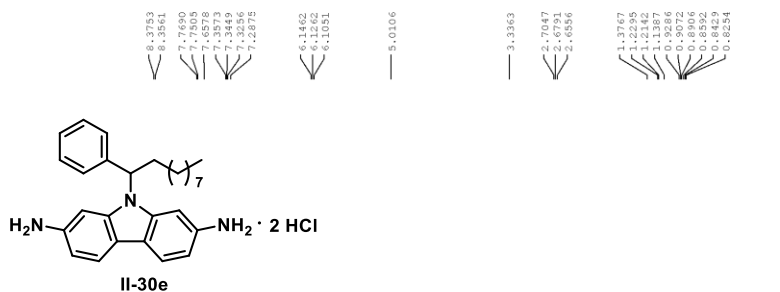






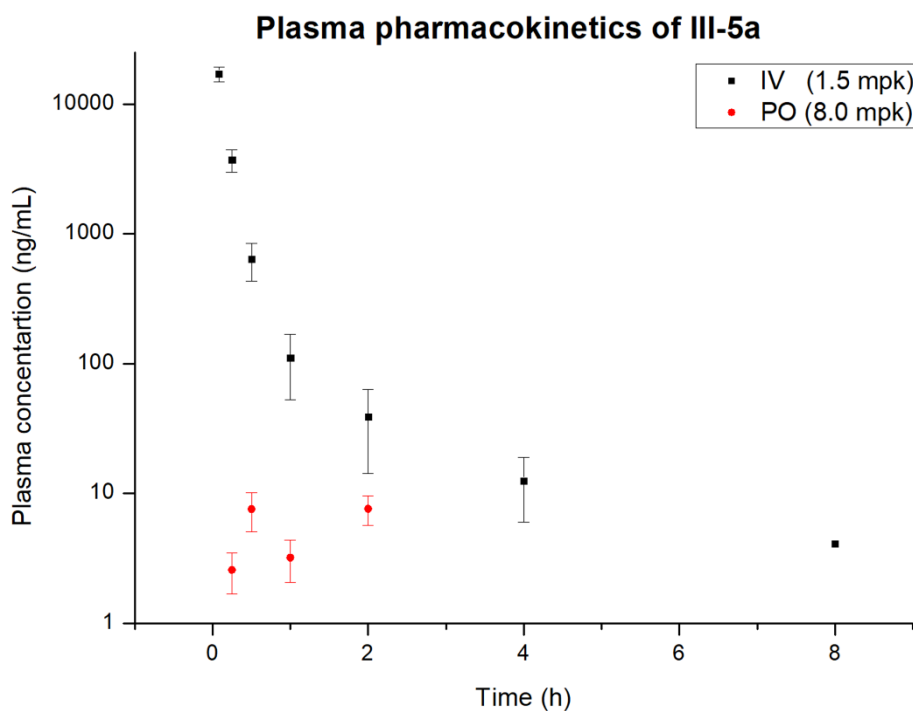






Chapter III

1. PK profiles and parameters of Compound III-5a



Parameter	IV (1.5 mg/kg)	PO (8.0 mg/kg)
t_{\max} (h) ^a		1
C_{\max} (ng/mL) ^b		7.8
AUC _{last} (h*ng/mL) ^c	4844	9.7
F (%) ^d		0.04

^aThe t_{\max} values were measured in triplicate and display mean.

^bThe C_{\max} values were measured in triplicate and display mean.

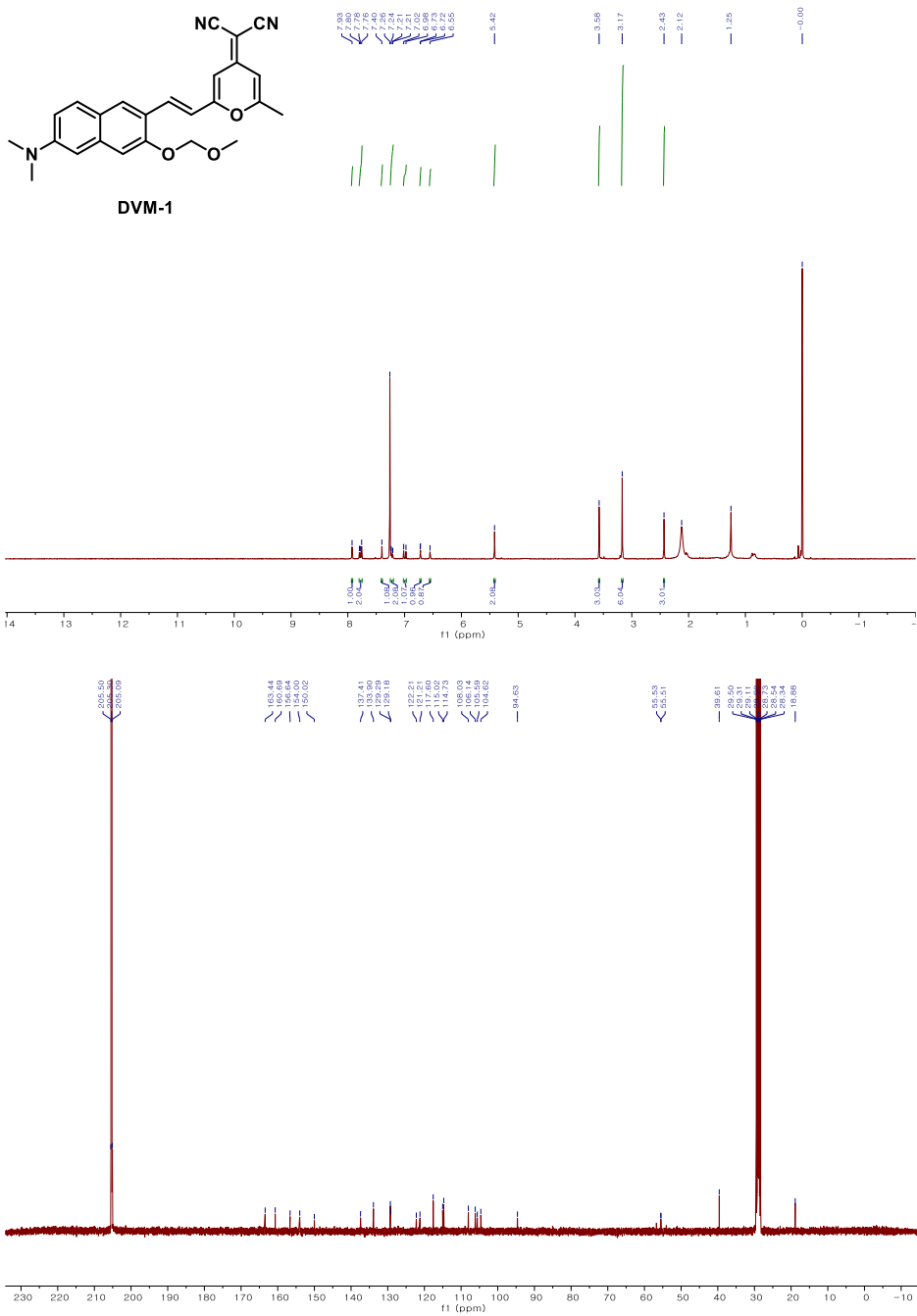
^cThe AUC values were measured in triplicate and display mean.

^dThe oral bioavailability was ratio of AUC value for IV and PO.

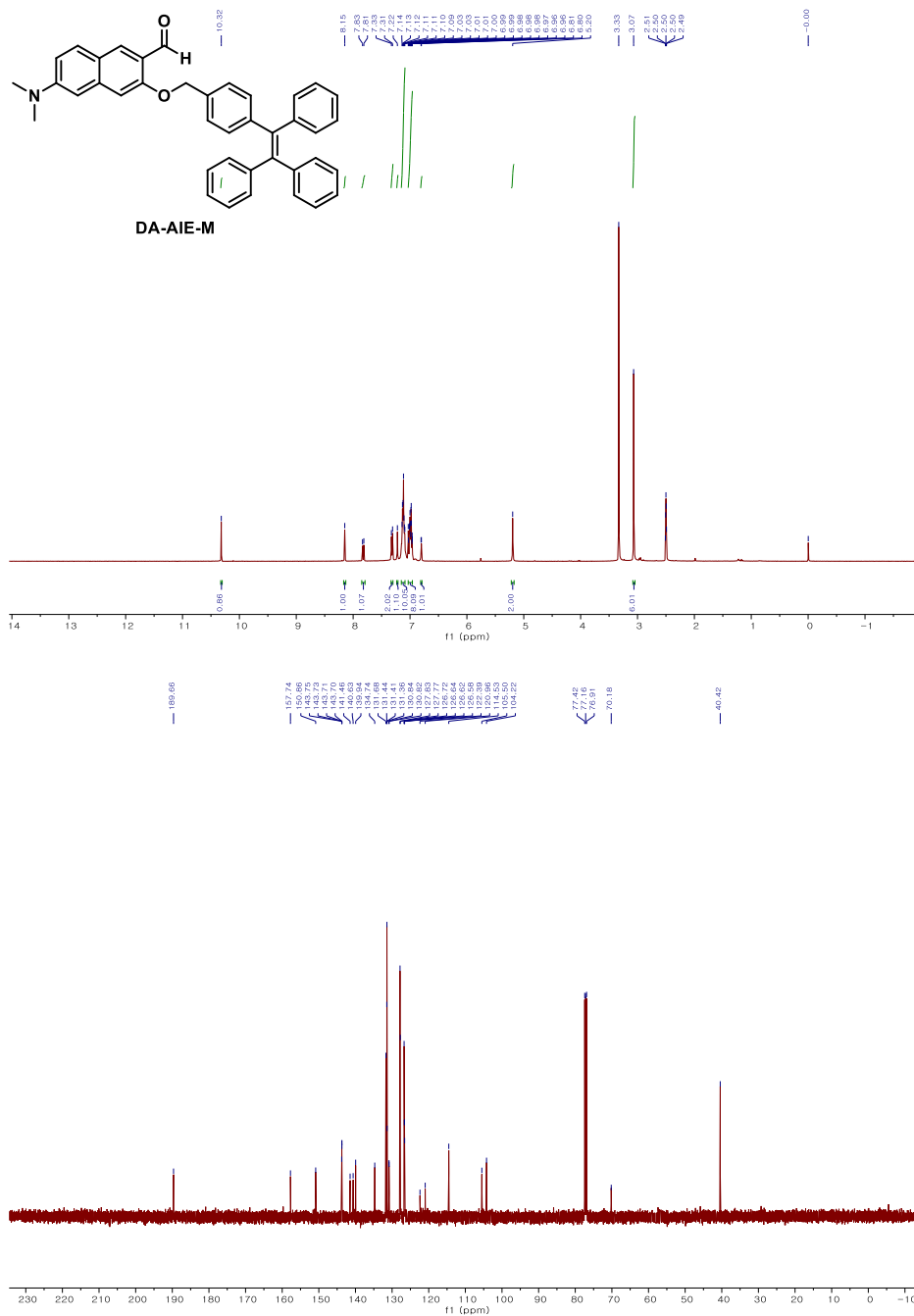
2. Raw PK data of Compound **III-10b** (only PO administered).

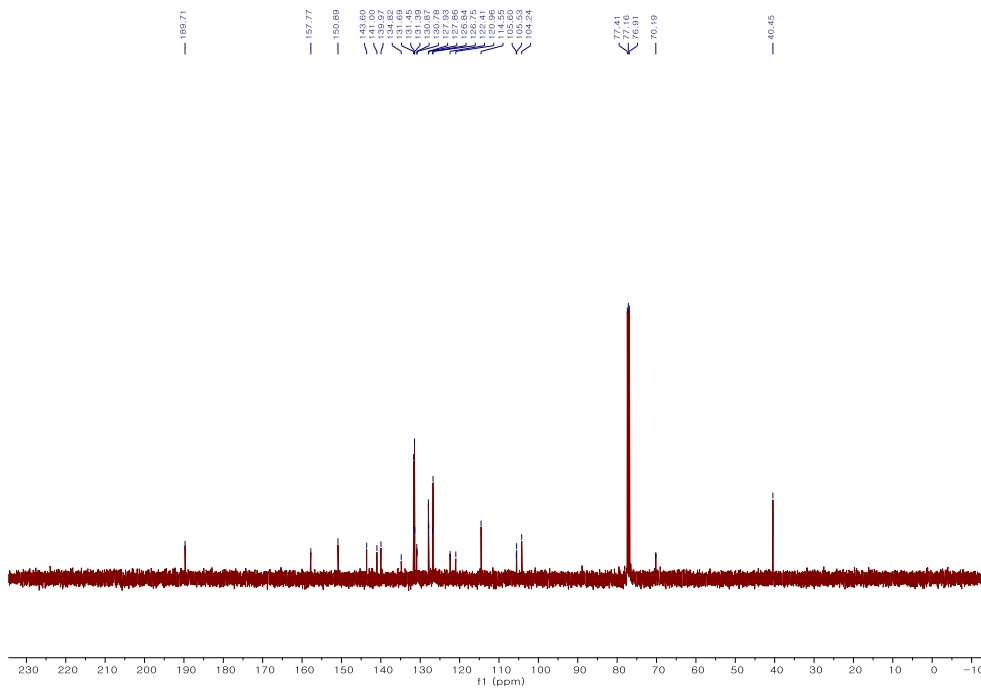
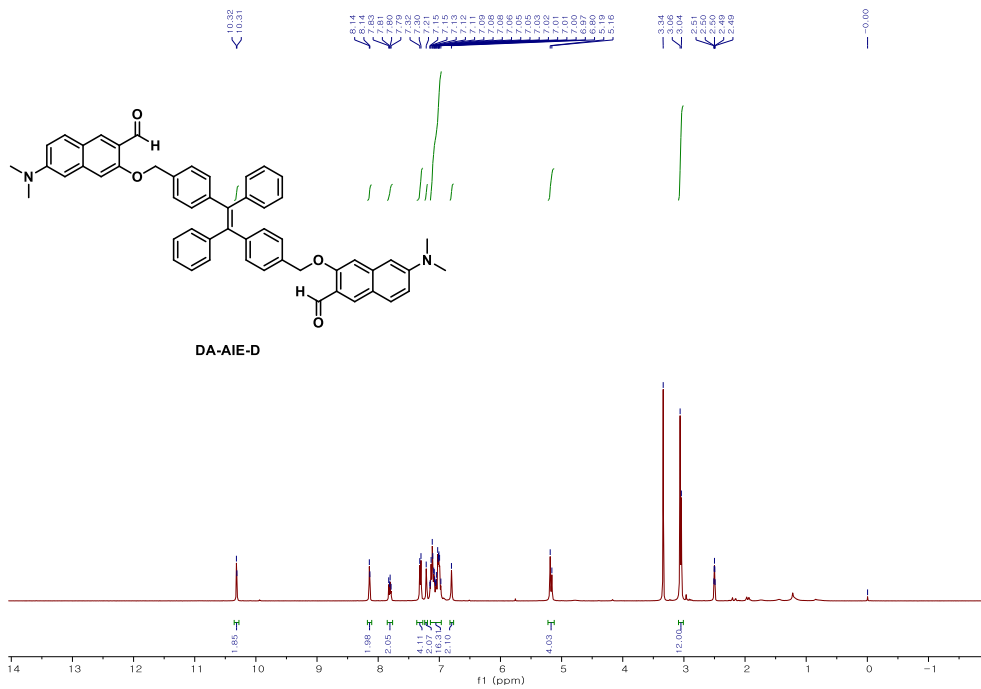
PO: 10 mg/kg		Plasma concentration (ng/mL)			
Time (h)/Animal No.	1001	1002	1003	Mean	SD
0	BLQ	BLQ	BLQ	NA	NA
0.25	BLQ	BLQ	BLQ	NA	NA
0.5	BLQ	BLQ	BLQ	NA	NA
1.0	2.4	BLQ	2.0	2.2	0.3
2	2.5	BLQ	BLQ	2.5	NA
4	BLQ	BLQ	BLQ	NA	NA
6	BLQ	BLQ	BLQ	NA	NA
8	BLQ	BLQ	BLQ	NA	NA
24	BLQ	BLQ	BLQ	NA	NA

Chapter IV

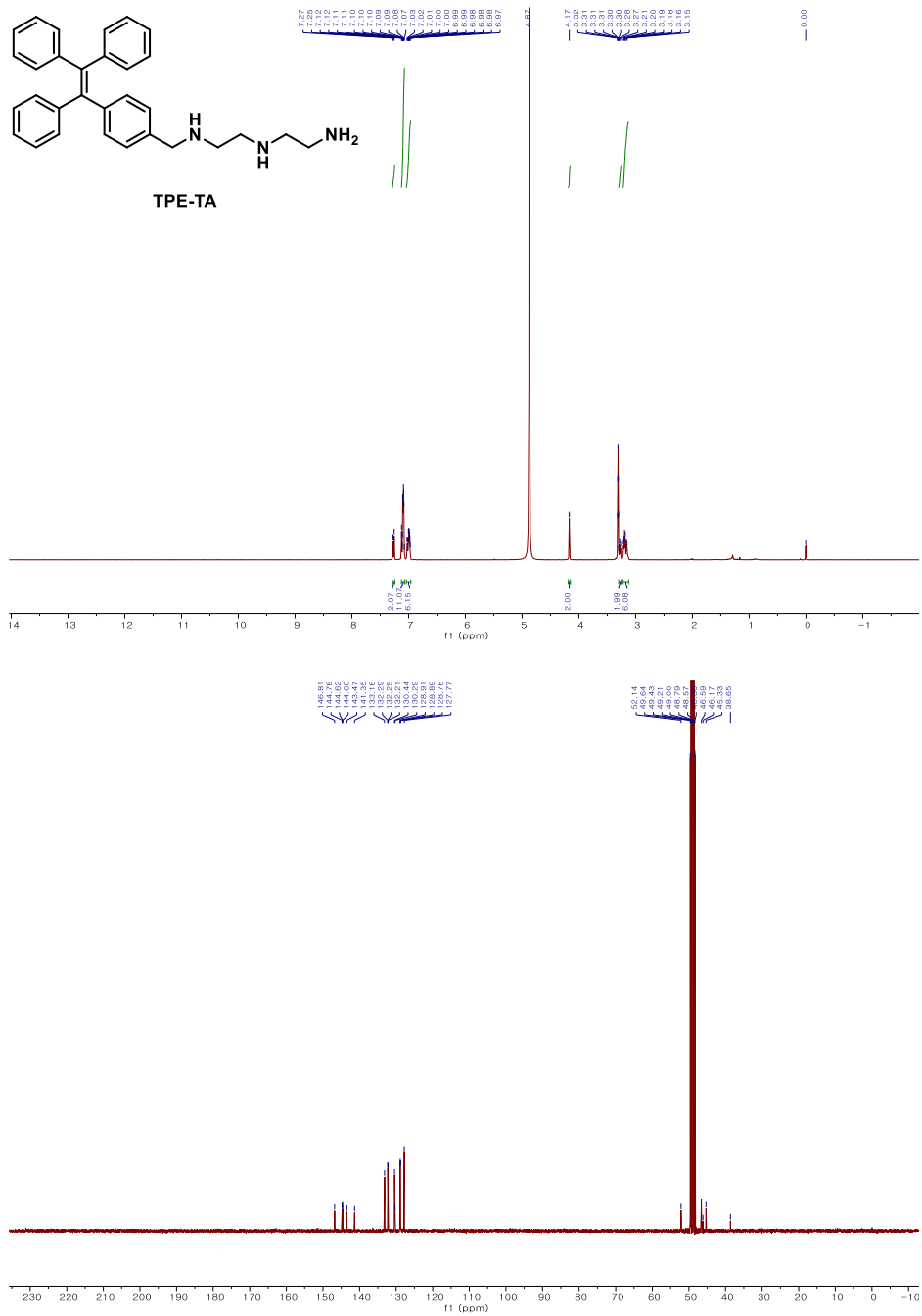


Chapter V





Chapter VI



국문초록

플루오렌 구조를 포함하는 새로운 C형간염 NS5A 저해제 개발 및 생체영상화를 위한 응집유도발광 기반의 새로운 유기 형광체의 합성

이 박사학위논문은 크게 C형간염 NS5A 저해제 개발과 새로운 유기 형광체 발굴에 관한 내용으로 나누어진다.

우선 C형간염 바이러스의 NS5A 단백질을 저해하는 효능을 지닌 여러 화합물을 발굴하는 과정을 서술한다. 새로운 저해제의 중심 골격으로 플루오렌으로 선택하였고 두번째 장에서는 그 중 9번 위치가 치환된 여러 2,7-다이아미노플루오렌 치환체들의 유전 독성 여부를 알아보았다. 그 결과 9,9-다이부틸-2,7-다이아미노플루오렌을 새로운 C형간염 NS5A 저해제의 중심 구조로 선택하였다. 세번째 장에서는 일련의 화합물들을 합성하여 생체 외 및 생체 내 검사를 통해 항바이러스성 활성을 가지고 있는지 여부를 조사하였다. 우리는 III-10b 화합물이 L31V, Y93H 돌연변이 뿐 아니라 동시에 둘의 돌연변이가 같이 일어난 NS5A 단백질에 대해서도 아주 훌륭한 저해 활성을 보임을 보고하였다.

다음으로는 생체영상화에 사용하기 위한 새로운 유기형광체의 설계 및 합성에 관하여 다룬다. 네번째 장에서는 근적외선 형광체인 DVM-1에 대하여 소개하고 있다. DVM-1은 물이나 완충액 등에서는 형광을 내지 않으므로 생체영상화에 사용하기 위해서 양쪽성 고분자를 이용, 마이셀 구조(DVM-1L)를 형성하였다. 이렇게 합성된 물질은 물에서 높은 용해도 및 근적외선 영역에서의 형광을 나타내었고 세포 기질 내에서 밝은 형광 신호를 보여주었다. 다섯번째 장에서는 기존의 전자주개-받개 형광체와 응집유도발광 기반의 형광체가 sp^3 결합으로 연결된 새로운 형광체에 대해 다루었다. 새롭게 합성된 형광체들은 기존의 전자주개-받개 형광체와 유사한 광학적 특성을 보이는데 이는 HOMO와 LUMO 구조가 전자주개-받개 형광체에 의해서 결정되기 때문이다. 여섯번째 장에서는 응집유도발광 현상을 이용한 ATP를 탐지하는 형광탐침자에 대해 서술하고 있다. 새로운 형광체는 응집유도발광 성질을 지닌 TPE 물질에 ATP와의 선택적인 정전기적 인력을 이용하기 위해서 3개의 아민기를 도입하여 설계, 합성되었다. AAP-1이라 명명한 형광체는 암세포나 심지어 배아줄기세포 내에서도 ATP의 영상화에 성공적으로 이용되었다.

주요어: 유전 독성, NS5A 저해제, 형광탐침자, 근적외선 센서, 응집유도발광.

학번: 2017-26933